INFORMATION TO USERS

.

University of Alberta

Nonlinear effects in
two-layer, frontal-geostrophic models
of surface ocean fronts

by

Richard H. Karsten ©

A thesis submitted to the Faculty of Graduate Studies and Research
in partial fulfillment of the requirements for the degree of
Doctor of Philosophy

in

Applied Mathematics

Department of Mathematical Sciences

Edmonton, Alberta
Fall, 1998

Canada

University of Alberta

Library Release Form

Name of Author: Richard H. Karsten
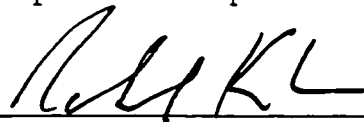
Title of Thesis: Nonlinear effects in two-layer, frontal-geostrophic models of surface ocean fronts

Degree: Doctor of Philosophy

Year this Degree Granted: 1998
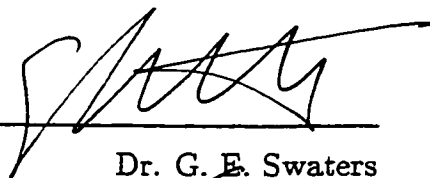
Department of Mathematical Sciences
University of Alberta
Edmonton, Alberta
Canada, T6G 2G1

August 19, 1998
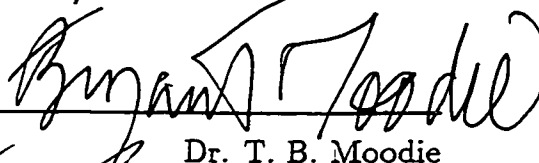
University of Alberta

Faculty of Graduate Studies and Research
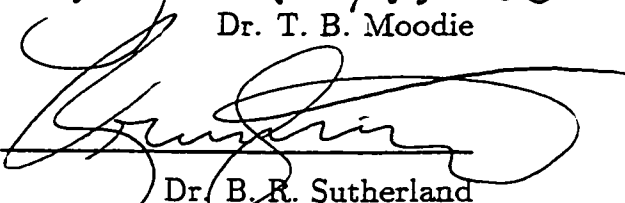
The undersigned certify that they have read and recommend to the Faculty of Graduate Studies and Research for acceptance, a thesis entitled **Nonlinear effects in two-layer, frontal-geostrophic models of surface ocean fronts** submitted by **Richard H. Karsten** in partial fulfillment of the requirements for the degree of **Doctor of Philosophy** in **Applied Mathematics.**
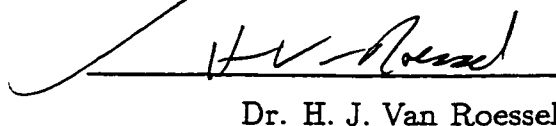
Dr. G. E. Swaters
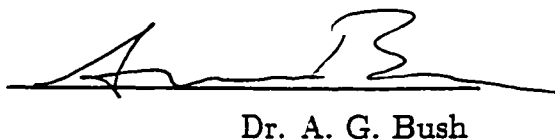
Dr. T. B. Moodie
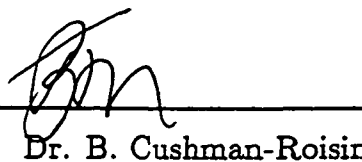
Dr. B. R. Sutherland

Dr. H. J. Van Roessel

Dr. A. G. Bush

Dr. B. Cushman-Roisin
Dartmouth College

Date: August 11, 1998

Abstract

We examine two-layer, frontal-geostrophic (FG) models concentrating on non-linear effects. The FG models are geostrophic to leading order but allow large variations in layer depths by including the large inertial terms associated with frontal effects.

Using a baroclinic/barotropic formalism. a general two-layer FG model on a β-plane is derived. This model leads to the discussion of four important models, which differ in the scaling of the layer depth ratio and the β-plane effect. We examine the nonlinear effects in these models using three forms of analysis. First. we establish nonlinear invariants of the model and use these to establish nonlinear stability theorems. Second, we present a finite amplitude analysis which examines the effect of nonlinearities on a linear wave solution. Finally. we present the results of numerical simulations of each model.

For the models where the β-plane effect dominates the barotropic equation. linear instability can only occur if the potential vorticity gradients vanish and all linearly sloping fronts are nonlinearly stable. Nonlinear effects act to reorganize linear waves into wave packet/soliton structures that have a larger but bounded amplitude. While the presence of shear in the flow may lead to initial instability, this instability acts only to remove the shear and releases little potential energy. In the long term, variations to a zonal flow evolve toward large-scale, small-amplitude meanders or alternating jets of weak-zonal flow.

If on the other hand the barotropic equation includes strong quasigeostrophic terms, the barotropic flow acts to destabilize the front. If the baroclinic equation does not include frontal effects, rapid linear growth occurs at small scales. However, if frontal effects are included in the baroclinic equation, they act to steepen the den-

sity gradient. This counteracts the small-scale growth, and leads to the dominance of waves with finite wavelength. Nonlinear effects act to suppress linear growth at small zonal length scales but enhance this growth at large zonal scales. This leads to large-scale meanders of frontal outcroppings that can pinch off to form warm-core eddies or entrap lower-layer fluid to form cold-core eddies. These large-scale structures efficiently release the mean potential energy of the front.

And the three men I admire most-
the Father, Son, and the Holy Ghost-
They caught the last train for the coast
The day the music died

<div align="right">Don McLean</div>

Acknowledgement

In the past years I have received invaluable support from a variety of sources. First and foremost, my supervisor Dr. Gordon Swaters deserves special recognition. I had the fortune of having him as my guide into the world of scientific research and geophysical fluid dynamics. His enthusiasm, insight, and dedication served as great inspiration. For all his contributions to this thesis, and more importantly to my life, I owe an unpayable debt of gratitude.

I would also like to thank the members of my defence committee. Their contributions throughout the process of writing this thesis have vastly improved the final product. As well, I owe a great deal to my colleagues, Carol Slomp, Curtis Mooney, Francis Poulin, Pat Montgomery, and, especially, Matt Reszka, who through countless discussions have not only aided my research but made it an enjoyable experience. I'd like to thank all the professors and staff of the Department of Mathematical Sciences who have assisted and supported me throughout the years. And a special thanks to all the graduate students and friends who have provided the proper amount of diversion to keep me sane.

I'd like to thank my family who have provided support in so many ways. Finally, I'd like to thank my wife Julie. Her encouragement, patience, and love made this thesis possible.

Table of Contents

List of Figures

List of Tables

Chapter 1.

Introduction

Large-scale oceanic fronts are a common phenomenon in the world's oceans. A front consists of a large change in the density (often a change in temperature and/or salinity) over a short length scale, and is seen in observations as a concentration of isopycnals (lines of constant density). For example, observations taken in the North Pacific (Roden, 1975) illustrate a typical surface front as a series of concentrated isopycnals intersecting the surface (see discussion in §2 and Figure 2.1). Roden (1975) documented observations of numerous fronts of the North Pacific including the Subtropical and Subarctic fronts as well as Asian coastal currents such as the Kuroshio and the Oyashio (see Figure 1.1). Coastal currents, which exist in all the world's oceans, may also take the form of isolated fronts overlying bottom topography. These vary from weaker eastern boundary currents such as the California Current (see Ikeda *et al.*, 1984) to the crucial western boundary currents such as the Kuroshio (see Robinson, 1983).

Fronts can play two important but opposite roles depending on their stability. When stable, these fronts are important natural barriers (Cushman-Roisin, 1986). They act to hinder both horizontal and vertical motion restricting the transfer of heat and momentum as well as biological nutrients. Stable fronts also play a role in mid-depth water formation, as they force the subduction of cooler waters travelling equatorward (Spall, 1995). Such stable fronts as those observed in the Subtropical Convergence Zone of the North Atlantic are known to play an important role in general ocean circulation.

On the other hand, when fronts are unstable they enhance horizontal and vertical motion. Fronts are large sources of potential energy, which is stored as they form. This energy can be released if the front becomes unstable and small variations in the front grow to form large meanders and eddies. Such meanders and eddies are a source of a great deal of the mesoscale mixing and transport that occurs in the oceans. Mixing and transport play an essential role in the general circulation of the oceans. A major source of error in ocean circulation models is the improper resolution and inclusion of the effects of eddy transport and mixing that occur on the western boundary currents and along the frontal outcroppings of

1

Figure 1.1: Various fronts and boundary currents of the North Pacific as shown in Roden (1975). The arrows represent the currents that help maintain the fronts. The location of the subtropical front cross-section shown in Figure 2.1 is also labelled.
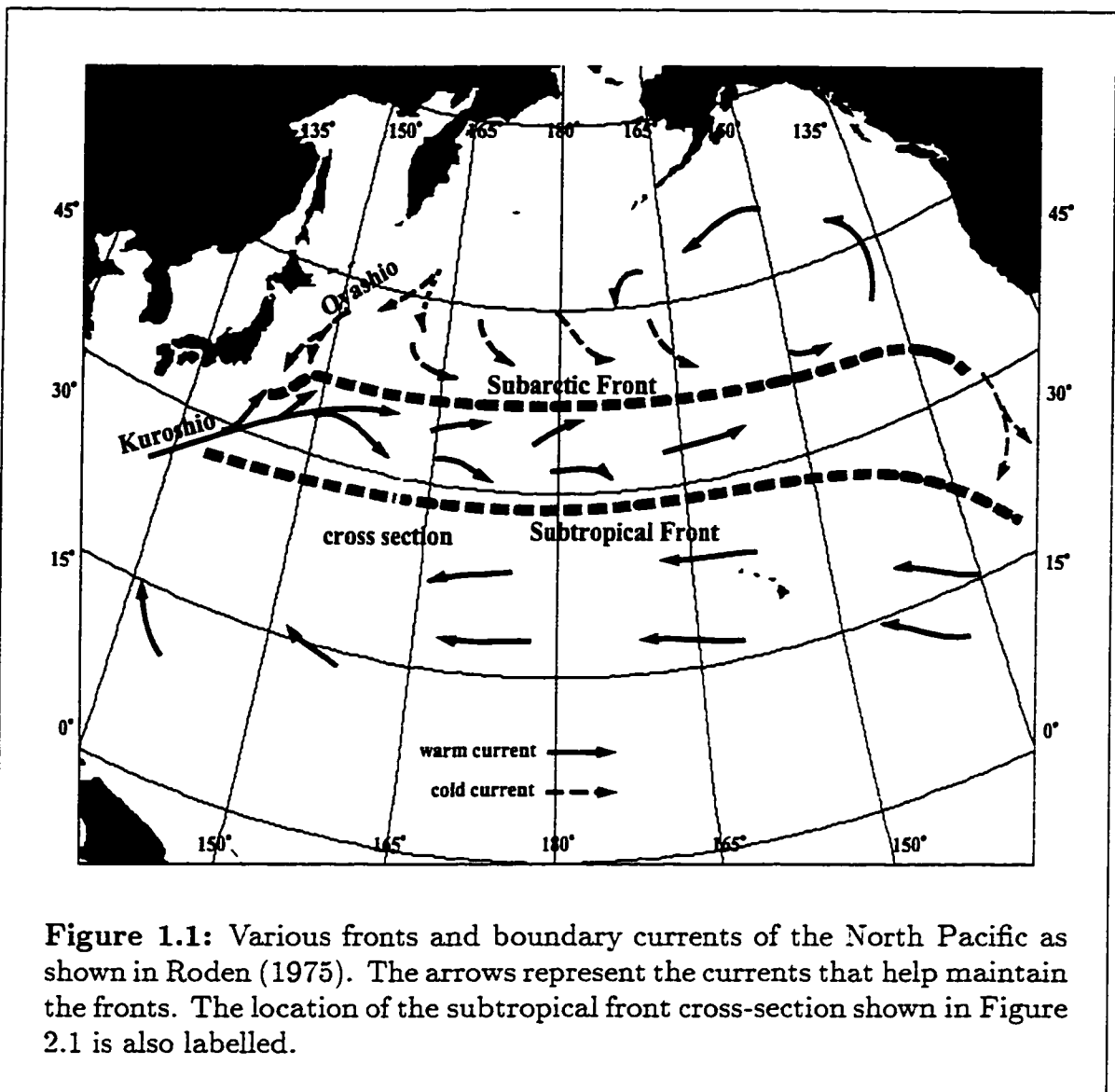
isopycnals (see Barth, 1989a and Bush *et al.*, 1995). The parametrization of these effects is an active area of research (see for example Greatbatch, 1998 and Visbeck *et al.*, 1997.) As well, unstable coastal currents play a significant role in the upwelling of nutrients and the creation of cross-shore flows (see Ikeda and Emery, 1984, Ikeda *et al.*, 1984, McCreary *et al.*, 1991, Haidvogel *et al.*, 1991, and Barth. 1989a).

Observations have illustrated mesoscale variations existing in fronts. The variations take the form of large-scale meanders which often form cold-core and warm-core eddies as well as smaller-scale jets and squirts (see Stern, 1986, Stern, 1987, McCreary *et al.*, 1991, Haidvogel *et al.*, 1991, and Barth, 1989a). Ocean

1. Introduction

surface fronts are largely geostrophic in nature, that is, the velocity is chiefly determined by pressure gradients and the effective force of the Earth's rotation on these gradients (Robinson, 1983). Thus, sloping isopycnals give rise to a geostrophically determined baroclinic flow (see Roden, 1975 for examples). Yet, it is the departure from geostrophy, the ageostrophic effects, that largely determines the existence and nature of instabilities.

The experimental work of Griffiths and Linden (1981) and Griffiths *et al.* (1982) was instrumental in inspiring and directing this area of research. The first illustrated the slow, nonlinear instability of an isolated front: a front with a single outcropping and a corresponding unidirectional flow. The second illustrated the highly unstable nature of a coupled front: a front bounded by two outcroppings with a sheared flow consisting of a jet in both directions. Both papers made clear the necessity of a leading-order geostrophic model that also described the highly dynamic nature of ageostrophic frontal variations.

The difficulty in studying fronts analytically is the large variation in isopycnals that are prevalent in them. These large deflections cause relatively large velocities and the nonlinear advection terms cannot be assumed small. As such, the classic quasigeostrophic (QG) model, which assumes small isopycnal deflection and thus, small velocities, is not applicable (see Pedlosky, 1987 for details of the QG model). As well, these fronts are known to be unstable when QG theory would have predicted stability (Paldor and Killworth, 1987). The goal is to approximate the primitive equations in such a manner as to allow greater analysis. while including finite-amplitude isopycnal deflection and the associated ageostrophic effects.

In Griffiths *et al.* (1982), a reduced-gravity model that models a front as a single layer with constant potential vorticity over a deep, inactive ocean is analyzed in the long wavelength limit. Despite its simple nature, the model allowed for instability without the necessity of an extremum in the potential vorticity. As well, it illustrated the importance of including the large inertial forces associated with a rapidly varying front. It is the kinetic energy in the large velocities concentrated at the boundaries that allows an initial release of potential energy to grow into the instabilities observed. While coupled fronts were shown to be linearly unstable, isolated fronts were shown to be linearly stable in the subsequent works of Killworth (1983), Paldor (1983a), and Paldor (1983b) unless a reversal of flow occurs (Killworth, 1983). In Killworth *et al.* (1984), Paldor and Killworth (1987),

1. Introduction

and Paldor and Ghil (1990) these results were extended to a two-layer model and finite wavelengths. It was shown that the coupled-front instability was essentially a barotropic instability, while isolated fronts were baroclinic. As well, it was found that in the one-layer model, the flow was dominated by long waves, while in the two-layer model short waves with a linearly increasing growth rate dominated. As such, the addition of a lower layer is essential in the study of isolated fronts. In Paldor and Ghil (1991), the short wave instabilities seen for coupled fronts were also found for isolated fronts using a two-layer constant PV model.

The analysis discussed above has been very successful in describing frontal instability and yet has two drawbacks when it comes to modelling surface ocean fronts. First, while assuming constant PV simplifies the highly nonlinear terms in the models, this assumption places a considerable constraint on the form of the front (see Slomp and Swaters, 1997). The sensitivity of the results to the PV structure of a front (see Killworth, 1983) suggests that variations from a constant PV could result in widely varying stability characteristics. Second, the analysis cannot be generalized to include the effects of the β-plane approximation or bottom topography (Benilov and Reznik, 1996). Yet the former is essential in any study of large-scale, open-ocean fronts, while the latter is essential in the study of coastal currents.

In Cushman-Roisin (1986), a frontal geostrophic (FG) model was developed to specifically deal with ocean fronts within the β-plane approximation (see Cushman-Roisin and Tang, 1990 for further details). This model assumed the fronts were geostrophic, but unlike the QG models, where geostrophy is a result of small isopycnal deflections, geostrophy resulted from the large length scales associated with the fronts. As a result of the large length scale, the models may have to incorporate the dependence of the Coriolis force on latitude through the β-plane approximation (see §2.1). As illustrated in Chapter 2 this leads to an intermediate length scale model, in that the length scale is limited below by the necessity of geostrophy and above by the β-plane approximation. The model was developed for a single layer over a deep passive layer and is referred to as the reduced gravity (RED) model. The time scales in the model are necessarily much slower than QG scales, making the model suitable for the slow growth scales associated with large fronts. Despite this simplification, the model still included highly nonlinear, second order relationships between the frontal-layer potential vorticity and stream function. Analysis

4

1. Introduction

of this model has shown that all monotonic fronts are stable (Benilov, 1992b), and that a wedge front gives rise to dispersive, frontally-trapped waves which propagate with the front to the left (Cushman-Roisin, 1986).

In Chassignet and Cushman-Roisin (1991), an examination of eddies using both one-layer and two-layer FG models indicated the importance of including the second layer. Following this work, Cushman-Roisin *et al.* (1992) constructed a general two-layer, β-plane model for all scales of flow. They examined a range of parameter values and found that several key models could describe the flow of thin fronts in the FG limit. These models had a similar structure to that of the reduced gravity model but included lower-layer effects. The necessity of several FG models was justified by the range of length and depth scales of observed fronts (see Table 3 in Benilov and Reznik, 1996). In Benilov (1992a), two more models, which allowed layers of equal depth, were derived. Benilov has examined the linear stability of large-scale fronts using these two-layer, FG models (Benilov, 1992a and Benilov and Cushman-Roisin, 1994). It was demonstrated that fronts were generally linearly stable when dominated by the background vorticity gradient supplied by the β-plane, and unstable when this effect was weak. As well, the linear singularity corresponding to extrema in the frontal profile was shown to be a source of instability (Benilov, 1995a). Concurrently, and independently, Swaters (1993b) developed and analyzed one of the models found in Cushman-Roisin *et al.* (1992), but for a surface flow over gently sloping bottom topography. This model allowed fronts to be stable or unstable depending on a balance between the background vorticity gradient (here provided by topography) and the vorticity gradient associated with the front. Once again, the difference between the two-layer model and the reduced gravity model was stressed.

While linear analysis is always useful, instabilities exist in fronts that are linearly stable and are thus attributed to nonlinear effects (Paldor, 1987). Observations (Barth, 1989a) and experiments (Griffiths and Linden, 1981) have shown that finite-amplitude phenomena such as wave breaking and eddy formation are prevalent in the evolution of fronts. As well, nonlinear interactions are seen to increase the wavelength of these phenomena (Ikeda and Emery, 1984 and Ikeda *et al.*, 1984). In Paldor (1987) and Ghil and Paldor (1994), it was shown that by including nonlinear effects in constant PV models, linear growth could be suppressed, leading to periodic modulation. Nonlinear analysis of jets using QG models has illustrated

5

1. Introduction

the modulation of linearly unstable modes into large meanders leading to the pinch off of eddies (Feliks and Ghil, 1996). However. it was also concluded that extended QG theory would not properly describe the nonlinear dynamics because it does not discriminate between cyclones and anticyclones. while the latter are favoured in primitive equation models and observations (Boss *et al.*. 1996).

In Slomp and Swaters (1997), a finite amplitude analysis of the RED model was undertaken. It was shown that nonlinear effects modulate linearly stable waves, leading to the evolution of travelling wave/soliton structures. In Reszka (1997), a finite amplitude calculation using the model of Swaters (1993b) suggested that non-linearities could both stabilize and further destabilize linearly unstable waves. Most dramatically, numerical solutions illustrated the development of eddies from both isolated and coupled fronts. These numerical solutions gave credibility to the belief that this relatively simple two-layer FG model was capturing the essential physical process of eddy formation and nonlinear interactions as seen in the numerical studies of Barth (1994), Spall (1995), and Haidvogel *et al.* (1991).

We can make four conclusions from the works discussed above. First. QG models are insufficient to analyze frontal processes. but the instabilities observed share a similar structure to that produced by QG models. A model that has leading-order geostrophy built in is desired. Second, the large-amplitude deflections and velocities associated with fronts must be included in any model designed to capture their dynamic nature. Third. while the instability of coupled fronts can be barotropic in nature, the instability of isolated fronts is baroclinic in nature and. therefore, is dependent on the inclusion of a lower layer. Finally. nonlinear effects play an essential role in the evolution of instabilities. These conclusions lead us to the focus of this thesis: the study of nonlinear effects in two-layer FG models.

The plan of this thesis is as follows. In Chapter 2, we discuss the approximations and scalings that lead to the models examined. Beginning with the two-layer, shallow-water equations, we follow the analysis of Benilov and Reznik (1996) and introduce barotropic and baroclinic velocities and the associated equations. Then a scale analysis is used to reduce the equations to a nondimensional model. Here we make the *FG assumptions* that changes in the upper-layer depth are of the same scale as the upper-layer depth itself and that the leading-order balance in the baroclinic motion is the *geostrophic balance* between the pressure gradient and the constant Coriolis force. This ensures that the Rossby number is small, and the

1. Introduction

baroclinic velocity can be expanded in a power series in it. By substituting this expansion of the baroclinic velocity into the remaining equations, one obtains the general FG model.

The general FG model still allows variation in the scaling of the β-plane effect, depth ratio, time, and barotropic stream function. Following the work of Cushman-Roisin *et al.* (1992), the time and barotropic stream function scales are determined once other scales are chosen. It is demonstrated that all possible choices can be examined by studying four two-layer, frontal-geostrophic models. These four models are labelled the ST model, the VSE model, the SE model, and the WVT model. We choose to identify these models by the effect of the β-plane as being very strong (VS), strong (S), or weak (W), and the upper-layer depth as being equal (E) to the lower layer, thin (T), or very thin (VT). As such, the ST model is a model in which the effect of the β-plane is strong and the upper layer is thin, and so forth for the three remaining models.

We complete Chapter 2 by introducing the potential vorticity, boundary conditions, and nonlinear invariants associated with the general FG model. Though the body of the thesis concentrates on β-plane models, the connection to flows over bottom topography is made clear in Appendix 1. This allows the models to be applied to a much greater range of fronts and allows for comparison to the analysis of Swaters (1993b) and Reszka (1997). As well, it allows comparison to bottom-trapped flow models, specifically the model developed in Swaters and Flierl (1991) and Swaters (1991) using the FG assumption.

The FG models have been studied in a variety of works, however the nonlinear aspects of the models have not been fully discussed. In Table 1.1, we summarize the previous work that has been done using the FG models and the areas that this thesis will cover. We include the four two-layer, FG models as well as the reduced gravity FG model (the RED model) and the lower-layer, strong-topography model (the LST model) since these models will be used for comparison. In Chapters 3, 4, and 5 we examine in detail the ST, VSE, and SE models, emphasizing the examination of nonlinear aspects. In each chapter, we begin by presenting the model equation, the potential-vorticity description, and a brief review of the linear stability characteristics and solutions. Note that Benilov and Reznik (1996) provides a good overview of all four two-layer FG models and the linear analysis that has been done. As such, we are brief in our presentation of these results. Next, based on

Model	Derivation	Linear Analysis	Nonlinear Stability Analysis	Finite Amplitude Analysis	Numerical Solutions
ST	$CRST_\beta$	BCR_β	**Chapter 3**	**Chapter 3**	**Chapter 3**
VSE	Ben_β	Ben_β	**Chapter 4**	**Chapter 4**	**Chapter 4**
SE	Ben_β	Ben_β	**Chapter 5**	**Chapter 5**	**Chapter 5**
WVT	$CRST_\beta$ $SwatC_T$	$SwatC_T$	$SwatC_T$ $KarsC_T$	$Reszka_T$	$Reszka_T$
RED	CR_β	CR_β	$Slomp_f$ $SwatB_f$	$Slomp_f$	CRT_β $Pavia_f$
LST	$SwatA_T$	$SwatA_T$ $KarsA_T$	$SwatB_T$ $KarsB_T$	$Mooney_T$	$SwatD_T$

TABLE 1.1. The table summarizes where previous analysis has been carried out and the analysis given in this thesis. The subscript β indicates a model with only the β-plane effect, the subscript T indicates a model with only bottom topography, and the subscript f indicates an f-plane model with neither the β-plane effect nor bottom topography. The paper abbreviations are as follows: CRST=Cushman-Roisin *et al.* (1992), BCR=Benilov and Cushman-Roisin (1994), Ben=Benilov (1992a), SwatA = Swaters (1991), SwatB = Swaters (1993a), SwatC = Swaters (1993b), SwatD = Swaters (1998), Reszka = Reszka (1997), CR = Cushman-Roisin (1986), Slomp = Slomp (1995), CRT = Cushman-Roisin and Tang (1990), Pavia = Pavia (1992), Mooney = Mooney and Swaters (1996), KarsA = Karsten *et al* (1995), KarsB = Karsten and Swaters (1996a), KarsC = Karsten and Swaters (1996b).

the nonlinear invariants, we present a nonlinear stability analysis. Then, using the linear solutions, we present a finite amplitude analysis that examines the evolution of a slowly varying wavetrain under the influence of weak nonlinear effects. Finally, we summarize the chapter by presenting numerical solutions to the full model.

Since each chapter is similar in form, we present many of the details and explanation of the analysis only once, in Chapter 3 where the ST model is discussed. As well, in order to limit the length of the thesis, many of the details of the calculations are left to the appendices. Since much of the analysis of the WVT model is based on previous work (see Table 1.1) we present only brief details of the analysis in Appendix 2.

1. Introduction

In Chapter 6, comparisons are made between the various models and the results of the previous chapters. Finally, the conclusions of the thesis and comments on future work are presented.

Chapter 2

Derivation of Two-Layer,

Frontal-Geostrophic Models

2.1 Shallow Water Equations

In the study of fluid dynamics many approximations are made to reduce the physical laws, often referred to as the primitive equations, to a set of equations more easily manipulated. The reason for doing so is twofold: first, the full equations are difficult to solve; second, analyzing the full equations including all scales of motion often obscures physical insight. It is beyond the scope of this thesis to discuss all the possible approximations or to go into the detailed arguments of when the approximations are valid. We give a brief description of the approximations made in deriving the frontal geostrophic models and include appropriate references for further detail.

The starting point for modelling oceanographic flow is to assume the dynamics of the ocean are described by the fluid continuum equations of motion (Pedlosky, 1987). These equations follow from Newton's laws and the conservation of physical quantities (mass, energy, etc.), and their derivation can be found in most elementary fluid dynamics texts (Kundu, 1990, Pedlosky, 1987). The defining characteristic of geophysical fluid dynamics (hereafter GFD) is that the motion occurs in a rotating frame of reference, namely the earth. Ideally, the equations of motion would be developed in a rotating, spherical coordinate system. This, of course, presents a great deal of complexity. In general, for studies of oceanic phenomena that do not extend across ocean basins it is not necessary to consider the entire spherical surface of the earth. For the purposes of this study, the scale of the motion is small enough that the spherical surface of the earth can be approximated by a flat plane centred at a chosen latitude, θ, and longitude, ϕ. Such an approximation is generally accepted as valid for motions with length scales on the order of hundreds of kilometres and less (see Pedlosky, 1987, chapter 6 for discussion.) The geometry is represented locally with rectangular horizontal coordinates, x running west to

2. Derivation of Two-Layer, Frontal-Geostrophic Models

east and y running south to north, and a vertical coordinate. z. The $z-$ axis is at an angle $\pi/2 - \theta$ to the axis of the earth's rotation. which is directed south to north. The vectors e_1, e_2, and e_3 represent unit vectors in the x. y. and z directions. respectively.

In transforming the equations of motion from an inertial frame to a rotating frame, a new force, the Coriolis force, is found in the rotating frame. This force is perpendicular to the velocity and hence does no work. In the northern hemisphere it appears as a force tending to deflect horizontal motion to the right. This force plays an essential role in GFD and, as we will see, is part of the dominant balance in the oceanic fronts we are studying. Forces associated with the centripetal acceleration due to the earth's rotation are included in the definition of the gravitational force. Readers interested in the details of deriving the equations of motion on a rotating frame are referred to Kundu (1990) or Pedlosky (1987).

The Coriolis force is described by the Coriolis parameter

$$f(\theta) = 2|\Omega| \sin \theta.$$

In accordance with the approximate rectangular coordinates. we approximate the variation of the Coriolis parameter with latitude as a linear function in the meridional coordinate, y. Assuming the flow occurs over a small range of latitude , $\Delta\theta \ll 1$. centred on the latitude θ_0. the Coriolis parameter can be expanded in a Taylor series about θ as follows:

$$f = f(\theta_0) + \left.\frac{\partial f}{\partial \theta}\right|_{\theta_0} \Delta\theta + O(\Delta\theta)^2.$$

Using $\Delta\theta = y/R_e$, where R_e is the radius of the earth, gives

$$f = 2|\Omega| \sin \theta_0 + \frac{2|\Omega| \cos \theta_0}{R_e} y + O(\Delta\theta)^2.$$

Ignoring quadratic terms in $\Delta\theta$ gives the approximate Coriolis parameter

$$f \approx f_0 + \beta_0 y, \tag{2.1.1}$$

2. Derivation of Two-Layer, Frontal-Geostrophic Models

where

$$f_0 = 2|\Omega| \sin \theta_0, \tag{2.1.2}$$

$$\beta_0 = \frac{2|\Omega| \cos \theta_0}{R_e}. \tag{2.1.3}$$

This approximation, commonly called the β-plane approximation. is valid provided the flow occurs over a small range of latitude and the flow occurs away from the poles where $\cos \theta_0 = 0$. For simplicity we will discuss only the Northern Hemisphere where $\theta_0 > 0$, so that f_0 and β_0 are both positive quantities. If the meridional variation is very small, even the linear variations in the Coriolis parameter will be small compared to the constant part, i.e., $\beta_0 y \ll f_0$. Then the Coriolis parameter may be considered a constant, known as the f-plane approximation.

It should be noted that while including the β-plane approximation we have not included terms associated with the variation of the metric that occur when changing from a spherical reference frame to a Cartesian frame. These terms relate longitude variations to eastward length changes and are only negligable at low latitudes (see Pedlosky, 1987, chapter 6 for a complete discussion). However, since the goal of this work is to examine nonlinear effects in previously studied models, we will not include these terms. as they have not been included in the previous derivations of the two-layer, FG models. We leave the examination of how these metric variation terms change the model equations to future work.

The next approximation, and possibly the most controversial. is to assume the ocean is not only incompressible but consists of layers of constant density. While incompressibility is a common and reasonable approximation for ocean water. the ocean is known to be continuously stratified. We work with a layered model for two reasons. The first is simplicity. In order to do a detailed analysis including nonlinear effects, as this work intends to do, a simple model that allows some analytical results is necessary. Second, the work on continuously stratified flows has illustrated that layered models do capture the main characteristics of baroclinic instability associated with fronts. For example it has been shown that similar analysis of the Phillips layered model and the Eady continuously stratified model give qualitatively equivalent results (Pedlosky, 1970). The linear analysis of the FG models studied here has been extended to continuously stratified models with very similar results (see Benilov, 1993, Benilov, 1994, and Benilov, 1995b).

12

Figure 2.1: The figure on the left is the observed temperature profile of the Subtropical front as seen in Roden (1975). The figure on the right is the idealized representation of the front as an instantaneous jump of temperature between two layers of constant temperature.
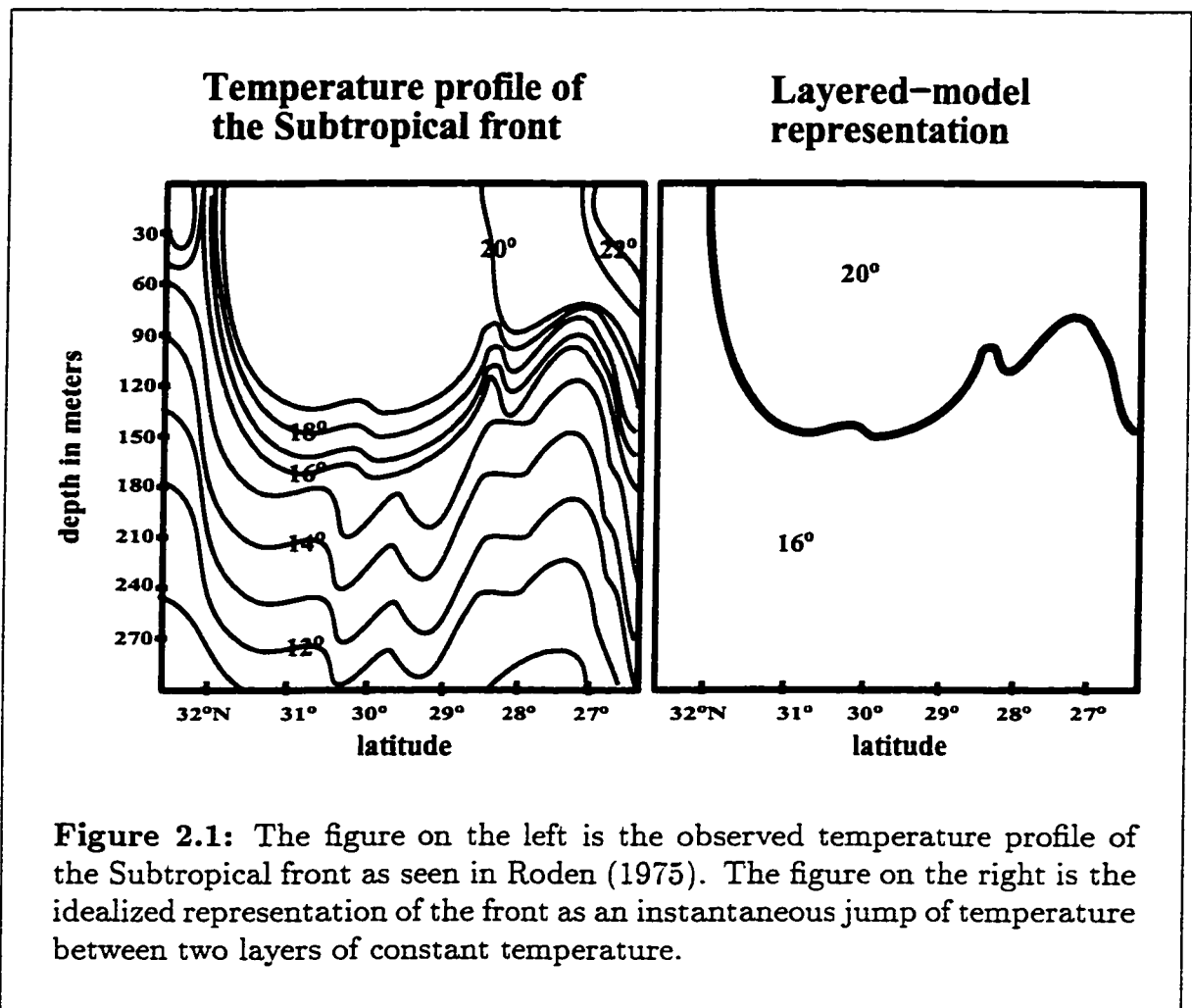
By approximating the ocean as two layers of constant density, a front is represented as a discontinuity in density across the interface between the two layers. Such an approximation most accurately models ocean fronts where large density changes occur over small scales resulting in a concentration of isopycnals. In Figure 2.1, observations of the Subtropical front taken from Roden (1975) are shown with the idealized two-layer representation of such a front. The location of the cross-section is shown in Figure 1.1. Note that the two-layer representation chooses the interface to be an isopycnal (given by the isotherm) not a depth level.

We will assume that the ocean water is inviscid. That is, all forces due to friction between the fluid and solid surfaces and that between adjacent fluid parcels are taken to be zero. Friction can have dramatic effects on a flow but these are usually limited to boundary layers near solid surfaces (coastlines, ocean bottom),

or to small-scale dynamics. As such these motions will have little effect on the large-scale, open-ocean, surface motions of this study. Having said this, it should be noted that when studying numerical solutions the effects of friction, though small, can often be used to smooth numerical errors.

For most of our analysis we will assume that the ocean has a flat bottom, as bottom variations have little effect on mid-ocean fronts. This is not true however for coastal fronts, where the sloping continental shelf can have important effects, or for bottom-trapped flows, where the bottom topography is obviously more important. The equations that result when bottom topography is included are discussed in the more general model derivation found in Appendix 1. In the context of the analysis presented in this thesis, bottom topography has effects very similar to the β-plane approximation, and most results can be simply extrapolated from those presented here. As well, models that have strong bottom topography influences have been examined previously in the FG context (see Swaters, 1991, Mooney and Swaters, 1996, Swaters, 1993b, and Reszka, 1997).

We also assume a rigid lid, that is, we treat the upper boundary of the ocean as a solid surface, eliminating surface waves and deflections. As argued in Cushman-Roisin *et al.* (1992), this approximation is equivalent to setting the external radius of deformation to infinity. The external radius of deformation is the length scale over which gravitational forces balance Coriolis forces and is given by

$$L_D = \frac{\sqrt{gH}}{f_0}, \qquad (2.1.4)$$

where g and H are the gravitational acceleration and the depth scale. Given that for typical ocean depths the external radius of deformation is on the scale of 2000 km, such motions should be examined using spherical coordinates and, thus, are beyond the scope of this thesis. This approximation effectively filters out all surface gravity waves.

The final approximation is the shallow water approximation. The reduction to the shallow water equations is based on the assumption that the scale of the vertical motions, H, is much less than the scale of the horizontal motions, L; that is, the aspect ratio is very small, $H/L \ll 1$. This argument holds well for oceanic models since the ocean is actually a very thin layer of fluid over the large surface of the earth. Taking a typical depth of the ocean, say 5 km, as a maximum scale

2. Derivation of Two-Layer, Frontal-Geostrophic Models

for vertical motion and comparing this to the horizontal length scale of the currents and eddies this paper discusses, which is greater than 50 km. gives that $H/L \leq 0.1$. It should be noted that the vertical scale of the motion in the models derived here is usually bounded by the thinner, frontal layer, which has a depth less than. and often much less than, the total ocean depth making this approximation more accurate. For example, the front shown in Figure 2.1has a horizontal length scale on the order of 50 km and a vertical length scale on the order of 150 m giving $H/L \leq 0.03$. The assumption reduces the vertical momentum equation to the *hydrostatic balance* where vertical changes in pressure are balanced by the weight of the overlying fluid. As well, horizontal motion is assumed independent of depth and, thus, uniform throughout a column of fluid. The derivation of the shallow water equations can be found in any text on GFD (see Pedlosky, 1987 or Kundu, 1990).

The geometry of the flow for a rigid-lid, two-layer ocean over a flat bottom is shown in Figure 2.2. The model variables use the subscript 1 for the upper layer and 2 for the lower layer. The governing equations for the two-layer, constant-density, shallow-water model with a rigid lid and flat bottom are

$$\frac{\partial u_1}{\partial t} + (u_1 \cdot \nabla)u_1 + (f_0 + \beta_0 y)e_3 \times u_1 = -\nabla \tilde{p}_1, \qquad (2.1.5)$$

$$\frac{\partial h_1}{\partial t} + \nabla \cdot [h_1 u_1] = 0. \qquad (2.1.6)$$

$$\frac{\partial u_2}{\partial t} + (u_2 \cdot \nabla)u_2 + (f_0 + \beta_0 y)e_3 \times u_2 = -\nabla \tilde{p}_2. \qquad (2.1.7)$$

$$\frac{\partial h_2}{\partial t} + \nabla \cdot [h_2 u_2] = 0. \qquad (2.1.8)$$

$$\tilde{p}_1(x,y,t) = g'h_1 + \tilde{p}_2(x,y,t). \qquad (2.1.9)$$

$$h_1 + h_2 = H. \qquad (2.1.10)$$

where $u_{1,2}(x,y,t) = (u_{1,2}, v_{1,2})$, $\tilde{p}_{1,2}(x,y,t)$, $h_{1,2}(x,y,t)$, and H are the horizontal fluid velocities, dynamic pressures per unit mass, layer depths for the upper and lower layers, and total ocean depth, respectively, $\nabla = (\partial_x, \partial_y)$ is the horizontal gradient and we use the notation $e_3 \times u = (-v, u)$. In equation (2.1.9), g' is the reduced gravity defined by

$$g' = \frac{g\Delta\rho}{\rho} = \frac{g(\rho_2 - \rho_1)}{\frac{1}{2}(\rho_2 + \rho_1)}. \qquad (2.1.11)$$

15

Figure 2.2: The two-layer, rigid-lid, flat-bottom model studied in this thesis. The subscripts $1, 2$ indicate variables corresponding to the upper and lower layer, respectively. When the subscript is dropped from the variable h it refers to the upper-layer depth.
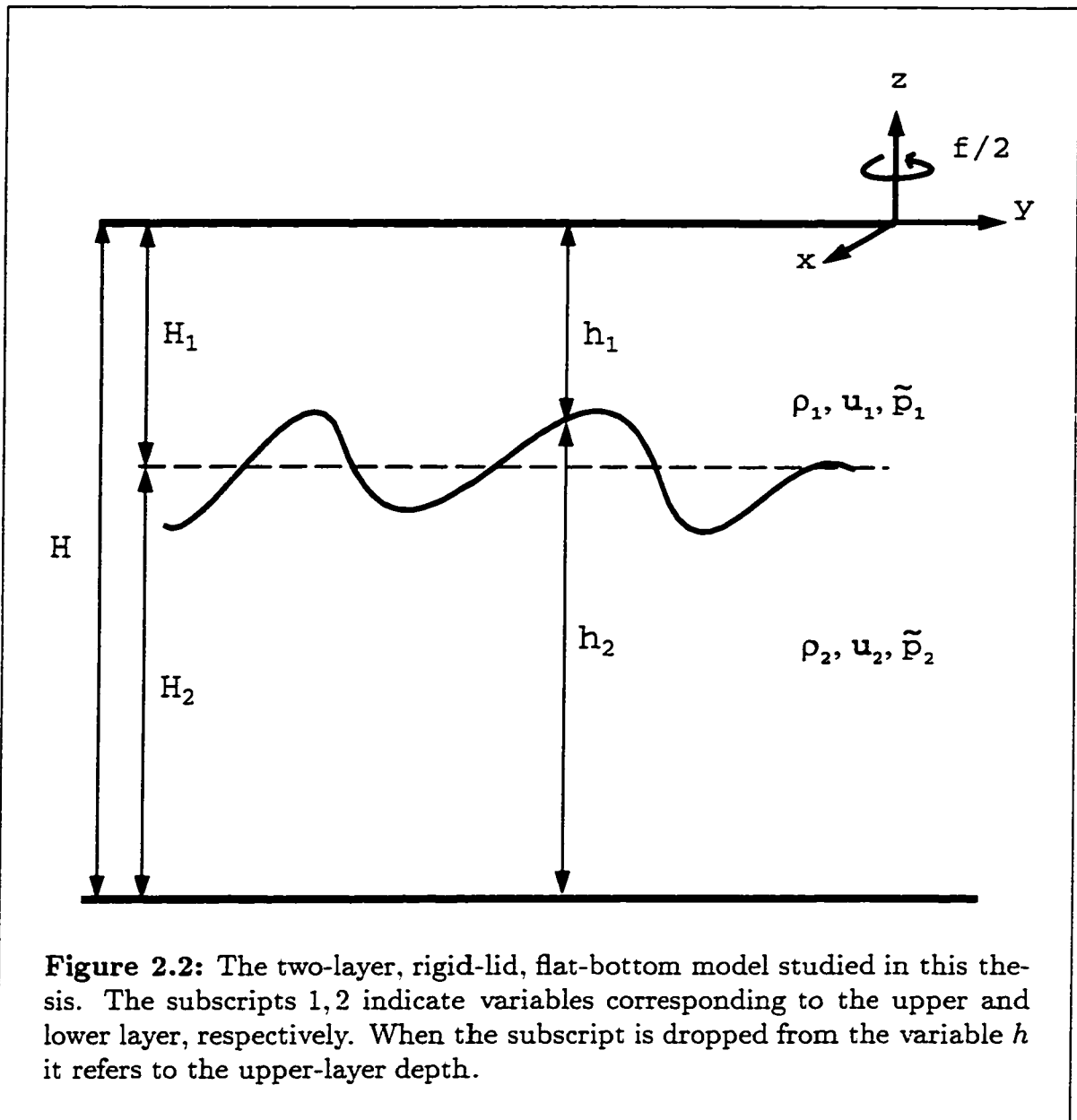
In general the density differences are very small, so that $\Delta\rho \ll \rho$ and as a consequence $g' \ll g$.

Equations (2.1.5) and (2.1.7) represent the conservation of momentum in the upper and lower layer, respectively. Equations (2.1.6) and (2.1.8) represent the conservation of mass in the upper and lower layer, respectively. Equation (2.1.9) follows from the hydrostatic approximation and represents the continuity of pressure across the interface between the layers. And equation (2.1.10) simply states that

2. Derivation of Two-Layer, Frontal-Geostrophic Models

the layer depths must sum to the total ocean depth which is constant. The reader is referred to Kundu (1990) and Pedlosky (1987) for further details. Note that the equations and the geometry are symmetric in the two layers up to a constant in the pressures. As such, the flow of an upper-layer front is identical to the flow of a lower-layer front and we can, without loss of generality, assume that $H_1 \leq H_2$. This is not true when bottom topography is included (see discussion in Appendix 1).

2.2 Barotropic and Baroclinic Equations

In reducing the governing equations to the geostrophic models studied in this thesis, we follow the technique in Benilov and Reznik (1996) by first rewriting the governing equations in terms of barotropic and baroclinic components. It is possible to derive many of the models without introducing these components (see Cushman-Roisin *et al.*, 1992), but we believe it clarifies the relationship between the barotropic and baroclinic dynamics. As well, it allows the development of a model not found using the layer approach of Cushman-Roisin *et al.* (1992).

We introduce the barotropic and baroclinic velocities given by

$$\boldsymbol{u}_{bt} = \frac{h_1 \boldsymbol{u}_1 + h_2 \boldsymbol{u}_2}{H}. \tag{2.2.1}$$

$$\boldsymbol{u}_{bc} = \boldsymbol{u}_1 - \boldsymbol{u}_2, \tag{2.2.2}$$

respectively. The barotropic velocity is a depth-averaged velocity and is divergence free. This can be seen by adding (2.1.6) and (2.1.8), using that $H_t = 0$ and dividing by H, to get

$$\nabla \cdot \boldsymbol{u}_{bt} = 0. \tag{2.2.3}$$

The baroclinic velocity measures the difference between the flow in the two layers and so, is directly attributed to the density front.

Now, we can write the layer velocities in terms of these new velocities, that

17

is,

$$u_1 = u_{bt} + \frac{h_2}{H}u_{bc}, \qquad (2.2.4)$$

$$u_2 = u_{bt} - \frac{h_1}{H}u_{bc}. \qquad (2.2.5)$$

Rewriting (2.1.6) and (2.1.8) using (2.2.4) and (2.2.5) gives

$$\frac{\partial h_1}{\partial t} + \nabla \cdot (h_1 u_{bt}) + \nabla \cdot (H\gamma_{h*}u_{bc}) = 0. \qquad (2.2.6)$$

$$\frac{\partial h_2}{\partial t} + \nabla \cdot (h_2 u_{bt}) - \nabla \cdot (H\gamma_{h*}u_{bc}) = 0, \qquad (2.2.7)$$

where we have introduced (or will use shortly) the shorthand notation given by

$$\gamma_{h*} = \frac{h_1 h_2}{H^2} = \frac{h_1(H - h_1)}{H^2}, \qquad (2.2.8)$$

$$\gamma_{h-} = \frac{h_2 - h_1}{H} = \frac{H - 2h_1}{H}. \qquad (2.2.9)$$

We form the barotropic equation by taking $h_1*(2.1.5)$ $+h_2*(2.1.7)$, dividing by H, and using (2.2.4) and (2.2.5). After some simplification, the use of (2.2.6) and (2.2.7) to eliminate the time derivatives of the layer depths, and the use of (2.1.9) to eliminate p_2, we obtain

$$\frac{\partial u_{bt}}{\partial t} + (u_{bt} \cdot \nabla)u_{bt} + \gamma_{h*}u_{bc} \cdot \nabla u_{bc} + u_{bc}\nabla \cdot (\gamma_{h*}u_{bc})$$
$$+ (f_0 + \beta_0 y)e_3 \times u_{bt} + \nabla\left(p_1 - g'h_1 + \frac{1}{2}\frac{g'}{H}\nabla h_1^2\right) = 0. \qquad (2.2.10)$$

We form the baroclinic equation by taking (2.1.5)–(2.1.7) and using (2.2.4) and (2.2.5), which, after some simplification, gives

$$\frac{\partial u_{bc}}{\partial t} + \gamma_{h-}(u_{bc} \cdot \nabla)u_{bc} + \frac{1}{2}u_{bc}(u_{bc} \cdot \nabla\gamma_{h-}) + (u_{bt} \cdot \nabla)u_{bc}$$
$$+ (u_{bc} \cdot \nabla)u_{bt} + (f_0 + \beta_0 y)e_3 \times u_{bc} + g'\nabla h_1 = 0. \qquad (2.2.11)$$

2. Derivation of Two-Layer, Frontal-Geostrophic Models

Since the barotropic velocity is divergence free, that is, (2.2.3) holds, it is possible to introduce a stream function satisfying

$$u_{bt} = e_3 \times \nabla \psi. \tag{2.2.12}$$

Taking the curl of (2.2.10), that is, $\nabla \times$ (2.2.10), gives

$$\frac{\partial \nabla^2 \psi}{\partial t} + J(\psi, \nabla^2 \psi) + \beta_0 \psi_x$$
$$+ (\gamma_{h*} u v)_{xx} - (\gamma_{h*} u v)_{yy} - \left[\gamma_{h*}(u^2 - v^2)\right]_{xy} = 0, \tag{2.2.13}$$

where now, and henceforth, $u_{bc} = u = (u, v)$, and $J(A, B) = A_x B_y - A_y B_x$ is the Jacobian. Rewriting the baroclinic equation (2.2.11) using the barotropic stream function gives

$$\frac{\partial u}{\partial t} + \gamma_{h-} (u \cdot \nabla) u + \frac{1}{2} u (u \cdot \nabla \gamma_{h-}) + J(\psi, u)$$
$$+ (u \cdot \nabla) (e_3 \times \nabla \psi) + (f_0 + \beta_0 y) e_3 \times u + g' \nabla h = 0. \tag{2.2.14}$$

As well, the continuity equations (2.2.6, 2.2.7) both reduce to

$$\frac{\partial h}{\partial t} + J(\psi, h) + \nabla \cdot (H \gamma_{h*} u) = 0, \tag{2.2.15}$$

where now, and henceforth, $h_1 = h$, and $h_2 = H - h$. Although it appears we have lost an equation, this is not the case. The sum of the two continuity equations was used explicitly in inferring the existence of the barotropic stream function, that is, in deriving (2.2.3). The governing equations are (2.2.13), (2.2.14), and (2.2.15).

2.3 Geostrophic Equations

In order to make the model equations applicable to a variety of physical situations, the equations are nondimensionalized by letting

$$(x, y) = L(x, y)^*, \quad u = U u^*, \quad \psi = \Psi \psi^*, \quad h_1 = H_1 h_1^*, \quad t = T t^*, \tag{2.3.1}$$

where L, U, Ψ, H_1, T, are typical length, baroclinic velocity, barotropic stream function, upper-layer depth, and time scales for the flow, respectively, and

2. Derivation of Two-Layer, Frontal-Geostrophic Models

the asterisked quantities are nondimensional. Note that in contrast to QG theory we do not introduce a separate scaling for the interfacial displacement. We assume that changes in the layer depth are the same scale as the layer depth itself. For a more detailed examination of the relationship between QG and FG scaling see the detailed derivation given in Appendix 1 or Cushman-Roisin *et al.* (1992).

Applying the scaling (2.3.1) to the governing equations (2.2.13), (2.2.14), and (2.2.15), and dropping the asterisks, gives

$$
\epsilon_T \epsilon_\psi \frac{\partial \nabla^2 \psi}{\partial t} + \epsilon_\psi^2 J(\psi, \nabla^2 \psi) + \epsilon_\beta \epsilon_\psi \psi_x
$$
$$
+ \epsilon^2 \left[(\gamma_{h*} uv)_{xx} - (\gamma_{h*} uv)_{yy} - \left[\gamma_{h*}(u^2 - v^2) \right]_{xy} \right] = 0,
$$
(2.3.2)

$$
\epsilon_T \frac{\partial \boldsymbol{u}}{\partial t} + \epsilon \gamma_{h-} (\boldsymbol{u} \cdot \nabla) \boldsymbol{u} + \epsilon \frac{1}{2} \boldsymbol{u} (\boldsymbol{u} \cdot \nabla \gamma_{h-}) + \epsilon_\psi J(\psi, \boldsymbol{u})
$$
$$
+ \epsilon_\psi (\boldsymbol{u} \cdot \nabla)(\mathbf{e}_3 \times \nabla \psi) + (1 + \epsilon_\beta y)\mathbf{e}_3 \times \boldsymbol{u} + \frac{\epsilon}{F_I^2} \nabla h = 0.
$$
(2.3.3)

$$
\epsilon_T \delta \frac{\partial h}{\partial t} + \epsilon_\psi \delta J(\psi, h) + \epsilon \nabla \cdot (\gamma_{h*} \boldsymbol{u}) = 0.
$$
(2.3.4)

where now from (2.2.8) and (2.2.9) we have

$$
\gamma_{h*} = \delta h(1 - \delta h),
$$
(2.3.5)

$$
\gamma_{h-} = 1 - 2\delta h,
$$
(2.3.6)

and we have introduced the nondimensional parameters

$$
\epsilon = \frac{U}{f_0 L}, \quad \epsilon_T = \frac{1}{f_0 T}, \quad \epsilon_\psi = \frac{\Psi}{f_0 L^2}, \quad \epsilon_\beta = \frac{\beta_0 L}{f_0},
$$
$$
\delta = \frac{H_1}{H}, \quad F_I = \frac{U}{\sqrt{g' H_1}}.
$$
(2.3.7)

The parameter ϵ is the Rossby number, classically defined in terms of the baroclinic velocity. It is a ratio of the velocity of the flow, here the baroclinic velocity, to a Coriolis velocity. When the Rossby number is order one or less the Coriolis force is important. When the Rossby number is small, the Coriolis force dominates the flow. The other parameters, ϵ_*, are similar in that they compare motion scales to the Coriolis effect, and can be thought of as Rossby numbers but

2. Derivation of Two-Layer, Frontal-Geostrophic Models

depending on different effects: time changes. barotropic velocities. and β-plane effects. The parameter δ represents a depth-scale ratio. Under the assumption that $H_1 \leq H_2$ we have that $\delta \leq \frac{1}{2}$. The parameter F_I is the internal Froude number, which compares inertial forces to buoyancy forces (Kundu, 1990).

Next we assume that the baroclinic velocity is in *geostrophic balance*. That is, the flow is dominated by the Coriolis force and the corresponding pressure balance. This assumption is based on the fact that frontal measurements of ϵ, ϵ_T. ϵ_β. and ϵ_ψ show they are all small, that is,

$$\epsilon, \epsilon_\psi, \epsilon_T, \epsilon_\beta \ll 1. \tag{2.3.8}$$

This means the baroclinic and the barotropic velocities are smaller than the velocity induced by the Coriolis force. The time scale is sub-inertial. slower than that associated with the Coriolis force, and the β-plane effect. the effect of the meridional variation of the Coriolis force, is small in comparison to the constant Coriolis force. The baroclinic equation is dominated by the constant Coriolis term (the $e_3 \times u$ term in (2.3.3)) and pressure gradient (the last term in (2.3.3)), seen in the baroclinic equation through the pressure difference, h. For a balance to hold these terms must scale similarly, that is, $F_I^2 = \epsilon$, or in terms of the velocity scales,

$$U = \frac{g'H_1}{f_0 L}. \tag{2.3.9}$$

Once again this stresses the connection between the baroclinic velocity and the front. It is the variation of the interface between the two layers or equivalently the pressure difference across the interface that drives the baroclinic velocity. The assumption (2.3.8) is not only physically reasonable but serves the purposes of eliminating high frequency motion making analysis easier. Note that in classical QG theory $F_I = \epsilon$; see Appendix 1. The fact that $F_I = \epsilon^{\frac{1}{2}}$ in FG models stresses the fact that inertial forces are larger when large isopycnal deflections are allowed.

If we use (2.3.9) in the definition of the Rossby number (see (2.3.7)) we find that

$$\epsilon = \frac{g'H_1}{f_0^2 L^2} = \left(\frac{R_I}{L}\right)^2, \tag{2.3.10}$$

21

2. Derivation of Two-Layer, Frontal-Geostrophic Models

where $R_I = \sqrt{g'H_1}/f_0$ is the internal deformation radius. The requirement that the Rossby number be small requires that the length scale exceed the internal deformation radius (Cushman-Roisin *et al.*, 1992). Note that the fact that the Rossby number is the square of the ratio of the length scales means that $L > 3R_I$ is sufficient to make the Rossby number small, $\epsilon < 1/9$. As well, the fact that ϵ_β is small places an upper bound on the length scale, $L \ll f_0/\beta_0 = L_\beta$, where L_β is the planetary scale, the length scale where meridional variations in the Coriolis force are equal to the constant Coriolis force. This leads to the models being called intermediate length scale models.

To leading order, equation (2.3.3) gives that the baroclinic velocity is determined geostrophically by

$$u = e_3 \times \nabla h + O(\epsilon, \epsilon_T, \epsilon_\beta, \epsilon_\psi). \tag{2.3.11}$$

That is, the baroclinic velocity is, to leading order, determined entirely by pressure gradients or equivalently the gradient of interfacial displacements. By (2.3.11), h is the leading-order stream function for the baroclinic velocity; the leading-order baroclinic flow follows contours of constant frontal height, h. The expression (2.3.11) can be used to simplify the next order terms in (2.3.3) to obtain

$$\begin{aligned} u = (1 - \epsilon_\beta y)e_3 \times \nabla h &- \epsilon_T \nabla h_t - \epsilon \gamma_{h-} J(h, \nabla h) \\ &- \epsilon_\psi J(\psi, \nabla h) - \epsilon_\psi J(h, \nabla \psi) + O(\epsilon_\beta, \epsilon, \epsilon_\psi, \epsilon_T)^2. \end{aligned} \tag{2.3.12}$$

Substituting this expression into (2.3.2) and (2.3.4) gives

$$\begin{aligned} \epsilon_T \epsilon_\psi \frac{\partial \nabla^2 \psi}{\partial t} &+ J(\psi, \epsilon_\psi^2 \nabla^2 \psi + \epsilon_\beta \epsilon_\psi y) \\ &+ \delta \epsilon^2 J \left[h, h(1 - \delta h)\nabla^2 h + \frac{1}{2}(1 - 2\delta h)|\nabla h|^2 \right] = 0, \end{aligned} \tag{2.3.13}$$

$$\begin{aligned} \epsilon_T \frac{\partial h}{\partial t} &+ J \left[\epsilon_\psi \psi + \epsilon \epsilon_\beta h(1 - \delta h)y + \epsilon^2 \left(h\nabla^2 h + \frac{1}{2}|\nabla h|^2 \right), h \right] \\ &+ \delta \epsilon^2 \nabla \cdot \left[h(-3h + 2\delta h^2)J(h, \nabla h) \right] = 0, \end{aligned} \tag{2.3.14}$$

where we have ignored the higher order terms in the small parameters. These are the general two-layer, FG model equations as derived in Benilov and Reznik (1996).

2. Derivation of Two-Layer, Frontal-Geostrophic Models

2.4 Frontal-Geostrophic Models

Given the model equations (2.3.13) and (2.3.14), it is not possible to choose a scaling such that all terms are of the same order (Benilov and Reznik. 1996). As argued in Cushman-Roisin *et al.* (1992), "it is reasonable to believe that the system will select its own pace of evolution and that, at least after some time, barotropic and baroclinic modal amplitudes will somehow equilibrate." As such, the parameters ϵ_T and ϵ_ψ are functions of the other parameters, and, thus, called secondary. The ϵ_T parameter is determined by enforcing that a balance exists between the largest of the prognostic terms, those involving time derivatives, and the largest of the diagnostic terms, those not involving time derivatives, in the baroclinic equation. The ϵ_ψ parameter is determined by enforcing that a balance exists between the largest barotropic terms, those involving the barotropic stream function, and the largest baroclinic terms, those not involving the barotropic stream function, in the barotropic equation. This is known as the baroclinic limit since the baroclinic equation is used to determine the time scale. One can discuss the barotropic limit but all models derived in this limit also exist in the baroclinic limit (Cushman-Roisin *et al.*, 1992).

We begin by enforcing the time balance in the baroclinic equation (2.3.14). Examining (2.3.14), such a balance implies that

$$\epsilon_T = \max(\epsilon_\psi, \epsilon\epsilon_\beta, \epsilon^2). \tag{2.4.1}$$

Enforcing the barotropic-baroclinic balance in the barotropic equation, (2.3.13), gives

$$\epsilon_\psi = \frac{\delta\epsilon^2}{\max(\epsilon_T, \epsilon_\beta)} = \frac{\delta\epsilon^2}{\max(\epsilon_\psi, \epsilon_\beta, \epsilon^2)}. \tag{2.4.2}$$

where we've used from (2.4.1) that

$$\epsilon_T \geq \epsilon_\psi. \tag{2.4.3}$$

As well, it follows from (2.4.2) that if $\epsilon_\psi > \epsilon$ then $\epsilon_\psi < \sqrt{\delta}\epsilon$, a contradiction since $\delta \leq \frac{1}{2}$ and hence, it follows that

$$\epsilon \geq \epsilon_\psi. \tag{2.4.4}$$

2. Derivation of Two-Layer, Frontal-Geostrophic Models

These two equations, (2.4.3) and (2.4.4), again indicate the baroclinic nature of the model. The time scale as measured by the temporal Rossby number, ϵ_T, and the baroclinic-motion scale as measured by the Rossby number, ϵ, is larger than the barotropic-motion scale, as measured by the barotropic Rossby number, ϵ_ψ. Hence the motion is baroclinic as the limit implies. It should also be noted that (2.4.2) implies that

$$\epsilon_\psi > \delta\epsilon^2, \qquad (2.4.5)$$

so that the final term in (2.3.14) must always be smaller than the leading-order balance and can be dropped.

The solution to (2.4.1) and (2.4.2) can be plotted in the $\delta - \epsilon_\beta$ plane as shown in Figure 2.3. In the graph, the axes are scaled in powers of ϵ. The axes are not literal, in that the origin is not $\delta = 1$ but is $\delta = O(1)$. The shaded area represents areas where solutions cannot exist, that is, δ is at most $O(1)$ and $\epsilon_\beta \ll 1$. The lines on the graph represent boundaries where ϵ_T and/or ϵ_ψ change values. Short dashed lines indicate ϵ_T changes value as the boundary is crossed, long dashed lines indicate ϵ_ψ changes, and solid lines indicate both ϵ_T and ϵ_ψ change. The values for ϵ_T and ϵ_ψ in the regions of the graph are given. The graph illustrates that there is a continuum of possible models to choose from, but only five choices for ϵ_T and ϵ_ψ, as given by the five regions of the graph.

Important models occur at the vertices where the boundary lines intersect (the ϵ_β axis is also considered to be a boundary). A model chosen with the scaling at a vertex embodies all the characteristics of the surrounding regions. Any model resulting from a scaling in one of the surrounding regions must be a simple limit of the model at the vertex. (By a simple limit we mean a limit in which a parameter tends to zero and terms in the model equations vanish.) The graph indicates there are four important models labelled VSE, SE, ST, and WVT. The names of the models are based on the strength of the β-plane effect and a comparison of the upper-layer depth to the lower-layer depth. If $\epsilon_\beta = O(\epsilon)$, the β-plane effect is considered strong (S). If $\epsilon_\beta > O(\epsilon)$, the β-plane effect is considered very strong (VS). If $\epsilon_\beta < O(\epsilon)$, the β-plane effect is considered weak (W). Similarly, if $\delta = O(1)$, $\delta = O(\epsilon)$, or $\delta = O(\epsilon^2)$, then the upper-layer depth is equal (E), thin (T), or very thin (VT), in comparison to the lower-layer depth, respectively. The naming of the models is summarized in Table 2.1. These models correspond to the four models

Figure 2.3: The solution to (2.4.1, 2.4.2) is plotted in the $\delta - \epsilon_\beta$ plane. The lines represent boundaries between regions where ϵ_T and/or ϵ_ψ change values. The intersections of the boundaries, as marked by the Xs, give rise to the models, as labelled, studied in this thesis. The RED and BCHY labels and arrows indicate where the model tends to these models as the baroclinic and barotropic motion decouple.

2. Derivation of Two-Layer, Frontal-Geostrophic Models

Model name	β-plane effect	Upper-layer depth
VSE	Very Strong (VS), $\epsilon_\beta = O(\epsilon^{\frac{1}{2}})$	Equal (E) to lower layer. $\delta = O(1)$
SE	Strong (S), $\epsilon_\beta = O(\epsilon)$	Equal (E) to lower layer, $\delta = O(1)$
ST	Strong (S), $\epsilon_\beta = O(\epsilon)$	Thin (T) compared to lower layer, $\delta = O(\epsilon)$
WVT	Weak (W), $\epsilon_\beta = O(\epsilon^2)$	Very Thin (VT) compared to lower layer, $\delta = O(\epsilon^2)$

TABLE 2.1. The table summarizes the scales and resulting names of the four FG models. The models differ in the size of the β-plane effect, ϵ_β, and the layer depth ratio, δ.

derived in Benilov and Reznik (1996) and elsewhere (see Table 1.1).

It must be stressed that the different choices for the parameters ϵ_β and δ are equivalent to choosing different horizontal and vertical length scales of the motion. (In the FG limit, the scale height of the upper layer, H_1, is the vertical scale of the motion.) This can be seen if we rearrange the definitions of these parameters, (2.3.7), giving

$$L = \frac{\epsilon_\beta f_0}{\beta_0} = \epsilon_\beta L_\beta \quad \text{and} \quad H_1 = \delta H. \tag{2.4.6}$$

In Figure 2.4, we replot Figure 2.3 in terms of the physical length scales of the motion. For clarity, we examine a flow at a latitude of $45°\text{N}$, an ocean of depth 5 km, and a small Rossby number, $\epsilon = 0.1$. The planetary scale is set equal to the radius of the Earth, which is taken to be 6000 km. This allows actual values for the horizontal and vertical length scales. As well, we now give the resulting time and barotropic stream function scales relative to the advective time scaling, $T_A = L/U = 1/\epsilon f_0 \simeq 1$ day and the QG barotropic scaling, $\Psi_Q = H_1 U L/H$. This allows direct comparison to QG scalings. It should be noted that the values on the axis vary with the size of the Rossby number and the latitude chosen (both length scales increase with the Rossby number). From Figure 2.4, it can now be clearly seen that the VSE and SE models are large-scale models, the ST model represents smaller vertical scales, and the WVT model represents both small vertical and

Figure 2.4: Replotting Figure 2.3 using the definitions for the horizontal (L) and vertical (H_1) length scales defined by (2.4.6) as axes for a typical latitude and Rossby number. Once again the four models are indicated. Now the time scales and barotropic scales are given as ratios to those found in classical QG scaling.
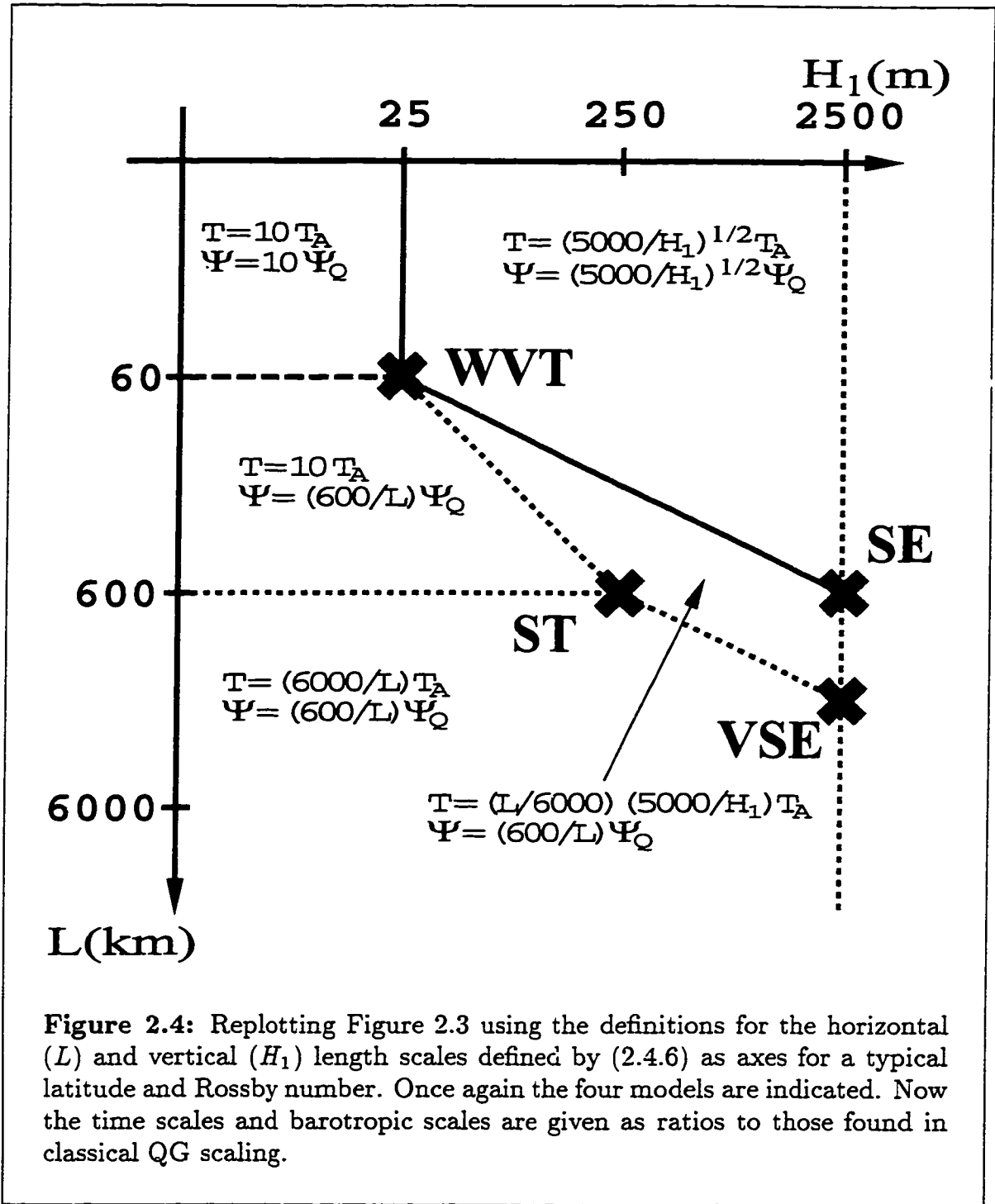
2. Derivation of Two-Layer, Frontal-Geostrophic Models

horizontal scales. Time scales are larger than the advective scale and increase as H_1 decreases. The barotropic scales can be both larger and smaller than the QG scaling and decrease with increasing L.

Alternatively, one can examine the length scale of the motion in comparison to the Rossby deformation radii. We've already defined the internal Rossby deformation radius, R_I, and noted that the length scale must exceed this scale if the Rossby number is small, that is, from (2.3.10) $L = \epsilon^{-\frac{1}{2}} R_I$. Equivalently we can define an internal Rossby deformation radius, R_{I_H}, associated with the total depth of the ocean, that is, $R_{I_H} = \sqrt{g'H}/f_0$. Using this length scale, (2.3.10) can be reformulated to give $L = (\delta/\epsilon)^{\frac{1}{2}} R_{I_H}$. For the VSE and SE models where $\delta = O(1)$, the length scale of the motion must exceed R_{I_H} since $\epsilon \ll 1$. This is necessary since $R_I \sim R_{I_H}$ when $H_1 \sim H$. As the depth ratio decreases the length scale tends to R_{I_H} and eventually becomes smaller. Therefore, for the ST model we have $L = R_{I_H}$, while for the WVT model we have $L = \epsilon^{1/2} R_{I_H}$.

The existence of different models resulting from different scalings is supported by the data of Roden (1975) and Nowlin and Klink (1986) as summarized in Benilov and Reznik (1996). We present a summary of Tables 3 and 4 found in Benilov and Reznik (1996) in Table 2.2 (see Figure 1.1 for location of the fronts). We use the data given there and the model classification they decided upon. The data clearly show a wide range of values for the parameters δ and ϵ_β and indicate that study of all the models is validated. In Benilov and Reznik (1996) no fronts fitting the WVT model were discussed since all the fronts examined had small Rossby numbers and relatively large depth ratios. However, other fronts, and especially boundary currents, where the Rossby number is larger fit the scaling of this model. The Rossby numbers in Table 2.2 are all very small and it is expected that many of the fronts do include regions of greater flow and, thus, larger Rossby numbers. This would shift some of the fronts to the SE and WVT models. As discussed in the prelude to Figure 2.3, it is expected that models may apply well beyond the strict parameter values they are derived with. This is true for many models derived using asymptotic series. Note that we examine this possibility by introducing parameters that allow for order one variations in the β-plane and depth ratio in the models that are studied.

Following the analysis of Chassignet and Cushman-Roisin (1991), (2.3.14) can be used to establish conditions that determine when the equations for the

	K	O	SA	ST$_1$	ST$_2$	ST$_3$	ACC$_1$	ACC$_2$	ACC$_3$
ϵ	0.040	0.026	0.021	0.016	0.021	0.050	0.011	0.022	0.023
δ	0.109	0.073	0.091	0.064	0.064	0.091	0.400	0.500	0.514
ϵ_β	0.034	0.020	0.031	0.062	0.059	0.059	0.024	0.019	0.009
Model	ST	ST	ST	ST	ST	ST	VSE	SE	SE

TABLE 2.2. The table summarizes the data found in Benilov and Reznik (1996), giving the Rossby number, ϵ, the layer depth ratio, δ, and the β-plane effect, ϵ_β, for various frontal systems in the Pacific. The abbreviations are as follows: K=Kuroshio, O=Oyashio, SA=subarctic front, ST$_1$ = subtropical front, northern jet, ST$_2$ = subtropical front, middle jet, ST$_3$ = subtropical front, southern jet, ACC$_1$ = Antarctic Circumpolar Current, northern jet, ACC$_2$ = Antarctic Circumpolar Current, middle jet, ACC$_3$ = Antarctic Circumpolar Current, southern jet.

barotropic and baroclinic motions decouple, that is, when the baroclinic flow evolves independently of the barotropic flow. These conditions are simply those that ensure that terms in ψ are negligible in (2.3.14), that is,

$$\epsilon_\psi \ll \max(\epsilon_T, \epsilon\epsilon_\beta, \epsilon^2).$$

Using the solution shown in Figure 2.3, this requires that

$$\delta \ll \max\left(\epsilon^2, \epsilon_\beta \cdot \frac{\epsilon_\beta^2}{\epsilon}\right). \tag{2.4.7}$$

This condition is not identical to that derived in Chassignet and Cushman-Roisin (1991) for the validity of the RED model due to our use of barotropic/baroclinic dynamics as opposed to layer dynamics. Condition (2.4.7) allows for two types of uncoupled models. First, if $\epsilon_\beta > \epsilon$ and (2.4.7) holds, the model is decoupled with the baroclinic dynamics determined by the baroclinic, hyperbolic equation (hereafter the BCHY model)

$$h_t - \beta h(1 - \delta h)h_x = 0. \tag{2.4.8}$$

The one-layer version of this model, $\delta = 0$, is also mentioned in Cushman-Roisin

2. Derivation of Two-Layer, Frontal-Geostrophic Models

(1986) as the dominant β effect limit of the general reduced gravity FG model derived there. If, on the other hand, $\epsilon_\beta \leq \epsilon$, then (2.4.7) implies that $\delta \ll \max(\epsilon^2, \epsilon_\beta) \ll 1$. We obtain the condition found in Chassignet and Cushman-Roisin (1991) and the RED model is valid. The RED model was also discussed in Cushman-Roisin (1986) and is given by

$$h_t + J\left(h\nabla^2 h + \frac{1}{2}|\nabla h|^2 + \beta h y, h\right) = 0. \tag{2.4.9}$$

This model is a direct limit of the ST model and will be discussed in §3. In Figure 2.3, the two regions that reduce to the BCHY and the RED models are indicated by the BCHY and the RED labels, respectively. Note that the ST and VSE models border the region of the BCHY model and the ST and WVT models border the region of the RED model, indicating that these models share characteristics of the corresponding uncoupled model.

2.5 Potential Vorticity

In comparing and analyzing the models of the previous section it is useful to introduce the concept of potential vorticity (PV). PV is a quantity related to vorticity that is conserved following the flow. It has been deemed that PV is the essential variable in GFD, and that "it is hard to exaggerate the importance of potential vorticity conservation" (Pedlosky, 1987).

For the shallow water equations given by (2.1.5–2.1.9), the potential vorticity, q, for each layer is given by

$$q_1 = \frac{f_0 + \beta_0 y + \nabla \times u_1}{h_1}, \tag{2.5.1}$$

$$q_2 = \frac{f_0 + \beta_0 y + \nabla \times u_2}{h_2}, \tag{2.5.2}$$

respectively. All variables in the above expressions are dimensional. The PV for each layer consists of the absolute vorticity of each layer averaged over the depth of the given layer. The absolute vorticity is the sum of the planetary vorticity, $f_0 + \beta_0 y$, the vorticity due to the Earth's spinning and the relative vorticity, $\nabla \times u$,

2. Derivation of Two-Layer, Frontal-Geostrophic Models

the vorticity due to the motion of the layer. It can easily be shown that the PV for each layer is indeed conserved by the equations (2.1.5–2.1.9). As well, the governing equations can be derived/written in a form stemming from the conservation of PV in each layer but this does not add great insight to our current work.

Using the substitutions (2.2.4) and (2.2.5) for the layer velocities, the barotropic stream function definition (2.2.12), and the scaling given by (2.3.1) with $q_1 = f_0/H_1 q_1^*$ and $q_2 = f_0/H q_2^*$, (2.5.1) and (2.5.2) become the nondimensional potential vorticities given by

$$q_1 = \frac{1 + \epsilon_\beta y + \epsilon_\psi \nabla^2 \psi + \epsilon \nabla \times [(1 - \delta h)\mathbf{u}]}{h}. \qquad (2.5.3)$$

$$q_2 = \frac{1 + \epsilon_\beta y + \epsilon_\psi \nabla^2 \psi - \delta \epsilon \nabla \times [h\mathbf{u}]}{1 - \delta h}. \qquad (2.5.4)$$

where we have dropped the asterisks and used the notation given in (2.3.7). Finally, using the leading-order baroclinic geostrophic velocity, (2.3.11), allows us to write the PV expressions (2.5.3) and (2.5.4) as

$$q_1 = \frac{1 + \epsilon_\beta y + \epsilon_\psi \nabla^2 \psi + \epsilon \left[(1 - \delta h)\nabla^2 h - \delta |\nabla h|^2\right]}{h} + h.o.t.. \qquad (2.5.5)$$

$$q_2 = \frac{1 + \epsilon_\beta y + \epsilon_\psi \nabla^2 \psi - \epsilon \left[\delta h \nabla^2 h + \delta |\nabla h|^2\right]}{(1 - \delta h)} + h.o.t.. \qquad (2.5.6)$$

where *h.o.t.* stands for higher order terms in the small parameters.

One final note on PV formulations: QG models are often studied using basic-state solutions that have constant PV. Since PV is conserved, it remains constant for all time and presents an interesting and informative analysis. However, for the models derived here in the FG limit, imposing leading-order constant PV in the upper layer imposes the condition that its depth be constant. This, of course, precludes any interesting motion, and therefore will not be used as a basic-state solution. It also illustrates the difficulty in dealing with outcroppings from a PV standpoint, in that the leading-order, upper-layer PV becomes infinite as h vanishes.

2. Derivation of Two-Layer, Frontal-Geostrophic Models

2.6   Boundary Conditions

The models presented in §2.4 must be studied over some domain. In the open ocean, most fronts extend across the oceans in the East-West direction between bands of water. This is most easily modelled by a zonally periodic channel given by

$$\Omega = \{(x,y)|x_L < x < x_R, -\infty \leq W_1 < y < W_2 \leq \infty\},$$

where $|W_{1,2}|$ may be very large. The periodicity represents the extended length scale in the east-west direction. The upper, frontal layer is confined to the region $FR \subseteq \Omega$ given by

$$FR = \{(x,y)|x_L < x < x_R, W_1 \leq \phi_1(x,t) < y < \phi_2(x,t) \leq W_2\}.$$

When the upper layer does not extend to the walls, that is, when $\phi_1 > W_1$ or $\phi_2 < W_2$, the curves $y = \phi_{1,2}(x,t)$ represent the curves defined by the outcroppings where the upper layer vanishes, $h = 0$. The curves $\phi_{1,2}$ are periodic in x. As well, we define the domain $NF = \Omega \backslash FR$ to be the domain where only the lower layer exists, i.e., where $h = 0$. (These domains are also suitable for coastal fronts that extend for long distances along the shoreline.)

It should be noted that boundaries and the conditions imposed on them can play essential roles in determining ocean dynamics. The formation of the western boundary currents, for example the Gulf Stream in the Atlantic and the Kuroshio, in the Pacific, are classic examples of boundary influences. Having noted this, in this thesis we are concentrating on open-ocean, inviscid motion and, hence, we wish to eliminate, or at least reduce, the impact of the boundaries on the analysis. In the analysis, the domain and boundary conditions will play a significant role in determining the possible solutions, but we want this role to be at most quantitative rather than qualitative. In the numerical simulations, we attempt to reduce the impact of the boundaries for both simplicity of computation and comparison to analysis.

Boundary conditions must be specified on all horizontal boundaries, the boundary of Ω , and at the outcroppings, the boundary of FR . For simplicity, it will be assumed that the upper layer lies between $\phi_1 \leq y \leq W_2$. That is, the upper layer has a single outcropping at $y = \phi_1$ and the upper layer meets the channel wall at

2. Derivation of Two-Layer, Frontal-Geostrophic Models

$y = W_2$. In this manner, the boundary conditions for the upper layer at both an outcropping and a channel wall will be derived. In order to work with a different domain, it will be a matter of replacing one set of conditions with the other. The possibility of an infinite domain is allowed with $W_2 = \infty$.

At the channel walls there is no normal flow in both layers, which in turn implies that there is no normal baroclinic or barotropic flow.

$$v_{bc} = 0 \quad \text{on} \quad y = W_{1,2}, \tag{2.6.1}$$

$$v_{bt} = 0 \quad \text{on} \quad y = W_{1,2}. \tag{2.6.2}$$

In the case where the channel extends infinitely in the positive y direction, the velocities must remain bounded, that is,

$$|\boldsymbol{u}_{bt}, \boldsymbol{u}_{bc}| < \infty \quad \text{as} \quad y \to \infty. \tag{2.6.3}$$

Boundary conditions are also required at the dynamical outcropping $y = \phi_1$. By definition, the frontal height must vanish at such an outcropping so that

$$h_1 = 0 \quad \text{on} \quad y = \phi_1, \tag{2.6.4}$$

which also implies that the lower layer occupies the entire water column, that is,

$$h_2 = H \quad \text{on} \quad y = \phi_1. \tag{2.6.5}$$

The second condition, known as the kinematic condition, stipulates that a particle on the boundary remain on the boundary as the flow evolves. The kinematic condition is given by

$$\frac{D}{Dt}(\phi_1 - y) = (\phi_1)_t + u(\phi_1)_x - v = 0 \quad \text{on} \quad y = \phi_1.$$

Using (2.2.4) with (2.6.5) reduces this equation to

$$\phi_{1_t} + (\boldsymbol{u}_{bc} + \boldsymbol{u}_{bt}) \cdot (\phi_{1_x}, -1) = 0 \quad \text{on} \quad y = \phi_1. \tag{2.6.6}$$

2. Derivation of Two-Layer, Frontal-Geostrophic Models

Finally, since the channel is periodic, all variables are smoothly periodic. that is,

$$(u_{bt}, u_{bc}, h, p, \phi_1, +derivs.)|_{x_L} = (u_{bt}, u_{bc}, h, p, \phi_1, +derivs.)|_{x_R}. \qquad (2.6.7)$$

where *derivs.* stands for all derivatives of the given functions. It should be noted that on any curve that is a material curve, a curve that always consists of the same fluid particles, Kelvin's circulation theorem applies (see Pedlosky, 1987).

By introducing the scaling $\phi_1 = \phi_1/L$, using the scaling given by (2.3.1), and the definitions of the barotropic stream function (2.2.12) and the leading-order baroclinic velocity, (2.3.11), (2.6.1–2.6.7) reduce to

$$h_x = 0 \quad \text{on} \quad y = W_2. \qquad (2.6.8)$$

$$\psi_x = 0 \quad \text{on} \quad y = W_{1,2}, \qquad (2.6.9)$$

$$|\nabla h|, |\nabla \psi| < \infty \quad \text{as} \quad y \to \infty. \qquad (2.6.10)$$

$$h|_{y=\phi_1} = 0. \qquad (2.6.11)$$

$$(\psi, h, \phi_1, +derivs.)|_{x_L} = (\psi, h, \phi_1, +derivs.)|_{x_R}. \qquad (2.6.12)$$

Note that we have dropped (2.6.6). Using the expressions for the baroclinic and barotropic velocities. (2.3.12) and (2.2.12). equation (2.6.6) becomes

$$\epsilon_T \phi_{1_t} + J\left(\epsilon h + \epsilon_\psi \psi + \epsilon^2 \frac{1}{2}|\nabla h|^2, \phi_1 - y\right)\bigg|_{y=\phi_1} = 0, \qquad (2.6.13)$$

where we have used (2.4.5) to drop a term. If we examine (2.3.14) and take the limit as $y \to \phi_1$, we get

$$\left[\epsilon_T \frac{\partial h}{\partial t} + J\left(\epsilon_\psi \psi + \epsilon^2 \frac{1}{2}|\nabla h|^2, h\right)\right]\bigg|_{y=\phi_1} = 0, \qquad (2.6.14)$$

where we have used (2.6.11). Now, (2.6.13) follows directly from (2.6.11) and equation (2.3.14) and therefore is redundant.

Similarly we can derive a boundary condition on the channel wall by taking the limits of (2.3.13) and (2.3.14) as $y \to W_2$, and making use of (2.6.8) and (2.6.9).

34

2. Derivation of Two-Layer, Frontal-Geostrophic Models

Doing so gives

$$\epsilon_T \epsilon_\psi \frac{\partial \nabla^2 \psi}{\partial t} + \epsilon_\psi^2 J(\psi, \nabla^2 \psi)$$

$$+ \delta \epsilon^2 J \left[h, h(1 - \delta h) \nabla^2 h + \frac{1}{2}(1 - 2\delta h)|\nabla h|^2 \right] = 0, \qquad (2.6.15)$$

$$\epsilon_T \frac{\partial h}{\partial t} + \epsilon^2 J \left[\left(h \nabla^2 h + \frac{1}{2}|\nabla h|^2 \right), h \right] = 0, \qquad (2.6.16)$$

evaluated at $y = W_2$. Taking $\delta(2.6.16) + (2.6.15)$ gives

$$\delta \epsilon_T \frac{\partial h}{\partial t} = -\epsilon_T \epsilon_\psi \frac{\partial \nabla^2 \psi}{\partial t} - \epsilon_\psi^2 J(\psi, \nabla^2 \psi) + \delta^2 \epsilon^2 J(h, h^2 \nabla^2 h + h|\nabla h|^2), \qquad (2.6.17)$$

evaluated at $y = W_2$. Equation (2.6.17) does not appear to give a useful condition until one considers the model limits found in §2.4. For the ST, VSE, and SE models it follows that all terms on the right of (2.6.17) are an order smaller than the term on the left. Thus, to leading order for these models, (2.6.17) reduces to

$$\frac{\partial h}{\partial t} = 0 \quad \text{on} \quad y = W_2. \qquad (2.6.18)$$

2.7 Model Invariants

Associated with any dynamical system there are quantities that remain invariant as time evolves. In deriving the shallow water equations, it is used that momentum and mass are necessarily conserved. In §2.5, the fact that potential vorticity is conserved was used to derive an alternative form of the governing equations. In this section, we examine global invariants, that is, invariants that are not conserved locally following the flow as the PV is, but over the entire domain, $(x, y) \in \Omega$ and $z \in [-H, 0]$.

Under Newton's laws in the absence of any dissipative forces, the total energy of the system must be conserved. The total energy for the two-layer, shallow-water system (2.1.5–2.1.9) is given by

$$E = \frac{1}{2} \int\!\!\int_\Omega \left(g' h_1^2 + h_1 \boldsymbol{u}_1 \cdot \boldsymbol{u}_1 + h_2 \boldsymbol{u}_2 \cdot \boldsymbol{u}_2 \right) dx dy, \qquad (2.7.1)$$

35

2. Derivation of Two-Layer, Frontal-Geostrophic Models

where the first term represents the potential energy and the second and third terms represent the kinetic energy associated with the upper and lower layers, respectively. The quantity E given by (2.7.1) is invariant under the flow described by (2.1.5-2.1.9). Using the relationship of the layer velocities to the barotropic and baroclinic velocities (see (2.2.4) and (2.2.5)) and introducing the barotropic stream function (2.2.12) gives

$$E = \frac{1}{2} \int\int_{\Omega} \left(g'h^2 + H|\nabla\psi|^2 + \frac{h(H-h)}{H}\boldsymbol{u}_{bc} \cdot \boldsymbol{u}_{bc} \right) dxdy.$$

Scaling the equation using (2.3.1) and $E = \left(L^2 H_1^2 g'\right) E^*$ and dropping the asterisks gives the nondimensional total energy

$$E = \frac{1}{2} \int\int_{\Omega} \left(h^2 + \frac{\epsilon_\psi^2}{\delta\epsilon}|\nabla\psi|^2 + \epsilon h(1 - \delta h)\boldsymbol{u} \cdot \boldsymbol{u} \right) dxdy. \tag{2.7.2}$$

Using (2.7.2) with the expression for the leading-order geostrophic velocity, (2.3.11), gives

$$E = \frac{1}{2} \int\int_{\Omega} \left(h^2 + \frac{\epsilon_\psi^2}{\delta\epsilon}|\nabla\psi|^2 + \epsilon h(1 - \delta h)|\nabla h|^2 \right) dxdy + h.o.t. \tag{2.7.3}$$

In the FG limit where $\epsilon, \epsilon_\psi^2/\delta\epsilon \ll 1$ (see (2.4.1) and (2.4.2)), the leading-order total energy is given solely by the potential energy associated with the upper layer (Cushman-Roisin et al., 1992), that is,

$$E^{(0)} = \frac{1}{2} \int\int_{\Omega} h^2 \, dxdy. \tag{2.7.4}$$

This quantity is conserved under the FG model given by (2.3.13) and (2.3.14). Note that we cannot simply assume that the remaining terms are invariant under the FG model. The next order problem would balance the evolution of the next order energy as governed by the leading-order model (2.3.13) and (2.3.14) with the evolution of the leading-order energy (2.7.4) as governed by the next order model, that is, those terms dropped in the derivation of (2.3.13) and (2.3.14). This brings us to an important conclusion: given an invariant of the two-layer, shallow-water

36

2. Derivation of Two-Layer, Frontal-Geostrophic Models

system only the leading-order term within the assumptions of the FG model is conserved by the FG model (2.3.13) and (2.3.14).

The fact that (2.7.4) is a conserved quantity is hardly surprising and also follows from examining the PV for the upper layer. As discussed previously, the PV is conserved following the flow, and, as such, any smooth function of the PV, say $\Phi(q)$, is conserved as well. Therefore it follows that an invariant of the flow can be formed by integrating any smooth function of the PV over the domain. Doing so for each layer gives the invariants

$$Q_1 = \iint_{FR} h_1 \Phi_1(q_1)\, dx dy, \qquad (2.7.5)$$

$$Q_2 = \iint_{\Omega} h_2 \Phi_2(q_2)\, dx dy, \qquad (2.7.6)$$

where the multiplication by the layer depth is a result of the vertical integration. If (2.7.5) and (2.7.6) are nondimensionalized and written in the notation of the FG models, we have that

$$Q_1 = \iint_{FR} h \Phi_1(q_1)\, dx dy, \qquad (2.7.7)$$

$$Q_2 = \iint_{\Omega} (1 - \delta h) \Phi_2(q_2)\, dx dy \qquad (2.7.8)$$

are invariants of the flow (2.3.13) and (2.3.14) for any smooth functions $\Phi_{1,2}$ where $q_{1,2}$ are given by (2.5.5) and (2.5.6), respectively.

From (2.5.5) it follows that the leading-order. upper-layer PV is

$$q_1^{(0)} = \frac{1}{h},$$

and hence it follows from (2.7.7) that

$$\mathfrak{C}_1 = \iint_{FR} \Phi(h)\, dx dy \qquad (2.7.9)$$

is conserved by the FG model for any smooth function Φ. As a consequence of (2.7.9) we get the conservation of area of the upper-layer domain by choosing $\Phi(h) = 1$ and the conservation of volume of the upper layer by choosing $\Phi(h) = h$. (The

37

2. Derivation of Two-Layer, Frontal-Geostrophic Models

conservation of volume is also the conservation of mass since the layer is of constant density.) As well, we again obtain the conservation of potential energy by choosing $\Phi(h) = h^2$, a result we have already ascertained in (2.7.4). The leading-order term of (2.7.6) is also an invariant of the FG model. However, since the leading-order, lower-layer PV differs for the different models under consideration, the specific form of this invariant is left to the discussion of the individual models.

We have not used the fact that the full expression for energy, (2.7.2), and the full expression for upper-layer PV, (2.7.7), are invariant. It follows that any linear combination of (2.7.2) and (2.7.7) for any function Φ_1 is also an invariant of the two-layer shallow water system. Thus, following Cushman-Roisin *et al.* (1992), if we combine these two expressions such that the leading-order terms cancel each other, we will have constructed a higher order functional that must accordingly be an invariant of the FG model. The obvious choice is setting $\Phi_1(q_1) = 1/q_1$ and constructing the function

$$\mathcal{E} = E - \frac{1}{2}Q_1, \qquad (2.7.10)$$

which will result in the leading-order terms cancelling. Using the expression for the upper-layer PV, (2.5.5), gives

$$\frac{h}{q_1} = \frac{h^2}{1 + \epsilon_\beta y + \epsilon_\psi \nabla^2 \psi + \epsilon[(1 - \delta h)\nabla^2 h - \delta|\nabla h|^2]} + h.o.t.$$
$$= h^2 \left(1 - \epsilon_\beta y - \epsilon_\psi \nabla^2 \psi - \epsilon\left[(1 - \delta h)\nabla^2 h - \delta|\nabla h|^2\right]\right) + h.o.t. \qquad (2.7.11)$$

Substituting (2.7.3) and (2.7.11) into (2.7.10) gives

$$\mathcal{E} = \frac{1}{2}\int\int_\Omega \left\{ \frac{\epsilon_\psi^2}{\delta\epsilon}|\nabla\psi|^2 + \epsilon h(1 - \delta h)|\nabla h|^2 \right.$$
$$\left. + h^2\left(\epsilon_\beta y + \epsilon_\psi \nabla^2 \psi + \epsilon\left[\underline{(1 - \delta h)\nabla^2 h} - \delta|\nabla h|^2\right]\right) \right\} dxdy,$$

which can be simplified by integrating the underlined terms by parts to obtain

$$\mathcal{E} = \frac{1}{2}\int\int_\Omega \left\{ \frac{\epsilon_\psi^2}{\delta\epsilon}|\nabla\psi|^2 + h^2\left(\epsilon_\beta y + \epsilon_\psi \nabla^2 \psi\right) - \epsilon h(1 - \delta h)|\nabla h|^2 \right\} dxdy. \qquad (2.7.12)$$

2. Derivation of Two-Layer, Frontal-Geostrophic Models

It follows by construction that the leading-order term in (2.7.12) is conserved by the FG dynamics given by (2.3.13) and (2.3.14). This energy-PV or pseudo-energy invariant contains much of the interesting dynamics of the models and can be used in stability arguments. This is not the only invariant that can be constructed using the energy and the PV invariants, as it is also possible to use the lower-layer PV invariant or a combination of both PV invariants to construct a pseudo-energy. Such is the case for the VSE model where the form of (2.7.12) becomes trivial.

It is well known that symmetries in a given system lead to associated invariants (see Marsden and Ratiu, 1994, Shepherd, 1990). The most well known examples are the conservation of momentum and angular momentum when the system is appropriately symmetric. The presence of the β-plane removes the meridional and rotational symmetry from the models we are studying. However the models are zonally symmetric and the associated invariant is the absolute zonal momentum or impulse (Shepherd, 1990). The absolute zonal momentum for a shallow water layer on a β-plane is given by $u - f_0 y - \frac{1}{2}\beta_0 y^2$ and leads to the two-layer zonal momentum invariant

$$
\begin{aligned}
\mathfrak{M} &= \int\!\!\int_\Omega h_1 \left(u_1 - f_0 y - \frac{1}{2}\beta_0 y^2 \right) + h_2 \left(u_2 - f_0 y - \frac{1}{2}\beta_0 y^2 \right) \, dx dy \\
&= \int\!\!\int_\Omega h u_1 + (H - h)u_2 - H(f_0 y + \frac{1}{2}\beta_0 y^2) \, dx dy.
\end{aligned}
\tag{2.7.13}
$$

This quantity is conserved by the two-layer shallow water equations. Introducing the barotropic and baroclinic velocities, dropping the constant term and making use of the barotropic stream function and the appropriate scaling, (2.7.13) reduces to

$$
\mathfrak{M} = - \int\!\!\int_\Omega \psi_y \, dx dy,
\tag{2.7.14}
$$

which is necessarily a conserved quantity of the FG model. It is easy to show that the invariance of (2.7.14) implies that

$$
\widetilde{\mathfrak{M}} = \int\!\!\int_\Omega y \nabla^2 \psi \, dx dy
\tag{2.7.15}
$$

39

is an invariant of the flow. Rewriting (2.7.15) gives

$$
\begin{aligned}
\widetilde{\mathfrak{M}} &= \iint_\Omega y\psi_{xx} + y\psi_{yy}\, dxdy \\
&= \iint_\Omega (y\psi)_{xx}\, dxdy - \iint_\Omega \psi_y\, dxdy + \int_{x_L} x_R\psi_y\big|_{y=W_1}^{y=W_1}\, dx \qquad (2.7.16) \\
&= \mathfrak{M} - \int_{x_L} x_R u_{bt}\big|_{y=W_1}^{y=W_1}\, dx,
\end{aligned}
$$

where we've integrated by parts and used the periodic boundary conditions. The final term in (2.7.16) is independent of time by Kelvin's circulation theorem, and therefore the invariance of $\mathfrak{M}$ and $\widetilde{\mathfrak{M}}$ is equivalent.

We shall also consider the one-layer zonal momentum. which when scaled and written in the notation of our models is given by

$$
\mathfrak{M}_1 = -\iint_\Omega (hy + \epsilon_\psi h\psi_y + \epsilon hh_y)\, dxdy + h.o.t.,
$$

where we've used the leading-order geostrophic velocity (2.4.1). In the FG limit, it follows that the leading-order, one-layer zonal momentum invariant is

$$
\mathfrak{M}_1 = -\iint_\Omega yh\, dxdy. \qquad (2.7.17)
$$

The invariant (2.7.17) is the zonal momentum invariant found in Slomp (1995) for the RED model. As we shall see, (2.7.17) is in fact an invariant for two of the two-layer FG models as well.

It should be noted that these invariants are often discussed within the structure of the noncanonical Hamiltonian formulation of a given model (see Shepherd, 1990). However, not all of the FG models have such a structure. The WVT and SE models do while the ST and VSE do not. As such, in the body of the thesis we will not examine the details of the Hamiltonian formulation. We will provide a brief description of the Hamiltonian formulation of the SE model in Appendix 4. Interested readers are directed to Swaters (1993b) and Karsten and Swaters (1996b) for a discussion of the Hamiltonian formulation of the WVT model and to Slomp (1995) and Slomp and Swaters (1997) for discussion of the Hamiltonian formulation of the RED model.

Chapter 3

ST model

We begin by examining the ST model. We start with this model because it has been argued that its scaling is most similar to large-scale oceanic fronts (Benilov and Reznik, 1996). First we present the model and the potential vorticity as derived in §2 for the scaling of the ST model. Then we briefly examine the linear, normal-mode model following the analysis of Benilov and Cushman-Roisin (1994). Next, we examine the invariants of the flow, and derive a nonlinear stability theorem. Subsequently, we do a weakly nonlinear analysis of the linear solutions. And finally, we examine all these aspects through numerical simulations. As mentioned previously, this model shares much in common with the RED model and the analysis that follows applies to the RED model in the appropriate limit.

3.1 Model Equations

The ST model corresponds to the scaling

$$\delta = \mu\epsilon, \quad \epsilon_\beta = \beta\epsilon, \quad \epsilon_T = \epsilon_v = \epsilon^2, \tag{3.1.1}$$

where μ and β represent changes in the layer depth ratio and β-plane effect, respectively, and are included to illustrate how these effects change the model dynamics and can give rise to reduced models. (Note that since $\delta \leq 1/2$ for all models, we choose the typical value of μ to be one half. All other typical values of the parameters, if not explicitly stated, are chosen to be one.) The scaling corresponds to a model where the effect of the β-plane is strong (S) and the upper-layer depth is thin (T). This model is referred to as the strong beta model in previous work, (see Benilov and Cushman-Roisin, 1994 and Benilov, 1995a). The model equations

3. ST model

(2.3.13) and (2.3.14) reduce to

$$\beta\psi_x + \mu J \left[h. h\nabla^2 h + \frac{1}{2}|\nabla h|^2 \right] = 0. \tag{3.1.2}$$

$$h_t + J \left[\psi + \beta hy + h\nabla^2 h + \frac{1}{2}|\nabla h|^2, h \right] = 0. \tag{3.1.3}$$

The barotropic stream function is related to the upper-layer depth and the lower-layer pressure, p, by the relationship

$$\psi = \frac{\mu}{2}h^2 + p. \tag{3.1.4}$$

The equations can be recast with p as a variable as opposed to ψ (see Benilov and Cushman-Roisin, 1994 and Benilov, 1995a). One can form a third equation from (3.1.2) and (3.1.3) by eliminating the nonlinear h terms to get

$$\mu h_t + J(\psi, \mu h + \beta y) + \mu J(\beta hy, h) = 0. \tag{3.1.5}$$

Considering only (3.1.3) in the limit as $\psi \rightarrow 0$ gives the RED model.

Note that when the upper layer vanishes, $h = 0$, the model reduces to the equation

$$\psi_x \equiv p_x = 0.$$

These equations do not describe any dynamics at all, but basically state that, in the absence of the upper layer, the lower-layer flow is any arbitrary zonal flow. This causes difficulty when an outcropping occurs as it does not allow for linear solutions in the frontal region to be properly matched to solutions in the nonfrontal region. For this reason, the nonfrontal region is not discussed in detail though this difficulty is mentioned when appropriate.

The potential vorticities for the ST model are found using the scaling (3.1.1)

3. ST model

in (2.5.5) and (2.5.6) giving

$$q_1 = q_1^{(0)} + \epsilon q_1^{(1)} + O(\epsilon^2) = \frac{1}{h} + \epsilon \frac{\nabla^2 h + \beta y}{h} + O(\epsilon^2), \qquad (3.1.6)$$

$$q_2 = 1 + \epsilon q_2^{(0)} + O(\epsilon^2) = 1 + \epsilon(\mu h + \beta y) + O(\epsilon^2). \qquad (3.1.7)$$

Note that the barotropic stream function does not appear in the leading-order potential vorticities indicating that this model is dominated by the baroclinic dynamics. It should be noted that in the upper layer, the leading-order stream function, h, advection of the leading-order PV, $1/h$, is zero. Hence, the leading-order upper-layer PV evolves as a response to the advection of the leading-order PV by the second-order, ageostrophic stream function, $\psi + \frac{1}{2}|\nabla h|^2$, and the advection of the second-order PV by the leading-order, geostrophic stream function, h (see Cushman-Roisin, 1986 for further discussion).

The boundary conditions for the ST model are given by (2.6.8), (2.6.9), (2.6.11), (2.6.12), and (2.6.18) with (2.6.10) applied when the channel extends to infinity.

3.2 Linear Analysis

To analyze the model equations, we need a basic-state flow that is a solution to the full nonlinear model. From (3.1.2) and (3.1.3) it follows that any zonal flow, where the model variables are allowed to vary in the meridional direction only, is a solution to the fully nonlinear ST model. (In fact, any zonal flow is a solution to the general FG model (2.3.13) and (2.3.14).) The flow is zonal since the leading order velocities as given by (2.3.11) and (2.2.12) are in the zonal direction when h and ψ depend only on y. Such flows are often called parallel shear flows since they run parallel to the meridional channel walls and allow for meridional shear. Although it is possible to carry out some analysis on general steady flows, for the purpose of this thesis we will examine only zonal flows. Hereafter, we will indicate the basic-state, zonal flow with a subscript zero, that is, $h_0(y), \psi_0(y)$ is the basic-state, zonal flow.

We examine such flows by setting the model variables to be the sum of the

3. ST model

basic state and some perturbation, that is,

$$h = h_0(y) + \widehat{h}(x, y, t),$$
$$\psi = \psi_0(y) + \widehat{\psi}(x, y, t), \qquad (3.2.1)$$
$$\phi_1 = a_1 + \widehat{\phi}(x, t),$$

where the hatted quantities are the perturbations, ϕ_1 marks the position of the outcropping of the total flow while the basic-state flow has an outcropping at $y = a_1$, that is,

$$h_0(a_1) = 0. \qquad (3.2.2)$$

Substituting (3.2.1) into the model (3.1.2) and (3.1.3) gives, after dropping the hats,

$$
\beta\psi_x + \mu\left[-h_0'h_0\nabla^2 h_x - (h_0')^2 h_{xy} + (h_0 h_0'')' h_x \right.
$$
$$
+ h_0''' h h_x - h_0' h \nabla^2 h_x - h_0'(h_x h_{xx} + h_y h_{xy})
$$
$$
+ h_0 J(h, \nabla^2 h) + h_0' J(h, h_y)
$$
$$
\left. + J\left(h, h\nabla^2 h + \frac{1}{2}|\nabla h|^2\right) \right] = 0. \qquad (3.2.3)
$$

$$
h_t + h_0'\psi_x - \psi_0' h_x + J(\psi, h)
$$
$$
-\left[-h_0'h_0\nabla^2 h_x - (h_0')^2 h_{xy} + (h_0 h_0'')' h_x \right.
$$
$$
+ h_0''' h h_x - h_0' h \nabla^2 h_x - h_0'(h_x h_{xx} + h_y h_{xy})
$$
$$
+ h_0 J(h, \nabla^2 h) + h_0' J(h, h_y)
$$
$$
\left. + J\left(h, h\nabla^2 h + \frac{1}{2}|\nabla h|^2\right) \right]
$$
$$
- \beta\left(h_0 h_x + h h_x\right) = 0. \qquad (3.2.4)
$$

In the following analysis, it is easier to work with these equations if we form the equation that eliminates the linear terms in ψ by taking $\beta \times (3.2.4) - h_0' \times (3.2.3)$. Secondly, for simplicity, we eliminate the nonlinear Jacobian term by taking $(3.2.3)+$

44

3. ST model

$\mu \times$ (3.2.4). This gives

$$\beta h_t + (\beta + \mu h_0') \left[h_0' h_0 \nabla^2 h_x + (h_0')^2 h_{xy} \right]$$
$$- \left[\beta \psi_0' + \beta^2 h_0 + (\beta + \mu h_0')(h_0 h_0'')' \right] h_x =$$
$$- \beta J(\psi, h) + \beta^2 h h_x$$
$$+ (\beta + \mu h_0') \left[h_0'' h h_x - h_0' h \nabla^2 h_x \right. \tag{3.2.5}$$
$$+ -h_0'(h_x h_{xx} + h_y h_{xy}) + h_0 J(h, \nabla^2 h)$$
$$\left. + h_0' J(h, h_y) + J \left(h, h \nabla^2 h + \frac{1}{2} |\nabla h|^2 \right) \right].$$

$$(\beta + \mu h_0') \psi_x = -\mu \left[h_t - (\psi_0' + \beta h_0) h_x + J(w, h) - \beta h h_x \right]. \tag{3.2.6}$$

In this thesis, we will be looking at nonlinear interactions. But in order to do so, it is necessary to understand the linear stability of parallel shear flows. The linear equations are found by keeping only the terms that are linear in the perturbation quantities h, ψ in equations (3.2.5) and (3.2.6) giving

$$\beta h_t + (\beta + \mu h_0') \left[h_0' h_0 \nabla^2 h_x + (h_0')^2 h_{xy} \right]$$
$$- \left[\beta \psi_0' + \beta^2 h_0 + (\beta + \mu h_0')(h_0 h_0'')' \right] h_x = 0, \tag{3.2.7}$$
$$(\beta + \mu h_0') \psi_x = -\mu \left[h_t - (\psi_0' + \beta h_0) h_x \right]. \tag{3.2.8}$$

It is important to note that the equations have been decoupled in the linear limit. That is, (3.2.7) contains no terms in ψ and thus can be solved for h independently of (3.2.8). Once h has been determined, (3.2.8) can be used to determine ψ. This is always possible when a linear limit is taken but it is noteworthy that here higher derivative terms need not be introduced to decouple the equations (see Swaters, 1993b or Reszka, 1997 for linear analysis of the WVT model). As well, though decoupled, (3.2.7) is not the linear RED model, but becomes so in the limit as $\mu \to 0$.

Several other limits deserve discussion at this point. If h_0 is constant, (3.2.7) reduces to the wave equation

$$h_t - (\psi_0' + \beta h_0) h_x = 0,$$

45

3. ST model

which has solutions $h = h\left[x + (\psi_0' + \beta h_0)t, y\right]$ (see Whitham, 1974). In this limit, $\psi_x = 0$ and the barotropic flow is a pure zonal flow. In the limit $\beta + \mu h_0' = 0$, the equation reduces to the same wave equation only now there is no equation governing the barotropic stream function.

In order to continue our analysis, we make the further assumption that the perturbations take the form of travelling waves, that is,

$$
\begin{aligned}
h(x, y, t) &= \widetilde{h}(y) \exp[i(kx - \omega t)] + c.c., \\
\psi(x, y, t) &= \widetilde{\psi}(y) \exp[i(kx - \omega t)] + c.c., \\
\phi(x, t) &= \widetilde{\phi} \exp[i(kx - \omega t)] + c.c.,
\end{aligned}
\tag{3.2.9}
$$

where k is the along-front wavenumber, ω is the frequency, and $c.c.$ means complex conjugate. The phase speed and group speed of the travelling wave are given by

$$
c = \frac{\omega}{k} \quad \text{and} \quad c_G = \frac{\partial \omega}{\partial k},
$$

respectively. The group velocity is the speed at which wave energy travels (see Pedlosky, 1987). In this thesis, we will use both the frequency and phase speed notation depending on which is most convenient. The frequency (and phase speed) may be complex, that is, $\omega = \omega_R + i\omega_I = k(c_R + ic_I)$. The normal-mode models examined in this thesis all have real coefficients and, hence, if they give rise to complex values of ω these values must appear as complex conjugate pairs. Thus, if $\omega_I \neq 0$ there exists a normal mode wave with an amplitude that will grow in time with a growth rate of $\sigma = |\omega_I| = k|c_I|$. If $\omega_I = 0$ the wave is neutrally stable and the amplitude remains constant in time.

The linear travelling-wave or normal-mode equations are found by substituting (3.2.9) into (3.2.7) and (3.2.8) giving

$$
\begin{aligned}
(\mu h_0' + \beta)[h_0(h_0'\widetilde{h}' - h_0''\widetilde{h})]' & \\
- \left[(\mu h_0' + \beta)h_0 h_0'^2 k^2 + \beta(\beta h_0 + \psi_0' + c)\right] \widetilde{h} &= 0,
\end{aligned}
\tag{3.2.10}
$$

$$
\widetilde{\psi} = \frac{\mu}{\beta + \mu\alpha}(c + \psi_0' + \beta h_0)\widetilde{h}.
\tag{3.2.11}
$$

3. ST model

The boundary conditions (2.6.8–2.6.12) reduce to

$$\widetilde{h} + h_0'\widetilde{\phi} = 0 \quad \text{on} \quad y = a_1, \tag{3.2.12}$$

$$\widetilde{h}, \widetilde{h}' < \infty \quad \text{as} \quad y \to a_1^+, \tag{3.2.13}$$

$$\widetilde{h}, \widetilde{\psi} = 0 \quad \text{on} \quad y = W_2, \tag{3.2.14}$$

$$|\widetilde{h}|, |\widetilde{\psi}| < \infty \quad \text{as} \quad y \to \infty, \tag{3.2.15}$$

where the first condition is the Taylor expansion of the condition that h vanish at $y = a_1 + \widetilde{\phi}$, and the second condition is derived by ensuring the continuity of pressure and mass flux across the material interface at $y = a_1$ in the manner of LeBlond and Mysak (1978) or Swaters (1993b).

In addition, at an outcropping it is necessary to impose continuity conditions on the barotropic stream function. Usually (see for example Swaters, 1993b or Swaters, 1991) these reduce to the condition that the lower-layer pressure is C^1 across the outcropping. Here, this condition would reduce to having $\widetilde{v}$ smoothly continuous across the outcropping. However, since the model does not describe motion in the absence of an upper layer, imposing such a condition would eliminate all possible wave motion at the outcropping. This is a grave limitation of the model.

This model does allow a linear solution for basic-state fronts with an outcropping if we allow a certain approximation to be made at the outcropping. By definition, an outcropping where h_0 vanishes must be governed by small-scale, non-linear dynamics since it no longer holds that $\widetilde{h} \ll h_0$. Therefore, we assume that the outcropping constitutes a nonlinear boundary layer that allows the linear solution to be smoothly matched to the nonfrontal, no-wave-motion region. Such an assumption is reasonable, but the inability to describe the solution in this region restricts the applicability of these solutions. Whenever we analyze the linear solution to the ST model that has an outcropping, we will remind the reader of the difficulty with the solution and the assumption made. Thus, all results from this solution must be considered with the proper amount of discretion.

It is useful to present the analysis for another reason. As mentioned previously, the analysis can be applied to the RED model in the limit as $\psi \to 0$. The analysis for the wedge front that follows is valid for the RED model (see Cushman-Roisin, 1986) in that the assumption of no motion in the lower layer requires no matching conditions. The finite amplitude analysis of §3.6 is also valid for the RED model

3. ST model

and is original work extending the f-plane analysis of Slomp and Swaters (1997) to include the β-plane approximation.

In Benilov and Cushman-Roisin (1994), the normal mode stability of the ST model is examined by letting

$$\widetilde{h} = h_0' \eta. \tag{3.2.16}$$

This transformation is valid provided $h_0' \neq 0$ anywhere in the domain. Thus, we are restricting the following analysis to monotonic fronts. Substituting (3.2.16) into (3.2.10) gives

$$[h_0 {h_0'}^2 \eta']' - \left[h_0 {h_0'}^2 k^2 + \frac{\beta\,(\beta h_0 + \psi_0' + c)}{\mu h_0' + \beta} \right] h_0' \eta = 0. \tag{3.2.17}$$

Multiplying (3.2.17) by the complex conjugate of η and integrating over $a_1 < y < W_2$ gives

$$\int_{a_1}^{W_2} \left\{ h_0 (h_0')^2 [|\eta'|^2 + k^2 |\eta|^2] + \frac{\beta\,(\beta h_0 + \psi_0' + c)}{\mu h_0' + \beta} h_0' |\eta|^2 \right\} dy = 0, \tag{3.2.18}$$

where we've integrated by parts and used (3.2.2), (3.2.13), and (3.2.14). The imaginary part of (3.2.18) is given by

$$c_I \int_{a_1}^{W_2} \frac{\beta h_0'}{\mu h_0' + \beta} |\eta|^2 dy = 0. \tag{3.2.19}$$

It follows directly from (3.2.19) that if

$$\frac{\beta h_0'}{\mu h_0' + \beta} > 0, \forall \quad y \in [a_1, W_2], \tag{3.2.20}$$

or

$$\frac{\beta h_0'}{\mu h_0' + \beta} < 0, \forall \quad y \in [a_1, W_2], \tag{3.2.21}$$

then the integrand in (3.2.19) is strictly positive or negative, respectively, for non-trivial solutions, implying $c_I = 0$, and hence, $\omega_I = 0$ for all wavenumbers. Therefore if (3.2.20) or (3.2.21) holds, the front is neutrally stable. Instability can only result

48

3. ST model

if the basic-state front violates (3.2.20) or (3.2.21). For a smooth front, this can only occur if $h'_0 = 0$ or $h'_0 = -\beta/\mu$, for some value of y. These two points are singular points of equation (3.2.10).

The manner in which instability arises when these singularities exist in the basic flow is discussed in Benilov (1995a). There, two techniques were used to remove the singularities thus regularizing the problem. The singularity at frontal extreme points, $h'_0 = 0$, is shown to be very similar to the RED model case. Instabilities exist for all values of the parameters μ and β with the addition of barotropic/lower-layer dynamics shifting the instability to larger wavelengths than that seen in the RED model. The β-plane effect is seen to weaken the instability but not eliminate it.

For the second singular point, $h'_0 = -\beta/\mu$, a smaller growth instability is possible. The growth rate is dependent on the mean flow velocity at the singular point. The second point arises from the inclusion of the lower layer and the β-plane and is not found in the RED model. These instabilities are not the focus of this thesis, and we will assume in our further analysis that we are not near these singular points. We will, however examine their effect in numerical solutions to the model in §3.11. It should be noted that the regularization of these models requires the addition of terms not found in the the original model (see Benilov, 1995a) and therefore the instability may not occur in numerical simulations of the full nonlinear model.

In the ST model, the leading-order potential vorticities in each layer given by (3.1.6) and (3.1.7) have gradients given by

$$\frac{dq_1^{(0)}}{dy} = -\frac{h'_0}{h_0^2}, \quad \text{and} \quad \frac{dq_2^{(0)}}{dy} = \mu h'_0 + \beta.$$

Flows can become unstable only if one of these gradients vanishes. This is a much stronger necessary condition for instability than in a QG model where if the PV gradient reverses sign across the layer interface instability is possible. Here, for instability, one of the PV gradients must vanish as in the RED model. This result emphasizes the weak coupling of the lower layer in the ST model. Since the barotropic stream function evolves diagnostically via (3.1.2), it does not change the stability conditions.

A final note on linear stability. In Benilov and Reznik (1996), the possibility of short-wave instability is examined by scaling the results of a two-layer, QG model

3. ST model

according to the ST model scaling. Their results suggest that short waves are stable if $0 \leq -\mu h_0' \leq \beta$ and unstable otherwise. However, these short waves exist at scales that are beyond the model's resolution and can only be modelled if QG terms that are higher order in the Rossby number are retained in the model. The examination of such a model is not the focus of this thesis and is left to future work.

We will discuss linear solutions for two basic-state fronts: a gently sloping (GS) front and an outcropping wedge (WD) front. More complicated frontal profiles can be examined for all the models examined in this thesis. However the solutions must be found numerically. Qualitatively the results are similar. This type of analysis is not the focus of this thesis and these results will be presented elsewhere. For a gently sloping front we take

$$h_0(y) = \aleph + \alpha \left(y - \frac{L}{2} \right), \qquad 0 \leq y \leq L,$$
$$\psi_0(y) = 0, \qquad 0 \leq y \leq L, \tag{3.2.22}$$

where $\aleph$ is a positive constant. We've chosen $W_1 = 0$ and $W_2 = L$, and the front extends across the entire channel so that the boundary conditions are

$$h = v = 0 \quad \text{on} \quad y = 0, L. \tag{3.2.23}$$

We also assume that the slope of the front, α, is small, that is,

$$\alpha = \Delta \tilde{\alpha}, \tag{3.2.24}$$

where $0 < \Delta \ll 1$ and $\tilde{\alpha} = O(1)$. In order that the leading-order terms in Δ in (3.2.10) include the higher order derivatives, we must also assume

$$\beta = \Delta \tilde{\beta}, \quad \omega = \Delta \tilde{\omega}, \quad c = \Delta \tilde{c}, \tag{3.2.25}$$

where $\tilde{\beta}$, $\tilde{\omega}$, and $\tilde{c}$ are $O(1)$ parameters. Then to leading order in Δ, (3.2.10) reduces to

$$\aleph \tilde{\alpha} (\mu \tilde{\alpha} + \tilde{\beta})(\tilde{h}'' - k^2 \tilde{h}) - \tilde{\beta}(\aleph \tilde{\beta} + \tilde{c})\tilde{h} = 0. \tag{3.2.26}$$

3. ST model

Together with (3.2.23) this defines an eigenvalue problem for the eigenvalue. $\tilde{c}$, and the corresponding eigenfunction, $\tilde{h}$. In order to satisfy (3.2.23). we have that

$$\tilde{h} = A\sin(\ell y), \qquad \ell = \frac{n\pi}{L}, \qquad n = 1, 2, 3, \dots \qquad (3.2.27)$$

Substitution of (3.2.27) into (3.2.26) gives

$$\tilde{c}(k, \ell) = -\aleph \left[\tilde{\beta} + \frac{\tilde{\alpha}(\mu\tilde{\alpha} + \tilde{\beta})\left(k^2 + \ell^2\right)}{\tilde{\beta}} \right], \qquad (3.2.28)$$

so that the wave is neutrally stable. The group velocity for this solution is given by

$$\tilde{c}_G(k, \ell) = -\aleph \left[\tilde{\beta} + \frac{\tilde{\alpha}(\mu\tilde{\alpha} + \tilde{\beta})\left(3k^2 + \ell^2\right)}{\tilde{\beta}} \right], \qquad (3.2.29)$$

and the barotropic stream function from (3.2.11) is given by

$$\tilde{\psi} = -\frac{\aleph\mu\tilde{\alpha}(k^2 + \ell^2)}{\tilde{\beta}}\tilde{h}. \qquad (3.2.30)$$

One important aspect of the solution above is when the phase speed. (3.2.28), of the waves changes sign. For most parameter values the phase speed is negative, but it is positive for the small region given by

$$-\frac{1}{\mu} \le \rho \le 0.$$
$$K^2 = k^2 + \ell^2 > \frac{\mu}{\mu\rho(\mu\rho + 1)}. \qquad (3.2.31)$$

where $\rho = \tilde{\alpha}/\tilde{\beta}$. Note that for $\alpha > 0$ the geostrophic flow is westward, $u = -h_0' < 0$, and the waves travel with the flow. When $\alpha < 0$ the geostrophic flow is eastward, $u = -h_0' > 0$, and the waves travel against the flow except when (3.2.31) is satisfied.

Benilov and Cushman-Roisin (1994) also found that a solution to the ST model could be found for a wedge-like front,

$$h_0(y) = \begin{cases} \alpha y, & \alpha y \ge 0, \\ 0, & y < 0, \end{cases} \qquad (3.2.32)$$

3. ST model

$$\psi_0(y) = 0, \qquad (3.2.33)$$

corresponding to a constant baroclinic flow with no barotropic flow. (In the original analysis a linearly sheared barotropic flow was included. For our analysis, this does not add qualitative differences and so for simplicity it is not included.) The solution is an extension of the linear solution found in Cushman-Roisin (1986) for the RED model and the wedge front (3.2.32). Again, it should be recognized that the solution below for the wedge front *does not* meet the condition that the leading-order barotropic stream function be smooth across the outcropping. Its validity is based on the assumption explained previously.

The flow meets the stability conditions and therefore gives rise to a linear solution of travelling waves. The normal mode equation (3.2.10) reduces to

$$y\widetilde{h}'' + \widetilde{h}' - \left[\alpha \kappa^2(k)y + \widehat{c} \right] \widetilde{h} = 0. \qquad (3.2.34)$$

where

$$\kappa(k) = \sqrt{\frac{k^2}{\alpha^2} + \frac{\widehat{\beta}\beta}{\alpha^3}}. \qquad (3.2.35)$$

$$\widehat{c} = \frac{\widehat{\beta}c}{\alpha^2}. \qquad (3.2.36)$$

$$\widehat{\beta} = \frac{\beta}{\mu\alpha + \beta}. \qquad (3.2.37)$$

From (3.2.11), $\widetilde{\psi}$ is given by

$$\widetilde{\psi} = \frac{\mu(c + \beta\alpha y)}{\beta + \mu\alpha}\widetilde{h}. \qquad (3.2.38)$$

The boundary conditions on h are simply that it and its y derivative are bounded at $y = 0$ and tend to zero as $\alpha y \to \infty$. The outcropping position from (3.2.12) is given by

$$\widetilde{\phi} = -\frac{\widetilde{h}(0)}{\alpha}.$$

3. ST model

Note that κ is real if

$$k^2 \geq -\frac{\widehat{\beta}\beta}{\alpha} = -\frac{\mu}{\mu\rho(\mu\rho + 1)},\tag{3.2.39}$$

where $\rho = \alpha/\beta$, and imaginary when (3.2.39) does not hold. Imaginary values of κ are only possible if $-1/\mu < \rho < 0$. Note that this region is identical to the region where the phase speed is negative in the previous solution.

When κ is real, the solution to (3.2.34) that satisfies the boundary conditions is

$$\widetilde{h}(y, k, n) = A \exp(-\alpha\kappa(k)y)L_n(2\alpha\kappa(k)y),\tag{3.2.40}$$

where L_n is the Laguerre polynomial of degree $n \geq 0$. with the corresponding dispersion relationship

$$\frac{\widehat{c}}{2\alpha\kappa(k)} + \frac{1}{2} = -n.$$

(see Cushman-Roisin, 1986 or Slomp. 1995 for details). Rearranging gives that $\widehat{c}$ satisfies

$$\widehat{c}(k. n) = -\alpha\kappa(k)(2n + 1).$$

Solving for c gives

$$c(k, n) = -\frac{\alpha^3\kappa(k)(2n + 1)}{\widehat{\beta}}.\tag{3.2.41}$$

and the group velocity

$$c_G(k, n) = -\frac{\alpha(2n + 1)}{\widehat{\beta}}\left(\frac{\alpha^2\kappa^2(k) + k^2}{\kappa(k)}\right).\tag{3.2.42}$$

Since κ is real, so is c and all modes are stable travelling waves. The waves can also be described as frontally trapped since they decay exponentially away from the front at $y = 0$. The meridional e-folding scale increases with the along front wavelength, and so a wave becomes more closely trapped to the frontal outcropping as its zonal length scale decreases. For $\rho > 0$, a front sloping down toward the North Pole with westward geostrophic flow, the waves travel westward with the

53

3. ST model

front on their left and the phase speed increases with increasing β and wavenumber. For $-1/\mu < \rho < 0$, a front sloping down toward the equator with weak eastward geostrophic flow and short waves satisfying (3.2.39), the waves travel eastward with the front on their left and the phase speed decreases with increasing β but increases with increasing wavenumber. For $\rho < -1/\mu$, a front sloping down toward the equator with strong eastward geostrophic flow, the waves travel westward with the front on their right and the phase speed increases with increasing β and wavenumber.

For κ complex, a continuous spectrum of stable travelling waves is realized (see Cushman-Roisin, 1986 for details). The solution is given in terms of Kummer/hypergeometric functions, M, as

$$\tilde{h}(y,k,n) = A\exp(i\alpha\kappa_I(k)y)M\left(\frac{1}{2} + \frac{i\widehat{c}}{2\kappa_I(k)}, 1, -2i\kappa_I(k)y\right). \qquad (3.2.43)$$

where $\kappa_I^2 = -\kappa^2$. This solution is not suitable for further analysis, and is not discussed in detail.

For both linear solutions, it should be noted that in the special case where $\beta = 0$ the model becomes degenerate and wave solutions are not possible. There are no longer any terms related to time derivatives, and thus the frequency ω. and as a result no dispersion relationship for ω. Physically, without the β-plane forcing there is no mechanism to generate barotropic waves.

The reduced-gravity limit for both models is obtained by letting μ tend to zero. When this is done, the region $-1/\mu < \rho < 0$ expands to the entire lower half plane. As such, waves that travel in the opposite direction as the basic-state flow are not possible in the RED model. For the wedge model, the results of Cushman-Roisin (1986) are obtained and then taking $\beta \to 0$ retrieves the result of Slomp (1995). It should be noted that in the single layer model with $\beta = 0$ waves are still possible.

3.3 Nonlinear Invariants and Stability

In this section we discuss the nonlinear invariants as derived in §2.7 for the ST model. Using these invariants, it is possible to establish a nonlinear stability theorem similar to that presented in Slomp (1995) for the RED model.

Under the scaling (3.1.1), the leading-order term in pseudo-energy invariant

3. ST model

(2.7.12), reduces to

$$\mathcal{E} = \frac{1}{2} \iint_{FR} \left(h\nabla h \cdot \nabla h - \beta h^2 y \right) dxdy. \tag{3.3.1}$$

Illustrating that this quantity is invariant can be shown using the governing equations and the boundary conditions but as it follows from the discussion in §2.7, we do not present it here.

From §2.7, we also have the invariants associated with the leading-order PV. For the upper layer, (2.7.9) holds so that

$$\mathfrak{C}_1(h) = \iint_{FR} \Phi_1(h) \, dxdy \tag{3.3.2}$$

is an invariant of the ST model where Φ_1 is any arbitrary, sufficiently smooth function of its argument with $\Phi_1(0) = 0$ so that any values associated with the variation of the outcropping are eliminated. This is not an additional restriction since the invariants are only determined to a constant that we are free to choose. For the lower layer, the leading-order PV is given by (3.1.7) and hence it follows from (2.7.6) that

$$\mathfrak{C}_2(h) = \iint_{\Omega} \Phi_2(\mu h + \beta y) \, dxdy \tag{3.3.3}$$

is an invariant of the ST model where Φ_2 is any arbitrary, sufficiently smooth function of its argument. (Note that (2.7.6) holds for any function of the lower-layer potential vorticity and, thus, holds for any function of $q_2 - 1$ giving the above result.)

The zonal momentum invariant (2.7.14) is not useful in the ST model since there are no terms governing the time evolution of the barotropic stream function, ψ. However, the similarity of the invariants (3.3.2) and (3.3.3) allows us to construct another invariant. Setting

$$\mathfrak{M} = \frac{\mathfrak{C}_1 - \mathfrak{C}_2}{2\mu\beta},$$

with $\Phi_1(h) = (\mu h)^2$ and $\Phi_2(\mu h + \beta y) = (\mu h + \beta y)^2$ gives that

$$\mathfrak{M}(h) = \iint_{FR} yh \, dxdy \tag{3.3.4}$$

3. ST model

is an invariant of the flow, where we've dropped the constant term. We recognize (3.3.4) as the zonal momentum invariant of the one-layer model (see (2.7.17)). This stresses the similarity of the ST model to the RED model.

Since none of the above invariants involves the barotropic stream function, it is not possible to use them to establish stability theorems that bound a perturbation norm involving both the upper-layer depth and the barotropic stream function. We can, however. find conditions on a zonal flow that establish nonlinear bounds on the perturbation upper-layer depth only. Nonlinear stability analysis often uses a constrained zonal momentum invariant, the zonal momentum invariant plus a Casimir, which is just the leading-order PV invariant (see Slomp, 1995 or Karsten and Swaters, 1996b). But, since the one-layer zonal momentum invariant derived above is a linear combination of the two PV invariants. it does not need to be included in the analysis. The analysis can be carried out using only the PV invariants emphasizing their importance in determining stability. As in Slomp (1995) and Karsten and Swaters (1996b), for the nonlinear analysis to hold we can only examine a basic-state front that extends across the entire domain and does not outcrop.

The stability conditions are determined by considering

$$\mathfrak{I}(h) = \mathfrak{C}_1(h) - \mathfrak{C}_1(h_0) + \mathfrak{C}_2(h) - \mathfrak{C}_2(h_0). \qquad (3.3.5)$$

where $h_0 = h_0(y)$ represents a basic-state zonal flow and $\mathfrak{C}_1$ and $\mathfrak{C}_2$ are given by (3.3.2) and (3.3.3), respectively, with the domains of integration extended to the entire domain Ω. Obviously, $\mathfrak{I}(h)$ is an invariant of the flow since $\mathfrak{C}_1(h)$ and $\mathfrak{C}_2(h)$ are. Using (3.3.2) and (3.3.3), (3.3.5) reduces to

$$\mathfrak{I}(h) = \iint_\Omega \Phi_1(h) - \Phi_1(h_0) + \Phi_2(\mu h + \beta y) - \Phi_2(\mu h_0 + \beta y) \, dx dy. \qquad (3.3.6)$$

We now consider the first variation of $\mathfrak{I}$, that is,

$$\delta \mathfrak{I}(h) = \iint_\Omega [\Phi_1'(h) + \mu \Phi_2'(\mu h + \beta y)] \, \delta h \, dx dy,$$

where variations of y and $h_0(y)$ are zero since they are independent of time. In order that $\delta \mathfrak{I}$ vanishes at $h = h_0$, the first order condition necessary in establishing

3. ST model

stability, we choose the functions Φ to satisfy

$$\Phi_1'(h_0) + \mu\Phi_2'(\mu h_0 + \beta y) = 0. \qquad (3.3.7)$$

Note that this condition does not determine Φ_1 and Φ_2, but only gives a single condition that they must satisfy.

For nonlinear conditions, we consider h to be composed of a basic-state flow, h_0, plus a finite amplitude perturbation, $\tilde{h}$, that is, $h = \tilde{h} + h_0$. Then, using (3.3.7), (3.3.6) reduces to

$$\Im(\tilde{h} + h_0) = \int\!\!\int_\Omega \left\{ \Phi_1(\tilde{h} + h_0) - \Phi_1(h_0) \right.$$
$$\left. + \Phi_2(\mu\tilde{h} + \mu h_0 + \beta y) - \Phi_2(\mu h_0 + \beta y) \right\} \, dx dy. \qquad (3.3.8)$$

Now, we assume that the functions Φ have bounded second derivatives, that is,

$$-\infty < A < \Phi_1''(\xi) + \mu^2\Phi_2''(\mu\xi + \beta y) < B < \infty. \qquad (3.3.9)$$

for some constants A and B, and for all $\xi \geq 0$ and $y \in [W_1, W_2]$. (Note that $\Phi_1(\xi)$ and $\Phi_2(\mu\xi + \beta y)$ are only defined for $\xi \geq 0$ since they are defined in terms of h, which is always positive.) If (3.3.12) is integrated twice with respect to ξ, first from h_0 to ξ and then from h_0 to $\tilde{h} + h_0$, and (3.3.7) is used, it follows that

$$\frac{A}{2}\tilde{h}^2 < \Phi_1(\tilde{h} + h_0) - \Phi_1(h_0) + \Phi_2(\mu\tilde{h} + \mu h_0 + \beta y) - \Phi_2(\mu h_0 + \beta y) < \frac{B}{2}\tilde{h}^2, \quad (3.3.10)$$

and hence, from (3.3.8) that

$$\int\!\!\int_\Omega \frac{A}{2}\tilde{h}^2 \, dx dy < \Im(\tilde{h} + h_0) < \int\!\!\int_\Omega \frac{B}{2}\tilde{h}^2 \, dx dy. \qquad (3.3.11)$$

The nonlinear stability result follows:
The zonal flow $h_0(y)$ is nonlinearly stable in the sense of Liapunov with respect to the perturbation norm

$$||\tilde{h}||^2 = \int\!\!\int_\Omega \tilde{h}^2 \, dx dy,$$

3. ST model

if there exists real constants A and B such that either

$$0 < A < \Phi_1''(\xi) + \mu^2 \Phi_2''(\mu\xi + \beta y) < B < \infty \tag{3.3.12}$$

or

$$-\infty < A < \Phi_1''(\xi) + \mu^2 \Phi_2''(\mu\xi + \beta y) < B < 0, \tag{3.3.13}$$

for all $\xi \geq 0$ and $y \in [W_1, W_2]$, where

$$\Phi_1'(h_0) + \mu \Phi_2'(\mu h_0 + \beta y) = 0. \tag{3.3.14}$$

The conditions (3.3.12) and (3.3.13) establish that $\mathfrak{J}$ is either positive or negative definite, respectively, and Liapunov stability conditions follow accordingly. Assume (3.3.12) holds. Then from (3.3.11) it follows that

$$\mathfrak{J}(\tilde{h} + h_0) < \frac{B}{2} \iint_\Omega \tilde{h}^2 \, dx dy \quad \text{and} \quad \iint_\Omega \tilde{h}^2 \, dx dy < \frac{2}{A} \mathfrak{J}(\tilde{h} + h_0). \tag{3.3.15}$$

It then follows from the invariance of $\mathfrak{J}$ that

$$||\tilde{h}||^2 < \frac{2}{A} \mathfrak{J}(\tilde{h} + h_0) = \frac{2}{A} \left. \mathfrak{J}(\tilde{h} + h_0)\right|_{t=0} < \frac{2}{A} \frac{B}{2} \left. ||\tilde{h}||^2 \right|_{t=0}.$$

Therefore, if

$$||\tilde{h}||_{t=0} < \left(\frac{A}{B}\right)^{\frac{1}{2}} \epsilon.$$

it follows that

$$||\tilde{h}|| < \epsilon,$$

establishing stability in the sense of Liapunov. Stability follows from (3.3.13) similarly.

The above stability argument breaks down when an outcropping occurs because (3.3.7) is only meaningful in the domain of h_0. Therefore, we are unable to bound the finite variations of the outcropping via the above argument as inequality (3.3.10) holds only over the domain of h_0 and not over the domain of $\tilde{h} + h_0$ as

required. Again, it should be noted that we have only bounded the perturbations in h in this theorem and not considered whether ψ could become unbounded. However. since it is growth in h that we are most interested in as it represents changes in the frontal structure and since ψ is determined diagnostically by h. these results are useful.

Unfortunately, interpreting and applying the nonlinear stability results is not a straightforward task. Given a specific front $h_0(y)$, determining suitable functions Φ_1 and Φ_2 is not trivial. This is further complicated by the fact that the stability conditions must hold for all nonnegative values of ξ and not only $\xi = h_0$ as in linear theory. However, it is possible to establish the nonlinear stability of all linearly sloping fronts, $h_0(y) = \alpha y + C$, where α and C are chosen so that the front extends across the domain and does not outcrop. Choosing $\Phi_1'(*) = \mu(\mu\alpha + \beta)(* - C)$ and $\Phi_2'(*) = \alpha(C - *)$ satisfies (3.3.14) and gives

$$\Phi_1''(\xi) + \mu^2 \Phi_2''(\mu\xi + \beta y) = \mu\beta.$$

Hence, (3.3.12) is satisfied and all linearly sloping fronts are nonlinearly stable. Note that it is not surprising that the singular points. $\alpha = 0$ and $\mu\alpha + \beta = 0$. do not cause instability since these fronts are also linearly stable as the linear equations reduce to linear wave equations (see §3.2).

3.4   Weakly Nonlinear Analysis

In the following sections, the effects of nonlinear terms in the model are examined. We begin by deriving the envelope equation governing the finite time and space evolution of the amplitude of a given wavetrain. This analysis naturally leads to a discussion of resonances. We include a section examining the case of long-wave–short-wave resonance as well as a brief note on three-wave resonance, including the second harmonic resonance. As well, we examine the special limit where zonal scales become large.

The method to derive a finite-amplitude equation governing the evolution of a slowly-varying wave amplitude follows that of Newell (1974) and Grimshaw (1977), and is similar to the analysis of the RED model studied in Slomp (1995). As in any weakly nonlinear calculation the details of the calculation are quite lengthy. In this thesis, several weakly nonlinear calculations are presented, and as such, we will

3. ST model

keep our discussion of the calculations to a minimum. In the body of the thesis, we will present only those details that directly lead to and affect the characteristics of the amplitude equation. Enough of the remaining details will be presented in the Appendices so that the calculations can be repeated with reasonable effort.

A necessary result for the weakly nonlinear analysis is the Fredholm Alternative Theorem (Zwillinger, 1989). The Fredholm Alternative Theorem (hereafter F.A.T.) states that an inhomogeneous ordinary differential equation of the form $\widetilde{\mathfrak{L}}G = \Phi$ has a solution if and only if

$$\langle \Phi, \phi \rangle = 0. \tag{3.4.1}$$

where $\phi \in Ker(\widetilde{\mathfrak{L}}^A)$ with $\widetilde{\mathfrak{L}}^A$ being the adjoint operator of $\widetilde{\mathfrak{L}}$. In our analysis, the operators are self adjoint so that the theorem implies a solution exists iff (3.4.1) holds for ϕ a homogeneous solution to $\widetilde{\mathfrak{L}}$, that is, $\widetilde{\mathfrak{L}}\phi = 0$. As well, for our analysis the inner product is given by

$$\langle \Phi, \phi \rangle = \int_{\Omega_y} \Phi \cdot \phi \, dy,$$

where Ω_y is the appropriate meridional domain.

3.5   The Gently Sloping Front

We begin by examining the gently sloping front as given by (3.2.22). We introduce the appropriate scalings for α and β as given by (3.2.24) and (3.2.25) dropping the tildes. In order to facilitate a weakly nonlinear analysis, slow space and time variables are introduced. These allow the space and time scales associated with nonlinear interaction of the fundamental mode to be examined. This is done by letting

$$t = \Delta t, \quad T = \Delta^2 t, \quad \tau = \Delta^3 t, \quad X = \Delta x, \tag{3.5.1}$$

where we have used that the rescaling of ω in (3.2.25) necessary for the linear solution is equivalent to a rescaling of time by Δ. The perturbations are small compared to the basic-state solution, and are to leading order scaled by the parameter Δ^2.

3. ST model

The perturbation quantities, h, ψ, are expanded in a power series in Δ, that is,

$$(h, \psi) = \Delta^2 (h, \psi)^{(0)} + \Delta^3 (h, \psi)^{(1)} + \Delta^4 (h, \psi)^{(2)} + \dots \qquad (3.5.2)$$

As in the linear problem, the boundary conditions, reduce to requiring that h and ψ vanish at $y = 0, L$ at all orders of Δ.

Taking into consideration (3.2.22), (3.5.1), and (3.5.2) the model equations (3.2.5) and (3.2.6) become

$$\mathcal{L}(\partial_t + \Delta \partial_T + \Delta^2 \partial_\tau, \partial_x + \Delta \partial_X, \partial_y) \left[h^{(0)} + \Delta h^{(1)} + \Delta^2 h^{(2)} \right] = \\ \Delta M_1 + \Delta^2 M_2 + O(\Delta^3), \qquad (3.5.3)$$

$$\left[\psi^{(0)} + \Delta \psi^{(1)} + \Delta^2 \psi^{(2)} \right]_x = - \frac{\mu}{\beta + \alpha\mu} [\partial_t - \beta \aleph \partial_x] \left[h^{(0)} + \Delta h^{(1)} + \Delta^2 h^{(2)} \right] \\ + \Delta P_1 + \Delta^2 P_2 + O(\Delta^3), \qquad (3.5.4)$$

where the linear operator $\mathcal{L}$ is given by

$$\mathcal{L}(\partial_t, \partial_x, \partial_y) = \beta \partial_t + \aleph \alpha (\beta + \alpha\mu) \nabla_x^2 - \aleph \beta^2 \partial_x. \qquad (3.5.5)$$

and M_i and P_i represent the expansion of the remaining terms. We do not give their full expressions here but will list only the simplified terms that are important as the discussion of the problem continues. If the definition of the slow variables, (3.5.1), is substituted into the linear operator, it can be expanded in powers of Δ to give

$$\mathcal{L}(\partial_t + \Delta \partial_T + \Delta^2 \partial_\tau, \partial_x + \Delta \partial_X, \partial_y,) = \mathcal{L}(\partial_t, \partial_x, \partial_y) \\ + \Delta \left[\beta \partial_T + \mathcal{L}_2 (\partial_t, \partial_x, \partial_y) \partial_X \right] \\ + \Delta^2 \left[\frac{1}{2} \mathcal{L}_{22} (\partial_t, \partial_x, \partial_y) \partial_{XX} + \mathcal{L}_1 (\partial_t, \partial_x, \partial_y) \partial_\tau \right], \qquad (3.5.6)$$

where subscripts indicate differentiation with respect to the indicated argument and we have used that $\mathcal{L}_1 = \beta$ so that $\mathcal{L}_{11} = \mathcal{L}_{12} = 0$. Using this expansion in (3.5.3) and setting the coefficients of terms in similar orders of Δ to zero gives a series of problems that must be solved. The solvability conditions that arise at each order

3. ST model

according to the F.A.T. give rise to an evolution equation for the slowly varying amplitude of the linear solution.

The leading-order problem is given by

$$\mathcal{L}(\partial_t, \partial_x, \partial_y, y)h^{(0)} = 0, \tag{3.5.7}$$

$$\psi_x^{(0)} = -\frac{\mu}{\beta + \alpha\mu}\left[\partial_t - \beta\aleph\partial_x\right]h^{(0)}. \tag{3.5.8}$$

Assuming a plane wave solution of the form

$$h^{(0)} = A(X, T, \tau)\widetilde{h}(y)\exp[i(kx - \omega t)] + c.c.,$$
$$\psi^{(0)} = A(X, T, \tau)\widetilde{\psi}(y)\exp[i(kx - \omega t)] + c.c.. \tag{3.5.9}$$

where $A(X, T, \tau)$ is the slowly varying amplitude, gives the equations

$$\mathcal{L}(-i\omega, ik, \partial_y)\widetilde{h} = 0, \tag{3.5.10}$$

$$\widetilde{\psi} = -\frac{\aleph\mu\alpha(k^2 + \ell^2)}{\beta}\widetilde{h}, \tag{3.5.11}$$

where

$$\mathcal{L}(-i\omega, ik, \partial_y) = ik\aleph\alpha(\beta + \alpha\mu)\left\{\partial_{yy} - \left[k^2 + \frac{\beta(\aleph\beta + c)}{\aleph\alpha(\mu\alpha + \beta)}\right]\right\}.$$

As discussed in §3.2, (3.5.10) defines an eigenvalue problem for ω and $\widetilde{h}$. The eigenvalue, $\omega(k, \ell)$, is determined by (3.2.28) with the corresponding eigenfunction, $\widetilde{h}(y, \ell)$, given by (3.2.27) and the stream function by (3.5.11). That is,

$$\mathcal{L}(-i\omega(k, \ell), ik, \partial_y)\widetilde{h}(y, \ell) = 0. \tag{3.5.12}$$

The eigenfunctions, $\widetilde{h}(y, \ell) = \sin(\ell y)$, form an orthonormal basis for the solution set, that is, functions that can satisfy the boundary conditions.

The $O(\Delta)$ problem, after using the leading-order solution to simplify terms

62

3. ST model

reduces to

$$\mathcal{L}(\partial_t, \partial_x, \partial_y) h^{(1)}$$

$$= \Bigg\{ -[\beta A_T + A_X \mathcal{L}_2(-i\omega(k,\ell), ik, \partial_y)] \widetilde{h}(y,\ell)$$

$$+ ik\alpha^2 \left[(\beta + \alpha\mu)(k^2 + \ell^2) + \beta^2\right] A\left(y - \frac{L}{2}\right) \sin(\ell y) \tag{3.5.13}$$

$$- ik\ell\alpha^2(\beta + \alpha\mu) A \cos(\ell y) \Bigg\} \exp[i(kx - \omega t)] + c.c.,$$

$$\psi_x^{(1)} = -\frac{\mu}{\beta + \alpha\mu} \Bigg\{ [\partial_t - \beta\aleph\partial_x] h^{(1)}$$

$$- \left[\left(A_T - \frac{\aleph[\alpha(\beta + \alpha\mu)(k^2 + \ell^2) + \beta^2]}{\beta} A_X\right) \widetilde{h}(y,\ell)\right. \tag{3.5.14}$$

$$\left. - ik\beta\alpha A\left(y - \frac{L}{2}\right) \sin(\ell y)\right] \exp[i(kx - \omega t)] + c.c. \Bigg\}.$$

We assume

$$h^{(1)} = B(X, T, \tau) G(y) \exp[i(kx - \omega t)] + c.c. + \Phi(y, X, T, \tau). \tag{3.5.15}$$

where the function Φ is a homogeneous solution to the left-hand side of (3.5.13) since it is independent of x and t. Its inclusion is necessary in the next order problem where its form will be derived. Substituting (3.5.15) into (3.5.13) gives

$$B(X, T, \tau)\mathcal{L}(-i\omega(k,\ell), -ik, \partial_y) G(y)$$

$$= -[A_T\beta + A_X \mathcal{L}_2(-i\omega(k,\ell), ik, \partial_y)] \widetilde{h}(y,\ell)$$

$$+ ik\alpha^2 \left[(\beta + \alpha\mu)(k^2 + \ell^2) + \beta^2\right] A\left(y - \frac{L}{2}\right) \sin(\ell y) \tag{3.5.16}$$

$$- ik\ell\alpha^2(\beta + \alpha\mu) A \cos(\ell y).$$

Equation (3.5.16) obviously has the homogeneous solution $G(y) = \widetilde{h}(y, \ell)$. It follows

3. ST model

from the F.A.T. that for a solution to exist it must hold that

$$\int_0^L \Bigg\{ - [\beta A_T + A_X \mathfrak{L}_2(-i\omega(k,\ell), ik, \partial_y)] \, \tilde{h}(y,\ell)$$

$$+ ik\alpha \left[\alpha(\beta + \alpha\mu)(k^2 + \ell^2) + \beta^2 \right] A \left(y - \frac{L}{2} \right) \sin(\ell y) \qquad (3.5.17)$$

$$- ik\ell\alpha^2(\beta + \alpha\mu) A \cos(\ell y) \Bigg\} \tilde{h}(y,\ell) \, dy = 0.$$

It follows from differentiating (3.5.12) with respect to k that

$$\mathfrak{L}_2(-i\omega(k,\ell), ik, \partial_y)\tilde{h}(y,\ell) = \frac{\partial\omega}{\partial k}(k,\ell)\mathfrak{L}_1(-i\omega(k,\ell), ik, \partial_y)\tilde{h}(y,\ell)$$

$$= \beta\frac{\partial\omega}{\partial k}(k,\ell)\tilde{h}(y,\ell). \qquad (3.5.18)$$

Using (3.5.18) and that

$$\int_0^L \tilde{h}^2(y,\ell) \, dy = \frac{L}{2},$$

$$\int_0^L \cos(\ell y)\tilde{h}(y,\ell) \, dy = \int_0^L \left(y - \frac{L}{2} \right) \sin(\ell y)\tilde{h}(y,\ell) \, dy = 0, \qquad (3.5.19)$$

reduces (3.5.17) to

$$A_T + \frac{\partial\omega}{\partial k}(k,\ell)A_X = 0. \qquad (3.5.20)$$

This is the simple statement that to this order the wave amplitude travels at the group speed, $c_G(k,\ell) = \frac{\partial\omega}{\partial k}$, given by (3.2.29). Introducing

$$\xi = X - c_G(k,\ell)T, \qquad (3.5.21)$$

with $A(X,T,\tau) = A(\xi,\tau)$ satisfies this equation. Similarly, all variables that are functions of X, T will now depend solely on ξ.

3. ST model

Now the solutions to (3.5.16) can be found as $B(X,T,\tau) = A(\xi,\tau)$ and

$$G = -\frac{\alpha(\beta + \alpha\mu)(k^2 + \ell^2) + \beta^2}{4\aleph\ell(\beta + \alpha\mu)}y(y - L)\cos(\ell y)$$
$$+ \frac{\alpha(\beta + \alpha\mu)(k^2 - \ell^2) + \beta^2}{4\aleph\ell^2(\beta + \alpha\mu)}\left(y - \frac{L}{2}\right)\sin(\ell y). \qquad (3.5.22)$$

Given (3.5.22), the solution to (3.5.14) is given by

$$\psi^{(1)} = A(\xi,\tau)F(y)\exp[i(kx - \omega t)] + c.c. + \Psi(y,X,T,\tau), \qquad (3.5.23)$$

where

$$F = i\frac{2\aleph\alpha\mu k}{\beta}A_\xi \sin(\ell y)$$
$$+ \frac{\alpha\mu(k^2 + \ell^2)[\alpha(\beta + \alpha\mu)(k^2 + \ell^2) + \beta^2]}{4\beta\ell(\beta + \alpha\mu)}y(y - L)\cos(\ell y) \qquad (3.5.24)$$
$$- \frac{\alpha[(\beta + \alpha\mu)(k^4 - \ell^4) + \beta^2(k^2 - 3\ell^2)]}{4\beta\ell^2(\beta + \alpha\mu)}\left(y - \frac{L}{2}\right)\sin(\ell y),$$

and Ψ is analogous to Φ and will be determined in the next order problem.

The $O(\Delta^2)$ problem, after using the leading-order solution, (3.5.9, 3.2.27,

65

3. ST model

3.2.30) and the $O(\Delta)$ solution, (3.5.15. 3.5.22, 3.5.24) reduces to

$$\mathcal{L}(\partial_t, \partial_x, \partial_y)h^{(2)} = -\left[-c_G(k,n)\mathcal{L}_1(0,0,\partial_y) + \mathcal{L}_2(0,0,\partial_y)\right]\Phi_\xi$$
$$+ 2k^2\ell(\beta + 2\alpha\mu)\left(|A|^2\right)_\xi \sin(2\ell y)$$
$$+ \left\{ -\left[\beta A_\tau + \frac{1}{2}A_{\xi\xi}\mathcal{L}_{22}(-i\omega(k,\ell), ik, \partial_y)\right]\widetilde{h}(y,\ell)\right.$$
$$- iAk\left[\beta\Psi_y + (\beta + 2\alpha\mu)(k^2 + \ell^2)\Phi_y\right. \tag{3.5.25}$$
$$\left. + (\beta + \alpha\mu)\Phi_{yyy}\right]\sin(\ell y)$$
$$\left. - iA\gamma(y) + A_\xi M_{A_\xi}(y)\right\}\exp[i(kx - \omega t)]$$
$$+ M_{e^2}\exp[2i(kx - \omega t)] + c.c.,$$

$$\psi_x^{(2)} = -\frac{\mu}{\beta + \alpha\mu}\left\{[\partial_t - \beta\aleph\partial_x]h^{(2)} - \Psi_\xi - \frac{\aleph\alpha^2(3k^2 + \ell^2)}{\beta}\Phi_\xi\right.$$
$$\left. - \frac{2\alpha\mu k^2\ell}{\beta}\left(|A|^2\right)_\xi \sin(2\ell y)\right\} \tag{3.5.26}$$
$$+ P_e\exp[i(kx - \omega t)] + P_{e^2}\exp[2i(kx - \omega t)] + c.c.,$$

where

$$\gamma(y) = k\alpha^2(\beta + \alpha\mu)\left[\left(y - \frac{L}{2}\right)\left(G'' - (k^2 + \frac{\beta^2}{\alpha(\beta + \alpha\mu)})G\right) + G'\right], \tag{3.5.27}$$

and where the terms $M_{A_\xi}, M_{e^2}, P_e, P_{e^2}$ are not needed in the following analysis and so are not expanded here.

The terms independent of x, t are secular; if a particular solution is found corresponding to these terms, it will grow unbounded in either x or t. This is just a special case of the F.A.T. where any function of y is a homogeneous solution and therefore the inhomogeneity must vanish. Therefore, we must choose Φ and Ψ such that these terms vanish in both (3.5.25) and (3.5.26), that is,

$$\left[-c_G\mathcal{L}_1(0,0,\partial_y) + \mathcal{L}_2(0,0,\partial_y)\right]\Phi_\xi = 2k^2\ell(\beta + 2\alpha\mu)\left(|A|^2\right)_\xi \sin(2\ell y), \tag{3.5.28}$$

$$\Psi_\xi = -\frac{\aleph\alpha^2(3k^2 + \ell^2)}{\beta}\Phi_\xi - \frac{2\alpha\mu k^2\ell}{\beta}\left(|A|^2\right)_\xi \sin(2\ell y). \tag{3.5.29}$$

3. ST model

The system (3.5.28) and (3.5.29) can in general be solved. but we must consider whether the operator in (3.5.28) has a homogeneous solution and hence requires an application of the F.A.T. First, we assume that

$$\Phi(y,\xi,\tau) = |A(\xi,\tau)|^2 \Phi(y),$$

where $\Phi(y)$ satisfies

$$[-c_G(k,\ell)\mathcal{L}_1(0,0,\partial_y) + \mathcal{L}_2(0,0,\partial_y)]\,\Phi = 2k^2\ell(\beta + 2\alpha\mu)\sin(2\ell y). \qquad (3.5.30)$$

The operator in (3.5.30) is similar to the small-wavenumber (long-wave) limit of the original linear operator. That is, if we expand (3.5.12) about $k = 0$ we get that a solution must satisfy

$$[-c_G(0,m)\mathcal{L}_1(0,0,\partial_y) + \mathcal{L}_2(0,0,\partial_y)]\,\widetilde{h}(y,m) = 0 \qquad (3.5.31)$$

as $k \to 0$, where we have chosen the mth meridional mode for the long wave to differentiate from the ℓth meridional mode used for the fundamental wave. It follows that the operator in (3.5.30) has a homogeneous solution given by

$$\Phi = \widetilde{h}(y,m)$$

iff

$$c_G(k,\ell) = c_G(0,m). \qquad (3.5.32)$$

It then follows by the F.A.T. that (3.5.30) will have a solution in this case iff

$$\int_0^L \sin(2\ell y)\widetilde{h}(y,m)\,\mathrm{d}y = 0. \qquad (3.5.33)$$

Only in the case where $m = 2\ell$ is (3.5.33) not satisfied. It follows that if

$$c_G(k,\ell) = c_G(0,2\ell), \qquad (3.5.34)$$

there is no solution to (3.5.30). Using the form of c_G, (3.5.34) occurs only when $k = \ell$. When $k = \ell$, we have what is known as mean flow or long-wave–short-wave

67

3. ST model

(LWSW) resonance where the group speed of the fundamental wave is equal to the group speed/phase speed of a long wave mode where $k = 0$. (At $k = 0$ the group speed and phase speed of a mode are equivalent.) For now, we will assume that $k \neq \ell$ and resonance does not occur and we leave the discussion of the LWSW resonance to §3.8.

The system (3.5.28) and (3.5.29) then has the solution

$$\Phi = \frac{2k^2\ell(\beta + 2\alpha\mu)}{3\alpha(\beta + \alpha\mu)(k^2 - \ell^2)}|A|^2 \sin(2\ell y), \tag{3.5.35}$$

$$\Psi = -\frac{2\aleph\mu k^2\ell\left[3k^2(\beta + \alpha\mu) + \ell^2(\beta + 5\alpha\mu)\right]}{3\beta(\beta + \alpha\mu)(k^2 - \ell^2)}|A|^2 \sin(2\ell y). \tag{3.5.36}$$

where it is clear that this solution is not valid when $k = \ell$.

We now return to equation (3.5.25). Assuming

$$h^{(2)} = B_1(X, T, \tau)N_1(y)\exp[i(kx - \omega t)]$$
$$+ B_2(X, T, \tau)N_2(y)\exp[2i(kx - \omega t)] + c.c..$$

and considering the $\exp[i(kx - \omega t)]$ problem for equation (3.5.25) with the solutions (3.5.35) and (3.5.36) and using (3.5.39), gives

$$B_1(X, T, \tau)\mathfrak{L}(-i\omega(k, \ell), ik, \partial_y)N_1(y)$$
$$= -\left[\beta A_\tau - \frac{i\beta}{2}\frac{\partial^2\omega(k, \ell)}{\partial k^2}A_{\xi\xi}\right]\tilde{h}(y, \ell)$$
$$- i2\beta\Sigma A|A|^2 \cos(2\ell y)\sin(\ell y)$$
$$- iA\gamma(y) + A_\xi M_{A_\xi}(y). \tag{3.5.37}$$

where

$$\Sigma = \frac{\mu}{\beta}\frac{\aleph k^3\ell^2[k^2(\beta^2 + \beta\mu\alpha + \alpha^2\mu^2) - 3\ell^2(\beta^2 + 3\beta\mu\alpha + 3\alpha^2\mu^2)]}{3\beta\alpha(k^2 - \ell^2)(\beta + \alpha\mu)}$$
$$= \frac{\mu}{\beta}\frac{\aleph k^3\ell^2[k^2(1 + \mu\rho + \mu^2\rho^2) - 3\ell^2(1 + 3\mu\rho + 3\mu^2\rho^2)]}{3\mu\rho(k^2 - \ell^2)(1 + \mu\rho)}, \tag{3.5.38}$$

where $\rho = \alpha/\beta$. In deriving (3.6.37) we used that if we differentiate (3.5.18) with

68

3. ST model

respect to k we get that

$$\mathfrak{L}_{22}(-i\omega(k,\ell), ik, \partial_y)\widetilde{h}(y,\ell) = -i\beta\frac{\partial^2\omega(k,\ell)}{\partial k^2}\widetilde{h}(y,\ell). \qquad (3.5.39)$$

where we've used that $\mathfrak{L}_{21} = 0$.

Once again, equation (3.6.37) has the homogeneous solution $N_1(y) = \widetilde{h}(y,\ell)$. It then follows from the F.A.T. that a solution exists iff

$$\int_0^L \left\{ -\left[\beta A_\tau - \frac{i\beta}{2}\frac{\partial^2\omega(k,\ell)}{\partial k^2}A_{\xi\xi}\right]\widetilde{h}(y,\ell) \right.$$
$$- i2\beta\Sigma A|A|^2\cos(2\ell y)\sin(\ell y) - iA\gamma(y) \qquad (3.5.40)$$
$$\left. + A_\xi M_{A_\xi}(y)\right\}\widetilde{h}(y,\ell)\,dy = 0.$$

Using (3.5.19) and that

$$\int_0^L \cos(2\ell y)\sin(\ell y)\widetilde{h}(y,\ell)\,dy = -\frac{L}{4},$$
$$\int_0^L M_{A_\xi}(y)\widetilde{h}(y,\ell)\,dy = 0$$

reduces (3.5.40) to

$$iA_\tau + \lambda A_{\xi\xi} + \Gamma A = \Sigma A|A|^2, \qquad (3.5.41)$$

where we have multiplied the equation by i, and let

$$\lambda = \frac{1}{2}\frac{\partial^2\omega(k,\ell)}{\partial k^2}$$
$$= -\frac{3\aleph\alpha(\beta + \alpha\mu)k}{\beta} \qquad (3.5.42)$$
$$= -\frac{\beta}{\mu}3\aleph\rho(1 + \mu\rho)k,$$

$$\Gamma = -\frac{2}{L\beta}\int_0^L \gamma(y)\widetilde{h}(y,\ell)\,dy. \qquad (3.5.43)$$

3. ST model

We can recast (3.5.41) into the standard form of the nonlinear Schrödinger equation (NLS) by letting

$$A = \exp(i\Gamma\tau)\widetilde{A}, \qquad (3.5.44)$$

so that from (3.5.41) $\widetilde{A}$ satisfies

$$i\widetilde{A}_\tau + \lambda\widetilde{A}_{\xi\xi} = \Sigma\widetilde{A}|\widetilde{A}|^2. \qquad (3.5.45)$$

The transformation (3.5.44) simply represents a shift in phase speed of the linear solution to account for the correction resulting from the higher order linear terms. That is, the phase speed of the linear solution to $O(\Delta^2)$ is given by

$$c - \frac{\Delta^2\Gamma}{k}. \qquad (3.5.46)$$

Note that the phase speed of the wave plays no role in the analysis that follows so the form of Γ is not required.

3.6 The Wedge Front

We now examine the weakly nonlinear behaviour with respect to the wedge front basic state as given by (3.2.32, 3.2.33). The steps in the analysis are very similar to that for the gently sloping front and therefore we will be brief. However differences do arise as a result of the differences in the structure of the linear solution. The analysis is important in illustrating the changes in the nonlinear effects as we move from a weak flow similar to QG formulations to a strong flow with an outcropping requiring the FG formulation. Again, though, the difficulties with modelling the outcropping, and the continuity of variables across the outcropping do limit the viability of this solution. We do believe that it is still a very worthwhile endeavor as it is valid in the RED model limit.

Since the derivation of the linear solution for the wedge model does not require parameters and time scales to be small, all parameters are $O(1)$ and the slow variable scaling is

$$t = t, \quad T = \Delta t, \quad \tau = \Delta^2 t, \quad X = \Delta x, \qquad (3.6.1)$$

70

3. ST model

as opposed to that in (3.5.1). As well. the perturbations are to leading order $O(\Delta)$. that is,

$$(h, \psi) = \Delta(h, \psi)^{(0)} + \Delta^2(h, \psi)^{(1)} + \Delta^3(h. \psi)^{(2)} + \dots, \qquad (3.6.2)$$

as opposed to (3.5.2). As well, the boundary conditions are those corresponding to the wedge front; all variables are bounded at $y = 0$ and as $y \to \infty$. Given a solution h, condition (2.6.11) can then be used to determine the variation of the outcropping ϕ at all orders.

Taking into consideration (3.2.32), (3.6.1). and (3.6.2) the model equations (3.2.5) and (3.2.6) become

$$\mathcal{L}(\partial_t + \Delta\partial_T + \Delta^2\partial_\tau, \partial_x + \Delta\partial_X, \partial_y, y)\left[h^{(0)} + \Delta h^{(1)} + \Delta^2 h^{(2)}\right]$$
$$= \Delta M_1 + \Delta^2 M_2 + O(\Delta^3). \qquad (3.6.3)$$

$$\left[\psi^{(0)} + \Delta\psi^{(1)} + \Delta^2\psi^{(2)}\right]_x = -\frac{\mu}{3 + \alpha\mu}[\partial_t - \beta\alpha y\partial_x]\left[h^{(0)} + \Delta h^{(1)} + \Delta^2 h^{(2)}\right]$$
$$+ \Delta P_1 + \Delta^2 P_2 + O(\Delta^3). \qquad (3.6.4)$$

where the linear operator $\mathcal{L}$ is given by

$$\mathcal{L}(\partial_t, \partial_x, \partial_y, y) = \beta\partial_t + \alpha^2(\beta + \alpha\mu)\left[y\nabla_x^2 + \partial_{yx}\right] - \beta^2\alpha y\partial_x, \qquad (3.6.5)$$

and M_i and P_i represent the expansion of the remaining terms (see Appendix 3 for more details). The linear operator can be expanded in powers of Δ, as before, to give (3.5.6).

The leading-order problem is given by

$$\mathcal{L}(\partial_t, \partial_x, \partial_y, y)h^{(0)} = 0, \qquad (3.6.6)$$

$$\psi_x^{(0)} = -\frac{\mu}{\beta + \mu\alpha}\left[h_t^{(0)} - \beta\alpha y h_x^{(0)}\right]. \qquad (3.6.7)$$

71

3. ST model

Again, we assume a plane wave solution of the form (3.5.9) giving the equations

$$\mathfrak{L}(-i\omega, ik, \partial_y, y)\widetilde{h}(y, k, n)$$

$$= i\alpha^2(\beta + \alpha\mu)k\left[y\frac{\partial^2\widetilde{h}}{\partial y^2} + \frac{\partial\widetilde{h}}{\partial y} - \left(\alpha^2\kappa^2(k)y + \frac{\widehat{\beta}\omega}{k\alpha^2}\right)\widetilde{h}\right] = 0, \qquad (3.6.8)$$

$$\widetilde{\psi} = \frac{\mu}{\beta + \alpha\mu}[c + \beta\alpha y]\widetilde{h}. \qquad (3.6.9)$$

where A is the slowly varying amplitude, with the notation (3.2.35–3.2.37). As discussed in §3.2, (3.6.8) defines an eigenvalue problem for ω and $\widetilde{h}$ that has the solution (3.2.40) with the frequency determined by (3.2.41) provided k satisfies (3.2.39). That is,

$$\mathfrak{L}(-i\omega(k, n), ik, \partial_y, y)\widetilde{h}(y, k, n) = 0. \qquad (3.6.10)$$

Note that the form of the eigenfunctions differs significantly for this model as compared to the GSF model (compare (3.2.40) to (3.2.27)). The eigenfunctions still form an orthonormal set, that is,

$$\int_0^\infty 2\alpha\kappa(k)\widetilde{h}(y, k, n)\widetilde{h}(y, k, m)\,dy = \delta_{mn}. \qquad (3.6.11)$$

where the $2\alpha\kappa(k)$ is simply a weighting factor.

We will use the following properties for the eigenfunctions. First, it follows from (3.6.8) that

$$\mathfrak{L}(-i\omega, ik, \partial_y, y)\widetilde{h}(y, k, n) = i\beta(\omega(k, n) - \omega)\widetilde{h}(y, k, n), \qquad (3.6.12)$$

and subsequently that

$$\int_0^\infty 2\kappa(k)\widetilde{h}(y, k, n)\mathfrak{L}(-i\omega(k, n), ik, \partial_y, y))F(y, k)\,dy = 0, \qquad (3.6.13)$$

for any function F in the space spanned by the eigenfunctions, that is,

$$F = \sum_{r=0}^\infty f_r\widetilde{h}(y, k, r), \qquad (3.6.14)$$

3. ST model

for some constants f_r. One important difference between this analysis and the previous one is that now the eigenfunctions, $\widetilde{h}(y, k, n)$, are dependent on the zonal wavenumber k. As such, the derivatives of $\widetilde{h}$ with respect to k arise in the following analysis. Since the Laguerre Polynomials span the space of polynomials, it follows that any derivative of $\widetilde{h}(y, k, n)$ with respect to k can be written as a sum of the eigenfunctions in the form of (3.6.14). It therefore follows that (3.6.13) holds for

$$F = \frac{\partial^r}{\partial k^r}\left(\widetilde{h}(y, k, n)\right),$$

for arbitrary r.

The $O(\Delta)$ problem is given by

$$\mathcal{L}(\partial_t, \partial_x, \partial_y, y)h^{(1)}$$
$$= -\left[\beta A_T + A_X \mathcal{L}_2(\partial_t, \partial_x, \partial_y, y)\right]\widetilde{h}(y, k, n)\exp(i\theta) \qquad (3.6.15)$$
$$+ iA^2 M_{e^2}\exp(2i\theta) + c.c.,$$

$$\psi_x^{(1)} = -\frac{\mu}{\beta + \mu\alpha}\left[h_t^{(1)} - \beta\alpha y h_x^{(1)}\right.$$
$$\left. + h_{T_1}^{(0)} - \beta\alpha y h_X^{(0)} + J(\psi^{(0)}, h^{(0)}) - \beta h^{(0)}h_x^{(0)}\right] - \psi_X^{(0)}. \qquad (3.6.16)$$

where M_{e^2} represents the quadratic interaction terms (see A.3.11). Note that there are no additional linear terms in (3.6.15) as there were in (3.5.13) since the $O(1)$ linear problem now contains all the linear terms except those associated with slow space/time derivatives. The solution to (3.6.15) will have the form

$$h^{(1)} = B(X, T, \tau)G(y)\exp[i(kx - \omega t)]$$
$$+ A^2\mathfrak{Z}(y)\exp(2i(kx - \omega t)) + c.c. + \Phi(y, X, T, \tau), \qquad (3.6.17)$$

where G and $\mathfrak{Z}$ satisfy

$$B(X, T, \tau)\mathcal{L}(-i\omega(k, n), ik, \partial_y, y)G$$
$$= -\left[\beta A_T + A_X \mathcal{L}_2(-i\omega(k, n), ik, \partial_y, y)\right]\widetilde{h}(y, k, n), \qquad (3.6.18)$$
$$\mathcal{L}(-2i\omega(k, n), 2ik, \partial_y, y)\mathfrak{Z}(y) = iM_{e^2}, \qquad (3.6.19)$$

3. ST model

and we have included the homogeneous solution Φ once again.

As before, it follows that (3.6.18) has the homogeneous solution $G(y) = \widetilde{h}(y, k, n)$ with the F.A.T. implying that (3.6.18) has a solution iff

$$\int_0^\infty \widetilde{h}(y, k, n)\Big[\beta A_T + A_X \mathfrak{L}_2(-i\omega(k, n), ik, \partial_y, y)\Big]\widetilde{h}(y, k, n)\, dy = 0. \tag{3.6.20}$$

Again this can be simplified by differentiating (3.6.10) with respect to k to give

$$\mathfrak{L}_2(-i\omega(k, n), ik, \partial_y, y)\widetilde{h}(y, k, n) = \beta\frac{\partial\omega}{\partial k}(k, n)\widetilde{h}(y, k, n) \\ - \mathfrak{L}(-i\omega(k, n), ik, \partial_y, y)\frac{\partial\widetilde{h}(y, k, n)}{\partial k}. \tag{3.6.21}$$

Multiplying (3.6.21) by $2\alpha\kappa(k)\widetilde{h}$ and integrating gives

$$\int_0^\infty 2\alpha\kappa(k)\widetilde{h}(y, k, n)\mathfrak{L}_2(-i\omega(k, n), ik, \partial_y, y)\widetilde{h}(y, k, n)\, dy = \beta\frac{\partial\omega}{\partial k}(k, n). \tag{3.6.22}$$

Using (3.6.22), (3.6.20) reduces to

$$A_T + \frac{\partial\omega}{\partial k}(k, n)A_X = 0. \tag{3.6.23}$$

Once again, the wave amplitude travels at the group speed given by (3.2.42) and we introduce $\xi = X - c_G(k, n)T$. Setting $B(X, T, \tau) = A_\xi(\xi, \tau)$ gives from (3.6.18) that

$$\mathfrak{L}(-i\omega(k, n), ik, \partial_y, y)G = \left[\beta\frac{\partial\omega}{\partial k}(k, n) - \mathfrak{L}_2(-i\omega(k, n), ik, \partial_y, y)\right]\widetilde{h}(y, k, n).$$

From (3.6.21) it follows that

$$G = -i\frac{\partial\widetilde{h}(y, k, n)}{\partial k}. \tag{3.6.24}$$

We now examine (3.6.19). It follows that (3.6.19) has the homogeneous solution $3 = \widetilde{h}(y, 2k, m)$ iff

$$2\omega(k, n) = \omega(2k, m), \tag{3.6.25}$$

74

3. ST model

for some integer m. When this occurs, we have the case of second harmonic resonance where the mth mode of wavenumber $2k$ wave has twice the frequency of the fundamental wave and is therefore resonant with quadratic interactions of the fundamental wave. The F.A.T. would apply and would indicate that no solution exists unless $A \equiv 0$. Thus, when resonance occurs the problem must be examined differently (see §3.9). For now, we assume this is not the case. A solution for $3(y)$ can be calculated by expressing it as a summation of the eigenfunctions $\tilde{h}(y, 2k, m)$ in the form

$$3(y) = \sum_{r=0}^{\infty} \zeta_r(k)\tilde{h}(y, 2k, r),$$ (3.6.26)

where

$$\zeta_r(k) = \frac{\int_0^{\infty} 2\alpha\kappa(2k)\tilde{h}(y, 2k, r)M_{e^2}\,dy}{\beta(\omega(2k, r) - 2\omega(k, n))},$$ (3.6.27)

with M_{e^2} given in Appendix 3. The coefficients ζ_r can be calculated numerically.

Given the solutions (3.6.24) and (3.6.26), (3.6.16) implies that

$$\psi^{(1)} = iA_\xi \tilde{\psi}_2(y)\exp(i\theta) + A^2\tilde{\psi}_3(y)\exp(2i\theta) + c.c. + \Psi(y, \xi, \tau),$$ (3.6.28)

where

$$\tilde{\psi}_2 = -\left[\frac{\mu(\hat{c} + \hat{\beta}\beta\alpha y)}{\beta}\right]\frac{\partial \tilde{h}(y, k, n)}{\partial k}$$

$$- \frac{\mu\hat{\beta}(c_G(k, n) + \beta\alpha y)}{k\beta}\tilde{h}(y, k, n) + \frac{\tilde{\psi}(y, k, n)}{k},$$ (3.6.29)

$$\tilde{\psi}_3 = \left[\frac{\mu(\hat{c} + \hat{\beta}\beta\alpha y)}{\beta}\right]3(y) + \frac{\mu\hat{\beta}}{2\beta}\left(\frac{\alpha\mu}{\beta + \mu\alpha} + 1\right)\left(\tilde{h}(y, k, n)\right)^2.$$ (3.6.30)

75

3. ST model

The $O(\Delta^2)$ problem is given by

$$\mathfrak{L}(\partial_t, \partial_x, \partial_y, y)h^{(2)} =$$
$$= -\left[-c_G(k,n)\mathfrak{L}_1(0,0,\partial_y,y) - \mathfrak{L}_2(0,0,\partial_y,y)\right]\Phi_\xi + M_0(|A|^2)_\xi$$
$$+ \Bigg\{ -\beta A_\tau + M_e$$
$$+ A_{\xi\xi}\Bigg\{ i\left[-\beta\frac{\partial\omega}{\partial k}(k,n) + \mathfrak{L}_2(-i\omega(k,n),ik,\partial_y,y)\right]\frac{\partial\widetilde{h}(y,k,n)}{\partial k}$$
$$\quad\quad - \frac{1}{2}\mathfrak{L}_{22}(\partial_t,\partial_x,\partial_y,y)\widetilde{h}(y,k,n)\Bigg\}\Bigg\}\exp(i\theta)$$
$$+ M_{e^2}\exp(2i\theta) + M_{e^3}\exp(3i\theta) + c.c.. \tag{3.6.31}$$

$$\psi_x^{(2)} = -\frac{\mu}{\beta+\mu\alpha}\Bigg\{ h_t^{(2)} + \beta\alpha y h_x^{(2)} - [c_G(k,n) + \beta\alpha y]h_\xi^{(1)}$$
$$+ J(\psi^{(1)},h^{(0)}) + J(\psi^{(0)},h^{(1)}) + J_1(\psi^{(0)},h^{(0)})$$
$$- \beta\left[h^{(0)}h_x^{(1)} + h^{(1)}h_x^{(0)} + h^{(0)}h_\xi^{(0)}\right]\Bigg\} - \psi_X^{(1)}. \tag{3.6.32}$$

where M_0 and M_e are given by (A.3.12) and (A.3.13), respectively, while M_{e^2} and M_{e^3} will not be required in the following analysis.

As before, we eliminate the constant terms from (3.6.31) by setting

$$\Phi(y,\xi,\tau) = |A(\xi,\tau)|^2\Phi(y),$$

where $\Phi(y)$ satisfies

$$\left[-c_G(k,n)\mathfrak{L}_1(0,0,\partial_y,y) + \mathfrak{L}_2(0,0,\partial_y,y)\right]\Phi = M_0,$$

or equivalently

$$i\alpha^2(\beta+\alpha\mu)k\left[y\partial_{yy} + \partial_y - \left(\alpha^2\kappa^2(0)y + \frac{\widehat{\beta}c_G(k,n)}{\alpha^2}\right)\right]\Phi = M_0. \tag{3.6.33}$$

3. ST model

The operator in (3.6.33) has a homogeneous solution given by

$$\Phi = \widetilde{h}(y, 0, m),$$

iff

$$c_G(k, n) = c_G(0, m). \tag{3.6.34}$$

where m is an integer representing the mth meridional mode. If (3.6.34) holds, it follows by the F.A.T. that (3.5.30) will not have a solution and we have long-wave-short-wave resonance as discussed in §3.8. For the wedge front, the values of k, n, and m that allow (3.6.34) to hold are not trivial and will be discussed in §3.8. Note that if $-1/\mu < \alpha/\beta < 0$ then $\kappa^2(0)$ is negative, κ is imaginary, and the operator in (3.6.33) has a continuous spectrum of solutions. Thus, resonance will always occur in this region and the remaining analysis pertains only to values of α/β outside this region. Also note that all solutions to (3.6.34) give a LWSW resonance as opposed to only the single solution for the gently sloping front analysis.

For now, we will assume that resonance does not occur and that (3.6.33) has the solution

$$\Phi(y) = \sum_{r=0}^{\infty} \phi_r \widetilde{h}(y, 0, r). \tag{3.6.35}$$

where

$$\phi_r = \frac{\int_0^{\infty} 2\alpha\kappa(0)\widetilde{h}(y, 0, r)M_0 \, dy}{\beta(c_G(0, r) - c_G(k, n))} \tag{3.6.36}$$

can be calculated numerically. Again, it is clear that a solution can only be found provided LWSW resonance does not occur. Given a solution for Φ, a solution for Ψ can be found from (3.6.32).

We now return to equation (3.6.31). Assuming

$$
\begin{aligned}
h^{(2)} =& B_1(X, T, \tau)N_1(y)\exp[i(kx - \omega t)] \\
&+ B_2(X, T, \tau)N_2(y)\exp[2i(kx - \omega t)] \\
&+ B_3(X, T, \tau)N_3(y)\exp[3i(kx - \omega t)] + c.c.,
\end{aligned}
$$

3. ST model

and considering the $\exp[i(kx - \omega t)]$ problem for the equation (3.6.31) with the solutions (3.6.35), gives

$$
\begin{aligned}
B_1(X,T,\tau)&\mathfrak{L}(-i\omega(k,\ell),ik,\partial_y,y)N_1(y) \\
&= -\beta\left[A_\tau - \frac{i}{2}\frac{\partial^2\omega(k,\ell)}{\partial k^2}A_{\xi\xi}\right]\widetilde{h}(y,k,n) \\
&\quad - \frac{A_{\xi\xi}}{2}\mathfrak{L}(-i\omega(k,n),ik,\partial_y,y)\frac{\partial^2\widetilde{h}(y,k,n)}{\partial k^2} - i2\beta A|A|^2\mathfrak{M}(y),
\end{aligned}
\tag{3.6.37}
$$

where $2\beta A|A|^2\mathfrak{M}(y)$ is the simplification of M_e with $\mathfrak{M}$ a function depending on the previous solutions (see (A.3.13)). In deriving (3.6.37) we have used that if we differentiate (3.6.21) with respect to k we find that

$$
\begin{aligned}
\mathfrak{L}_{22}&(-i\omega(k,n),ik,\partial_y,y)\widetilde{h}(y,k,n) \\
&- 2i\left[\beta\frac{\partial\omega}{\partial k}(k,n) + \mathfrak{L}_2(-i\omega(k,n),ik,\partial_y,y)\right]\frac{\partial\widetilde{h}(y,k)}{\partial k} \\
&= i\beta\frac{\partial^2\omega}{\partial k^2}(k,n)\widetilde{h}(y,k,n) - \mathfrak{L}(-i\omega(k,n),ik,\partial_y,y)\frac{\partial^2\widetilde{h}(y,k,n)}{\partial k^2}.
\end{aligned}
\tag{3.6.38}
$$

Once again, (3.6.37) has the homogeneous solution $N_1(y) = \widetilde{h}(y,k,n)$. It then follows from the F.A.T. that a solution exists iff it holds that

$$
iA_\tau + \lambda A_{\xi\xi} = \Sigma A|A|^2,
\tag{3.6.39}
$$

where

$$
\Sigma = \int_0^\infty \frac{2\alpha\kappa(k)}{\beta}\mathfrak{M}(y)\widetilde{h}(y,k,n)\,\mathrm{d}y
\tag{3.6.40}
$$

and

$$
\begin{aligned}
\lambda &= \frac{1}{2}\frac{\partial^2\omega(k,n)}{\partial k^2} \\
&= -\frac{(2n+1)}{\widehat{\beta}}\left(\frac{k(3\alpha^2\kappa^2(k)-k^2)}{\alpha\kappa^3(k)}\right).
\end{aligned}
\tag{3.6.41}
$$

3. ST model

3.7 Solutions to the Amplitude Equation

The NLS equation governing the evolution of the envelope of the linear solutions $A(\xi, \tau)$ given by (3.5.45) and (3.6.39) can be examined in many ways (see Newell, 1974, Craik, 1985, and Slomp, 1995). For our purposes we discuss two characteristics of the solutions as presented in Craik (1985). The first is the development of Benjamin-Feir (hereafter BF), or side-band, instability of a wavetrain leading to travelling waves. The second is the development of a soliton solution.

The equation is separated into two forms of solutions based upon the sign of the ratio Σ/λ. It is this ratio that determines whether or not the fundamental wave is susceptible to BF instability. To examine this possibility we follow Craik (1985). First, we recognize that (3.6.39) allows a Stokes wave solution of amplitude a_0 given by

$$A = a_0 \exp[-i\Sigma a_0^2 \tau]. \tag{3.7.1}$$

Now we examine the linear stability of this solution by letting

$$A = [a_0 + a_+ \exp(i\Re\xi + i\sigma\tau) + a_- \exp(-i\Re\xi - i\sigma\tau)] \exp[-ia^2\Sigma\tau], \tag{3.7.2}$$

where $\Re$ and σ are the slow scale wavenumber and frequency, and linearizing the system in the perturbation amplitudes, $a_\pm$. Applying solvability constraints for a nontrivial solution gives the dispersion relationship

$$\sigma^2 = \lambda\Re^2(\lambda\Re^2 + 2\Sigma a_0^2). \tag{3.7.3}$$

Imaginary, and hence unstable, roots will occur when the large-scale wavenumber $\Re$ satisfies

$$0 < \Re^2 < -\frac{2a_0^2\Sigma}{\lambda}. \tag{3.7.4}$$

Thus, a finite range of unstable wavenumbers $\Re$ exists whenever $\Sigma/\lambda < 0$, and wavetrains are stable to all wavenumbers $\Re$ if $\Sigma/\lambda > 0$. The wavenumber of maximum

3. ST model

growth and the maximum growth rate of the instability are given by

$$\mathcal{R}_{max} = \left(-\frac{a_0^2 \Sigma}{\lambda}\right)^{\frac{1}{2}},$$

$$\sigma_{max} = |\Sigma| a_0^2,$$

(3.7.5)

respectively.

It would appear that the possibility of instability would violate the nonlinear stability established in §3.3. However, as discussed in Newell (1974) and Slomp and Swaters (1997), this instability only allows the reorganization of neutral modes into travelling wave packets/soliton solutions whose amplitude is bounded by the initial state. Therefore, the fronts are nonlinearly stable.

We briefly review the stability characteristics of both the gently sloping front and wedge front solutions. For the gently sloping front. we find from (3.5.38) and (3.5.42) that

$$\frac{\Sigma}{\lambda} = -\frac{\mu^2}{\beta^2} \frac{k^2 \ell^2 [k^2(1 + \mu\rho + \mu^2\rho^2) - 3\ell^2(1 + 3\mu\rho + 3\mu^2\rho^2)]}{(3\mu\rho(1 + \mu\rho))^2 (k^2 - \ell^2)},$$

(3.7.6)

which changes signs when $k = \ell$ and $k = k_c$ where

$$k_c^2 = \ell^2 \left[\frac{3(1 + 3\mu\rho + 3\mu^2\rho^2)}{(1 + \mu\rho + \mu^2\rho^2)}\right].$$

(3.7.7)

In Figure 3.1, we plot the contours of the maximum growth rate given in (3.7.5) in the $\rho = \alpha/\beta - k/\ell$ plane. The darker the grey, the higher the growth rate, with the white regions being stable. The important boundaries are the lines $k = \ell$ and $k = k_c$ as marked on the graph. As well, the lines $\rho = 0$ and $\rho = -1/\mu$ are marked as dashed lines and represent the singular points of the linear model where the growth rate becomes infinite. Note that the graph is symmetrical about $\rho = -1/2\mu$. The graph illustrates that all solutions are unstable for large wavelengths with the growth rate becoming large as the long-wave–short-wave resonance is approached. As well, all solutions become unstable at small wavelengths with a growth rate that grows like k^3. It is important to note that in the region $-1/\mu < \rho < 0$, the wavetrain is more susceptible to unstable growth. This is also the region where the phase speed can be negative.

Figure 3.1: Plots of the maximum growth rate of the BF instability for the gently sloping front as given by (3.7.5). The darker the grey the greater the growth rate. (The contours are $0, 1, 2, 4 \ldots$ and so the growth rate doubles with each successive contour.) The white regions indicate where the wavetrain is stable. The vertical line marked $k = \ell$ is the wavenumber where long-wave–short-wave resonance occurs. The second line marks where $k = k_c$ and Σ smoothly changes sign. The dashed lines at $\alpha/\beta = 0, -1/\mu$ indicate the singular points in the model.

3. ST model

In the RED model limit, $\mu \to 0$, we have unstable waves for $0 < k < \ell$, long-wave–short-wave resonance at $k = \ell$, stable waves for $\ell < k < \sqrt{3}\ell$, and unstable waves for $k > \sqrt{3}\ell$. The results are now symmetrical about $\rho = 0$. As well, in the limit as the model tends toward equal layer depths, $\mu \to \infty$, we have stability for $\ell < k < 3\ell$, and instability otherwise. Again the results are now symmetrical about $\rho = 0$.

The above analysis can be repeated for the wedge front solution where Σ is given by (3.6.40) and λ by (3.6.41). The forms of these expressions are much more complicated and the possibilities of an even greater number of resonances clouds the issue further. In Figure 3.2, we plot the stability regions in the $\rho - k^2$ plane for the $n = 0$ meridional mode. The solid lines marked $m = 1, 2, 3$ are the curves where long-wave–short-wave resonance occurs with the long wave of the mth meridional mode. Here Σ becomes infinite and changes sign. The dashed line marks where Σ smoothly changes sign. We see that the greater number of resonances leads to a very complicated graph. As the zonal length scale $(1/k)$ decreases the size of both stable and unstable regions becomes very small. We can conclude that increasing the energy available in the basic state, seen here in moving from a gently sloping front to a front with an $O(1)$ slope, increases the possibility of resonance and reduces the importance of the BF instability in determining the nonlinear evolution of a wavetrain. In fact, especially when $\rho < 0$, the regions of instability become quite concentrated about the long-wave–short-wave resonances.

In Figure 3.3, the maximum growth rate as determined by (3.7.3) is plotted versus k^2 for $\rho = 1/2\mu$ (the dashed line on Figure 3.2). This graph further indicates the dominance of the long-wave–short-wave resonance in the wedge front model. The growth rate becomes extremely large for those values of k near resonance, indicating that the dynamics are governed by the long-wave–short-wave resonance and not the NLS equation. We do see an increase in the growth rates as k increases. It should be noted that if we choose to examine higher values of the meridional mode n, that is, shorter meridional scales, we see an increase in the number of resonances and increased growth rates. Thus, the instabilities grow more rapidly at smaller scales.

If we examine the limit as $\mu \to 0$, we see that in Figure 3.2 the region where the analysis breaks down extends to the entire lower half of the plane, that is, for all eastern flows where $\alpha > 0$. The results for the upper half plane are qualitatively

3. ST model
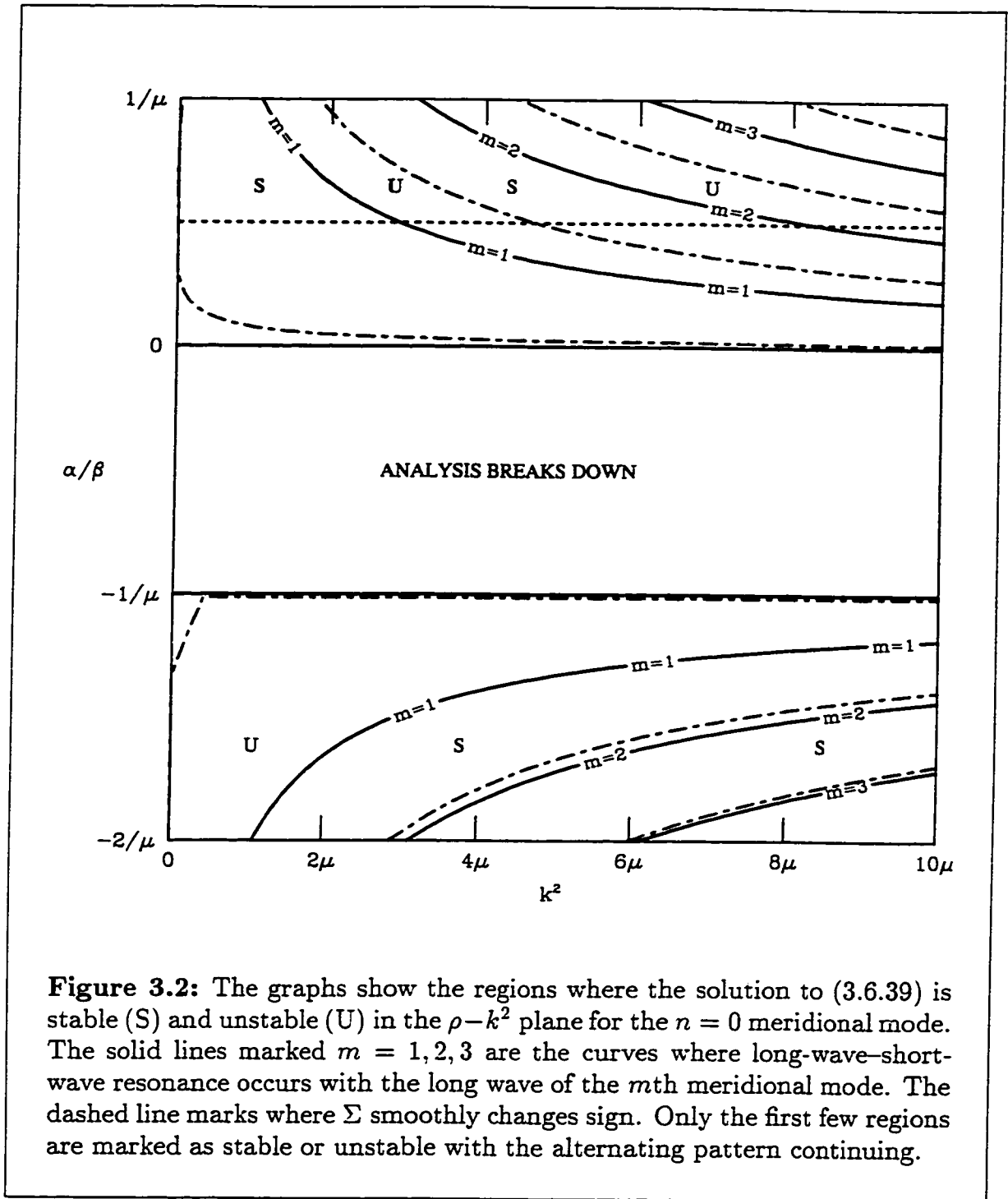
Figure 3.2: The graphs show the regions where the solution to (3.6.39) is stable (S) and unstable (U) in the $\rho-k^2$ plane for the $n = 0$ meridional mode. The solid lines marked $m = 1, 2, 3$ are the curves where long-wave–short-wave resonance occurs with the long wave of the mth meridional mode. The dashed line marks where Σ smoothly changes sign. Only the first few regions are marked as stable or unstable with the alternating pattern continuing.

Figure 3.3: The graph shows the maximum growth rate of the BF instability for the wedge front as determined by (3.7.3) versus k^2 for $\rho = 1/2\mu$ (the dashed line on Figure 3.2). The growth rate becomes infinite when long-wave–short-wave resonance occurs.
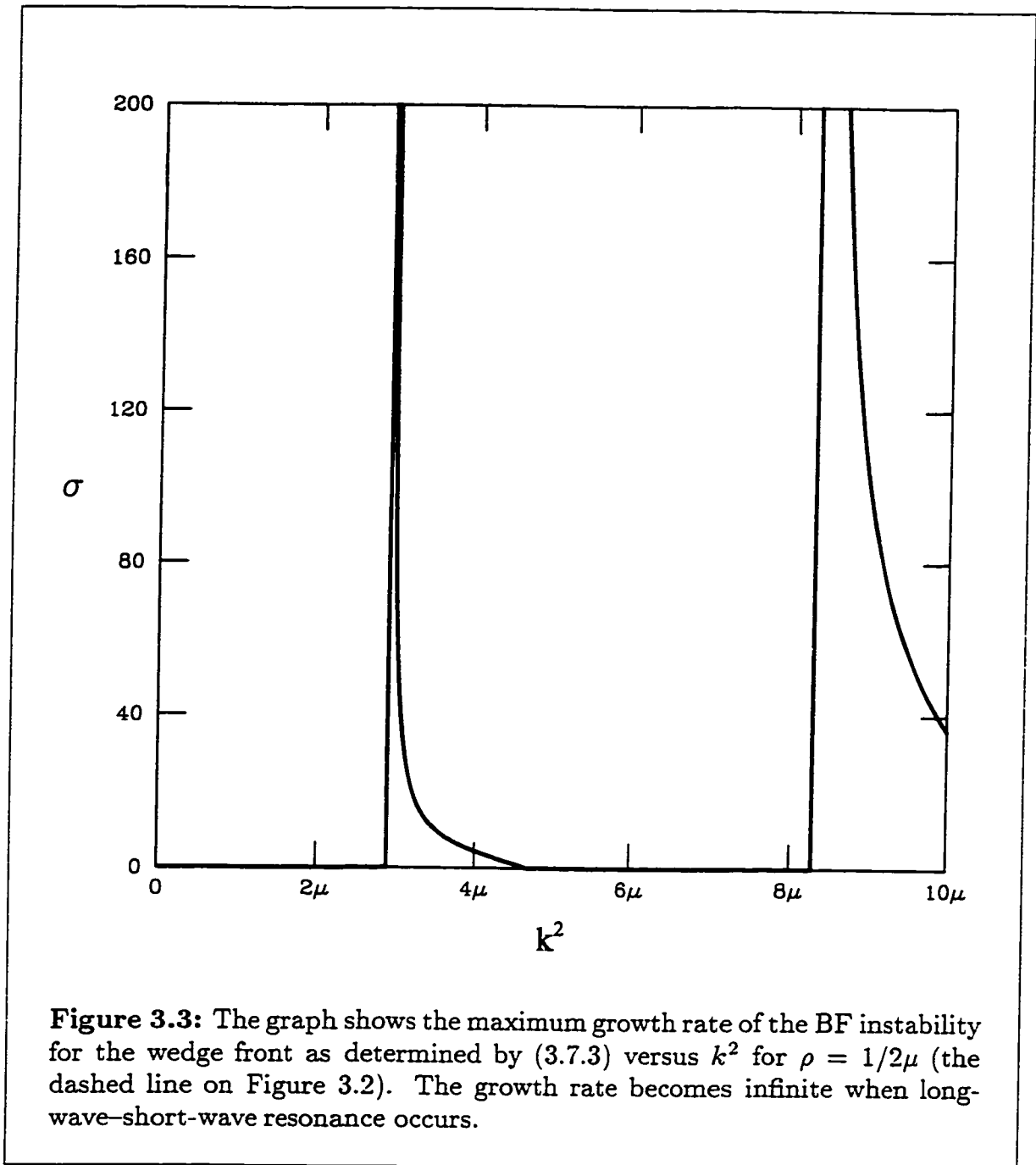
the same. Our results differ from those of Slomp (1995) for the analysis of the RED model on an f-plane. The results of Slomp (1995) were that even (odd) meridional modes were unstable (stable) with a growth rate proportional to k^4. No resonances occurred as these are a result of the addition of the β-plane.

Thus, the instability occurs for large wavelengths of the amplitude envelope,

but grow most rapidly for small scales in the original wave. As a result, small scales in the original wave will rapidly form larger scale wave packets. This leads to a cascade of energy from the smallest scales to larger-scale structures. The effect that such numerous stability boundaries has on the fully nonlinear evolution of a given mode, where many other modes, possibly stable or unstable, are excited is unclear analytically and will be discussed in the numerical section of this chapter (see §3.11).

Since we expect the formation of larger scale wave packets through the process of BF instability, it is interesting to look at possible final-state solutions to (3.6.39). Equation (3.6.39) can be solved using inverse scattering theory as shown in a multitude of works. These solutions show that when $\lambda \Sigma < 0$. "localized wave packets evolve into discrete envelope solitons and a dispersive tail" (Craik. 1985). These solitons are robust in nature and survive. unchanged. interactions with any other nonresonant solitons.

The travelling wave packets/soliton solutions can easily be examined by letting the amplitude take the form of a travelling wave.

$$A = \exp\left[i\mathcal{K}\xi - iV\tau\right] f(\xi - U\tau).$$

(3.7.8)

with

$$\mathcal{K} = \frac{U}{2\lambda}.$$

(3.7.9)

Substituting into (3.6.39) gives

$$f'' - \gamma_1 f + \gamma_2 f^3 = 0,$$

(3.7.10)

where

$$\gamma_1 = \mathcal{K}^2 - \frac{V}{\lambda} \quad \text{and} \quad \gamma_2 = -\frac{\Sigma}{\lambda}.$$

(3.7.11)

Equation (3.7.10) occurs several times in our analysis and a complete description of the solutions is given in Appendix 5. Since f represents a travelling wave it must be bounded for all values of its argument. Thus, the solutions in Appendix 5 that become unbounded are not applicable here. The solutions that can occur are those given in regions 1 and 2, when $\gamma_2 > 0$. and region 6 when $\gamma_2 < 0$.

3. ST model

When $\gamma_2 > 0$, the form of the wave is governed by its initial amplitude at the origin, $A_0 = A(0,0)$. If $A_0^2 > 2(V - \lambda \mathcal{R}^2)/\Sigma$ then the solution falls in region 1 and is given by a doubly periodic cnoidal wave (see (A.5.10)). If $A_0^2 < 2(V - \lambda \mathcal{R}^2)/\Sigma$ then the solution falls in region 2 and is given by a doubly periodic dnoidal wave (see (A.5.12)). Lying in between these solutions is the bright soliton solution given by (A.5.27). This solution requires that

$$A_0^2 = 2(V - \lambda \mathcal{R}^2)/\Sigma \qquad (3.7.12)$$

and reduces to

$$f(\xi - U\tau) = A_0 \ \mathrm{sech}\left[\mathfrak{w}(\xi - U\tau)\right], \qquad (3.7.13)$$

where

$$\mathfrak{w} = \left(-\frac{\Sigma A_0^2}{2\lambda}\right)^{\frac{1}{2}}. \qquad (3.7.14)$$

We can write the soliton solution using (3.7.8) and the definition of the leading-order solution of h to get

$$
\begin{aligned}
h^{(0)} = A_0 \ \mathrm{sech}\left[\Delta \mathfrak{w}\left[x - (c_G(k,\ell) + \Delta U)t\right]\right] \\
\times \left\{\exp\left[i\tilde{k}x + i\tilde{\omega}t\right]\tilde{h}(y,\ell) + c.c.\right\},
\end{aligned}
\qquad (3.7.15)
$$

where

$$\tilde{k} = k + \Delta \mathcal{R},$$

$$\tilde{\omega} = \omega(k,\ell) - \Delta \mathcal{R} c_G(k,\ell) + \Delta^2 V.$$

Thus, $\mathcal{R}$ denotes a small, arbitrary shift in the fundamental wavenumber k while the frequency is correspondingly shifted by the group speed times $\mathcal{R}$ plus a small, arbitrary shift V. The relationships between the soliton amplitude, A_0, the soliton width, $\mathfrak{w}$, the soliton speed U, the wavenumber shift $\mathcal{R}$, and the frequency shift V, are given by (3.7.9), (3.7.12) and (3.7.14). In this formulation, we see that the amplitude is modulated by the travelling soliton structure, which travels at a shifted group speed, $c_G(k,\ell) + \Delta U$. We've given the solution here in terms of the notation for the gently sloping front, but the solution holds identically for the wedge front.

3. ST model

In the stable limit, that is, when $\gamma_2 < 0$ and $\gamma_1 < 0$, the solution is determined by the slope of the solution at the origin, $f'(0) = A_{\xi 0} = A_\xi(0,0)$. The solution falls in region 6 and is given by (A.5.20). In the limit where $A_{\xi 0}^2 = -\gamma_1^2/2\gamma_2 = -\lambda(\mathscr{R}^2 - V/\lambda)^2/2\Sigma$, we get the dark soliton solution given by (A.5.35).

3.8 Long-wave–short-wave Resonance

In the solution of the amplitude equation presented in the previous section, it became apparent that the long-wave–short-wave (LWSW) resonance is extremely important in understanding the weakly nonlinear evolution of a given wavetrain. The BF instability analysis suggests that this resonance is the source of large unstable growth. The resonance occurs when a long-wave mode is a solution to the first order slow problem with a phase speed and group speed equal to that of the group speed of the fundamental. That is,

$$c_G(0,m) = c(0,m) = c_G(k,\ell).\tag{3.8.1}$$

where m is the meridional mode wavenumber of the long wave. This resonance, as it occurs in the nonlinear interaction of surface gravity waves, is studied in Grimshaw (1977) and Djordjevic and Redekopp (1977) and we briefly present some of their analysis.

We will carry out the analysis first for the gently sloping front, where resonance occurs for $k = \ell$ and $m = 2\ell$. In order to examine the effects of LWSW resonance, a long-wave solution must be included in the analysis from the beginning. That is, we assume the perturbation is composed of two parts: a fast varying or short wave analogous to the perturbation of the previous analysis and a slowly varying or long wave independent of the fast variables x, t. That is,

$$h = \Delta h_s(x,y,t;X,T,\tau) + \varepsilon_1 h_l(y;X,T,\tau),\tag{3.8.2}$$

$$\psi = \Delta \psi_s(x,y,t;X,T,\tau) + \varepsilon_1 \psi_l(y;X,T,\tau),\tag{3.8.3}$$

where we scale the two parts by small quantities Δ and ε_1, respectively, and the subscripts s and l indicate the short and long waves, respectively. As well, the slow time and space scales are changed so that we can enforce an appropriate balance.

3. ST model

We replace (3.5.1) with

$$\tilde{t} = \Delta t, \quad T = \varepsilon_2 \tilde{t}, \quad \tau = \varepsilon_2^2 \tilde{t}, \quad X = \varepsilon_2 x. \qquad (3.8.4)$$

where we introduce the appropriately scaled time, $\tilde{t}$, and parameters $(\tilde{\beta}, \tilde{alpha})$ associated with the GS front. Henceforth, we drop the tildes. The sizes of ε_1 and ε_2 are chosen so that we get a desired balance (see Grimshaw, 1977). We want the second order problem found in the previous analysis to be the same. This requires that $\Delta\varepsilon_2 \gg (\Delta\varepsilon_1, \varepsilon_2\varepsilon_1, \varepsilon_1^2)$. We then require that the second order slow derivative terms, $O(\Delta\varepsilon_2^2)$, balance the interaction of the long-wave and short-wave, $O(\Delta\varepsilon_1)$, giving that $\varepsilon_1 = \varepsilon_2^2$. Finally, we require that the second order slow derivatives of the long-wave, $O(\varepsilon_1\varepsilon_2^2)$, be balanced by the short-wave interactions that produce long-wave terms, $O(\Delta^2\varepsilon_2)$, giving $\varepsilon_1\varepsilon_2 = \Delta^2$. This reduces the scaling to $\varepsilon_1 = \Delta^{4/3}$ and $\varepsilon_2 = \Delta^{2/3}$.

We allow for the case of near resonance. That is, we choose

$$c_G(k, \ell) = (1 + \varepsilon_2 \zeta) c_G(0, m), \qquad (3.8.5)$$

where ζ is an $O(1)$ tuning parameter that specifies how close to exact resonance, $\zeta = 0$, we are. This may seem to be an unnecessary difficulty, but it is very important. As it turns out, relatively large variations in the wavenumber from the critical wavenumber of exact resonance result in only a small value for the tuning parameter. In the case of the gently sloping front, (3.8.5) can be expressed as a function of $k^2 - \ell^2$, a measure of the difference between the wavenumber and the wavenumber of exact resonance $k = \ell$. This gives

$$\begin{aligned}
\zeta &= \frac{1}{\varepsilon_2}\left(\frac{c_G(k, \ell)}{c_G(0, 2\ell)} - 1\right) \\
&= \frac{1}{\varepsilon_2}\left(\frac{3\alpha(\mu\alpha + \beta)(k^2 - \ell^2)}{\beta^2 + 4\alpha(\mu\alpha + \beta)\ell^2}\right).
\end{aligned} \qquad (3.8.6)$$

For typical parameter values, $\beta = \alpha = \ell = 1, \mu = 0.5$, this reduces to

$$\zeta = \frac{9}{14\varepsilon_2}(k^2 - \ell^2).$$

3. ST model

Therefore for $\varepsilon_2 = (0.1)^{2/3}$ the tuning parameter remains $O(1)$, that is, say, $|\zeta| < 5$, for $0 < k < 3.7$. Comparing this wave range to Figure 3.1 suggests that the evolution of the slowly varying amplitude is actually governed by the equations derived in this section for a substantial range of wavenumbers.

Using the above definitions, the analysis proceeds as in §3.5 and §3.6. At $O(\Delta)$ the linear solution, (3.2.27, 3.5.11), is obtained for the short wave, h_s, with the slowly varying amplitude A. At $O(\Delta^{4/3})$, the long wave trivially satisfies the equations. At $O(\Delta^{5/3})$, the solution (3.5.15, 3.5.22, 3.5.23, 3.5.24) for the short wave is obtained, with the stipulation that the amplitude travels at the group speed, $A = A(\xi, \tau)$ (we drop the mean-flow terms as they are no longer required). At $O(\Delta^2)$, the second harmonic problem is encountered, and can be solved as before though the results are not needed in the present analysis. Also at $O(\Delta^2)$, the long-wave equation (3.5.31) is obtained giving the solution $h_l = \tilde{B}(\xi, \tau)\tilde{h}(y, 0, 2\ell)$, where we have used (3.8.5) and (3.8.1). At $O(\Delta^{7/3})$, the second-order, slow-derivative terms of A, as given in (3.5.41), are balanced by the leading-order interaction of the short and long wave. If we repeat the analysis that leads to equation (3.5.41) we get

$$A_\tau - i\frac{1}{2}\frac{\partial^2 \omega}{\partial k^2}(k, \ell)A_{\xi\xi} = i\Phi_1 A\tilde{B},\tag{3.8.7}$$

where

$$\Phi_1 = \frac{\aleph(\beta + 2\alpha\mu)}{\beta}k\ell(3\ell^2 - k^2).\tag{3.8.8}$$

At $O(\Delta^{8/3})$, the slow-time-derivative term of $\tilde{B}$ and the tuning error term are balanced by the interaction of the leading and second order short wave solutions and slow, quadratic interactions of the short wave with itself as in (3.5.28). Repeating the analysis leading to the long-wave equation (3.5.28) gives

$$\tilde{B}_\tau - c_{G_n}\zeta\tilde{B}_\xi = \Phi_2(|A|^2)_\xi,\tag{3.8.9}$$

where Φ_2 is given by

$$\Phi_2 = \frac{\aleph(\beta + 2\alpha\mu)}{\beta}2k^2\ell.\tag{3.8.10}$$

3. ST model

Equations (3.8.7) and (3.8.9) are the long-wave–short-wave equations derived by Grimshaw (1977) and Djordjevic and Redekopp (1977) and studied in Ma (1978). They can be written in the normalized form

$$iA_\tau + \lambda A_{\xi\xi} = AB, \tag{3.8.11}$$

$$B_\tau = \nu B_\xi + \Phi(|A|^2)_\xi, \tag{3.8.12}$$

where $B = -\Phi_1\breve{B}$, $\nu = c_{G_n}\zeta$, $\lambda = \frac{1}{2}\frac{\partial^2\omega}{\partial k^2}(k,\ell)$, and $\Phi = -\Phi_1\Phi_2$. While (3.8.11, 3.8.12) can be solved using inverse scattering methods (see Ma. 1978) some insight can be gained from some straightforward analysis.

First, we repeat the stability analysis of the previous section by examining the stability of a constant amplitude solution by letting

$$A = [a_0 + a_+ \exp[i(\Re\xi + \sigma\tau)] + a_- \exp[i(-\Re\xi - \sigma\tau)]]\exp(-ib_0\tau),$$

$$B = b_0 + b\left[\exp[i(\Re\xi + \sigma\tau)] + \exp[i(-\Re\xi - \sigma\tau)]\right].$$

and examining the linear equations to get the dispersion relationship

$$\sigma^3 - \nu\Re\sigma^2 - \lambda^2\Re^4\sigma + 2\Phi\lambda a_0^2\Re^3 + \lambda^2\nu\Re^5 = 0. \tag{3.8.13}$$

If (3.8.13) has complex roots then the wavetrain is unstable. and the long-wave–short-wave equations have a BF instability similar to that discussed earlier. When the resonance is exact, $\nu = 0$, it follows that complex roots exist for a finite range of wavenumbers

$$0 \le \Re \le \left(\frac{\sqrt{27}|\Phi|a_0^2}{\lambda^2}\right)^{1/3}.$$

When tuning is present, the instability is inhibited if the tuning is positive and shifted to smaller scales if the tuning is negative. In Figure 3.4, the maximum growth rate, σ_{max}, and range of unstable wavenumbers, $\Re$, as determined by (3.8.13) are shown versus the wavenumber k using the relationship (3.8.6). It clearly shows the effect of tuning and illustrates that the maximum growth associated with the resonance occurs at a wavelength slightly less than exact resonance. Note that the

3. ST model

range of unstable wavenumbers $\Re$ appears deceptively small due to the large scale on the lower graph.

These results can be used to explain the discontinuous results of the previous section. In order to compare the growth rates associated with the LWSW resonance with that of the previous section, we must scale them appropriately using the new slow time scaling (3.8.4). For example, choosing $\Delta = 0.1$ and scaling the growth rates in actual time, t, we can combine the results for the LWSW resonance with the BF instability. We assume that the LWSW resonance dominates the flow for $k < k_c$ and that BF instability applies for $k > k_c$ where k_c is given by (3.7.7). Thus, we redraw Figure 3.1 to obtain Figure 3.5. Now the growth rates at smaller scales are more significant, the region of stability has been diminished, and the discontinuity across $k = \ell$ removed. Only the singular points $\rho = 0$ and $\rho = -1/\mu$ cause difficulty. Still, at large wavenumbers (small wavelengths) the growth rate of the BF instability becomes comparable to and eventually exceeds the growth rate associated with the LWSW resonance.

Once again, the analysis can be repeated for the wedge front. Resonance occurs at an infinite number of wavenumbers for a given meridional mode, with the restriction that the meridional mode of the long wave is greater than the fundamental mode. Table 3.1 lists the first four LWSW resonant pairs for the first five meridional modes. The coefficients Φ_1 and Φ_2 must now be calculated numerically (see (A.3.14) and (A.3.15)) and the possibility of multiple resonances for a given fundamental wave arises. Otherwise, the equations (3.8.11) and (3.8.12) still hold and instability arises as before. For simplicity, we only plot the the graph analogous to Figure 3.3 in Figure 3.6. The graph illustrates how the LWSW results, given by the solid lines labelled with the long wave meridional mode number m, compare to BF instability results, given by the dashed lines, for $\rho = 1/2\mu$. As before, the LWSW resonance is expected to dominate the BF instability suggesting unstable growth for all wavenumbers. As well, the possibility of several resonances complicates the picture, as the instabilities associated with different resonant modes overlap. Thus, it becomes unclear which instability will dominate the evolution, although it is clear that growth rates increase as the wavelength decreases. As noted earlier increasing the meridional mode of the fundamental wave increases the number of resonances, giving yet a more cluttered picture. One must conclude that increasing the slope of the front, and hence the amplitude of the zonal flow, allows for a greater number

3. ST model
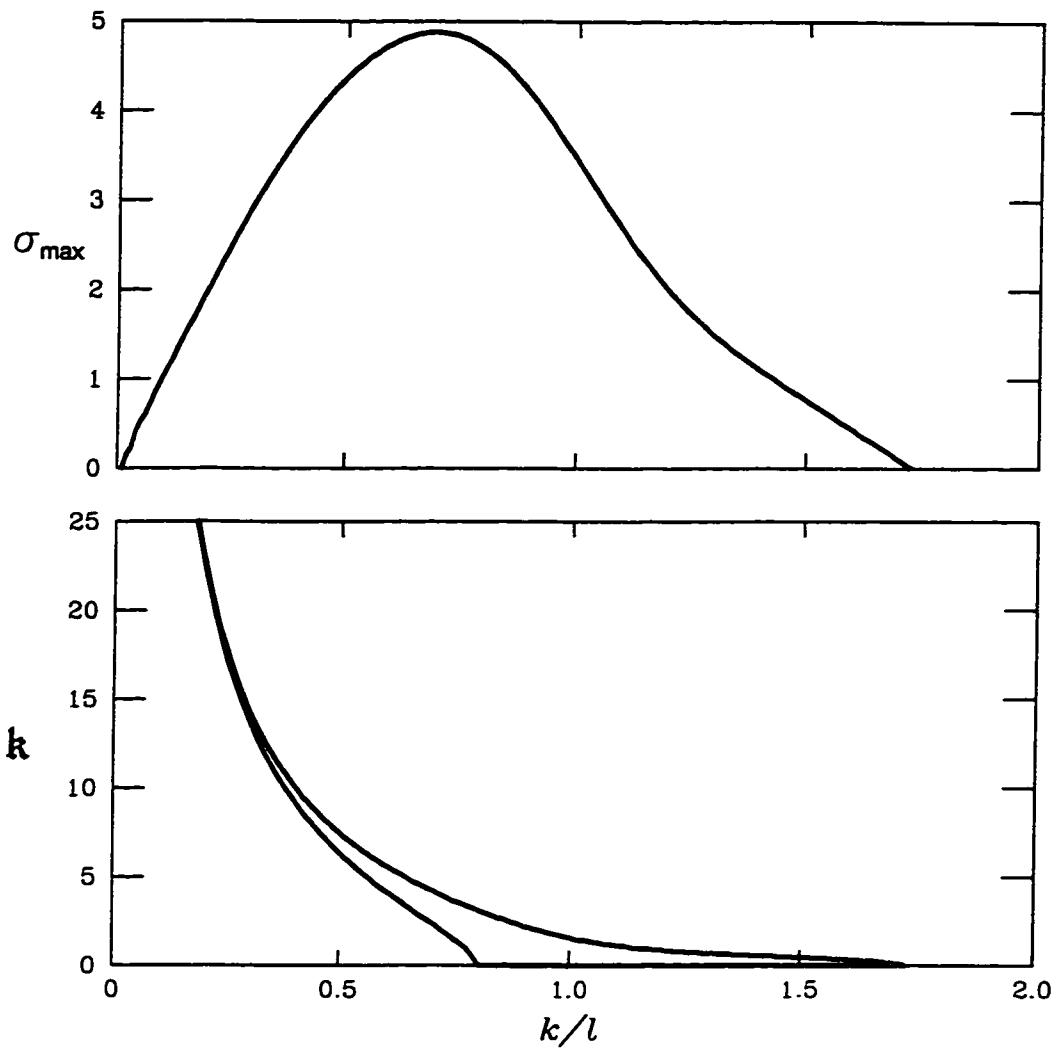
Figure 3.4: Stability characteristics of the LWSW resonance for the gently sloping front with $\ell = 1$. The upper graph shows the maximum growth rate as determined by (3.8.13) versus the small wavenumber k. The lower graph shows the minimum and maximum values of $\mathcal{K}$ for instability as given by (3.8.13) versus k. The small region in between the two curves is the region where instability occurs. At $k/\ell = 1$ we have exact resonance.

Figure 3.5: Contour plots of the maximum growth rate expected when both the effects of the LWSW resonance and BF instabilities are considered. White regions are stable while darker grey indicates higher growth rate. The contour level is 0.1.
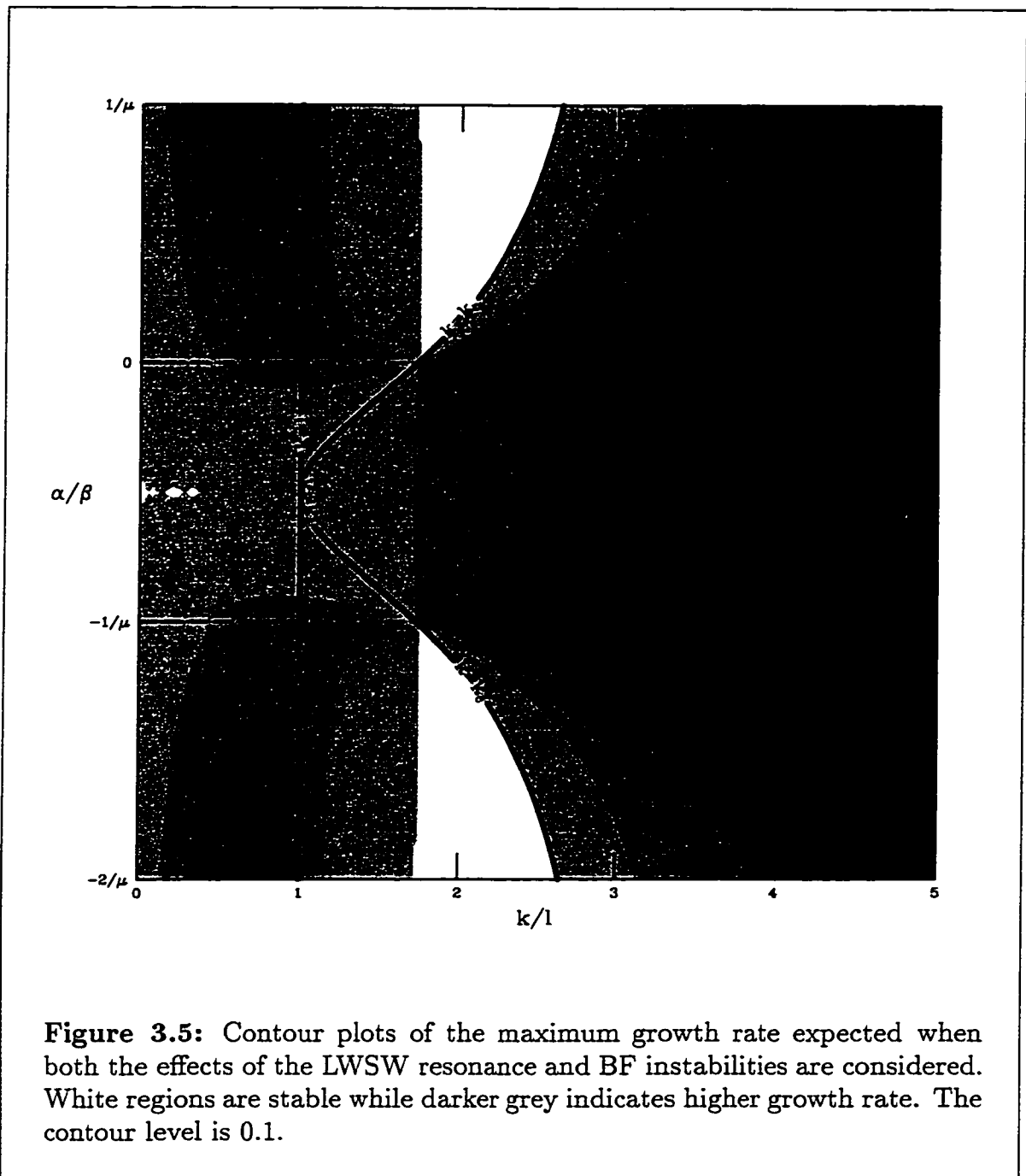
3. ST model

Short Wave (k, n)	Long Wave mode (m)	Short Wave (k, n)	Long Wave mode (m)
(1.203, 0)	1	(0.853, 2)	5
(2.036, 0)	2	(1.031, 2)	6
(2.856, 0)	3	(0.371, 3)	4
(3.673, 0)	4	(0.544, 3)	5
(0.595, 1)	2	(0.691, 3)	6
(0.913, 1)	3	(0.826, 3)	7
(1.203, 1)	4	(0.324, 4)	5
(1.484, 1)	5	(0.472, 4)	6
(0.445, 2)	3	(0.595, 4)	7
(0.663, 2)	4	(0.707, 4)	8

TABLE 3.1.   The first four long-wave–short-wave resonant pairs for the wedge front for each of the first five meridional modes. An infinite number of resonant pairs exists for each short wave meridional mode. The meridional mode of the long wave is always greater than the meridional mode of the short wave.

3. ST model

of unstable resonances. These resonances complicate the picture so that predicting a dominant pattern is difficult but they do suggest that all wavetrains will be unstable.

As discussed in Djordjevic and Redekopp (1977), a travelling wave solution to (3.8.11, 3.8.12) can also be found by letting

$$A = \exp\left[i\frac{U}{2\lambda}\xi - iV\tau\right] f(\xi - U\tau), \quad B = \frac{\Phi}{U + \nu}f^2,$$

which gives the equation

$$f'' - \gamma_1 f + \gamma_2 f^3 = 0,$$

with

$$\gamma_1 = \frac{U^2 - 4\lambda V}{4\lambda^2}, \quad \gamma_2 = -\frac{\Phi}{\lambda(U + \nu)}.$$

This is the equation studied in Appendix 5 and similar solutions exist to those found in §3.7. Note that γ_1 is given by the same definition as in §3.7. but that γ_2 differs and now depends not only on the nonlinear interactions. Φ. but also on the tuning and travelling wave's speed. The solution form again depends on the signs of γ_2 and γ_1 with all solutions necessarily bounded. When $\gamma_2 > 0$ ($\gamma_2 < 0$), we again have a bright (dark) soliton solution.

3.9 Three Wave Resonance

In the analysis in §3.6, the second order problem (3.6.19) could not be solved when second harmonic resonance occurs. Noting the importance of the long-wave–short-wave resonance in the stability analysis of the envelope evolution, it behooves us to examine this resonance and others like it. The second harmonic resonance is a special case of three wave resonance. Three wave resonance occurs when the quadratic interaction of two waves resonates, has the same frequency and wavelength, as a third wave. This leads to interaction of the three waves at the second order problem and results in equations that govern the envelope evolution of the three waves together.
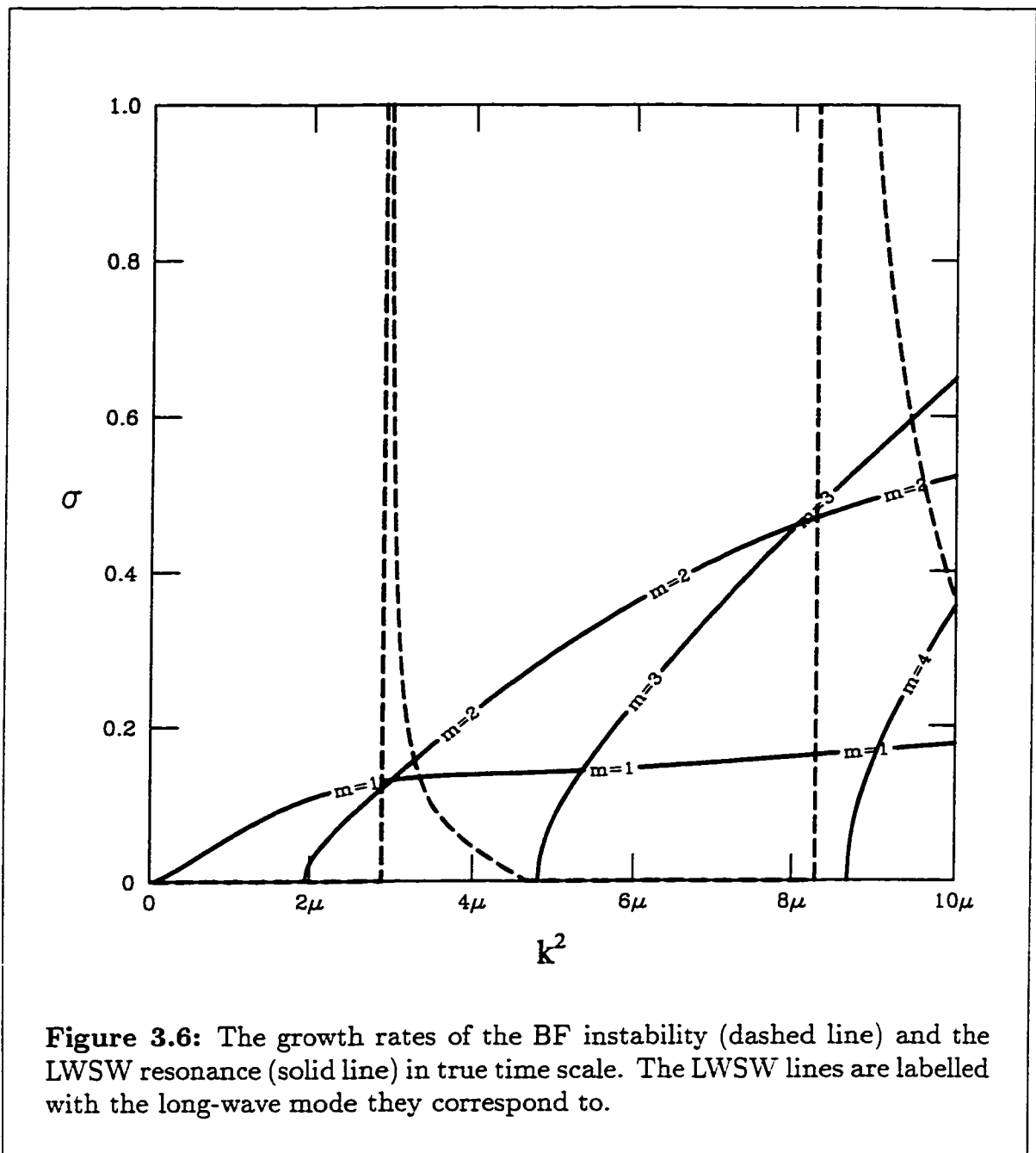
Figure 3.6: The growth rates of the BF instability (dashed line) and the LWSW resonance (solid line) in true time scale. The LWSW lines are labelled with the long-wave mode they correspond to.

3. ST model

To examine three wave resonance, consider a leading-order solution that is the superposition of three waves,

$$h = \sum_{j=1}^{3} A_j \widetilde{h}(y, k_j, n_j) \exp i\theta_j + c.c., \qquad (3.9.1)$$

where each wave has a slowly varying amplitude, A_j, and phase, $\theta_j = k_j x + \omega_j t$. Each wave is a solution to the leading-order problem with the corresponding dispersion relationship, $\omega_j = \omega(k_j, n_j)$ with $\omega(-k_j, n_j) = -\omega(k_j, n_j)$. The quadratic interaction of these waves will consist of waves proportional to $\exp i(\pm\theta_j \pm \theta_l)$ for $j, l = 1, 2, 3$. From the previous analysis, it is clear that a quadratic-interaction wave will influence the evolution of the fundamental wave if it possesses the identical structure in x, t, that is, if the interaction wave has the same wavelength and frequency and resonates with the fundamental. The evolution of the first wave, $A_1 \widetilde{h}_{n_1}(y, k_1) \exp i\theta_1$, will be influenced by quadratic-interaction waves that have phase $\pm\theta_j \pm \theta_l = \theta_1$. All such cases can be reduced to the restriction

$$\theta_1 + \theta_2 + \theta_3 = 0.$$

This gives two equations that govern when resonance occurs:

$$k_1 + k_2 + k_3 = 0, \qquad (3.9.2)$$

$$\omega_1 + \omega_2 + \omega_3 = 0. \qquad (3.9.3)$$

For the given dispersion relationship, (3.2.28), it can be determined that these equations can be satisfied at various values of k for specific meridional modes.

The case of second harmonic resonance occurs when $k_1 = k_2$, so that $k_3 = -2k_1$ and $\omega(2k_1, n_3) = -2\omega(k_1, n_1)$, which is condition (3.6.25) found in §3.6 that prohibits a solution to the problem (3.6.19). Similarly, the long-wave–short-wave resonance can be described by the triad $k_1 = k - \epsilon$, $k_2 = -k - \epsilon$, and $k_3 = -2\epsilon$. Substituting into (3.9.3), dividing by 2ϵ, and taking the limit as $\epsilon \to 0$ gives that $\frac{d\omega(k,n)}{dk} = c(0, n_3) = c_G(0, n_3)$, which is the condition (3.8.1) necessary for long-wave–short-wave resonance as discussed in §3.8. However, the infinitesimal size of the wavenumbers involved in this resonance influences the analysis and necessitates the separate treatment examined in §3.8.

3. ST model

To explore three wave resonance, we examine the gently sloping front model initially and then extend this analysis to the wedge front. The evolution of a three-wave resonance triad is determined by the $O(\Delta)$ problem. Using (3.9.1) with (3.9.2) and (3.9.3), the $O(\Delta)$ equation becomes

$$
\mathfrak{L}(\partial_t, \partial_x, \partial_y)h^{(1)} = \left\{ - \left[\beta \frac{\partial A_1}{\partial T} + \frac{\partial A_1}{\partial X} \mathfrak{L}_2(\partial_t, \partial_x) \right] \sin(\ell_1 y) \right.
$$
$$
+ i A_2^* A_3^* \frac{\aleph(\beta + 2\mu\alpha)}{2} \left[(k_2^2 + \ell_2^2) - (k_3^2 + \ell_3^2) \right] \times
$$
$$
\left\{ (k_2 \ell_3 - k_3 \ell_2) \sin\left(-(\ell_2 + \ell_3)y \right) \right.
$$
$$
\left. + (k_2 \ell_3 + k_3 \ell_2) \sin\left((\ell_3 - \ell_2)y \right) \right\}.
$$

(3.9.4)

where $\ell_i = n_i \pi / L$. As before, the F.A.T. applies to this equation and a condition that allows a solution is derived. Accordingly, we would multiply the right-hand side of the equation by $\sin(\ell_1 y)$ and integrate over the domain. If the quadratic term in the second and third waves is to contribute to the solvability condition we must have that either

$$
-(\ell_2 + \ell_3) = \pm \ell_1 \quad \text{or} \quad (\ell_3 - \ell_2) = \pm \ell_1.
$$

Both cases reduce to an additional requirement for three wave resonance that the meridional mode numbers must sum to zero, namely

$$
n_1 + n_2 + n_3 = 0,
$$

(3.9.5)

where n_i are nonzero integers. Assuming that (3.9.5) holds in addition to (3.9.3) and (3.9.2), the F.A.T. implies that a solution exists iff

$$
\frac{\partial A_1}{\partial T} + \frac{d\omega_1}{dk} \frac{\partial A_1}{\partial X} = i A_2^* A_3^* \frac{\aleph(\beta + 2\mu\alpha)}{2\beta} \left[(k_2^2 + \ell_2^2) - (k_3^2 + \ell_3^2) \right] (k_3 \ell_2 - k_2 \ell_3).
$$

98

3. ST model

Repeating the analysis for the other two waves leads to the three equations

$$\frac{\partial A_1}{\partial T} + \frac{d\omega_1}{dk}\frac{\partial A_1}{\partial X} = i\Im_{23}A_2^*A_3^*,$$

$$\frac{\partial A_2}{\partial T} + \frac{d\omega_2}{dk}\frac{\partial A_2}{\partial X} = i\Im_{31}A_3^*A_1^*, \qquad (3.9.6)$$

$$\frac{\partial A_3}{\partial T} + \frac{d\omega_3}{dk}\frac{\partial A_3}{\partial X} = i\Im_{12}A_1^*A_2^*,$$

where

$$\Im_{ab} = \frac{\aleph(\beta + 2\mu\alpha)}{2\beta}\left[(k_a^2 + \ell_a^2) - (k_b^2 + \ell_b^2)\right](k_b\ell_a - k_a\ell_b). \qquad (3.9.7)$$

A similar system of equations can be derived for the wedge model. Two differences should be noted. First, because the eigenfunctions for the wedge model given by (3.2.40) do not have as simple a form and because of the greater number of quadratic interactions, the terms on the right-hand side of the equation analogous to (3.9.4) are much more complicated and must be calculated numerically: see (A.3.16). Second, it so happens that a restriction on the meridional mode number akin to (3.9.5) is not required for the wedge model. This follows since the quadratic interaction of the eigenfunctions and their derivatives results in terms that are infinite sums of the eigenfunctions and so always contain a term proportional to the homogeneous solution of the right-hand side.

The equations (3.9.6) can be written in standard, normalized form by letting

$$A_1 = -i\frac{\widetilde{A}_1}{\sqrt{|\Im_{31}\Im_{12}|}}, \quad A_2 = -i\frac{\widetilde{A}_2}{\sqrt{|\Im_{23}\Im_{12}|}}, \quad A_3 = -i\frac{\widetilde{A}_3}{\sqrt{|\Im_{31}\Im_{23}|}},$$

to get, dropping the tildes,

$$\frac{\partial A_1}{\partial T} + \frac{d\omega_1}{dk}\frac{\partial A_1}{\partial X} = s_1 A_2^*A_3^*,$$

$$\frac{\partial A_2}{\partial T} + \frac{d\omega_2}{dk}\frac{\partial A_2}{\partial X} = s_2 A_3^*A_1^*, \qquad (3.9.8)$$

$$\frac{\partial A_3}{\partial T} + \frac{d\omega_3}{dk}\frac{\partial A_3}{\partial X} = s_3 A_1^*A_2^*,$$

where

$$s_1 = \text{sgn}(\Im_{23}), \quad s_2 = \text{sgn}(\Im_{31}), \quad s_3 = \text{sgn}(\Im_{12}). \qquad (3.9.9)$$

3. ST model

Resonant Triad (k_i, n_i)			Interaction Parameters		
(0.200, 1),	(4.800,-2),	(-5.000, 1)	1.	1.	-1
(0.250, 1),	(3.750,-2),	(-4.000, 1)	1.	1.	-1
(0.320, 1),	(2.805,-2),	(-3.125, 1)	1.	1,	-1
(0.400, 1),	(2.100,-2),	(-2.500, 1)	1,	1,	-1
(0.500. 1),	(1.500,-2),	(-2.000, 1)	1,	1,	-1
(0.800, 2),	(4.200.-4),	(-5.000, 2)	1,	1,	-1
(1.000, 2),	(3.000.-4),	(-4.000. 2)	1.	1.	-1
(1.280, 2),	(1.845.-4),	(-3.125, 2)	1.	1.	-1
(0.450, 2),	(0.800,-1).	(-1.250.-1)	-1,	-1.	1
(0.900, 4).	(1.600.-2).	(-2.500.-2)	-1.	-1.	1
(1.000, 5),	(3.000,-3).	(-4.000.-2)	-1.	-1.	1

TABLE 3.2. Resonant triads and interaction parameters for the gently sloping front. Note that one interaction parameter always differs in sign from the other two.

These are the standard three-wave interaction equations as derived in Craik (1985). It is also possible to examine the case of near resonance, where (3.9.2) and (3.9.5) are satisfied but (3.9.3) is replaced by

$$\omega_1 + \omega_2 + \omega_3 = \Delta\zeta, \qquad (3.9.10)$$

3. ST model

Resonant Triad (k_i, n_i)			Interaction Parameters		
(1.206, 2),	(1.206, 2),	(-2.412, 1)	-1,	-1,	1
(0.686, 3),	(0.686, 3),	(-1.372, 2)	-1,	-1,	1
(1.717, 4),	(1.717, 4),	(-3.434, 2)	-1,	-1,	1
(0.528, 4),	(0.528, 4),	(-1.055, 3)	-1,	-1,	1
(0.980, 5),	(0.980, 5),	(-1.960, 3)	-1,	-1,	1
(0.444, 5),	(0.444, 5),	(-0.888, 4)	-1,	-1,	1
(1.058, 2),	(3.108, 0),	(-4.166, 0)	-1,	-1,	1
(1.108, 2),	(3.175, 0),	(-4.283, 0)	-1,	-1,	1
(0.388, 3),	(3.558, 0),	(-3.946, 0)	-1,	-1,	1
(0.926, 3),	(4.306, 0),	(-5.232, 0)	-1,	-1,	1
(3.041, 3),	(4.045, 5),	(-7.086, 2)	-1,	-1,	1
(0.577, 4),	(4.906, 0),	(-5.483, 0)	-1,	-1,	1
(2.205, 4),	(3.841, 4),	(-6.046, 2)	-1,	-1,	1
(1.128, 5),	(2.194, 1),	(-3.322, 1)	-1,	-1,	1

TABLE 3.3. Resonant triads and interaction parameters for the wedge front. Note that one interaction parameter always differs in sign from the other two. The first 6 triads are examples of second harmonic resonance.

where here ζ is an $O(1)$ parameter representing how well the resonance is tuned. However, our analysis here is brief and the reader is referred to Craik (1985) for more details.

The solutions to (3.9.8) have been well studied (see Craik, 1985). Two types of solutions exist: bounded, periodic transfers of energy occurring between the three waves when one s differs in sign from the other two, and explosive growth of all the waves when the signs of the s's are the same. In all the resonant triads found for this model, the s's differ in sign (see Tables 3.2 and 3.3). It is possible to solve the equations (3.9.8) using the inverse scattering method and to present a solution that represents a "pump" wave, where one wave's amplitude grows as a result of the forcing of the other two. These solutions will not be discussed in detail here and interested readers are referred to Craik (1985). We simply conclude that three wave interactions do exist, and that these interactions result in periodic transfers of energy between the three waves. In Tables 3.2 and 3.3 we give a partial list of three wave resonances that are possible for the gently sloping and wedge front, respectively. The tables list the three pairs of zonal and meridional wavenumbers and the three interaction coefficients, s_i. Note that for all cases, the s's differ in sign. Also, for the wedge front model, the case of second harmonic resonance occurs where two of the wavenumber pairs are identical.

3.10   The Long Wave Solution

We look at one final idea associated with the weakly nonlinear analysis. In the previous analysis, it was assumed, though not stated outright, that the leading-order normal-mode solution was valid for $O(1)$ length scales, that is, k being $O(1)$. There are obvious points where the analysis breaks down if $k = 0$. Yet, considering these scales seems relevant to the large scales examined through the weakly nonlinear analysis and are also relevant to comparison of long wavelength analysis of previous works, for example Griffiths et al. (1982), and Paldor and Killworth (1987). As such, we consider the long-wave limit of the previous analysis.

The long-wave equations are derived by considering the limiting case as $k \to 0$. This can be done easily by considering the previous analysis with solutions that no longer vary in fast time and space. (Note: This analysis can also be carried out by

3. ST model

rescaling the model equations for large zonal length scales.) That is, we consider

$$\left(h^{(m)}, \psi^{(m)} \right) = \left(B^{(m)}(X, T, \tau) b_m(y), D^{(m)}(X, T, \tau) d_m(y) \right).$$

Now, when doing the nonlinear analysis, it follows that $\mathcal{L}(\partial_t, \partial_x, \partial_y) h^{(m)} = 0$ for all orders m and that all nonlinear interactions give rise only to long-wave terms. With these assumptions, the leading-order problem is trivially satisfied as the solution is independent of x and t. The $O(\Delta)$ problem is given by

$$\left[\mathcal{L}_1(0, 0, \partial_y) B_T^{(0)} + \mathcal{L}_2(0, 0, \partial_y) B_X^{(0)} \right] b_0(y) = 0. \tag{3.10.1}$$

Equation (3.10.1) is similar to one that arises for the constant terms in the $O(\Delta^2)$ analysis of the standard problem (see (3.5.28) and (3.6.33)). Equation (3.10.1) has the solution

$$B^{(0)}(X, T, \tau) b_0(y) = B^{(0)}(\xi, \tau) \widetilde{h}(y, 0, n).$$

with $\xi = X - c_G(0, n) T$, as before. Having obtained the form of $B^{(0)} b_0$, we also have that

$$D^{(0)}(X, T, \tau) d_0(y) = B^{(0)}(\xi, \tau) \frac{\mu}{3} \widetilde{\psi}(y, 0, n).$$

Note that in the long wave limit, the phase speed and group speed are equal and no longer depend on k. Therefore the system has become nondispersive.

Now, the $O(\Delta^2)$ problem is given by

$$\begin{aligned} B_\xi^{(1)} \left[-c_G(0, n) \mathcal{L}_1(0, 0, \partial_y) + \mathcal{L}_2(0, 0, \partial_y) \right] b_1(y) \\ = \beta B_\tau^{(0)} \widetilde{h}(y, 0, n) + B^{(0)} B_\xi^{(0)} \phi_B(y), \end{aligned} \tag{3.10.2}$$

where $\phi_B(y)$ is a function of y representing the slow quadratic interactions. As it turns out, ϕ_B is zero for the gently sloping front. This is not surprising since the quadratic terms also cancelled out in the $O(\Delta)$ problem of §3.5. This indicates that in order to examine the long-wave model for the gently sloping front, one must include another large spatial scale to obtain an equation at this order. If this is done, one obtains an evolution equation that is just the limit of (3.5.41) as $k \to 0$ with the appropriate slower time and space variables.

3. ST model

However, in the wedge front model, ϕ_B is not zero. Its form is complicated but it can be calculated numerically (see (A.3.17)). Examining (3.10.2). we see that the operator of the left has the homogeneous solution $\tilde{h}(y, 0, n)$ and therefore the F.A.T. applies. Thus, (3.10.2) has a solution iff

$$\int_0^\infty 2\alpha\kappa(0)\tilde{h}(y, 0, n)\left[\beta B_r^{(0)}\tilde{h}(y, 0, n) + B^{(0)}B_\xi^{(0)}\phi_B(y)\right]dy = 0,$$

which gives the equation

$$B_r^{(0)} = \Phi_B B^{(0)}B_\xi^{(0)},\qquad (3.10.3)$$

where

$$\Phi_B = \int_0^\infty \frac{2\alpha\kappa(0)}{\beta}\phi_B(y)\tilde{h}(y, 0, n)\,dy.\qquad (3.10.4)$$

As expected for this nondispersive model, the equation governing the amplitude is hyperbolic in nature. It should be noted that this equation is a reflection of the connection between the ST model and the uncoupled BCHY model (see (2.4.8) with $\delta = 0$). By examining the long-wave. slow-time limit we have essentially reduced the coupling and the frontal effects in the baroclinic equation thus allowing the β-plane effect to dominate as seen in the BCHY model.

Equation (3.10.3) can be solved using the method of characteristics. and it is well known that if the initial data allow for focusing of these characteristics. shocks will form (see Whitham, 1974). The condition that allows shocks to form in the solution of (3.10.3) is simply that

$$\Phi_B \frac{d}{d\xi}\left(B^{(0)}(\xi, 0)\right) > 0$$

for some ξ. The breaking time, τ_B, is given by

$$\tau_B = \frac{1}{\Phi_B \max\left(\frac{d}{d\xi}\left(B^{(0)}(\xi, 0)\right)\right)}.$$

The breaking time is inversely proportional to Φ_B, which depends on the model parameters. In Figure 3.7, we plot Φ_B versus α/β, for the first meridional mode,

3. ST model
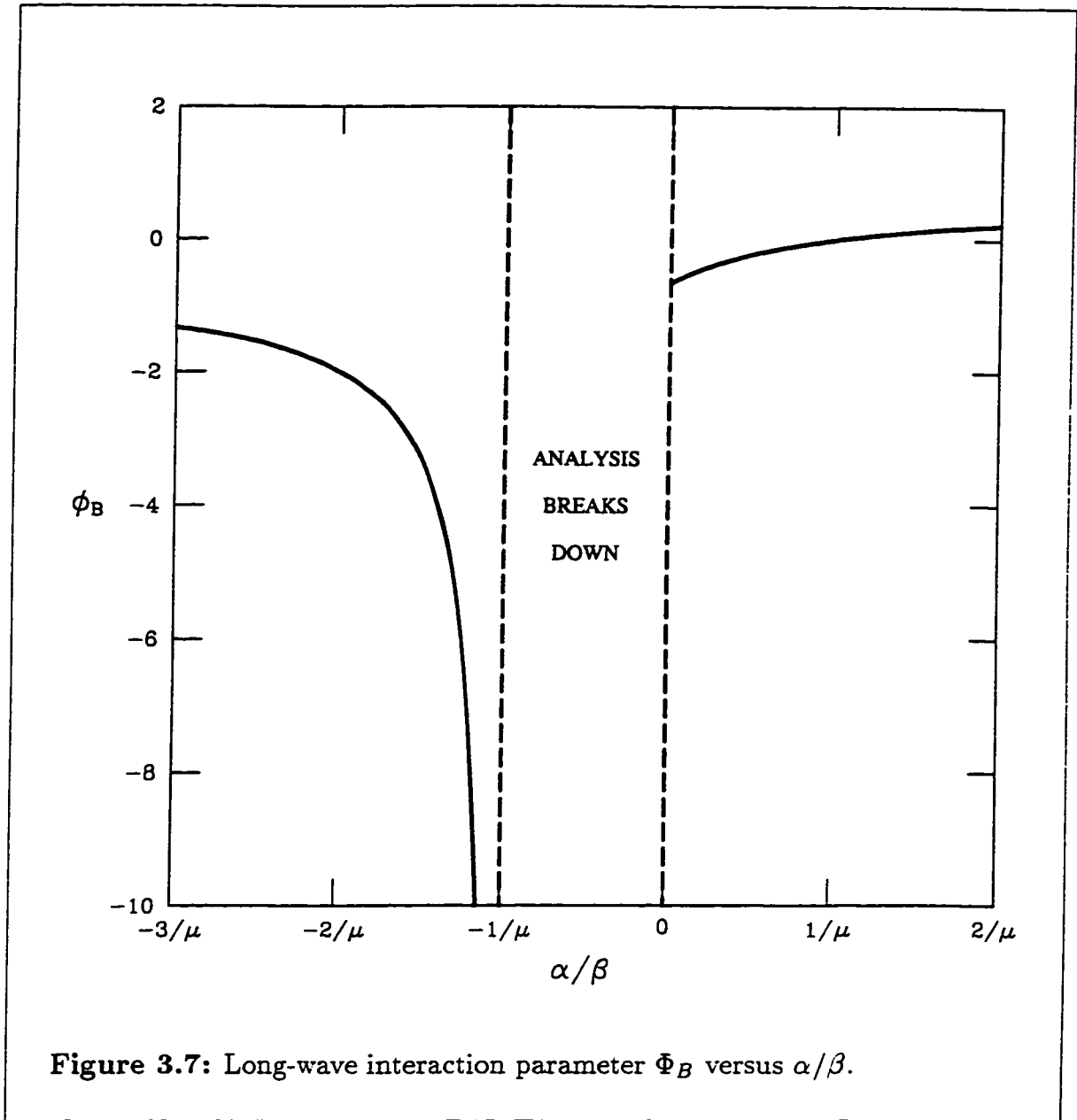
Figure 3.7: Long-wave interaction parameter Φ_B versus α/β.

$n = 0$. It can be seen that for $\alpha/\beta > 0$, $|\Phi_B| < 1$ and so the breaking time is large (assuming a wave with order one slopes). On the other hand, when $\alpha/\beta < 0$, $|\Phi_B|$ becomes large as the parameter values approach the point where $\alpha/\beta = -1/\mu$ and the breaking time becomes small. Thus we expect long waves to break for all parameter values, but generally after a long time. However long waves will break quickly if near the model singular point $\alpha/\beta = -1/\mu$.

The result of this analysis can be interpreted as follows. In the absence of

3. ST model

small-scale variations, large-scale waves will still develop. These waves are hyperbolic in nature and tend to form shocks. Such shocks lead to the formation of a front and small-scale variations that are then governed by the previous analysis. The idea of shocks within the context of PG equations has been examined before (see Dewar, 1992) and is thought to play an important role in frontal formation and thus general circulation.

3.11   Numerical Solutions

In this section, the full nonlinear model is solved using a straightforward numerical scheme. The purpose is to illustrate how the analytical results of §3.2–§3.10 manifest themselves. It is not our goal to provide an extensive investigation into all possible parameter values and frontal geometries. Rather we identify the important aspects of the model, most notably those corresponding to where the analysis of the previous section was successful in predicting behaviour and where it broke down. As well, the complications involved in the weakly nonlinear analysis do not allow for easy visualization of what the solutions entail. Nor is it a trivial task to extend these results beyond their limited, idealized configuration. Numerical solutions allow us to examine some of these difficulties

It should be noted that numerical studies of general geostrophic models including frontal effects have been undertaken previously. In Cushman-Roisin and Tang (1990) the general reduced gravity model is examined and in Tang and Cushman-Roisin (1992) the general two-layer model derived in Cushman-Roisin *et al.* (1992) is examined. Both studies examined general geostrophic models that allow for both FG and QG limits similar to that discussed in Appendix 1. The focus of these studies was geostrophic turbulence and not the evolution of specific fronts under the scaling of a given model. While the results of both studies are restricted to nonoutcropping fronts with a small depth ratio, $\delta \leq 0.1$, their results and analysis provide significant insight and will be commented on as appropriate.

The algorithm we use is straightforward: an explicit, finite difference scheme that is leapfrog in time and central in space. The Jacobian terms are approximated using the Arakawa (1966) scheme. This scheme preserves energy and enstrophy when used to approximate the classic QG equation,

$$q_t + J(\psi, q) = 0,$$

for the potential vorticity q and stream function ψ. Although our equations do not always fit this model, we will use the scheme nonetheless. The simulations are run in a zonally periodic channel. At the channel walls the no normal flow conditions are approximated using one-sided derivatives. The approximation on the channel walls is not sophisticated, rather the geometry of the flow is chosen to limit the effect the channel walls have on its evolution. Again we stress that although boundaries are important in GFD, in our modelling of open ocean fronts with no viscosity, they do not play an important role.

The algorithm is similar to that used in Reszka (1997) and Swaters (1998). with differences made for the different models. We solve the general frontal geostrophic equations, (2.3.13) and (2.3.14), choosing the parameters according to the model we wish to simulate. Equation (2.3.14) is stepped forward in time for all models. Equation (2.3.13) is solved in a manner depending on the model being solved. For the RED model, where the lower layer is motionless. (2.3.13) is not solved and the barotropic stream function is identically set to zero. For the ST and VSE models, where the barotropic relative vorticity terms. $\nabla^2 \psi$. are weak. the equation is solved for ψ_x (see (3.1.2) and (4.1.2)) and then integrated in x. For the SE model the equation is stepped forward in time giving the barotropic relative vorticity. The stream function is then found using a Laplacian inversion scheme. The WVT model is solved in a similar manner except that instead of solving (2.3.13). we solve a vorticity equation (see Appendix 2) to obtain similar results to Reszka (1997).

In the simulations we employ two types of numerical friction. The first eliminates negative values of the frontal height. These values are unphysical, since the frontal height is necessarily a nonnegative quantity. They occur in the numerical simulations due to numerical error. However, when they occur they cause rapid breakdown of the simulation. Why this occurs remains a mystery. The introduction of standard numerical friction schemes was unable to eliminate this breakdown and so whenever a negative value of the frontal height occurs it is simply set to zero. In effect, this is like very small-scale, delta-function friction acting on the scale of the numerical grid itself. We have no justification for this form of friction other than the fact that it works. Work continues on trying to explain why it works and whether it can be replaced by some other standard form of friction. Use of this form of friction does result in a small increase in mass and affects the conservation of the model invariants. Second, we make use of high power harmonic friction to smooth

3. ST model

results near outcroppings. We chose to use $(\nabla^2)^8$ friction. Note that a high power harmonic friction is necessary to overcome the cubic and quartic nonlinearities and the fourth order derivatives found in the model equations.

To obtain results that pertain to the model equations, we choose a very small Rossby number so that only terms that exist in each model contribute to the evolution. This allows us to directly simulate the model evolution and illustrate aspects of the analysis presented. However, by solving the general equation. we can also choose the Rossby number to be more reasonably sized. When we do so, terms that are higher order terms and do not appear in the model equations will have some effect on the evolution. In doing so we hope to illustrate the connections between the models.

The simulations are run using several different basic states chosen to illustrate aspects of the analysis. For all simulations the barotropic flow is initially set to zero. This allows us to concentrate on the baroclinic and frontal processes. In Figure 3.8 we plot several typical fronts and the corresponding zonal velocities as determined by leading-order geostrophic velocity. The first front, Figure 3.8(a), is a coupled front with two outcroppings given by the Gaussian curve

$$h_0(y) = h_{\max} \exp\left[-a^2 y^2\right] . \tag{3.11.1}$$

where $h_{\max}$ and a are the maximum frontal depth and steepness parameter. respectively. The corresponding velocity, Figure 3.8(b), has a jet in both the eastward and westward directions resulting in a strongly sheared flow at the middle of the front. This front allows us to examine the instability associated with the singular point $h_0' = 0$ as well as make comparisons to the experiments of Griffiths *et al.* (1982) and the numerical results of Pavia (1992) and Reszka (1997). The second front, Figure 3.8(c), is a smooth isolated front with the corresponding velocity, Figure 3.8(d), a jet with maximum velocity at the middle of the front. Both eastward and westward jets are considered and fronts with a more abrupt outcropping are also considered. As well, fronts that are nonmonotonic with regions of stronger shear are considered. These fronts most accurately model the open ocean fronts (see Figure 2.1 and Benilov and Reznik, 1996) and coastal currents (see Barth, 1989a and Reszka, 1997), and are used to examine the linear and nonlinear stability aspects of the analysis. The final two fronts are the wedge front, Figure 3.8(e), and the gently sloping front,
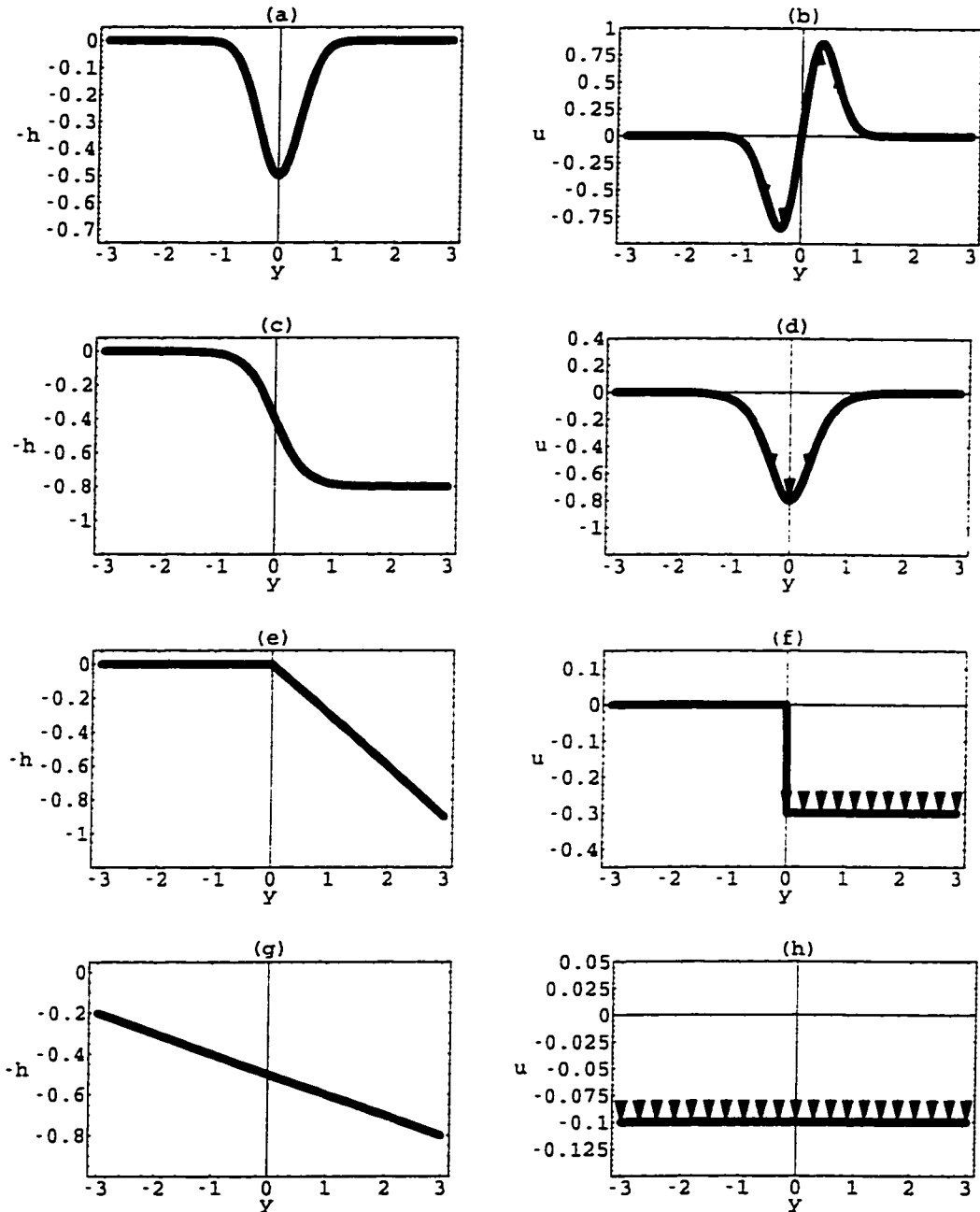
Figure 3.8: The graphs show typical frontal heights (left) and the corresponding zonal velocities (right) used in the numerical simulations. Plots (a) and (b) are for a coupled front, (c) and (d) are for an isolated front, (e) and (f) are for a wedge front, and (g) and (h) are for a gently-sloping front.

3. ST model

Figure 3.8(g), used in the weakly nonlinear analysis. The corresponding velocities, Figure 3.8(f) and (h), are constant flows. These fronts are used to examine the weakly nonlinear analysis and both eastward and westward jets are considered.

For the ST model, it was noted throughout the analysis that it shares a great deal in common with the RED model. Therefore, we present some results for the RED model while referencing the works of Cushman-Roisin, *et al.* (1990), and Pavia (1992) where further simulations were done. The purpose is twofold. The RED model is somewhat easier to run numerical simulations for and therefore allows for a greater variety of simulations to be run and more conclusions made about this form of model. But also, by comparing the simulations of the RED model and the ST we can discern the effect of including the lower-layer dynamics, even in the weak form as they are in the ST model.

We begin by examining the results for the coupled front. In such fronts, when the current is relatively narrow, we expect the instability to be predominantly barotropic, that is, feeding off the horizontal shear in the flow rather than the vertical shear between the layers (Paldor and Killworth, 1987). For this front we present detailed results for the RED model because, as it turns out, the evolution of the front is dominated by unstable growth in the upper layer as a result the strongly sheared flow. The two-layer results for the ST model and the WVT model (see Appendix 2) are small modifications to the RED model simulations and are qualitatively similar.

The standard coupled-front simulation is run using the RED model with $\beta = 1$, $h_{\max} = 0.5$, and $a = 2.0$. The simulation is initialized with a random perturbation of small amplitude, $1 \times 10^{-4} h_0$, added to the basic front (3.11.1). (These are typical of the values used in all the numerical simulations.) As the simulation begins, the perturbations adjust themselves and we see the growth of a wave of wavelength roughly one to one and a half times the width of the current. This wave continues to grow slowly until about $t = 4$. Then a rapid growth occurs and the front breaks up into a series of anticyclonic eddies as shown in Figures 3.9 and 3.10. In the figures, the grey region represents regions where no front exists, where we've chosen $h < 0.02$ to represent no upper layer. (Note that this value is chosen only to make the images clear. After longer periods of time, regions of very small frontal height are diffused by the numerical friction and truly become regions where $h = 0$.) We will not present a detailed analysis of the eddies as this has been done previously (see

3. ST model
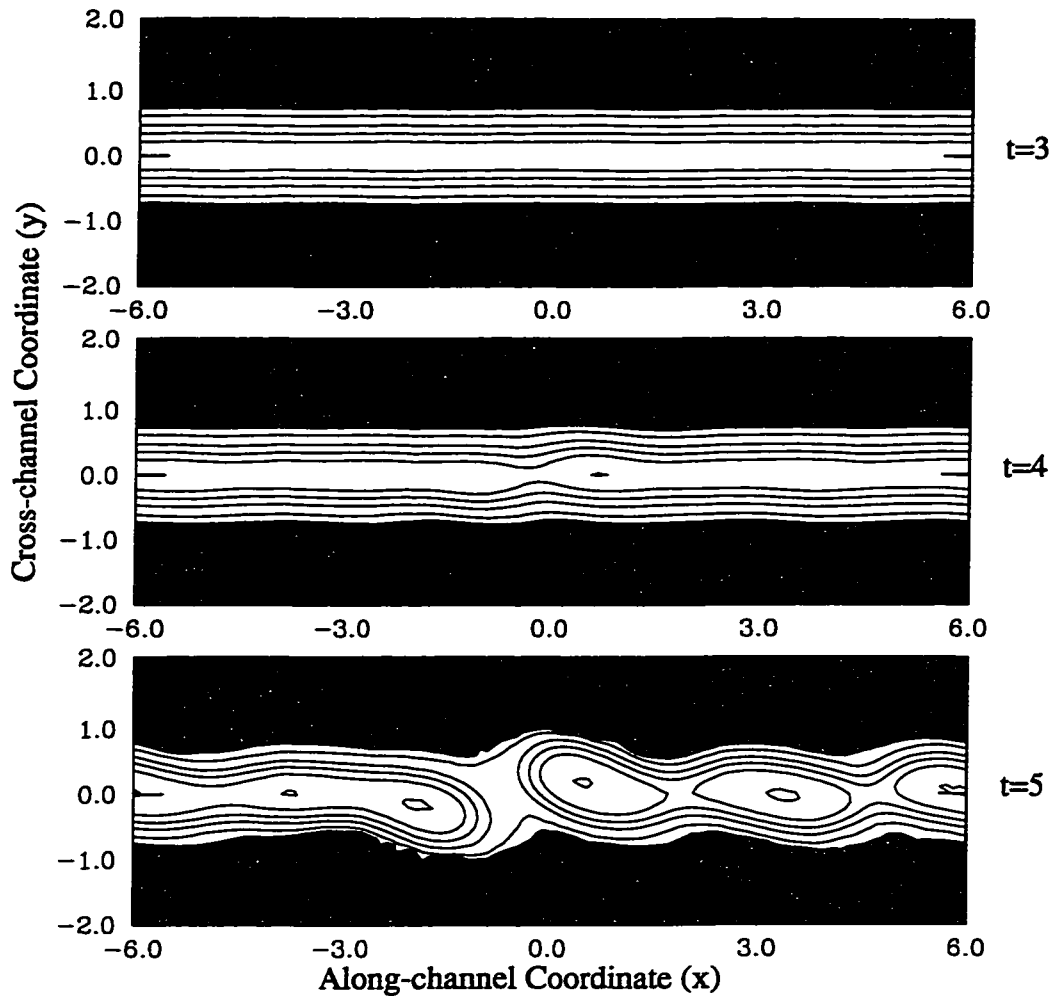
Figure 3.9: Results of the numerical simulation of the RED model coupled-front simulation for t=3–5. The graphs show the contours of the upper-layer height. The grey regions are regions where the upper layer vanishes and the contour interval is 0.1.

Cushman-Roisin, *et al.*, 1990, Chassignet and Cushman-Roisin, 1991, Pavia, 1992, and Cushman-Roisin and Merchant-Both, 1995). We note that they are elliptical in shape and that they rotate clockwise with a period of roughly 8 time units. Note that in Pavia (1992) a zero-PV primitive equation simulation gave very similar results leading to the conclusion that the RED model captures the major physical
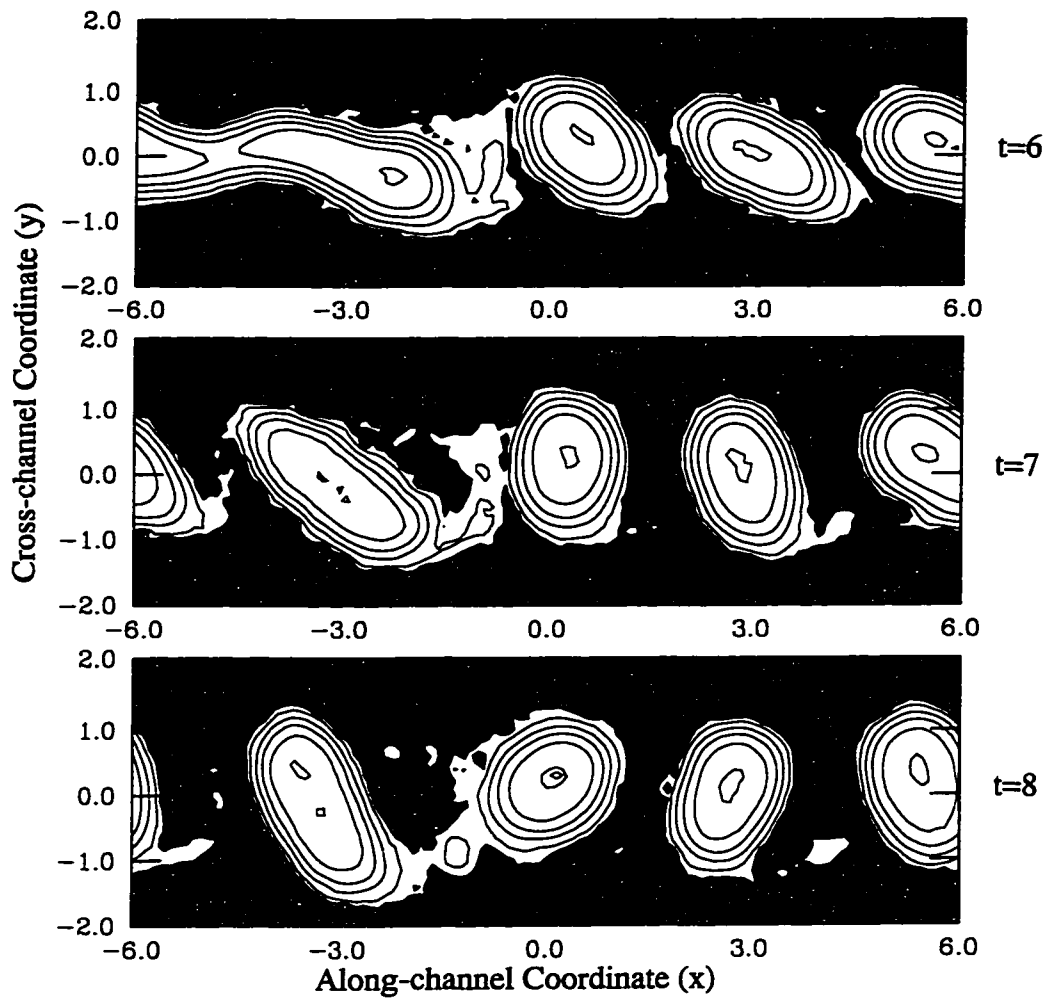
Figure 3.10: Results of the numerical simulation of the RED model coupled-front simulation for t=6–8. The graphs show the contours of the upper-layer height. The grey regions are regions where the upper layer vanishes and the contour interval is 0.1.

processes of the breakup of a coupled front. Note that the prevalence of anticyclones is not restricted to coupled fronts but is a general feature of geostrophic turbulence when scales are beyond the internal deformation radius (Cushman-Roisin and Tang, 1990).

We make one further observation about the eddies. After the eddies have fully

3. ST model
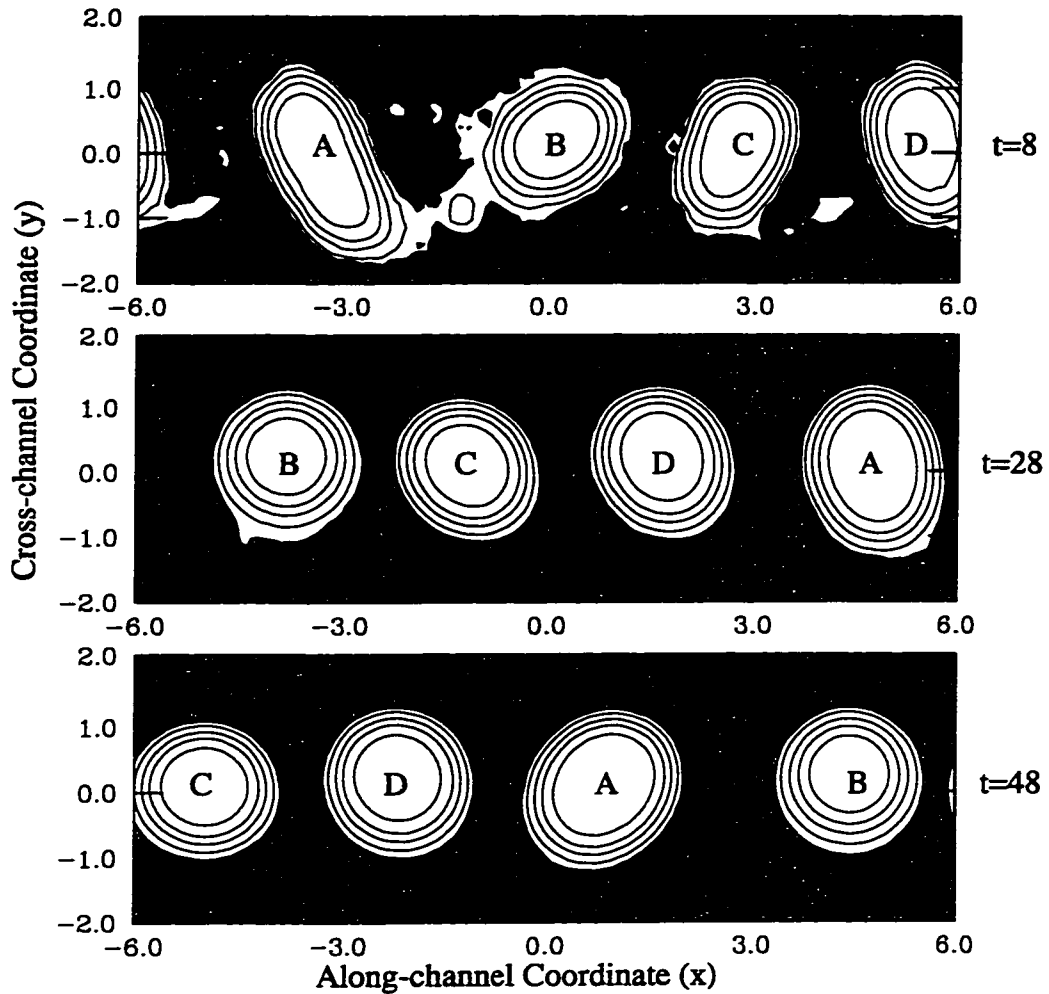
Figure 3.11: Results of the numerical simulation of the RED model coupled-front simulation for t=8–48 as in Figures 3.9 and 3.10. The eddies are labelled so that their westward drift can be observed.

formed, they begin to drift westward with a speed of approximately 0.2 units/time unit. This is illustrated in Figure 3.11 where we plot the eddies at times $t = 8, 28, 48$. We've labelled the eddies so that their drift is obvious as time proceeds. Several other simulations were run, varying the value of the parameter β and it was determined that the eddy drift varies linearly with this parameter and is zero

3. ST model

when $\beta = 0$. This eddy drift was not observed in Pavia (1992) and Reszka (1997) as they worked with f-plane models. (The WVT model has the f-plane RED model as its one-layer limit.) It should be noted that this eddy drift is purely related to the upper-layer dynamics and not a result of coupling to a lower-layer wave since the lower layer is assumed motionless. Eddy propagation is examined for isolated eddies in Cushman-Roisin, *et al.* (1990) where a similar drift rate is observed and a formula is presented for calculating this drift rate. Note that at longer times we see eddy mergers as discussed in Reszka (1997). In fact, the eddy propagation appears to encourage mergers as slight variances in propagation speed increase the chance that eddies come close enough to instigate the merger process.

At this time we introduce several diagnostics that we will use to examine and compare the numerical simulations. We will make use of the pseudo-energy invariants $\mathcal{E}$ found for each model (see §2.7). The conservation of this variable is used to estimate how well simulations are running and gauge the effects of numerical friction and errors. As well, we use it to discuss the energy exchanges that occur as instabilities occur. We also make use of a measure of the integrated, leading-order, baroclinic kinetic energy, $BCKE$, by calculating the quantity

$$BCKE = \iint_{FR} h(1 - \delta h)|\nabla h|^2 \, dx dy, \qquad (3.11.2)$$

and normalizing by its initial value. We will use the analogous definition to measure the barotropic kinetic energy, PKE, when discussing the two-layer models. that is.

$$PKE = \frac{\iint_{\Omega} |\nabla \psi|^2 \, dx dy}{BCKE|_{t=0}}. \qquad (3.11.3)$$

where we have normalized by the baroclinic kinetic energy since in most simulations the initial PKE is zero.

In order to examine the growth of the perturbations and the exchange of energy from the mean zonal flow, we define the mean upper-layer height as the zonal average, that is,

$$\bar{h}(y,t) = \langle h(x,y,t) \rangle = \frac{\int_{x_L}^{x_R} h(x,y,t) \, dx}{x_R - x_L}, \qquad (3.11.4)$$

114

3. ST model

and the perturbation height as

$$\widetilde{h} = h(x,y,t) - \bar{h}(y,t), \tag{3.11.5}$$

where

$$\langle \widetilde{h}(x,y,t) \rangle = 0. \tag{3.11.6}$$

The potential energy given by (2.7.4) is conserved for all models. We can expand the potential energy into mean and perturbation parts

$$
\begin{aligned}
PE &= \frac{1}{2} \iint_\Omega h^2 \, dx dy \\
&= \frac{1}{2} \iint_\Omega \bar{h}^2 \, dx dy + \iint_\Omega \bar{h}\widetilde{h} \, dx dy + \frac{1}{2} \iint_\Omega \widetilde{h}^2 \, dx dy \\
&= \frac{1}{2} \iint_\Omega \bar{h}^2 \, dx dy + \frac{1}{2} \iint_\Omega \widetilde{h}^2 \, dx dy \\
&= \overline{PE} + \widetilde{PE},
\end{aligned}
$$

where the middle term vanishes via (3.11.6). Since the potential energy is conserved, it then follows that

$$\frac{d}{dt}\left(\widetilde{PE}\right) = -\frac{d}{dt}\left(\overline{PE}\right). \tag{3.11.7}$$

Since $\widetilde{PE}$ is a measure of the magnitude of the perturbations, the perturbations can only grow if there is a release of mean potential energy. This is true for all the models studied and stresses the baroclinic nature of the instability. In the plots that follow, we normalize the $\overline{PE}$ and $\widetilde{PE}$ by the initial potential energy. For the baroclinic kinetic energy we make a similar dissection by introducing the mean kinetic energy given by

$$\overline{BCKE} = \frac{\iint_\Omega \bar{h}(1 - \delta\bar{h})|\nabla\bar{h}|^2 \, dx dy}{BCKE|_{t=0}}, \tag{3.11.8}$$

and the perturbation kinetic energy given by

$$\widetilde{BCKE} = \frac{\iint_\Omega h(1 - \delta h)|\nabla\widetilde{h}|^2 \, dx dy}{BCKE|_{t=0}}. \tag{3.11.9}$$

115

Figure 3.12: The potential energy (PE, upper plot) and the baroclinic kinetic energy ($BCKE$, lower plot) for the RED model simulation. The term zonal is used to indicate the mean zonal average, while pert. indicates the perturbation to this average.
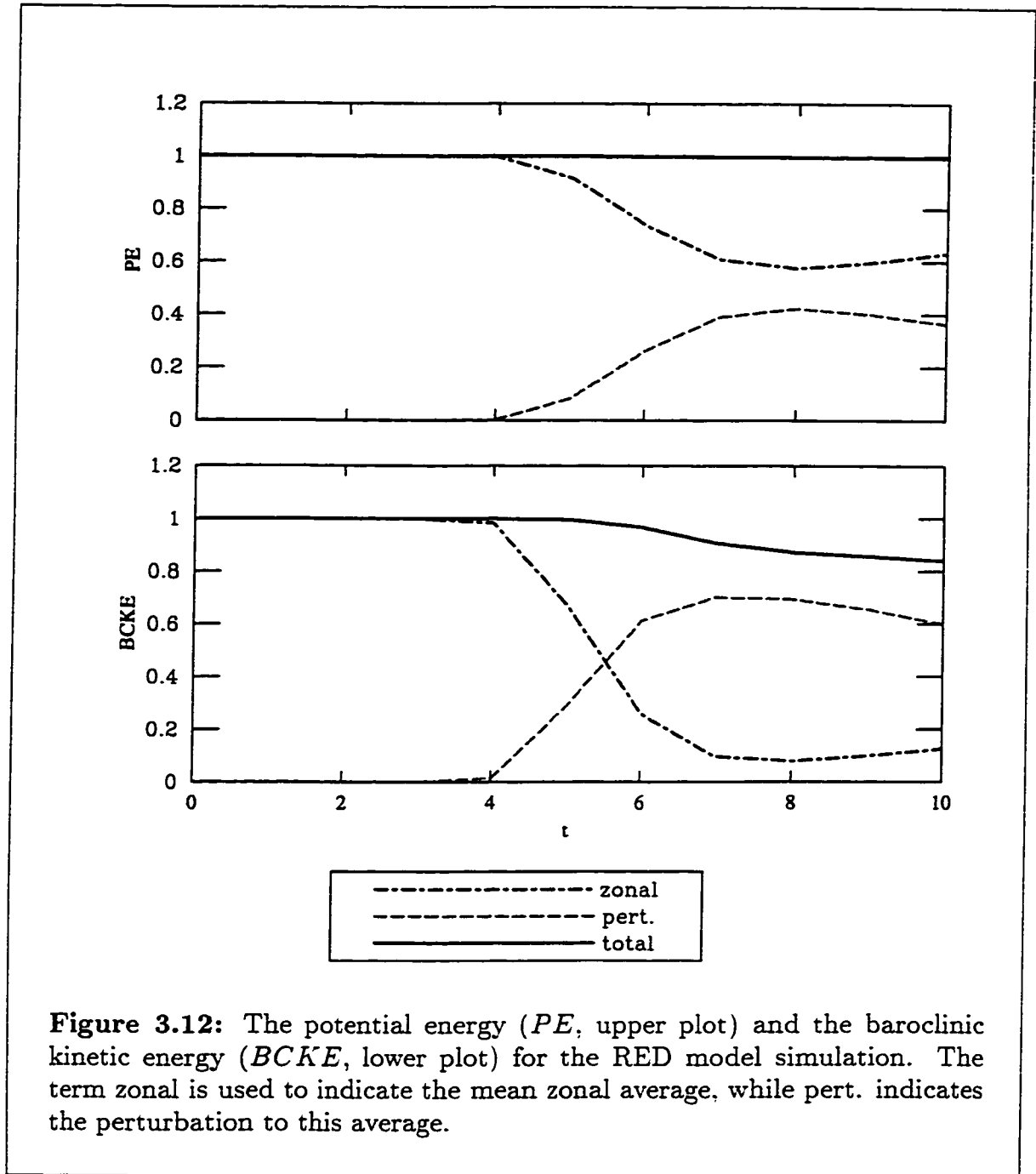
In Figure 3.12, we plot the potential energy (upper plot) and baroclinic kinetic energy (lower plot) for the RED model simulation for t=0–10. The total potential energy is conserved, while as the eddies grow, after $t = 4$, we see a rapid increase in the size of the perturbation PE at the expense of the mean PE as predicted above. Once the eddies have formed a small amount of energy oscillates between

the mean and perturbation PE as the eddies themselves oscillate. The baroclinic kinetic energy decreases very slowly during the initial perturbation growth and then decreases rapidly as the eddies form. This energy release is not feeding the instability but is attributed to small-scale motion and energy loss due to friction that occurs during this period. This is justified by noting that the pseudo-energy $\mathcal{E}$ is not well conserved during the eddy formation, varying up to 15% of its value. This is further verified by examining the f-plane limit where the baroclinic kinetic energy is also the pseudo-energy and is conserved. In these simulations we see the same decrease in $BCKE$. Examining the mean and perturbation $BCKE$ establishes that there is also a release of mean $BCKE$ to the growing perturbations. This energy release reduces the shear in the initial flow, by converting it to the more stable vortical motion of the eddies. The instability can be described as a mixed barotropic-baroclinic instability. Both potential and mean kinetic energy are released from the mean flow, though the PE is an order Rossby number larger in magnitude. Yet, it is an initial release of KE that instigates the instability and this occurs with no lower-layer interaction.

The different simulations for various values of β indicated that energy was being converted into the westward drift of the eddies. The balance in the pseudo-energy $\mathcal{E}$ suggests that $BCKE$ could rise if on average fluid moves northward. Despite a movement of fluid northward, the $BCKE$ is virtually identical in all simulations including that on an f-plane. As a result, $\mathcal{E}$ is not as well conserved as β increases in value. It is postulated that the kinetic energy being converted into the westward drift of the eddies is not included in the leading-order balance seen in $\mathcal{E}$.

In Figure 3.13, we extend the time range for the plots in Figure 3.12. After the eddies have formed, $t = 8$, and they are drifting westward while rotating about their axis, there is a small-amplitude oscillation in the exchange of mean and perturbation energy while the total $BCKE$ remains constant. At $t = 127$, two eddies merge, and again at $t = 150$ two more eddies merge. This merging initiates a much larger oscillation of the mean and perturbation energies. As the oscillation decays, it is observed that the eddy mergers have further increased the perturbation energies at the expense of the mean energies. Note that as eddy mergers occur, we again see a decrease in the total $BCKE$, which we again attribute to the increase in small-scale motions increasing the influence of numerical friction and errors.

3. ST model

Figure 3.13: The potential energy (PE, upper plot) and the baroclinic kinetic energy ($BCKE$, lower plot) for the RED model simulation for longer times. The term zonal is used to indicate the mean zonal average, while pert. indicates the perturbation to this average.
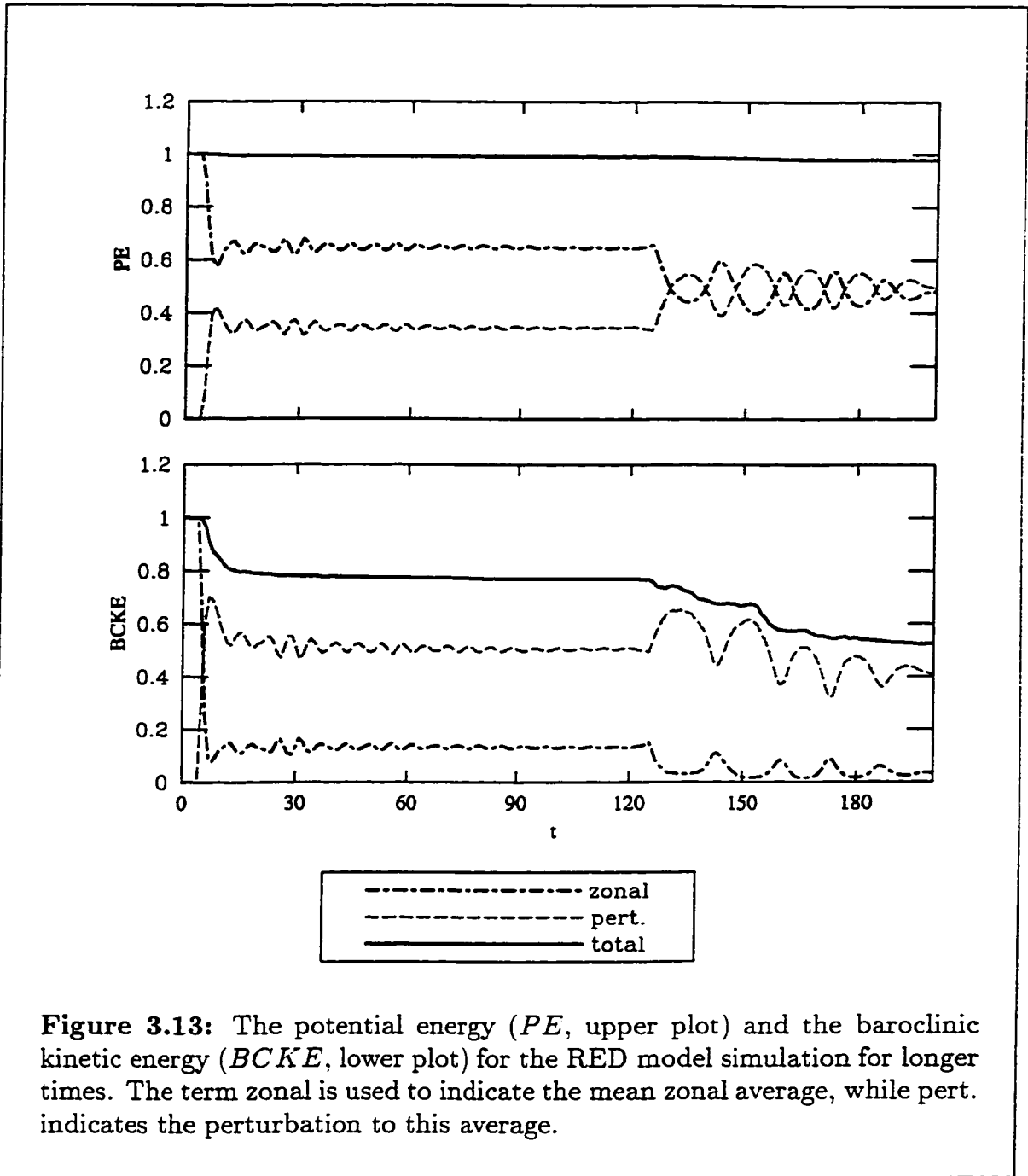
If we repeat this simulation, but use the ST model which includes the diagnostically evolving lower layer, we get very similar results. The instability is virtually identical with the lower layer having little effect. In Figure 3.14, we plot the results for several times that illustrate the development of eddies and the eventual development of corresponding barotropic cells (note the change in the time step for the

Figure 3.14: Results of the numerical simulation of the ST model for the coupled-front simulation. The graphs on the left show the contours of the upper-layer height. The grey regions are regions where the upper layer vanishes and the contour interval is 0.1. The graphs on the right show the contours of the barotropic stream function. The grey regions are regions where the stream function is negative and the contour interval is 0.01.

3. ST model

final two frames). The eddies develop in a similar fashion to the RED model. but the barotropic cells take quite some time to develop.

The addition of the lower layer does have two small effects, first it inhibits the instability and second it reduces the westward drift speed of the eddies after they have formed. Both effects are small and can be attributed to the energy drag that the formation of lower-layer cells requires. Note this result agrees with that of Chassignet and Cushman-Roisin (1991) where the inclusion of a lower layer was seen to have little effect on the propagation of lens-shaped eddies. The energy exchanges are to leading-order equivalent to that found in the RED model. In 3.15. we plot the PE and KE balances compared to the equivalent RED model simulation. It can be seen that the ST model lags the RED model slightly and has an increased KE loss. Both results are attributed to the energy required to form the barotropic cells, show in the KE plot. As time proceeds, the cells form with only a small amount of KE, and all energy balances are virtually identical to that of the RED model.

In examining isolated fronts, we expect that both the RED and ST models will not provide dramatic simulations. The linear analysis (see §3.2) suggests that frontally-trapped waves should develop at an outcropping. In the simulations, frontally-trapped waves do develop (see the final simulation in this section for examples). However, the outcropping appears to reduce their phase speed. and often creates a shear that tends to produce waves that have a small meridional wavelength. As well, the fact that the outcropping involves nonlinear dynamics and small frontal heights increases the effect of numerical errors and friction. These also tend to inhibit the wave structure predicted by linear theory. However. if the frontally trapped wave develops a stable structure in the outcropping regions it does propagate with phase speeds similar to what linear theory prescribes. While this gives some credibility to the linear theory, it is obvious that a better understanding of the form of the wave in the outcropping region is required.

The linear analysis also suggested that eastward flows with an outcropping would allow for the possibility of a continuous spectrum of waves and possible instability if $h_0' = -\beta$. Neither of these features has been observed in the numerical simulations. Eastward and westward flows show similar behaviour. The instability predicted by Benilov (1995a) when $h_0' = -\beta$ is dependent on including QG terms in the model equations and, thus, may be associated with the small-wave instability

3. ST model

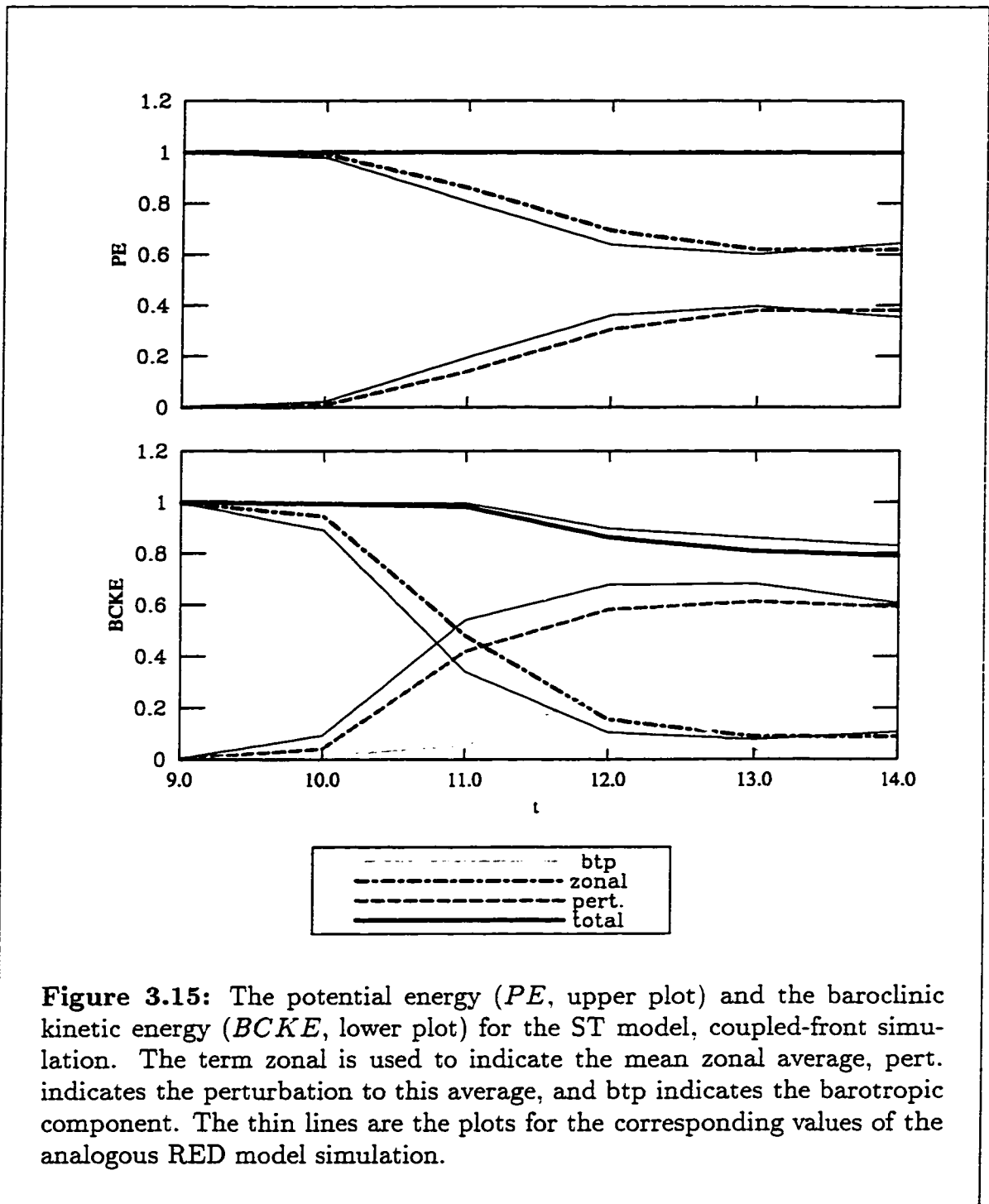**Figure 3.15:** The potential energy (PE, upper plot) and the baroclinic kinetic energy ($BCKE$, lower plot) for the ST model, coupled-front simulation. The term zonal is used to indicate the mean zonal average, pert. indicates the perturbation to this average, and btp indicates the barotropic component. The thin lines are the plots for the corresponding values of the analogous RED model simulation.

discussed in Benilov and Reznik (1996). Including these terms in the full nonlinear simulations changes the structure of the barotropic equation in that it adds the relative vorticity terms found in the SE and WVT models. How these equations should be solved within the scaling of the ST model is continuing work. Note that the instability associated with $h'_0 = 0$ is clearly observed in the coupled-front simulation discussed above.

The finite-amplitude analysis suggests that initial perturbations can reorganize themselves via resonances and BF instability into travelling wave packets. However, this process is slow and takes place over very large scales. The effects of an outcropping, numerical friction, and numerical errors often preclude the visualization of such effects. We illustrate two behaviours that are commonly observed in our simulations. The first is a progression to larger scales. In Figure 3.16. the zonal spectrum for a simulation using the ST model with a basic-state wedge front is presented. In the upper graph all wavenumbers are presented with the darker colours in the graph indicating higher values. In the lower graph the evolution of the amplitude of three waves is presented. The wavenumbers indicate the numbers of waves in the domain. The simulation was initiated with waves of random amplitude and wavenumbers that varied from 2 to 20 waves over the zonal domain (corresponding to wavelengths varying from 30 to 3 units). During the simulation, the size and energy of the perturbation continually decreased. From the spectral plot. it is clear that this decrease occurs dramatically at small scales while larger-scales waves initially increase in amplitude. By the end of this long time simulation. $t = 1000$, the largest waves retain an amplitude almost equivalent to their initial amplitude while all smaller waves have vanished.

The second identifiable finite-amplitude effect is the transfer of energy from a fundamental wave to a resonant long wave. This is clearly demonstrated using a gently-sloping front initiated with a single wave with $k = \ell$, that is, satisfying the resonant condition. This is illustrated in Figure 3.17. The first two plots are contour plots of the perturbation upper-layer depth at $t = 0$ and $t = 150$. Comparing the two indicates that almost all zonal variations have vanished and the meridional variations have shifted to a length scale half that of the original. This is made clear in the final two plots that examine the zonal and meridional spectrums. In the third plot the amplitude of the initial short wave, $k = 4$, and the excited long wave, $k = 0$, are plotted versus time. The initial wave excites the long wave
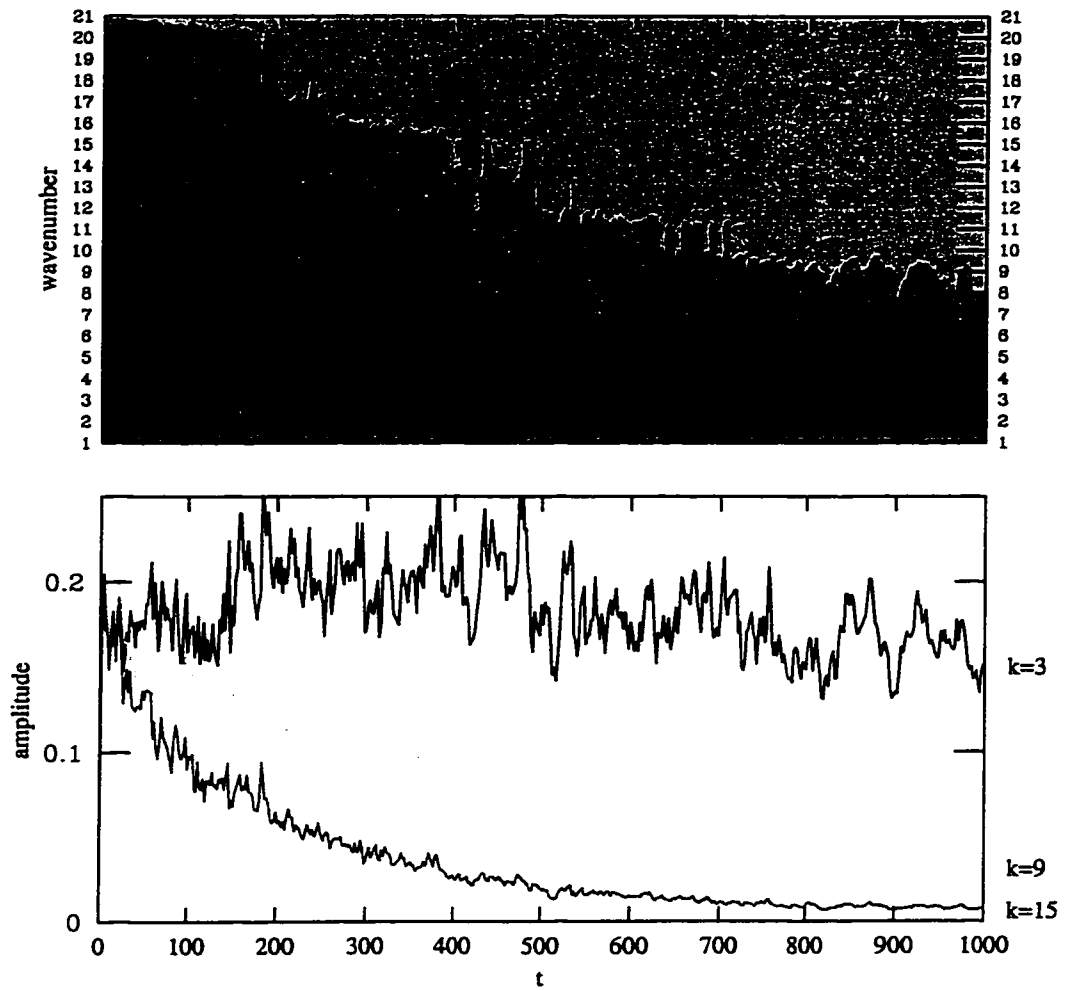
Figure 3.16: The upper graph plots the zonal spectrum for an ST model, wedge-front simulation. Darker colours indicate higher amplitudes of the given wavenumber. The wavenumber indicates the number of waves in the domain. The lower graph plots the time series for three wavenumbers, $k = 3, 9, 15$.

rapidly through long-wave–short-wave resonance and then decays. The long wave is stable and maintains its amplitude. Note that no other waves are excited to any measurable amplitude and that the long wave has a final amplitude approximately one tenth that of the initial short wave. The final plot is of the meridional spectrum for wavenumbers 0–12 and time 0–150. It illustrates that the initial wave, $\ell = 4$, excites many other wavelengths through nonlinear interactions. As time proceeds the amplitude of all the waves decays except the long wave that has half the initial meridional length scale, $\ell = 8$. Thus, the initial wave's amplitude decays, while a long-wave with twice the meridional wavenumber grows to a small amplitude. The final state of this simulation is a perturbation field consisting of alternating zonal jets. Such a final state is predicted in the work of Rhines (1975).

Since we have established that monotonic fronts are stable, one may conclude that the ST model would predict that large-scale, oceanic fronts would show little variation. This is true if the front is always monotonic. However, examinations of fronts often indicate that they are not monotonic and have regions of counter flow leading to a sheared flow (see Figure 2.1, Roden (1975), and Benilov and Reznik (1996)). Given the highly unstable nature of a coupled front, the question of how regions of sheared flow affect an isolated front is interesting. Thus, the final simulation for the ST model is run on an isolated front with a sheared flow that has a small jet of return flow (see Figure 3.18, $t = 0$ for a cross-section of the front).

The results of this simulation are shown in Figures 3.18, 3.19, and 3.20, which plot contours of frontal height and cross sections of zonally averaged height, energy balances, and zonal spectrums, respectively. The shear in the flow allows for unstable growth similar to the coupled-front simulation as seen in Figure 3.18, $t = 26$. This growth occurs at all scales but becomes largest at a wavelength of 3 units (see Figure 3.20). The instability results in a release of zonal $BCKE$ and a corresponding increase in perturbation $BCKE$ but little release in mean PE (see Figure 3.19). After the instability has grown, and the frontal shear has been eliminated, we see the development of frontally-trapped waves (see Figure 3.18). As time proceeds, we begin to see a decay in the small-scale waves (see Figure 3.20). However, the large-scale waves, especially that of wavenumber 4 (wavelength 6 units), decay very slowly and result in a front with large zonal length-scale, small-amplitude meanders (see Figure 3.18, t=66–106, and Figure 3.20). Note that the drop in $BCKE$ in this simulation is balanced by a movement of fluid southward (see Figure 3.18)
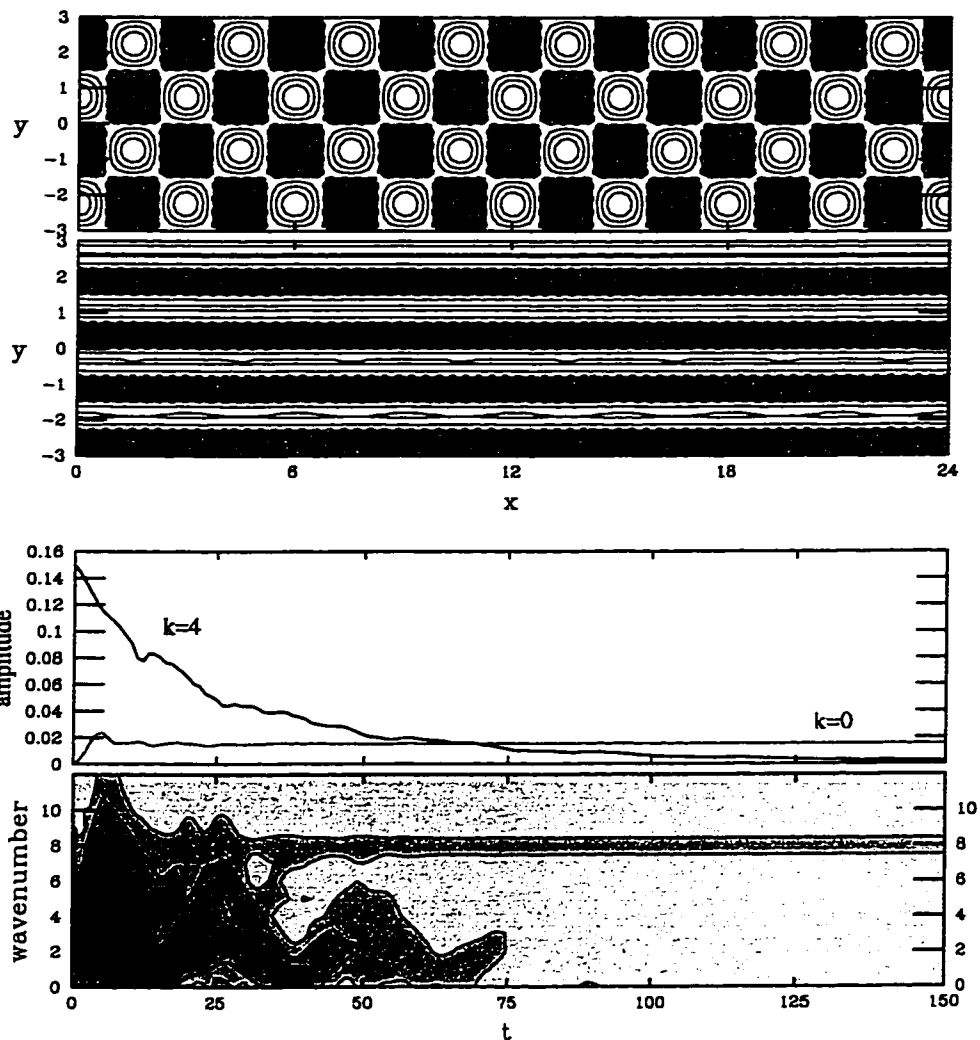
Figure 3.17: Plots illustrating the development of an alternating zonal jet in an ST model simulation. The top plot is a contour plot of the initial perturbation. The second plot is the perturbation upper-layer height at $t = 150$. In both plots, grey regions indicate negative values. The contour intervals are 0.025 and 0.0025, respectively. The third plot shows the evolution of the amplitude initial wave, zonal wavenumber 4, and the long wave, zonal wavenumber 0. The final plot shows the evolution of the meridional spectrum.

3. ST model

as required by the conservation of $\mathcal{E}$. Alternatively, the fact that this flow of fluid south can occur allows a release of $BCKE$, feeding the growth of the instability and the development of the waves. The simulation clearly indicates that meanders can develop and be maintained as a result of a sheared flow with little release of PE.

The evolution of fronts within the ST model is similar to that discussed in Tang and Cushman-Roisin (1992) for scales exceeding the Rhines scale. The Rhines scale is defined as

$$L_{Rh} = \left(R_I^2 L_\beta \frac{\Delta H}{H_1} \right)^{1/3},$$

which, using the definition of the nondimensional parameters in (2.3.7), the definition of the length scales, and that $\Delta H = H_1$ for the FG models, gives that

$$L_{Rh} = \left(\frac{\epsilon}{\epsilon_3} \right)^{1/3} L.$$

Therefore, the length scale of the ST model where $\epsilon \sim \epsilon_3$ is on the order of the Rhines scale. The fact that the β-plane effect is strong at such scales inhibits baroclinic instability, and the evolution is dominated by Rossby wave dispersion. The fact that the model does not contain QG terms removes the possibility that QG effects barotropize the flow as discussed in Tang and Cushman-Roisin (1992). However, we do see a cascade of energy toward large scales as suggested there. It should be noted that while the Rhines scale plays an important role in QG models as the length scale at which energy cascades toward (see discussion in Tang and Cushman-Roisin, 1992), it does not appear to be as important when frontal effects are strong (see discussion in Cushman-Roisin and Tang, 1990 and Tang and Cushman-Roisin, 1992).

3. ST model

Figure 3.18: Results of the numerical simulation of the ST model for an isolated front with shear. The graphs on the left show the contours of the upper-layer height. The grey regions are regions where the upper layer vanishes and the contour interval is 0.1. The plots on the right show the zonally averaged upper-layer height versus y.
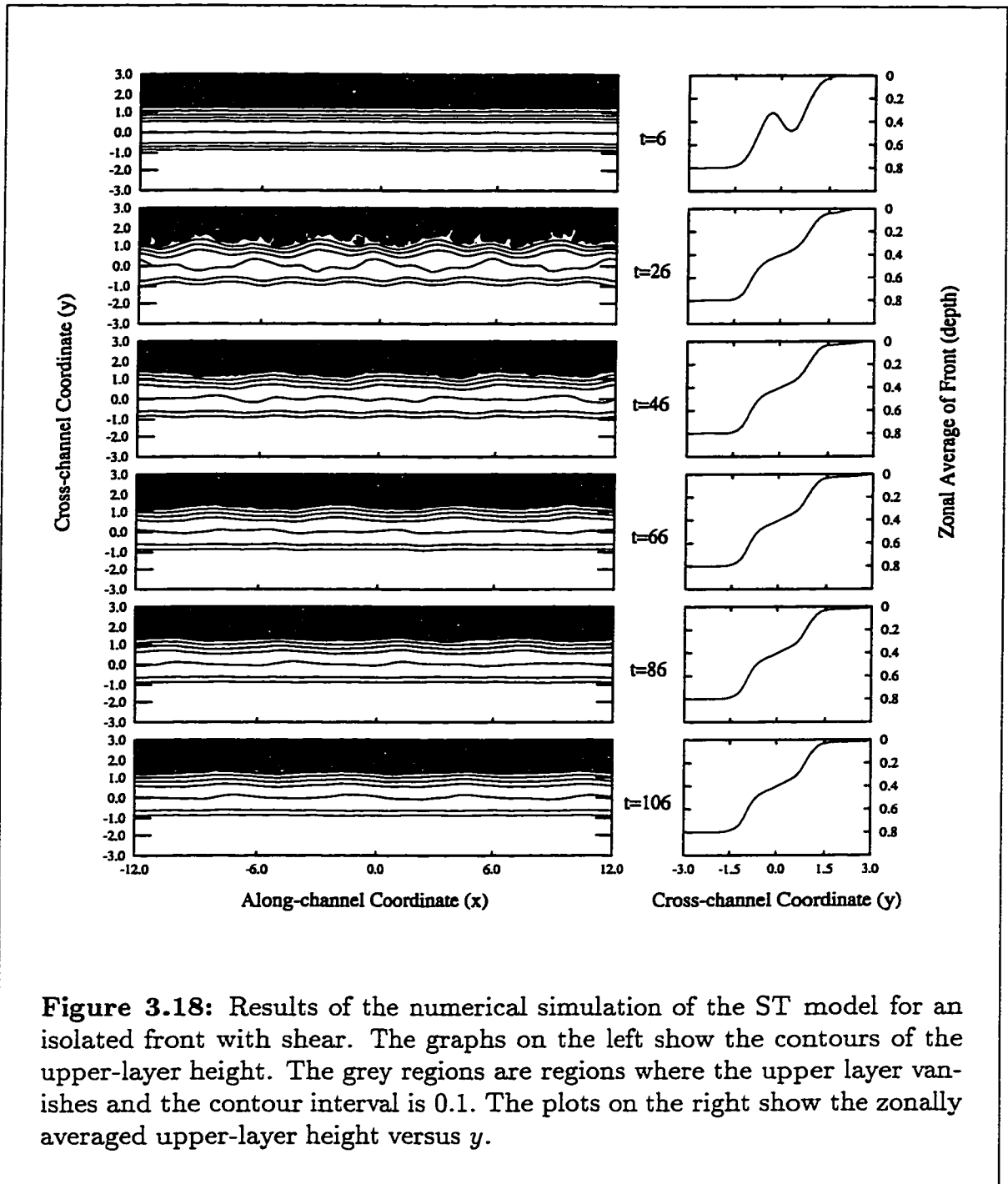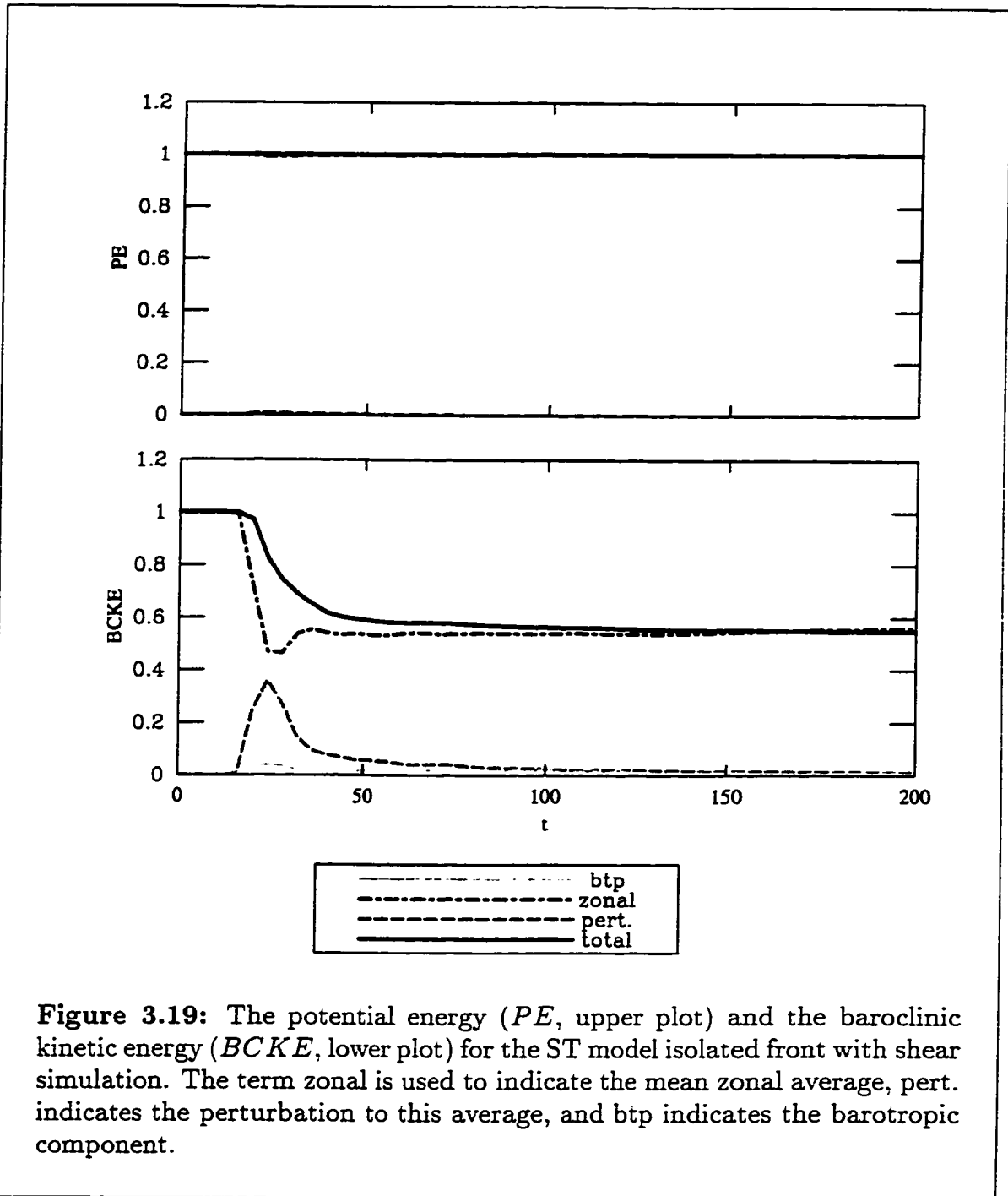
Figure 3.19: The potential energy (PE, upper plot) and the baroclinic kinetic energy ($BCKE$, lower plot) for the ST model isolated front with shear simulation. The term zonal is used to indicate the mean zonal average, pert. indicates the perturbation to this average, and btp indicates the barotropic component.

Figure 3.20: The graph plots the time series for several zonal wavenumbers. The wavenumbers indicate the number of waves in the domain.
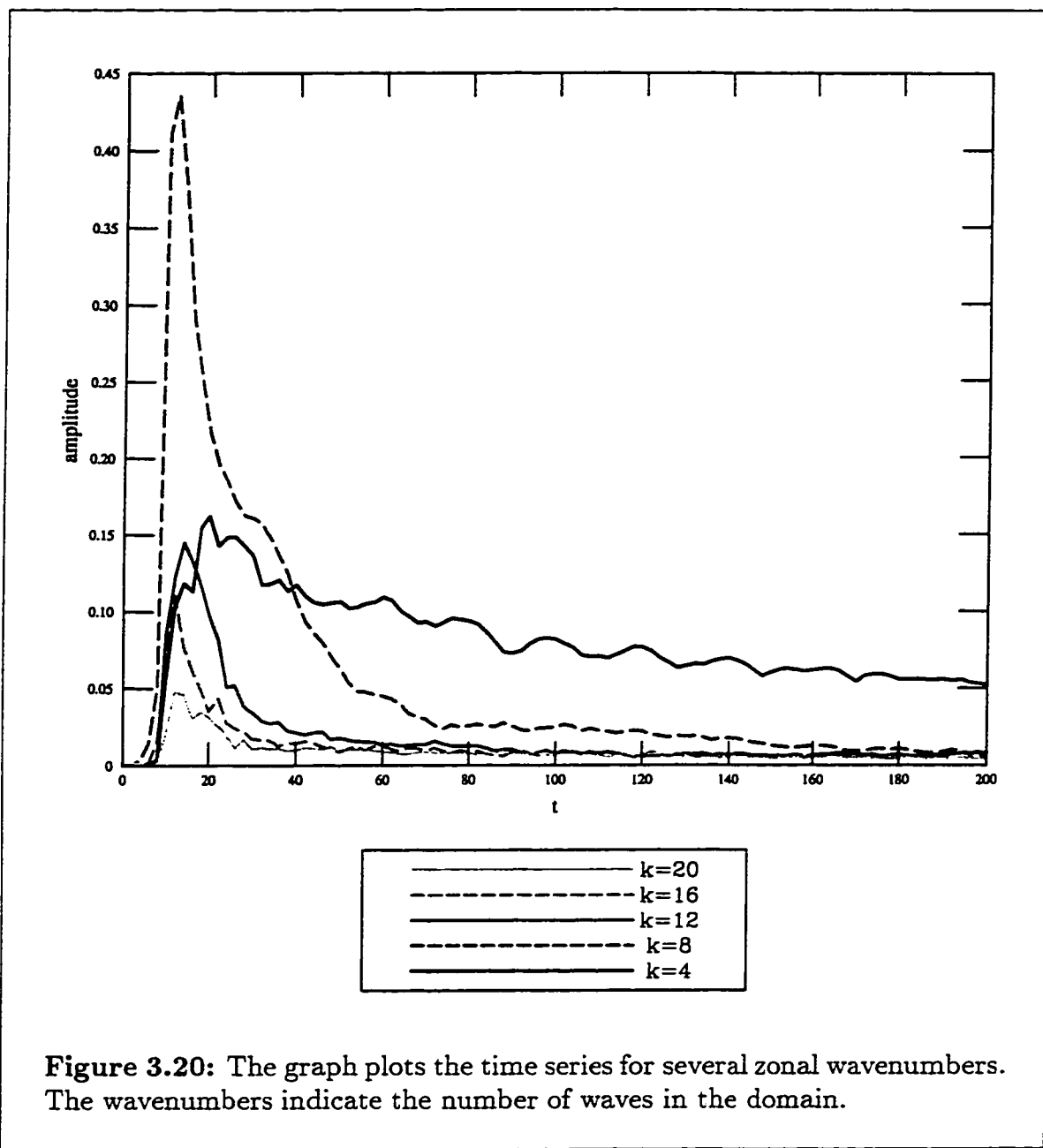
Chapter 4
VSE model

We now discuss the VSE model. The VSE model was first derived in Benilov (1992a) and shares many characteristics with the ST model. Much of the analysis presented in §3 follows similarly and so we will be brief in this section. The VSE model does provide important insight into breaking the restriction of a thin upper layer found in the ST model. By allowing for equal layer depths, a greater scale of vertical motion can be examined. However, this comes at the cost of requiring a large length scale, often so large that spherical coordinates may be required. Thus, the model is not as applicable to open ocean fronts. As well, the model can be described only in the context of baroclinic/barotropic flow and not as a layer model vis à vis Cushman-Roisin *et al.* (1992). This reflects the fact that the model describes the motion of the two layers equally and not of a single active layer coupled to a passive layer.

4.1   Model Equations

The VSE model corresponds to the scaling

$$\delta = \mu, \quad \epsilon_\beta = \beta\epsilon^{\frac{1}{2}}, \quad \epsilon_T = \epsilon_\psi = \epsilon^{\frac{3}{2}}. \tag{4.1.1}$$

and corresponds to a model where the β-plane effect is very strong (VS) and the layer depths are of the same order or equal (E). The equations (2.3.13) and (2.3.14) reduce to

$$\beta\psi_x + \mu J \left[h, h(1 - \mu h)\nabla^2 h + \frac{1}{2}(1 - 2\mu h)|\nabla h|^2 \right] = 0, \tag{4.1.2}$$

$$h_t + J\left(\psi + \beta h(1 - \mu h)y, h\right) = 0. \tag{4.1.3}$$

Note that in comparison to the ST model the nonlinear terms have been dropped in the baroclinic equation (4.1.3) while the $O(1)$ thickness of the upper layer leads to

4. VSE model

quartic nonlinearities in (4.1.2). Once again, when the upper layer vanishes. $h = 0$, the model reduces to the equation

$$\psi_x = 0.$$

As before, this causes difficulties when dealing with regions where the upper layer vanishes and continuity conditions across outcroppings are required. In the limit as μ becomes small. the model does not reduce to the RED model but to the BCHY model discussed in §2.4.

The barotropic stream function is related to the upper-layer depth and the lower-layer pressure by the relation

$$\epsilon^{\frac{1}{2}}\psi = \mu\frac{h^2}{2} + p. \tag{4.1.4}$$

This is an odd relation as all the variables are assumed to be $O(1)$ and it indicates that to leading order the RHS of (4.1.4) must vanish. Thus, the upper-layer depth and lower-layer pressure are strongly coupled. In Benilov (1992a). it is argued that this relation represents a *vertical nonlinear mode*. Because of this peculiarity, this model is difficult to derive without the introduction of the baroclinic and barotropic equations, say using the layer equations (A.1.30. A.1.31) and the corresponding continuity equations. (2.2.15) and its lower-layer analogue.

The potential vorticities for the VSE model are given by using the scaling (4.1.1) in (2.5.5) and (2.5.6) giving

$$
\begin{aligned}
q_1 &= q_1^{(0)} + \epsilon^{\frac{1}{2}}q_1^{(1)} + \epsilon q_1^{(2)} + O(\epsilon^{\frac{3}{2}}) \\
&= \frac{1}{h} + \epsilon^{\frac{1}{2}}\frac{\beta y}{h} + \epsilon\frac{(1-\mu h)\nabla^2 h - \mu|\nabla h|^2}{h} + O(\epsilon^{\frac{3}{2}}),
\end{aligned}
\tag{4.1.5}
$$

$$
\begin{aligned}
q_2 &= q_2^{(0)} + \epsilon^{\frac{1}{2}}q_2^{(1)} + \epsilon q_2^{(2)} + O(\epsilon^{\frac{3}{2}}) \\
&= \frac{1}{1-\mu h} + \epsilon^{\frac{1}{2}}\frac{\beta y}{1-\mu h} - \epsilon\frac{\mu h\nabla^2 h + \mu|\nabla h|^2}{1-\mu h} + O(\epsilon^{\frac{3}{2}}).
\end{aligned}
\tag{4.1.6}
$$

4. VSE model

4.2 Linear Analysis

Substitution of (3.2.1) into (4.1.2) and (4.1.3) gives, after dropping the hats,

$$
\begin{aligned}
\beta\psi_x + \mu\Bigg[& -h_0(1-\mu h_0)h_0'\nabla^2 h_x - (1-2\mu h_0)(h_0')^2 h_{xy} \\
& + (h_0(1-\mu h_0)h_0'')' h_x - 2\mu\left[(h_0 h_0'')' h h_x (h_0')^2 h h_{xy}\right] \\
& - (1-2\mu h_0)h_0'\left(h\nabla^2 + h_x h_{xx} + h_y h_{xy}\right) \\
& + h_0(1-\mu h_0)J\left(h,\nabla^2 h\right) + (1-2\mu h_0)h_0' J\left(h,h_y\right) \\
& - \mu h^2(h_0'\nabla^2 h_x - h_0''' h_x) + (1-2\mu h_0)J\left(h, h\nabla^2 h + \frac{1}{2}|\nabla h|^2\right) \\
& - \mu h J\left(h, h\nabla^2 h + |\nabla h|^2\right)\Bigg] = 0.
\end{aligned}
\tag{4.2.1}
$$

$$
\begin{aligned}
h_t + h_0'\psi_x - \psi_0' h_x + J(\psi,h) & \\
- \beta\left(h_0(1-\mu h_0)h_x + (1-2\mu h_0)h h_x - \mu h^2 h_x\right) & = 0.
\end{aligned}
\tag{4.2.2}
$$

In the following analysis, it is easier to work with these equations if we form the equation that eliminates the linear terms in v by taking $\beta \times (4.2.2) - h_0' \times (4.2.1)$. This gives

$$
\begin{aligned}
\beta h_t + \mu h_0'&\left[h_0(1-\mu h_0)h_0'\nabla^2 h_x + (1-2\mu h_0)(h_0')^2 h_{xy}\right] \\
& - \left[\beta\psi_0' + \beta^2 h_0(1-\mu h_0) + \mu h_0'(h_0(1-\mu h_0)h_0'')'\right]h_x \\
= \quad & -\beta J(\psi,h) + \beta^2\left((1-2\mu h_0)h h_x - \mu h^2 h_x\right) \\
& + \mu h_0'\Bigg[2\mu\left[(h_0 h_0'')' h h_x (h_0')^2 h h_{xy}\right] \\
& + (1-2\mu h_0)h_0'(h\nabla^2 + h_x h_{xx} + h_y h_{xy}) \\
& - h_0(1-\mu h_0)J(h,\nabla^2 h) + (1-2\mu h_0)h_0' J(h,h_y) \\
& + \mu^2 h^2(h_0'\nabla^2 h_x - h_0''' h_x) + 2\mu h_0 J\left(h, h\nabla^2 h + \frac{1}{2}|\nabla h|^2\right) \\
& + \mu h J\left(h, h\nabla^2 h + |\nabla h|^2\right)\Bigg].
\end{aligned}
\tag{4.2.3}
$$

4. VSE model

The linear equations, from (4.2.3) and (4.2.2), are

$$\beta h_t + \mu h_0' \left[h_0(1 - \mu h_0)h_0' \nabla^2 h_x + (1 - 2\mu h_0)(h_0')^2 h_{xy} \right]$$
$$- \left[\beta \psi_0' + \beta^2 h_0(1 - \mu h_0) + \mu h_0'(h_0(1 - \mu h_0)h_0'')' \right] h_x = 0. \tag{4.2.4}$$

$$h_0' \psi_x = -h_t + \left[\psi_0' + \beta h_0(1 - \mu h_0) \right] h_x. \tag{4.2.5}$$

Substitution of (3.2.9) into (4.2.4) and (4.2.5) gives

$$\mu h_0'[h_0(1 - \mu h_0)(h_0'h' - h_0''h)]'$$
$$- [\mu h_0(1 - \mu h_0)h_0'^2 k^2 + \beta(c + \psi_0') + \beta^2 h_0(1 - \mu h_0)]h = 0, \tag{4.2.6}$$

$$h_0'\psi = [c + \psi_0' + \beta h_0(1 - \mu h_0)]h. \tag{4.2.7}$$

with the boundary conditions (3.2.12–3.2.15). The difficulty in dealing with fronts that outcrop rises again. We will use the same approach to this problem as that presented for the ST model in §3.2.

Letting $h(y) = h_0'\eta(y)$ in (4.2.6) gives

$$\mu \left[h_0(1 - \mu h_0)(h_0')^2 \eta' \right]'$$
$$- \left[\mu h_0(1 - \mu h_0)h_0'^2 k^2 + \beta(c + \psi_0') + \beta^2 h_0(1 - \mu h_0) \right] \eta = 0. \tag{4.2.8}$$

Multiplying (4.2.8) by the complex conjugate of η and integrating over $a_1 < y < W_2$ gives, after an integration by parts and use of (3.2.2), (3.2.13), and (3.2.14),

$$\int_{a_1}^{W_2} \left\{ \mu h_0(1 - \mu h_0)(h_0')^2 \left[|\eta'|^2 + k^2 |\eta|^2 \right] \right\} dy$$
$$+ \int_{a_1}^{W_2} \left\{ \left[\beta(c + \psi_0') + \beta^2 h_0(1 - \mu h_0) \right] |\eta|^2 \right\} dy = 0. \tag{4.2.9}$$

The imaginary part of (4.2.9) is given by

$$\beta c_I \int_{a_1}^{W_2} |\eta|^2 dy = 0. \tag{4.2.10}$$

133

4. VSE model

It follows that the integrand in (4.2.10) is strictly positive for nontrivial solutions implying $c_I = 0$ and, therefore, the front is neutrally stable. Since the above analysis formally assumed that $h_0' \neq 0$ over the entire domain, it follows that all monotonic fronts are linearly stable.

In the VSE model, the leading-order potential vorticities in each layer given by (4.1.5) and (4.1.6) have gradients given by

$$(q_1^{(0)})_y = -\frac{h_0'}{h_0^2}, \quad \text{and} \quad (q_2^{(0)})_y = \frac{h_0'}{(1 - \mu h_0)^2}.$$

Flows can become unstable only if these gradients vanish. Once again, this is a much stronger necessary condition for instability than in a QG model where if the PV gradient reverses sign across the layer interface instability is possible. (Note the PV gradient reverses sign across the layer interface for all fronts in the VSE model.) This result is similar to that established for the ST model but now there is only the one singular point when $h_0' = 0$.

Once again, we examine two basic-state fronts for which we will discuss linear solutions: a gently sloping front and a wedge front. For a gently sloping front we consider the basic-state flow (3.2.22) with boundary conditions (3.2.23) and the conditions that the frontal slope, β-plane effect, and frequency are small as given by (3.2.24) and (3.2.25). Then to leading order in Δ, (4.2.6) reduces to

$$\tilde{h}'' - \left[k^2 + \frac{\tilde{\beta}}{\aleph\mu(1 - \aleph\mu)\tilde{a}^2} \left(\tilde{c} + \tilde{\beta}\aleph(1 - \aleph\mu) \right) \right] \tilde{h} = 0. \qquad (4.2.11)$$

In order to satisfy the boundary conditions we assume the perturbations have the form given in (3.2.27). Substitution of (3.2.27) into (4.2.11) gives the dispersion relationship

$$\tilde{c} = -\left[\frac{\aleph\mu(1 - \aleph\mu)\tilde{a}^2(k^2 + \ell^2)}{\tilde{\beta}} + \tilde{\beta}\aleph(1 - \aleph\mu) \right], \qquad (4.2.12)$$

so that the wave is neutrally stable. The group velocity for this solution is given by

$$c_G = -\left[\frac{\aleph\mu(1 - \aleph\mu)\tilde{a}^2(3k^2 + \ell^2)}{\tilde{\beta}} + \tilde{\beta}\aleph(1 - \aleph\mu) \right], \qquad (4.2.13)$$

134

4. VSE model

and the barotropic stream function by

$$\widetilde{\psi} = \frac{\widetilde{c} + \widetilde{\beta}\aleph(1 - \aleph\mu)}{\widetilde{\alpha}}\widetilde{h}.$$ (4.2.14)

Note that if we examine the limit as $\mu \to 0$ we do not get the result of the ST model, but instead get

$$\widetilde{c} = -\aleph\widetilde{\beta}.$$ (4.2.15)

which is the travelling-wave speed of the solution to the hyperbolic system BCHY as $\mu \to 0$ (see (2.4.8)).

We have not been able to find an exact linear solution to the VSE model. But, the similarity of the model to the ST model leads to a solution in the thin layer limit. If we examine the basic-state wedge front flow given by (3.2.32) and (3.2.33), the normal mode equation (4.2.6) reduces to

$$\left[\mu\alpha^3 y(1 - \mu\alpha y)\widetilde{h}'\right]' - \left[\alpha y(1 - \mu\alpha y)(\mu\alpha^2 k^2 + \beta^2) + \beta c\right]\widetilde{h} = 0.$$ (4.2.16)

This equation does not have obvious, simple solutions. However, if $(1 - \mu\alpha y) \doteq 1$ then the equation reduces to one of the form studied in §3.2. Thus, we consider the limit as $\mu \ll 1$, that is, as the upper layer becomes thin. Note that in this limit the VSE model approaches the limit where the ST model is valid, but the models are not identical, as will be seen here in the linear solution. As well, since by definition $\mu \leq \frac{1}{2}$ it is not unreasonable to assume that we can do a perturbation expansion in μ. In order that all other terms remain in the leading-order equation we assume that

$$\beta, c, \psi \simeq \mu^{\frac{1}{2}},$$

and so set

$$(\beta, c, \psi) = (\widetilde{\beta}, \widetilde{c}, \widetilde{\psi})\mu^{\frac{1}{2}}.$$ (4.2.17)

135

4. VSE model

Then (4.2.16) reduces to

$$\left(\alpha^3 y\widetilde{h}'\right)' - \left[\alpha y(\alpha^2 k^2 + \tilde{\beta}^2) + \tilde{\beta}\tilde{c}\right]\widetilde{h}$$
$$= \mu\alpha^2\left[\left(\alpha^4 y^2\widetilde{h}'\right)' - \left(\alpha^2 k^2 + \tilde{\beta}^2\right)y^2\right], \tag{4.2.18}$$

and the relationship for ψ from (4.2.7) is

$$\widetilde{\psi} = \frac{\tilde{c} + \tilde{\beta}\alpha y}{\alpha}\widetilde{h} - \mu\tilde{\beta}\alpha y^2\widetilde{h}. \tag{4.2.19}$$

Now, to leading order in μ we have that

$$y\widetilde{h}'' + \widetilde{h}' - \left[\alpha^2\kappa^2(k)y + \hat{c}\right]\widetilde{h} = 0. \tag{4.2.20}$$

where, now,

$$\kappa(k) = \sqrt{\frac{k^2}{\alpha^2} + \frac{\tilde{\beta}^2}{\alpha^4}}. \tag{4.2.21}$$

$$\hat{c} = \frac{\tilde{\beta}\tilde{c}}{\alpha^3}. \tag{4.2.22}$$

Note that now, as opposed to the analysis for the ST model. κ is always real. The boundary conditions are that h and its y derivative are bounded at $y = 0$ and tend to zero as $\alpha y \to \infty$, and the outcropping position is given by

$$\widetilde{\varphi} = -\frac{\widetilde{h}(0)}{\alpha}.$$

The solution to (4.2.20) that satisfies the boundary conditions is, as found in §3.2,

$$\widetilde{h}(y, k, n) = A\exp(-\alpha\kappa(k)y)L_n(2\alpha\kappa(k)y), \tag{4.2.23}$$

with the corresponding dispersion relationship

$$\frac{\hat{c}}{2\alpha\kappa(k)} + \frac{1}{2} = -n.$$

136

4. VSE model

Rearranging gives that c satisfies

$$\tilde{c}(k,n) = -\frac{\alpha^4 \kappa(k)(2n+1)}{\tilde{\beta}}. \qquad (4.2.24)$$

and the group speed is

$$\tilde{c}_G(k,n) = -\frac{\alpha^2(2n+1)}{\tilde{\beta}} \left(\frac{\alpha^2 \kappa^2(k) + k^2}{\kappa(k)} \right). \qquad (4.2.25)$$

Since κ is real, so is c and all modes are stable. frontally-trapped waves. Once again, in the special case where $\beta = 0$ the model becomes degenerate and wave solutions are not possible. Also note that this solution is only valid under the same assumptions described in the linear solution of the wedge front for the ST model.

Note that the phase speed and group speed for both solutions are always negative and, so. the waves and the energy travel westward regardless of the direction of the basic flow. This is a reflection of the strong influence of the β-plane and the similarity of these waves to westward travelling Rossby waves.

4.3 Nonlinear Invariants and Stability

In this section we discuss nonlinear invariants of the VSE model. Under the VSE scaling, the leading-order term in (2.7.12) is

$$\mathcal{E}_1 = \frac{1}{2}\beta \int\!\!\int_\Omega h^2 y \, dx dy. \qquad (4.3.1)$$

and thus, is an invariant of the flow. This is not an interesting energy invariant since it has no contribution from the kinetic energy. More interesting invariants can be examined by examining the PV invariants. From (2.7.7) and (2.7.8) it follows that the leading-order term in

$$\mathcal{C} = \int\!\!\int_\Omega h\Phi_1(q_1) + (1 - \mu h)\Phi_2(q_2) \, dx dy \qquad (4.3.2)$$

is an invariant of the flow for any smooth functions Φ_1 and Φ_2 with the potential vorticities given by (4.1.5) and (4.1.6). Using the expansions for the PVs given in

137

4. VSE model

(4.1.5) and (4.1.6) we can Taylor expand $\mathfrak{C}$ to get that

$$
\begin{aligned}
\mathfrak{C} = &\iint_\Omega h\Phi_{10} + (1 - \mu h)\Phi_{20}\, dx dy \\
&+ \epsilon^{\frac{1}{2}} \iint_\Omega (\Phi'_{10} + \Phi'_{20})\,\beta y\, dx dy \\
&+ \epsilon \iint_\Omega \Big\{ -\mu(\Phi'_{10} + \Phi'_{20})\left(h\nabla^2 h + |\nabla h|^2\right) \\
&\quad + \Phi'_{10}\nabla^2 h + \frac{1}{2}\left(\frac{\Phi''_{10}}{h} + \frac{\Phi''_{20}}{1 - \mu h}\right)(\beta y)^2 \Big\}\, dx dy + h.o.t.,
\end{aligned}
\tag{4.3.3}
$$

where the subscript 0 on the functions Φ_i and their derivatives indicate that they are evaluated at $q_i = q_i^{(0)}$ and the differentiation of Φ_i is with respect to its argument, that is,

$$
\Phi'_{10} = \frac{d}{d*}\big(\Phi_1(*)\big)\Big|_{*=1/h_0}.
$$

We get the leading-order PV invariant from the first term which. using the leading-order PVs. reduces to

$$
\mathfrak{C}_1 = \iint_{FR} \Phi_1(h)\, dx dy,
\tag{4.3.4}
$$

for any sufficiently smooth function Φ_1 with $\Phi_1(0) = 0$ so that any values associated with the variation of the outcropping are eliminated. This invariant is the leading-order PV invariant for both the upper and lower layers. If we choose the functions Φ to satisfy

$$
h\Phi_{10} + (1 - \mu h)\Phi_{20} = 0,
\tag{4.3.5}
$$

we get the next order PV invariant

$$
\mathfrak{C}_2 = \iint_{FR} \Phi_2(h)y\, dx dy,
\tag{4.3.6}
$$

for any sufficiently smooth function Φ_2 with $\Phi_2(0) = 0$. We recognize now that (4.3.1) is just a special case of this invariant. In order to construct a true pseudo-

138

4. VSE model

energy invariant we consider the expression for the scaled energy (2.7.3)

$$E = \frac{1}{2} \iint_{FR} \left(h^2 + \epsilon h(1 - \mu h)|\nabla h|^2 \right) dxdy + h.o.t. \qquad (4.3.7)$$

Now, in (4.3.3) we choose the functions Φ to satisfy

$$h\Phi_{10} + (1 - \mu h)\Phi_{20} = -\frac{h^2}{2}.$$

$$\Phi'_{10} + \Phi'_{20} = 0.$$

which has the particular solution

$$\Phi_{10} = \Phi_1 \left(\frac{1}{h} \right) = -\frac{h}{2} \left(1 - \frac{\mu h}{3} \right).$$

$$\Phi_{20} = \Phi_2 \left(\frac{1}{1 - \mu h} \right) = -\frac{\mu h^3}{6(1 - \mu h)}.$$

This reduces (4.3.3) to

$$\begin{aligned}
\mathfrak{C}_H = &-\iint_{FR} \frac{h^2}{2} \, dxdy \\
&+ \epsilon \iint_{FR} \frac{h^2}{2} \left(1 - \frac{2\mu h}{3} \right) \nabla^2 h - \frac{h}{\mu}(1 - \mu h) \left(\beta y \right)^2 dxdy.
\end{aligned} \qquad (4.3.8)$$

Adding (4.3.7) and (4.3.8) gives that

$$\mathcal{E} = \iint_{FR} h(1 - \mu h)|\nabla h|^2 + \frac{h^2}{2} \left(1 - \frac{2\mu h}{3} \right) \nabla^2 h - \frac{h}{\mu}(1 - \mu h)(\beta y)^2 dxdy \qquad (4.3.9)$$

is necessarily an invariant of the flow. Integrating the underlined term in (4.3.9) by parts, using the boundary conditions, and multiplying by μ gives that

$$\mathcal{E} = \frac{1}{2} \iint_{FR} \mu h(1 - \mu h)|\nabla h|^2 + h(1 - \mu h)(\beta y)^2 dxdy \qquad (4.3.10)$$

is the pseudo-energy invariant for the VSE model.

As in the ST model, the barotropic momentum function is not of use for the VSE model since an equation for the time evolution of ψ is not specified. Instead

4. VSE model

we again examine the zonal momentum impulse associated with the upper layer given by

$$\mathfrak{M}(h) = \int\int_{FR} yh \, dxdy. \tag{4.3.11}$$

We recognize this as a special case of (4.3.6) and therefore an invariant of the flow.

The nonlinear stability argument presented for the ST model follows accordingly for the VSE mode. The only change is the differing form of $\mathfrak{C}_2$. As such, we present a nonlinear stability theorem without proof. Once again the analysis only holds for fronts that do not outcrop.

The zonal flow $h_0(y)$ is nonlinearly stable in the sense of Liapunov with respect to the perturbation norm

$$||\tilde{h}||^2 = \int\int_{\Omega} \tilde{h}^2 \, dxdy,$$

if there exist real constants A and B such that either

$$0 < A < \Phi_1''(\xi) + y\Phi_2''(\xi) < B < \infty. \quad \forall \quad \xi \geq 0 \quad \text{and} \quad y \in [W_1, W_2], \tag{4.3.12}$$

or

$$-\infty < A < \Phi_1''(\xi) + y\Phi_2''(\xi) < B < 0. \quad \forall \quad \xi \geq 0 \quad \text{and} \quad y \in [W_1, W_2]. \tag{4.3.13}$$

where

$$\Phi_1'(h_0) + y\Phi_2'(h_0) = 0. \tag{4.3.14}$$

As with the ST model, all nonoutcropping, linearly sloping fronts, $h_0(y) = \alpha y + C$, are stable. This can be seen by choosing $\Phi_1'(*) = * - C$ and $\Phi_2'(*) = \alpha$, which satisfies (4.3.14) and gives

$$\Phi_1''(\xi) + y\Phi_2''(\xi) = 1.$$

Hence, (4.3.12) is satisfied and all linearly sloping fronts are nonlinearly stable.

4. VSE model

4.4 Weakly Nonlinear Analysis

In this section, the effects of nonlinear terms in the model are examined. The method and results are very similar to those of §3.5 and. therefore, we will be as brief as possible. Only the differences that arise will be explored in detail. We will examine only the gently sloping front, as the wedge front solution is already an approximation to the ST solution, has the difficulty associated with the outcropping, and does not give insight into the RED model as the ST model does.

To examine the gently sloping front as given by (3.2.22). we introduce the appropriate scalings for α and β as given by (3.2.24) and (3.2.25) dropping the tildes. In order to facilitate a weakly nonlinear analysis. slow space and time variables are introduced through (3.5.1). The perturbations are expanded in a power series given by (3.5.2). As in the linear problem, the boundary conditions reduce to requiring that h and p vanish at $y = 0, L$ at all orders of Δ.

Taking into consideration (3.2.22), (3.5.1). and (3.5.2) the model equations (4.2.3) and (4.2.2) become

$$\mathcal{L}(\partial_t + \Delta\partial_T + \Delta^2\partial_\tau. \partial_x + \Delta\partial_X. \partial_y)\left[h^{(0)} + \Delta h^{(1)} + \Delta^2 h^{(2)}\right]$$
$$= \Delta M_1 + \Delta^2 M_2 + O(\Delta^3),$$
(4.4.1)

$$\left[\psi^{(0)} + \Delta\psi^{(1)} + \Delta^2\psi^{(2)}\right]_x$$
$$= -\frac{\mu}{\beta + \alpha\mu}[\partial_t - \beta\aleph(1 - \aleph\mu)\partial_x]\left[h^{(0)} + \Delta h^{(1)} + \Delta^2 h^{(2)}\right]$$
$$+ \Delta P_1 + \Delta^2 P_2 + O(\Delta^3),$$
(4.4.2)

where the linear operator $\mathcal{L}$ is given by

$$\mathcal{L}(\partial_t, \partial_x, \partial_y) = \beta\partial_t + \aleph\mu(1 - \aleph\mu)\alpha^2\nabla_x^2 - \aleph(1 - \aleph\mu)\beta^2\partial_x,$$
(4.4.3)

and M_i and P_i represent the expansion of the remaining terms. It can clearly be seen that the problem varies only slightly from that given in §3.5. The only change in the linear operator is that (4.4.3) contains the coefficient $(1 - \aleph\mu)$, which tends to one as μ becomes small. If we proceed as in §3.5, we get similar results. As before the linear operator can be expanded in powers of Δ (see 3.5.6). The leading-order problem is simply the linear problem and has the solution given in the previous sections with $h^{(0)}$ and $\psi^{(0)}$ determined by (3.2.27) and (4.2.14), respectively, and the frequency

141

4. VSE model

given by (4.2.12). At the $O(\Delta)$ problem, application of the F.A.T. implies that the wave amplitude travels at the group speed, $c_G(k, \ell)$, given by (4.2.13) and we introduce ξ given by (3.5.21). The $O(\Delta)$ solutions have the form of (3.5.15) and (3.5.23) with

$$
\begin{aligned}
G = &- (1 - 2\aleph\mu) \left(\frac{\alpha^2\mu(k^2 + \ell^2) + \beta^2}{4\ell\alpha\aleph\mu(1 - \aleph\mu)} \right) y(y - L)\cos(\ell y) \\
&+ (1 - 2\aleph\mu) \left(\frac{\alpha^2\mu(k^2 - \ell^2) + \beta^2}{4\ell^2\alpha\aleph\mu(1 - \aleph\mu)} \right) \left(y - \frac{L}{2} \right) \sin(\ell y),
\end{aligned}
\tag{4.4.4}
$$

$$
\begin{aligned}
F = &i\frac{2\aleph\mu(1 - \aleph\mu)\alpha k}{\beta} A_\xi \sin(\ell y) \\
&+ (1 - 2\aleph\mu)(k^2 + \ell^2) \left(\frac{\alpha^2\mu(k^2 + \ell^2) + \beta^2}{4\ell\beta} \right) y(y - L)\cos(\ell y) \\
&- (1 - 2\aleph\mu) \left(\frac{\alpha^2\mu(k^4 - \ell^4) + (k^2 - 3\ell^2)\beta^2}{4\ell^2\beta} \right) \left(y - \frac{L}{2} \right) \sin(\ell y).
\end{aligned}
\tag{4.4.5}
$$

The $O(\Delta^2)$ problem is again very similar. As before we choose Φ and Ψ such that constant terms in the equations vanish. This cannot be done when long-wave–short-wave resonance occurs. that is. when

$$
c_G(k, \ell) = c_G(0, m).
\tag{4.4.6}
$$

Using the form of c_G, (4.4.6) occurs only when $k = \ell$. and is discussed in §4.6. Assuming that $k \neq \ell$ and resonance does not occur. we have the solution

$$
\Phi = \frac{4k^2\ell}{3\alpha(k^2 - \ell^2)}|A|^2 \sin(2\ell y),
\tag{4.4.7}
$$

$$
\Psi = -\frac{2\aleph\mu(1 - \aleph\mu)k^2\ell^2 \left[3k^2 + 5\ell^2 \right]}{3\beta(k^2 - \ell^2)}|A|^2 \sin(2\ell y),
\tag{4.4.8}
$$

where it is clear that this solution is not valid when $k = \ell$.

Finally, as in §3.5, by using the properties of the linear operator, (4.4.3), and applying the F.A.T. to the $\exp[i(kx - \omega t)]$ problem we obtain the amplitude evolution equation

$$
iA_\tau + \lambda A_{\xi\xi} + \Gamma A = \Sigma A|A|^2,
\tag{4.4.9}
$$

142

4. VSE model

where

$$\Sigma = -\frac{2\aleph\mu(1 - \aleph\mu)k^3\ell^2(k^2 - 9\ell^2)}{3\beta(k^2 - \ell^2)},$$ (4.4.10)

$$\lambda = \frac{1}{2}\frac{\partial^2\omega(k,\ell)}{\partial k^2} = -\frac{3\alpha^2\aleph\mu(1 - \aleph\mu)k}{\beta}.$$ (4.4.11)

$$\Gamma = -\frac{2}{L\beta}\int_0^L \gamma(y)\widetilde{h}(y,\ell)\,dy.$$ (4.4.12)

with

$$\begin{aligned}
\gamma(y) =&\, k\alpha^3\mu(1 - 2\aleph\mu)\left[\left(y - \frac{L}{2}\right)\left(G'' - (k^2 + \frac{\beta^2}{\alpha^2})G\right) + G'\right] \\
&- 2\alpha^4\mu^2 k\ell\left(y - \frac{L}{2}\right)\cos(\ell y) \\
&+ \alpha^4\mu^2 k\ell(k^2 + \ell^2 + \frac{\beta^2}{\alpha^2})k\ell\left(y - \frac{L}{2}\right)^2\sin(\ell y).
\end{aligned}$$ (4.4.13)

4.5 Solutions to the Amplitude Equation

The NLS equation governing the evolution of the envelope of the linear solutions, $A(\xi,\tau)$, is identical to that found in §3.5 and the analysis found in §3.7 applies. As before, we use the definition of λ and Σ, as given by (4.4.12) and (4.4.10), to plot the regions in which BF instability occurs. By (4.4.12), λ is always negative, and therefore BF instability occurs when $\Sigma > 0$ (see (3.7.4)). The critical value of k for which the sign of Σ changes is

$$k_c^2 = 9\ell^2.$$ (4.5.1)

Thus the regions of stability/instability are easily defined. For $\ell < k < 3\ell$, $\Sigma < 0$ and the wavetrain is stable. For $k < \ell$ or $k > 3\ell$, $\Sigma > 0$ and the wavetrain is subject to BF instability. In Figure 4.1, we plot the contours of the maximum growth rate (see (3.7.5)) in the $\rho - k/\ell$ plane. The grey regions are regions of unstable growth, the darker the grey the higher the growth rate, and the white region is stable. The dashed line marks the singularity that occurs at $\alpha = 0$. We have BF instability for $k < \ell$ with an increasing growth rate as $k \to \ell$, i.e., as resonance occurs, stability

143
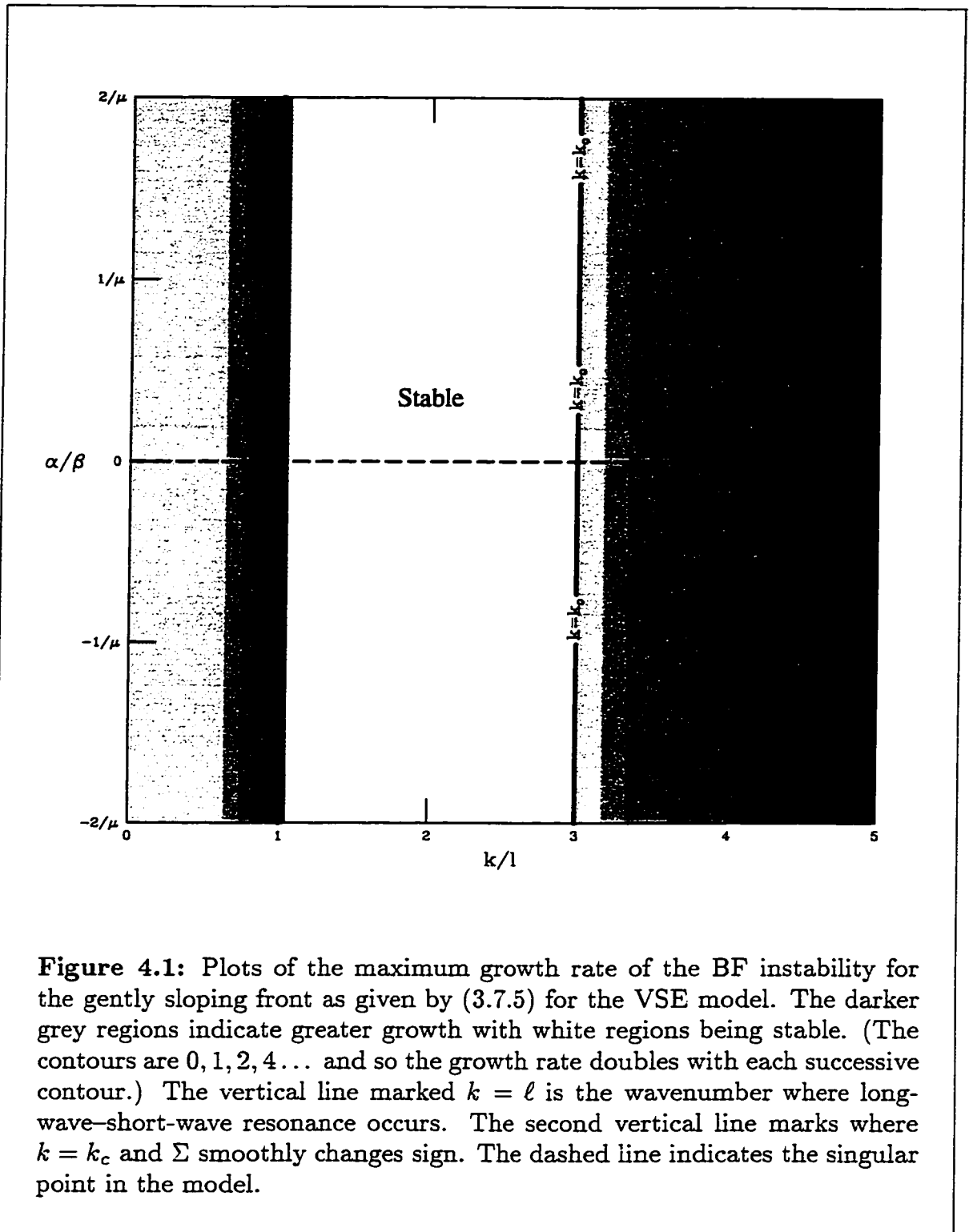
4. VSE model

Figure 4.1: Plots of the maximum growth rate of the BF instability for the gently sloping front as given by (3.7.5) for the VSE model. The darker grey regions indicate greater growth with white regions being stable. (The contours are $0, 1, 2, 4 \ldots$ and so the growth rate doubles with each successive contour.) The vertical line marked $k = \ell$ is the wavenumber where long-wave–short-wave resonance occurs. The second vertical line marks where $k = k_c$ and Σ smoothly changes sign. The dashed line indicates the singular point in the model.

144

4. VSE model

for $\ell < k < 3\ell$, and instability for $k > 3\ell$, with an increasing growth rate with decreasing length scales. Note that this situation is exactly that predicted by the ST model in the limit as $\mu \to \infty$ (see Figure 3.1 and the discussion in §3.7). We therefore conclude that although the models differ, the specific form of the gently sloping front solution eliminates these differences in this analysis. The travelling wave solutions discussed in §3.7 apply here as well.

4.6 Long-wave–short-wave Resonance

As for the ST model, long-wave–short-wave resonance is extremely important in understanding the weakly nonlinear evolution of the VSE model. The Benjamin-Feir instability analysis suggests that this resonance is the source of large unstable growth. As before. the resonance occurs when a mean-flow mode or long-wave mode is a solution to the first order slow problem with a phase speed and group speed equal to that of the group speed of the fundamental.

If we carry out the analysis found in §3.8 for the VSE model we once again obtain equations (3.8.7) and (3.8.9) with

$$\Phi_1 = 2k\ell\aleph\mu(1 - \aleph\mu)(3\ell^2 - k^2), \tag{4.6.1}$$

$$\Phi_2 = 4k^2\ell\aleph\mu(1 - \aleph\mu). \tag{4.6.2}$$

Once again the constant amplitude solution is subject to BF instability and these results can be used to explain the discontinuous results of the previous section. The analogue of Figure 3.5 for the VSE model is shown in Figure 4.2. Once again, we assume that the long-wave–short-wave resonance dominates the flow for $k < k_c$ and that BF instability applies for $k > k_c$ where k_c is given by (4.5.1). Comparing 4.2 to Figure 4.1 we find that the growth rates at smaller scales are more significant, the region of stability has been diminished, and the discontinuity across $k = \ell$ removed. Only the singular point $\rho = 0$ causes difficulty. Still, at large wavenumbers (small wavelengths) the growth rate of the BF instability becomes comparable to and eventually exceeds the growth rate associated with the long-wave–short-wave resonance. The travelling wave solutions discussed in §3.8 apply here as well.

Figure 4.2: Contour plots of the maximum growth rate expected when both the effects of the long-wave–short-wave resonance and BF instabilities are considered. White regions are stable while darker grey indicates higher growth rate. The contour level is 0.05.
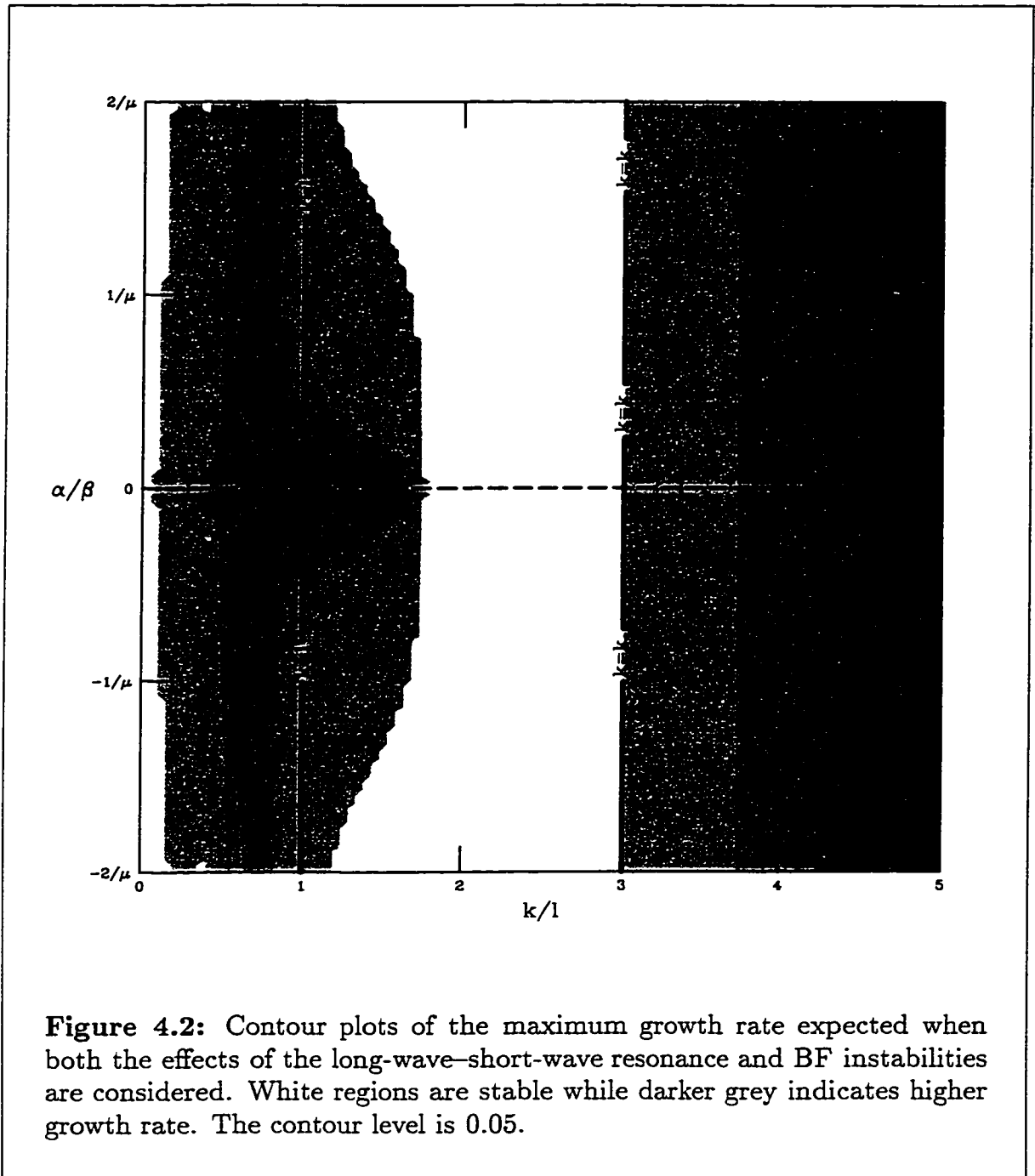
4. VSE model

4.7 Numerical Solutions

In this section, the full nonlinear model is solved using the numerical scheme discussed in §3.11. We first repeat the analysis for the coupled front (3.11.1). For the VSE model the reduced gravity dynamics are not those of the RED model but the BCHY model. We therefore expect different results from those for the ST model. In Figure 4.3, we plot the results of the simulation showing the contour plots of both the upper-layer depth (the baroclinic stream function) and the barotropic stream function. As predicted the results are different from the ST model. Unstable growth occurs as before with small waves developing, growing large, and eventually coupling the outcroppings to begin the formation of eddies. But, as the eddies form they take an odd shape, pointed at the western tip and rounded at the rear, as fluid appears to pile up on itself eventually leading to the development of two circular eddies. This can be explained as a result of the hyperbolic nature of the reduced model. The phase speed in the hyperbolic model is inversely proportional to the fluid depth. Therefore, near the head of the forming eddy the disturbances are travelling slower than those in the fluid behind it, thus the fluid piles up on itself to form the eddy. In the ST and RED model, the nonlinear Jacobian terms counteract this process producing the oval eddies seen there. The barotropic stream function develops clear dipolar cells corresponding to each eddy. Note that while the nondimensional time of eddy formation is roughly three to four times that seen in the ST model, the dimensional times are comparable. Also, once the circular eddies have formed, they drift westward as in the ST and RED models. This emphasizes that the nonlinear Jacobian terms play little role in the eddy drift and that the drift is a result of the β-plane term.

If we plot the energy balances (see §3.11 for definitions) we find that the instability does release mean PE and baroclinic KE as found previously. However, now the growth of the instability is accompanied by an increase in total $BCKE$. This is possible as the energy balance in the pseudo-energy $\mathcal{E}$ given by (4.3.10) allows for an increase in $BCKE$ if upper-layer fluid spreads outward from $y = 0$. This occurs as the eddies form, and results in the increase in $BCKE$. We see a release of mean $BCKE$ and an increase in perturbation $BCKE$ as the shear in the flow is reduced. Once the eddies have formed, friction and numerical error dissipate some of the energy. The energy transfer to the barotropic cells is greater than that seen in the ST model as the coupling between the barotropic and baroclinic flow is

4. VSE model
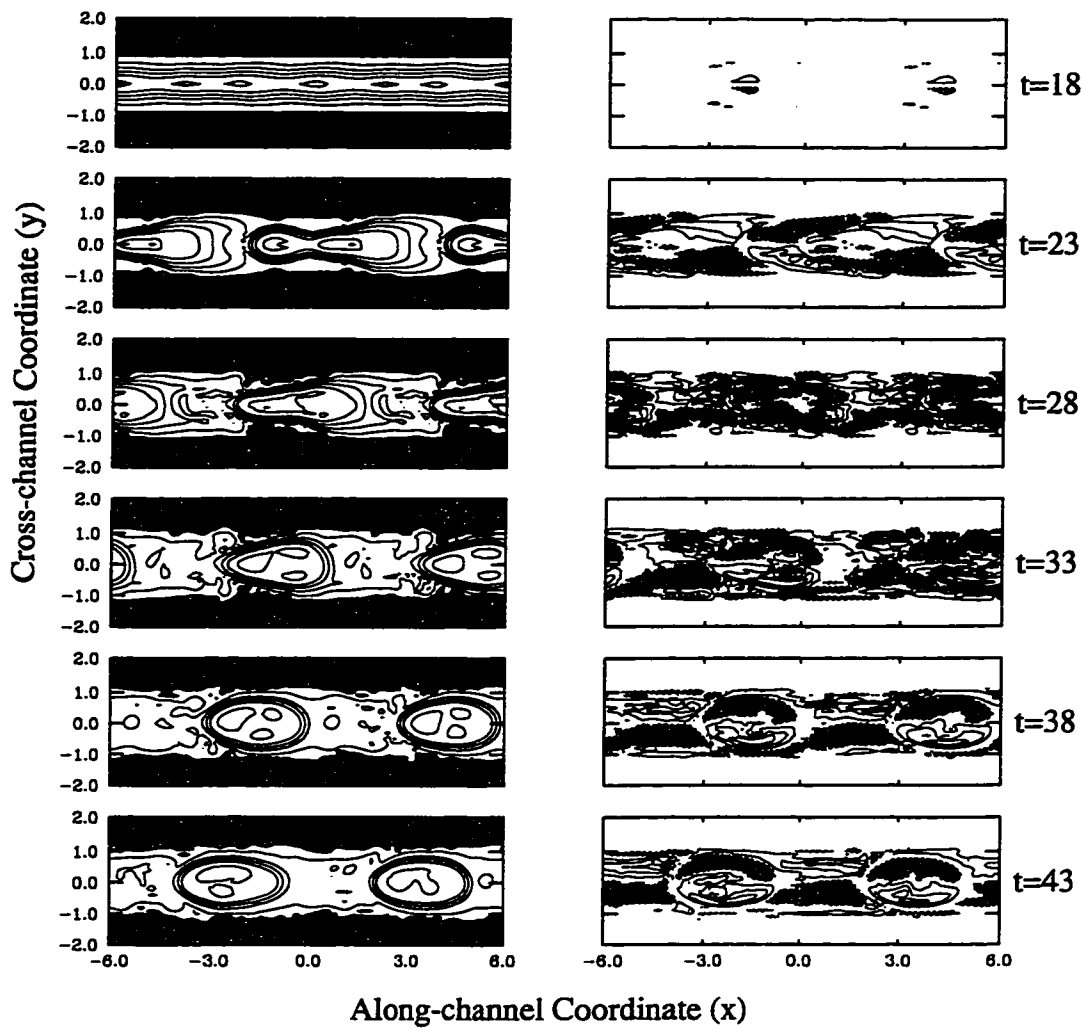
Figure 4.3: Results of the numerical simulation of the VSE model coupled-front simulation for t=18–43. The plots on the left show the contours of the upper-layer height. The grey regions are regions where the upper layer vanishes and the contour interval is 0.1. The plots on the right show the contours of the barotropic stream function. The grey regions are regions where the stream function is negative and the contour interval is 0.1.

148

4. VSE model

Figure 4.4: The potential energy (PE, upper plot) and the baroclinic kinetic energy ($BCKE$, lower plot) for the VSE model simulation. The term zonal is used to indicate the mean zonal average, pert. indicates the perturbation to this average, and btp indicates the barotropic component.
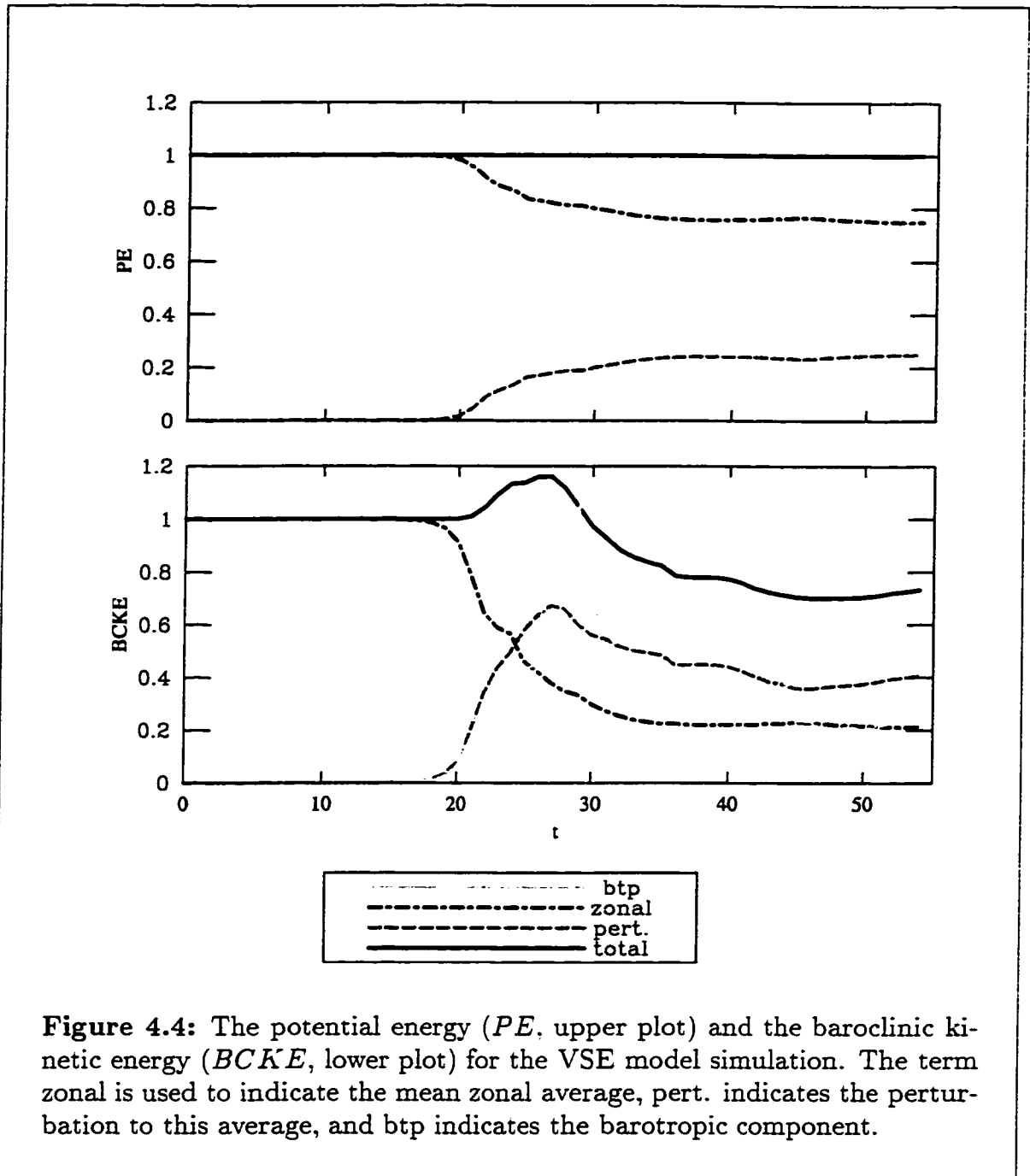
stronger.

For the VSE model, monotonic fronts are linearly stable. This result carries over to the numerical results. Monotonic fronts, even those with outcroppings, do not show unstable growth and initial perturbations are diffused away by the numerical friction especially near outcroppings. As for the ST model, we ran simulations

4. VSE model

that illustrated the decay of small waves and the formation of long waves. We do not include these simulations here as the long space and time scales they involve may be unphysical. Instead, we repeat the final simulation run for the ST model that includes the effects of shear.

The results of a simulation for an isolated front with shear are shown in Figures 4.5, 4.6, and 4.7, which plot contours of frontal height and cross-sections of zonally averaged height, energy balances, and zonal spectra, respectively. Again, the shear results in the growth of an instability. This instability develops slower than for the ST model (in nondimensional units) and persists for some time (see Figure 4.5, $t = 26, 46$). The instability is driven by release of KE not PE (see Figure 4.6). The instability develops at all scales, but energy is quickly transferred to the largest scales, and then all scales decay (see Figure 4.7). The long-waves are not as robust as those seen in the ST model and the front returns to a stable configuration (see Figure 4.5). Once again there is a movement of fluid southward. However, this alone does not allow for a release of $BCKE$ as in the ST model. Examining the pseudo-energy $\mathcal{E}$, (4.3.10), we see that a release of $BCKE$ can only occur if $h(1 - \delta h)$ increases. Thus, while the initial instability grows, we see the front flatten out the shear (see Figure 4.5, $t = 26, 46$). Up to this point $\mathcal{E}$ is conserved very well. During the rest of the simulation the continued decrease in $BCKE$ is not accompanied by an equivalent increase in the second term of $\mathcal{E}$, in fact this term decreases. We attribute this second phase, which results in the decay of small-scale motions, as being dominated by small-scale processes, numerical friction, and error, resulting in a smoothing of the front.
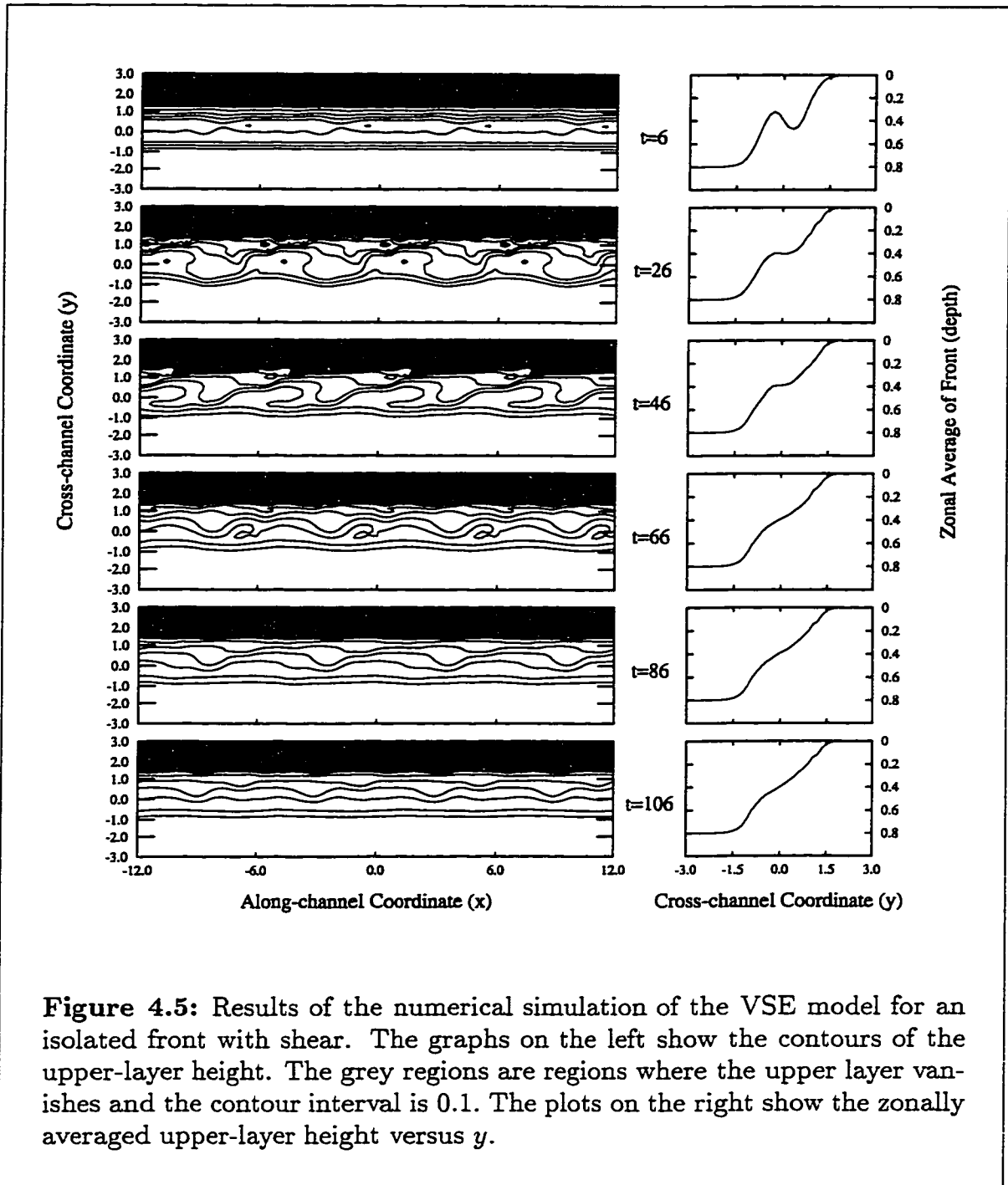
150

4. VSE model

Figure 4.5: Results of the numerical simulation of the VSE model for an isolated front with shear. The graphs on the left show the contours of the upper-layer height. The grey regions are regions where the upper layer vanishes and the contour interval is 0.1. The plots on the right show the zonally averaged upper-layer height versus y.

Figure 4.6: The potential energy (PE, upper plot) and the baroclinic kinetic energy ($BCKE$, lower plot) for the VSE model for an isolated front with shear. The term zonal is used to indicate the mean zonal average, pert. indicates the perturbation to this average, and btp indicates the barotropic component.

Figure 4.7: The graph plots the time series for several zonal wavenumbers. The wavenumbers indicate the number of waves in the domain.
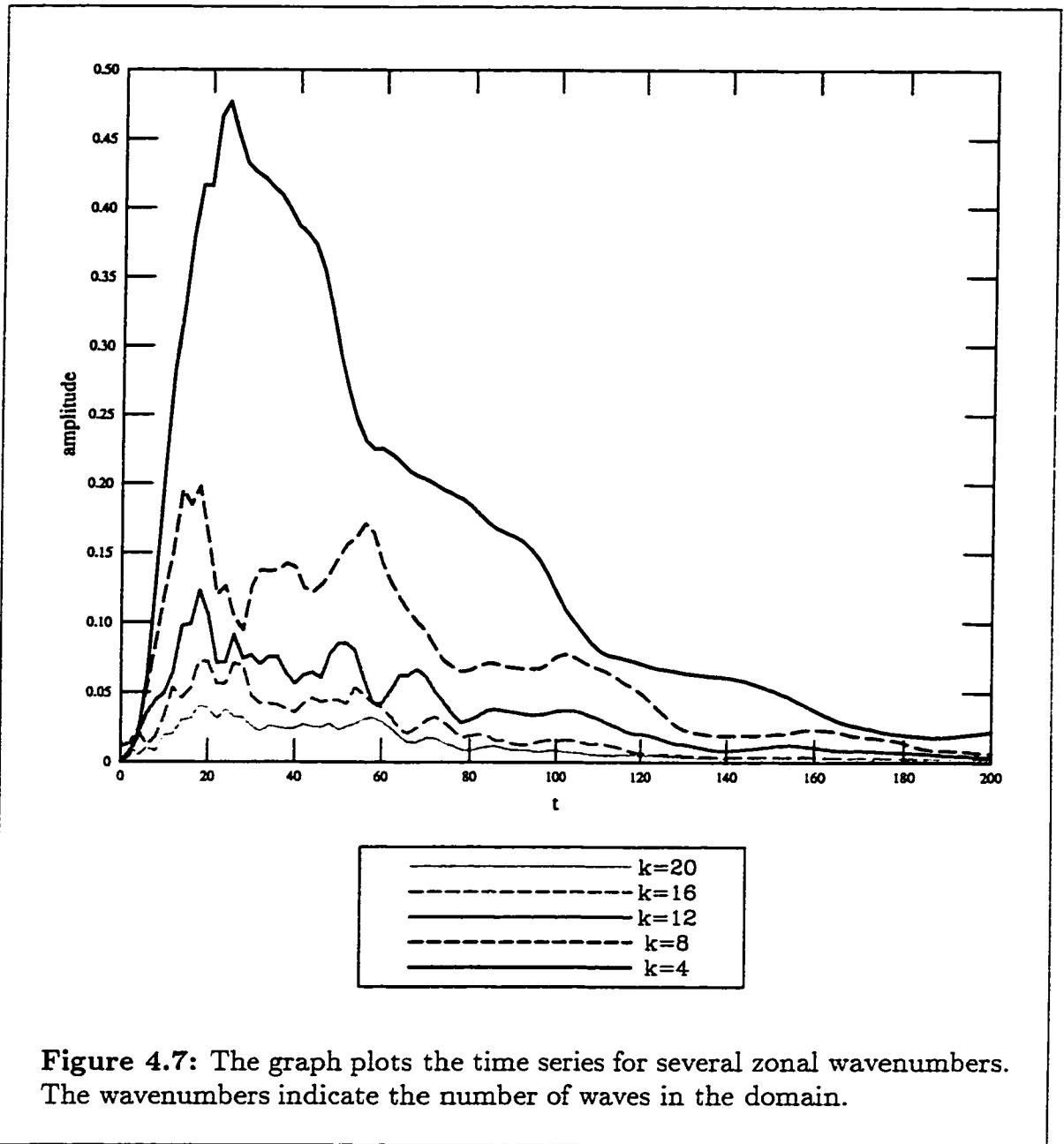
Chapter 5

SE model

The final model we examine in detail in this thesis is the SE model. It was first examined in Benilov (1992a). A reduced limit of this model. the WT model discussed in Appendix 1, was analyzed in Benilov and Cushman-Roisin (1994). The SE model differs substantially from the ST model and the VSE model in that barotropic dynamics are truly involved in this model as a result of balancing large vertical scales with large horizontal scales. The result is a model that is very unstable and subject to ultraviolet catastrophe as the following analysis illustrates. The model has little in common with the RED model. but shares many characteristics with the WVT model. As such. the analysis below has similarities to that presented in Swaters (1993b) and Reszka (1997).

5.1 Model Equations and Transformed Model

The SE model corresponds to the scaling

$$\delta = \mu, \quad \epsilon_\beta = \beta\epsilon, \quad \epsilon_T = \epsilon_v = \epsilon. \tag{5.1.1}$$

and corresponds to a model where the effect of the β-plane is strong (S) and the layer depths are of the same order or equal (E). The model equations (2.3.13) and (2.3.14) reduce to

$$\nabla^2 \psi_t + J(\psi, \nabla^2\psi + \beta y)$$
$$+ \mu J\left[h, h(1-\mu h)\nabla^2 h + \frac{1}{2}(1-2\mu h)|\nabla h|^2\right] = 0, \tag{5.1.2}$$

$$h_t + J(\psi, h) = 0. \tag{5.1.3}$$

The barotropic stream function is related to the upper-layer depth and the lower-layer pressure, p, by the relationship

$$\psi = \frac{\mu}{2}h^2 + p. \tag{5.1.4}$$

154

5. SE model

Note that due to the increased upper-layer depth the equations now contain quartic terms in h, as in the VSE model but not seen in the WVT model. The stronger coupling between the baroclinic and barotropic modes (the two are scaled equally) and the weaker β-plane have reduced the baroclinic equation so that it only contains the coupling term. Also note the inclusion of relative barotropic vorticity terms, $\nabla^2 \psi$, in the barotropic equation similar to those seen in the QG and WVT models. A consequence of this is that when the upper layer vanishes, the equations still describe dynamics via the appropriate limit of (5.1.2), namely

$$\nabla^2 \psi_t + J(\psi, \nabla^2 \psi + \beta y) = 0. \tag{5.1.5}$$

Thus the difficulties in dealing with outcroppings found for the ST and VSE models do not arise here.

The potential vorticities for the SE model are found by using the scaling (5.1.1) in (2.5.5) and (2.5.6) giving

$$
\begin{aligned}
q_1 &= q_1^{(0)} + \epsilon q_1^{(1)} + O(\epsilon^2) \\
&= \frac{1}{h} + \epsilon \frac{\nabla^2 \psi + (1 - \mu h)\nabla^2 h - \mu |\nabla h|^2 + \beta y}{h} + O(\epsilon^2).
\end{aligned}
\tag{5.1.6}
$$

$$
\begin{aligned}
q_2 &= q_2^{(0)} + \epsilon q_2^{(1)} + O(\epsilon^2) \\
&= \frac{1}{1 - \mu h} + \epsilon \frac{\nabla^2 \psi - \mu h \nabla^2 h - \mu |\nabla h|^2 + \beta y}{(1 - \mu h)} + O(\epsilon^2).
\end{aligned}
\tag{5.1.7}
$$

The boundary conditions for the SE model are given by (2.6.8), (2.6.9), (2.6.11), (2.6.12) and (2.6.18). It should be noted that in the limit $\mu \ll 1$, the model reduces to the 'weak beta' model discussed in Benilov and Cushman-Roisin (1994), which is also the WT model discussed in Appendix 1.

The SE model given by (5.1.2, 5.1.3) can be simplified through a transformation of variables presented in Benilov (1992a). The transformation changes the frontal height $h(x, y, t)$ to a new variable $\hbar(x, y, t)$ given by

$$\hbar(x, y, t) = \int_0^{h(x,y,t)} \sqrt{\mu \xi (1 - \mu \xi)}\, d\xi. \tag{5.1.8}$$

155

5. SE model

It is not straightforward to define the physical significance of $\hbar$ although it does appear as some sort of average of the scaled layer depths μh and $1 - \mu h$. It follows from (5.1.8) that

$$\frac{\partial \hbar}{\partial *} = \sqrt{\mu h (1 - \mu h)} \frac{\partial h}{\partial *},$$

$$J(\hbar, \nabla^2 \hbar) = \mu J\left(h, h(1 - \mu h)\nabla h + \frac{1}{2}(1 - 2\mu h)|\nabla h|^2\right), \tag{5.1.9}$$

where $*$ can be any of x, y, t. Then from (5.1.2, 5.1.3) we have

$$\nabla^2 \psi_t + J(\psi, \nabla^2 \psi + \beta y) + J(\hbar, \nabla^2 \hbar) = 0. \tag{5.1.10}$$

$$\hbar_t + J(w, \hbar) = 0. \tag{5.1.11}$$

Again, it should be noted that this model is identical to the transformed weak beta model discussed in Benilov and Cushman-Roisin (1994), where the transformation is (5.1.8) in the limit $\mu \ll 1$.

It should be noted that under the transformation (5.1.8) certain regularity conditions must be imposed on the frontal height h at an outcropping where $h = 0$ if $\hbar$ is to be well defined there. Rather than discuss these conditions in detail, we will only use the transformed model to discuss fronts that do not outcrop. This suits the purpose of the nonlinear analysis that is the focus of this thesis. The boundary conditions for a front that does not outcrop and extends across a finite-width channel, (2.6.11) and (2.6.12), reduce to

$$\hbar_x|_{y=W_{1,2}} = 0, \tag{5.1.12}$$

$$\hbar|_{x_L} = \hbar|_{x_R}. \tag{5.1.13}$$

Note that while this transformation makes possible some of the analysis that follows, it obscures the physics in the analysis somewhat since the connection between the quantity $\hbar$ and physical quantities such as the baroclinic velocity and potential vorticity is unclear. The fact that the transformation is not readily invertible is another drawback. As well, the use of a nonlinear transformation to study

156

5. SE model

linear and nonlinear aspects of a model is somewhat confusing. Yet, the transformation allows us to examine solutions that do not have restrictions on the initial amplitude of the basic-state flow. This is a very desirable attribute as it allows us to examine the extension of the analysis of gently-sloping fronts to the strong flows that the FG models were originally designed to describe.

5.2 Linear Analysis

Once again, we examine the basic solution given by the zonal flow described in §3.2. We substitute (3.2.1) into the model equations (5.1.2) and (5.1.3) giving, after dropping the hats,

$$
\begin{aligned}
&\nabla^2 \psi_t + \psi_0''' \psi_x - \psi_0' \nabla^2 \psi_x + J(\psi, \nabla^2 v + \beta y) \\
&+\mu \Bigg[-h_0(1-\mu h_0) h_0' \nabla^2 h_x - (1 - 2\mu h_0)(h_0')^2 h_{xy} \\
&\quad + (h_0(1-\mu h_0) h_0'')' h_x - 2\mu \left[(h_0 h_0'')' h h_x (h_0')^2 h h_{xy} \right] \\
&\quad - (1 - 2\mu h_0) h_0' (h\nabla^2 + h_x h_{xx} + h_y h_{xy}) \\
&\quad + h_0(1-\mu h_0) J(h, \nabla^2 h) + (1 - 2\mu h_0) h_0' J(h, h_y) \\
&\quad - \mu h^2 (h_0' \nabla^2 h_x - h_0''' h_x) + (1 - 2\mu h_0) J \left(h, h\nabla^2 h + \frac{1}{2} |\nabla h|^2 \right) \\
&\quad - \mu h J \left(h, h\nabla^2 h + |\nabla h|^2 \right) \Bigg] = 0,
\end{aligned}
\tag{5.2.1}
$$

$$
h_t + h_0' \psi_x - \psi_0' h_x + J(\psi, h) = 0.
\tag{5.2.2}
$$

Similarly, we can use

$$
\hbar = \hbar_0(y) + \widehat{\hbar}(x, y, t),
$$

with (3.2.1) in equations (5.1.10) and (5.1.11) to get, dropping the hats,

$$
\begin{aligned}
&\nabla^2 \psi_t + \psi_0''' \psi_x - \psi_0' \nabla^2 \psi_x + J(\psi, \nabla^2 \psi + \beta y) \\
&\quad + J(\hbar, \nabla^2 \hbar) + \hbar_0''' \hbar_x - \hbar_0' \nabla^2 \hbar_x = 0,
\end{aligned}
\tag{5.2.3}
$$

$$
\hbar_t + \hbar_0' \psi_x - \psi_0' \hbar_x + J(\psi, \hbar) = 0.
\tag{5.2.4}
$$

5. SE model

It is obvious that the transformation has greatly simplified the model.

Once again, we review some of the previous linear analysis and present linear solutions to the model. The linear SE model from (5.2.1) and (5.2.2) is

$$\nabla^2 \psi_t + (\psi_0''' + \beta)\psi_x - \psi_0' \nabla^2 \psi_x$$
$$+ \mu \Big[-h_0(1 - \mu h_0)h_0' \nabla^2 h_x - (1 - 2\mu h_0)(h_0')^2 h_{xy} \tag{5.2.5}$$
$$+ (h_0(1 - \mu h_0)h_0'')' h_x \Big] = 0,$$

$$h_t + h_0' \psi_x - \psi_0' h_x = 0, \tag{5.2.6}$$

and the linear transformed model from (5.2.3) and (5.2.4) is

$$\nabla^2 \psi_t + (\psi_0''' + \beta)\psi_x - \psi_0' \nabla^2 \psi_x + \hbar_0''' \hbar_x - \hbar_0' \nabla^2 \hbar_x = 0, \tag{5.2.7}$$

$$\hbar_t + \hbar_0' \psi_x - \psi_0' \hbar_x = 0. \tag{5.2.8}$$

The linear travelling-wave or normal-mode equations are then found by substituting (3.2.9) into (5.2.5) and (5.2.6) giving

$$(c + \psi_0')\widetilde{\psi}'' - [(c + \psi_0')k^2 + \psi_0''' + \beta]\widetilde{\psi}$$
$$+ \mu \Big[\big[h_0(1 - \mu h_0)(h_0'\widetilde{\hbar}' - h_0''\widetilde{\hbar}) \big]' - h_0(1 - \mu h_0)h_0' k^2 \widetilde{\hbar} \Big] = 0. \tag{5.2.9}$$

$$-[c + \psi_0']\widetilde{\hbar} + h_0'\widetilde{\psi} = 0, \tag{5.2.10}$$

with the boundary conditions (3.2.12–3.2.14). Although they are not discussed in detail, linear boundary conditions at outcroppings can be derived as in Swaters (1993b).

Using

$$\hbar(x, y, t) = \widetilde{\hbar}(y) \exp[i(kx - \omega t)] + c.c., \tag{5.2.11}$$

158

5. SE model

the transformed normal-mode equations from (5.2.7) and (5.2.8) are

$$(c + \psi_0')\widetilde{w}'' - [(c + \psi_0')k^2 + v_0''' + \beta]\widetilde{w}$$
$$+ [\hbar_0'\hbar'' - (\hbar_0''' + k^2\hbar_0')\widetilde{\hbar}] = 0. \tag{5.2.12}$$

$$-[c + \psi_0']\widetilde{\hbar} + \hbar_0'\widetilde{\psi} = 0. \tag{5.2.13}$$

The boundary condition (5.1.12) reduces to

$$\widetilde{\hbar} = 0 \quad \text{on} \quad y = W_{1,2}. \tag{5.2.14}$$

Analysis of these equations is given in Benilov (1992a) and in Benilov and Cushman-Roisin (1994) for the identical transformed weak beta model. We quickly recap the stability argument. Once again we use the substitution (3.2.16) in (5.2.9) and (5.2.10) to get that

$$(c + \psi_0')\widetilde{w}'' - \left[(c + \psi_0')k^2 + v_0''' + \beta \right] \widetilde{w}$$
$$+ \mu \left[h_0(1 - \mu h_0)h_0'^2 \eta' \right]' - \mu k^2 h_0(1 - \mu h_0)h_0'^2 \eta = 0. \tag{5.2.15}$$

$$-[c + v_0']\eta + \widetilde{w} = 0. \tag{5.2.16}$$

Solving (5.2.16) for $\widetilde{w}$ and substituting into (5.2.15) gives

$$\left\{ \left[(c + \psi_0')^2 + \mu h_0(1 - \mu h_0)h_0'^2 \right] \eta' \right\}'$$
$$- \left\{ \left[(c + \psi_0')^2 + \mu h_0(1 - \mu h_0)h_0'^2 \right] k^2 + \beta(c + \psi_0') \right\} \eta = 0. \tag{5.2.17}$$

We will assume that there is no outcropping. Taking η^* times (5.2.17) and integrating over $W_1 < y < W_2$ gives, after an integration by parts and use of (3.2.14) at both channel walls,

$$\int_{W_1}^{W_2} \left\{ \left[(c + \psi_0')^2 + \mu h_0 h_0'^2(1 - \mu h_0) \right] \left[|\eta'|^2 + k^2|\eta|^2 \right] \right\} dy$$
$$+ \int_{W_1}^{W_2} \left\{ \beta(c + \psi_0')|\eta|^2 \right\} dy = 0. \tag{5.2.18}$$

159

5. SE model

Assume the flow is stable, that is, c is real. Rearranging (5.2.18) gives

$$\int_{W_1}^{W_2} \left\{ \left[(c + \psi_0')^2 + \mu h_0 {h_0'}^2 (1 - \mu h_0) \right] |\eta'|^2 \right. $$

$$+ \left[\left(c + \psi_0' + \frac{\beta}{2k^2} \right)^2 + \mu h_0 {h_0'}^2 (1 - \mu h_0) \right] k^2 |\eta|^2 \bigg\} dy \qquad (5.2.19)$$

$$= \int_{W_1}^{W_2} \frac{\beta^2}{4k^2} |\eta|^2 dy.$$

For bounded solutions it follows that

$$\lim_{k \to \infty} \frac{\beta^2}{4k^2} \int_{W_1}^{W_2} |\eta|^2 \, dy = 0.$$

which implies that the limit of the right-hand side of (5.2.19) is also zero, or specifically that

$$\lim_{k \to \infty} \int_{W_1}^{W_2} \left[\left(c + \psi_0' + \frac{\beta}{2k^2} \right)^2 + \mu h_0 {h_0'}^2 (1 - \mu h_0) \right] k^2 |\eta|^2 dy = 0. \qquad (5.2.20)$$

Equation (5.2.20) can only hold if

$$(c + \psi_0')^2 + \mu h_0 {h_0'}^2 (1 - \mu h_0) = 0, \quad \forall \quad W_1 \le y \le W_2.$$

which implies that

$$h_0' = 0, \quad \forall \quad W_1 \le y \le W_2,$$

since h_0 and $1 - \mu h_0$ are nonnegative. Therefore only fronts with constant h_0, that is, fronts of constant height, are stable. All other monotonic, nonoutcropping fronts are unstable as $k \to \infty$. Since stronger shears and outcroppings are expected to destabilize fronts, we expect that all fronts are unstable as $k \to \infty$.

It should be noted that as $k \to \infty$ some of the assumptions made in deriving the model break down. Specifically, it was assumed that all terms in (5.1.10) and (5.1.11) were $O(1)$. Using the normal mode analysis, $\nabla^2 h \approx k^2 h$. For these terms to remain $O(1)$, k^2 must be $O(1)$, so $k^2 < 1/\epsilon$. As k becomes large, this assumption

5. SE model

is invalid; the length scales have become too small to be modelled under the scaling assumed for this model. This problem. where a model is highly unstable at small scales beyond the scope of the model. is called ultraviolet catastrophe and is common to PG models (de Verdiére. 1986). It will be discussed in more detail in the context of a linear solution below. This form of instability was also observed in the analysis of Paldor and Ghil (1990), Paldor and Ghil (1991). and Barth (1994).

In the SE model, the leading-order potential vorticities in each layer given by (5.1.6) and (5.1.7) have gradients of opposite sign at all points except when $h_0' = 0$, since

$$(q_1^{(0)})_y = -\frac{h_0'}{\mu h_0^2} \quad \text{and} \quad (q_2^{(0)})_y = \mu h_0'.$$

Thus, all flows satisfy the necessary condition for instability in a QG model that the PV gradient reverses sign across the layer interface (Pedlosky. 1987). Assuming instability occurs it is possible to derive restrictions on the values of c_R and c_I analogous to Howard's semi-circle theorem (Drazin and Reid. 1981). But as the focus of this thesis is nonlinear aspects. we leave this analysis for another work.

As before, we present the solution for a gently sloping front and a wedge front of large amplitude. Note that the analysis below does hold for a constant barotropic flow, $\psi_0' = U_0$, but as can be seen from (5.2.12) and (5.2.13) the effect of such a flow is only to vary the phase speed by the value U_0. As before. we begin with the gently sloping front given by (3.2.22). with boundary conditions (3.2.23). and with the definitions (3.2.24) and (3.2.25). Making these substitutions into (5.2.9) and (5.2.10) gives to leading order in Δ.

$$\tilde{c}\tilde{v}'' - \left[\tilde{c}k^2 + \tilde{\beta}\right]\tilde{v} + \mu\aleph(1 - \mu\aleph)\tilde{\alpha}\left[\tilde{h}'' - k^2\tilde{h}\right] = 0,$$
$$-\tilde{c}\tilde{h} + \tilde{\alpha}\tilde{\psi} = 0. \tag{5.2.21}$$

Eliminating $\tilde{\psi}$ gives

$$\left[\tilde{c}^2 + \mu\aleph(1 - \mu\aleph)\tilde{\alpha}^2\right]\left[\tilde{h}'' - k^2\tilde{h}\right] + \tilde{\beta}\tilde{c}\tilde{h} = 0. \tag{5.2.22}$$

In order to satisfy (3.2.23), we have that

$$\tilde{h} = A\sin(\ell y), \qquad \ell = \frac{n\pi}{L}, \qquad n = 1, 2, 3, \ldots \tag{5.2.23}$$

5. SE model

Substitution of (5.2.23) into (5.2.22) gives the dispersion relation

$$\left(k^2 + \ell^2\right) \tilde{c}^2 + \tilde{\beta}\tilde{c} + \aleph\mu(1 - \mu\aleph)\tilde{\alpha}^2 \left(k^2 + \ell^2\right) = 0,$$

which has solution

$$\tilde{c}(k, \ell) = \frac{-\tilde{\beta} \pm \sqrt{\tilde{\beta}^2 - 4\mu\aleph(1 - \mu\aleph)\tilde{\alpha}^2 K^4}}{2K^2}, \qquad (5.2.24)$$

where K is the total wavenumber given by $K^2 = k^2 + \ell^2$. The barotropic stream function is given by

$$\tilde{w} = \frac{\tilde{c}}{\tilde{\alpha}}\tilde{h}. \qquad (5.2.25)$$

These solutions are unstable when the imaginary part of $\tilde{c}$ is nonzero, that is, when

$$\tilde{\beta}^2 - 4\mu\aleph(1 - \mu\aleph)\tilde{\alpha}^2 K^4 < 0. \qquad (5.2.26)$$

which holds if the total wavenumber satisfies

$$K^4 > \frac{\tilde{\beta}^2}{4\mu\aleph(1 - \mu\aleph)\tilde{\alpha}^2}. \qquad (5.2.27)$$

This implies that all fronts will become unstable as k and ℓ become large, that is, as the wavelength of the motion becomes small. When the wave is unstable its growth rate σ is given by

$$\tilde{\sigma} = k\tilde{c}_I = k\frac{\sqrt{-\tilde{\beta}^2 + 4\mu\aleph(1 - \mu\aleph)\tilde{\alpha}^2 K^4}}{2K^2}, \qquad (5.2.28)$$

which grows linearly with k for large k. The expressions for the growth rate and conditions for instability allow for a complete discussion of ultraviolet catastrophe. We now see that fronts become unstable as the wavelength of the perturbation becomes small. But, since the growth rate grows with k, the small-wavelength instabilities grow faster as their size decreases. Thus, the linear analysis leads to the conclusion that there will be explosive (or catastrophic) unstable growth at small

162

5. SE model

(ultraviolet) wavelengths. The occurrence of ultraviolet catastrophe in PG models is common (de Verdiére, 1986). This is because there are no relative vorticity terms in (5.1.3) that would prevent growth at small scales. The balance in (5.1.2) is not able to suppress this growth in the linear model. In Paldor and Ghil (1990), it is suggested that it is the availability of baroclinic energy as seen through Reynolds stresses or phase differences between the two layers that leads to this vigorous short wave instability when layer depths are of the same order. Whether or not nonlinear effects can suppress this growth is the focus of §5.5.

Examining other parameters, we see that the growth rate grows linearly with α and decreases like β. That is, increasing the gradient of the front enhances the instability, while increasing the background planetary vorticity gradient inhibits it. The growth rate grows like $\sqrt{\mu\aleph(1 - \mu\aleph)}$ and therefore is greatest when the two layers are of equal depth, $\mu\aleph = \frac{1}{2}$. The group speed for this solution is

$$\tilde{c}_G(k, \ell) = \frac{\partial \tilde{\omega}}{\partial k} = \frac{\tilde{\beta}\tilde{c}(k^2 - \ell^2) - 2\mu\aleph(1 - \mu\aleph)\tilde{a}^2 K^{-4}}{2\tilde{c}K^2 + \tilde{\beta}}. \tag{5.2.29}$$

Benilov and Cushman-Roisin (1994) found that an exact solution to the transformed weak beta model could be found by considering the wedge front. This solution naturally extends to the SE model. The wedge front is given by

$$\begin{aligned} \hbar_0(y) &= \aleph + \alpha y, \\ \upsilon_0(y) &\equiv 0. \end{aligned} \tag{5.2.30}$$

where the frontal slope, α, is no longer assumed to be small and, thus, corresponds to a strong flow similar to the wedge front studied for the ST model. The parameters are chosen so that the upper layer extends across the channel, that is, there is no outcropping. In this case the linear normal mode equations (5.2.12) and (5.2.13) reduce to

$$\begin{aligned} -c[\tilde{\psi}'' - k^2\tilde{\psi}] + \beta\tilde{\psi} - \alpha(\tilde{\hbar}'' - k^2\tilde{\hbar}) &= 0, \\ -c\tilde{\hbar} + \alpha\tilde{\psi} &= 0. \end{aligned} \tag{5.2.31}$$

Eliminating $\tilde{\psi}$ gives

$$(c^2 + \alpha^2)(\tilde{\hbar}'' - k^2\tilde{\hbar}) + \beta c\tilde{\hbar} = 0.$$

163

5. SE model

In this case, where the front extends across the channel. the boundary conditions become simply $\psi = \tilde{h} = 0$ on $y = 0, L$. In order to satisfy the boundary conditions, we have that

$$\tilde{h} = A\sin(\ell y), \qquad \ell = \frac{n\pi}{L}, \qquad n = 1,2,3,\ldots \qquad (5.2.32)$$

Substitution of (5.2.32) into (5.2.31) gives the dispersion relation

$$K^2 c^2 + \beta c + K^2 \alpha^2 = 0.$$

which has solution

$$c = \frac{-\beta \pm \sqrt{\beta^2 - 4\alpha^2 K^4}}{2K^2}. \qquad (5.2.33)$$

The solution is virtually identical to that given for the gently sloping front. In the dispersion relationship the dependence on $\aleph$ and μ has disappeared as might be expected given the form of the transformation (5.1.8). These solutions are unstable when the imaginary part of c is nonzero. that is. when

$$\beta^2 - 4\alpha^2 K^4 < 0. \qquad (5.2.34)$$

which holds if the total wavenumber satisfies

$$K^4 > \frac{\beta^2}{4\alpha^2}. \qquad (5.2.35)$$

When the wave is unstable its growth rate σ is given by

$$\sigma = kc_I = k\frac{\sqrt{-\beta^2 + 4\alpha^2 K^4}}{2K^2}. \qquad (5.2.36)$$

The group speed for this solution is

$$c_G = \frac{\partial \omega}{\partial k} = \frac{\beta c(k^2 - \ell^2) - 2\mu\alpha^2 K^4}{2cK^2 + \beta}. \qquad (5.2.37)$$

The similarity of the two solutions indicates that the solution for the gently sloping front captures many of the essential characteristics of the model despite assuming a small-amplitude flow. However, these solutions are limited since they do not include an outcropping.

5. SE model

5.3 Nonlinear Invariants and Stability

As for the other models we now discuss the invariants of §2.7 and use these invariants to attempt to establish nonlinear stability. As mentioned previously, the SE model can be studied using its noncanonical Hamiltonian formulation. However, within the context of this thesis the Hamiltonian formulation of the SE model does not add great insight. Therefore we leave the Hamiltonian formulation to Appendix 4 and discuss the invariants of the flow as we have done for the previous models.

Under the scaling (5.1.1), the leading-order term in pseudo-energy invariant (2.7.12) reduces to

$$\mathcal{E} = \frac{1}{2} \int\int_{\Omega} |\nabla\psi|^2 \, dxdy - \frac{\mu}{2} \int\int_{FR} h(1 - \mu h)|\nabla h|^2 - h^2 \left(\nabla^2\psi + \beta y\right) dxdy. \quad (5.3.1)$$

Illustrating that this quantity is invariant using the governing equations and the boundary conditions is straightforward but as it follows from the discussion in §2.7 we do not present it here. As well from §2.7, we have the invariants associated with the leading-order PV. For the upper layer. (2.7.9) holds so that

$$\mathfrak{C}_1 = \int\int_{FR} \Phi_1(h) \, dxdy \quad (5.3.2)$$

is an invariant of the SE model where Φ_1 is any arbitrary. sufficiently smooth function of its argument. For the lower layer. the leading-order PV is given by (5.1.7) and hence it follows from (2.7.8) that

$$\mathfrak{C}_* = \int\int_{FR} \Phi(1 - \mu h) \, dxdy \quad (5.3.3)$$

is an invariant of the SE model. Obviously, (5.3.2) and (5.3.3) are equivalent.

The equivalence of (5.3.8) and (5.3.3) leads to the search for another invariant associated with the PVs, one in which the leading-order terms would cancel each other. From (2.7.7) and (2.7.8) it follows that the leading-order term of

$$\mathfrak{C}_* = \int\int_{FR} \mu h \Phi_1(q_1) + (1 - \mu h)\Phi_2(q_2) \, dxdy$$

is an invariant of the flow for any smooth functions Φ_1 and Φ_2. Using the expansion of the PVs given by (5.1.6) and (5.1.7) and Taylor expanding the functions $\Phi_{1,2}$

165

5. SE model

gives that

$$\mathfrak{C}_* = \iint_{FR} \mu h \Phi_1(q_1^{(0)}) + (1 - \mu h)\Phi_2(q_2^{(0)})\,dxdy$$
$$+ \epsilon \iint_{FR} \mu h q_1^{(1)} \Phi_1'(q_1^{(0)}) + (1 - \mu h)q_2^{(1)}\Phi_2'(q_2^{(0)})\,dxdy$$
$$+ h.o.t.$$

Now we choose Φ_2 so that the leading-order terms cancel, that is,

$$(1 - \mu h)\Phi_2\left(q_2^{(0)}\right) = -\mu h \Phi_1\left(q_1^{(0)}\right). \tag{5.3.4}$$

Using (5.3.4) and the expressions for the higher order PVs given by (5.1.6) and (5.1.7), dividing by ϵ and dropping the higher order terms gives

$$\mathfrak{C}_2 = \iint_{FR} \left\{ (\nabla^2 w + \beta y - \mu |\nabla h|^2)\left(\frac{\Phi_{10}'}{h} - \Phi_{10}\right) + \mu \Phi_{10} h \nabla^2 h \right\} dxdy.$$

where we have used the subscript zero to indicate that the function Φ_1 is evaluated at $q_1^{(0)}$. Integrating the final term by parts gives

$$\mathfrak{C}_2 = \iint_{FR} (\nabla^2 w + \beta y)\left(\frac{\Phi_{10}'}{h} - \Phi_{10}\right) dxdy.$$

an invariant of the flow for any arbitrary Φ_{10}. Therefore, we have the invariant

$$\mathfrak{C}_2 = \iint_{FR} (\nabla^2 \psi + \beta y)\,\Phi(h)\,dxdy \tag{5.3.5}$$

for any arbitrary function Φ.

We can also examine the case when the upper layer vanishes, $h \equiv 0$. It then follows from (5.1.7) that the leading-order, lower-layer PV is

$$q_2^{(0)} = \nabla^2 \psi + \beta y, \tag{5.3.6}$$

and hence it follows from (2.7.8) that

$$\mathfrak{C}_3 = \iint_{NF} \Phi(\nabla^2 \psi + \beta y)\,dxdy \tag{5.3.7}$$

166

5. SE model

is an invariant of the flow. We can combine (5.3.2), (5.3.5), and (5.3.7) into a single invariant given by

$$
\mathfrak{C}(\psi, h) = \iint_{NF} \Phi_2(\nabla^2 \dot{\psi} + \beta y) \, dx dy
$$
$$
+ \iint_{FR} \left[(\nabla^2 \psi + \beta y) \, \Phi_1(h) + \Phi_3(h) \right] dx dy.
$$

(5.3.8)

where Φ_1, Φ_2, and Φ_3 are sufficiently smooth functions of their arguments and

$$
\Phi_2|_{y=\phi_1} = \Phi_1(0) \left(\nabla^2 \psi + \beta y \right)|_{y=\phi_1} + \Phi_3(0),
$$

(5.3.9)

so that any values associated with the variation of the outcropping are eliminated. This is not an additional restriction since the invariant is only determined to a constant that we are free to choose.

The fact that (5.3.5) is an invariant of the flow implies that the final term in the energy-PV invariant (5.3.1) is an invariant by choosing $\Phi(h) = h^2$. This allows us to reduce the pseudo-energy invariant to

$$
\mathcal{E} = \frac{1}{2} \iint_{\Omega} |\nabla \psi|^2 \, dx dy - \frac{\mu}{2} \iint_{FR} h(1 - \mu h)|\nabla h|^2 \, dx dy.
$$

(5.3.10)

This invariant specifies that the difference between the barotropic KE and the baroclinic KE remains constant. This has important consequences for stability since it allows both the barotropic and baroclinic modes to increase their KE concurrently (see §5.9). The zonal momentum invariant (2.7.15) becomes

$$
\mathfrak{M} = \iint_{\Omega} y \nabla^2 \psi \, dx dy.
$$

(5.3.11)

We can attempt to derive nonlinear stability conditions as in §3.3 and Karsten and Swaters (1996b). To do so we form the invariant function

$$
\mathfrak{I}(h) = \mathfrak{M}(\psi, h) - \mathfrak{M}(\psi_0, h_0) + \mathfrak{C}(\psi, h) - \mathfrak{C}(\psi_0, h_0),
$$

(5.3.12)

where $(\psi_0, h_0) = (\psi_0(y), h_0(y))$ represents a basic-state zonal flow and $\mathfrak{M}$ and $\mathfrak{C}$ are given by (5.3.11) and (5.3.8), respectively, with the domains of integration extended

5. SE model

to the entire domain Ω. (Note that the first term in (5.3.8) vanishes since $\mathcal{NF}$ vanishes when the upper layer is extended to the entire domain.) Then, from (3.3.5), we have

$$\mathfrak{I} = \iint_\Omega \Big\{ [y + \Phi_1(h)] \left(\nabla^2\psi + \beta y\right) - [y + \Phi_1(h_0)]\left(\nabla^2\psi_0 + \beta y\right) \\ + \Phi_3(h) - \Phi_3(h_0)\Big\}\, dxdy. \tag{5.3.13}$$

We now consider the first variation of $\mathfrak{I}$, that is,

$$\delta\mathfrak{I} = \iint_\Omega \Big\{ \left[\Phi_1'(h)\left(\nabla^2\psi + \beta y\right) + \Phi_3'(h)\right]\delta h + [y + \Phi_1(h)]\,\nabla^2\delta\psi \Big\}\, dxdy.$$

In order that $\delta\mathfrak{I}$ vanishes at $(\psi, h) = (\psi_0, h_0)$, we choose Φ_1 and Φ_3 to satisfy

$$\Phi_1(h_0) = -y. \tag{5.3.14}$$

$$\Phi_3'(h_0) = -\left(\nabla^2\psi_0 + \beta y\right)\Phi_1'(h_0). \tag{5.3.15}$$

Now we consider $(\psi, h) = (\tilde\psi, \tilde h) + (\psi_0, h_0)$ where $(\tilde\psi, \tilde h)$ is a finite amplitude perturbation to the basic-state flow. Then, from (5.3.13) using (5.3.14), we have

$$\mathfrak{I}(\tilde h + h_0, \tilde\psi + \psi_0) \\ = \iint_\Omega \left[\Phi_1(\tilde h + h_0) - \Phi_1(h_0)\right]\left(\nabla^2\tilde\psi + \nabla^2\psi_0 + \beta y\right) dxdy \\ + \iint_\Omega \Phi_3(\tilde h + h_0) - \Phi_3(h_0)\, dxdy. \tag{5.3.16}$$

Now we assume that Φ_1 and Φ_3 satisfies the bounds

$$\alpha_1 < \Phi_1''(\xi)\left(\nabla^2\psi_0 + \beta y\right) + \Phi_3''(\xi) < \beta_1, \quad \forall\xi \quad \text{and} \quad \forall y \in \Omega, \tag{5.3.17}$$

$$\alpha_2 < \Phi_1'(\xi) < \beta_2, \quad \forall\xi, \tag{5.3.18}$$

for some constants $\alpha_{1,2}$ and $\beta_{1,2}$. If (5.3.17) is integrated twice, first from h_0 to ξ and then from h_0 to $\tilde h + h_0$, and (5.3.18) is integrated once from h_0 to $\tilde h + h_0$ using

5. SE model

(5.3.15) and taking the absolute value, it follows that

$$\frac{\alpha_1}{2}\tilde{h}^2 < \left[\Phi_1(\tilde{h}+h_0) - \Phi_1(h_0)\right](\nabla^2\psi_0 + \beta y)$$
$$+ \Phi_3(\tilde{h}+h_0) - \Phi_3(h_0) < \frac{\beta_1}{2}\tilde{h}^2. \tag{5.3.19}$$

$$\left|\Phi_1(\tilde{h}+h_0) - \Phi_1(h_0)\right| < \max(\alpha_2, \beta_2)|\tilde{h}|. \tag{5.3.20}$$

Using (5.3.19) and (5.3.20) with (5.3.16) gives

$$\iint_\Omega \left\{\frac{\alpha_1}{2}\tilde{h}^2 - \max(\alpha_2, \beta_2)|\tilde{h}||\nabla^2\tilde{\psi}|\right\} dxdy$$
$$< \Im(\tilde{h}+h_0, \tilde{\psi}+\psi_0) < \tag{5.3.21}$$
$$\iint_\Omega \left\{\frac{\beta_1}{2}\tilde{h}^2 + \max(\alpha_2, \beta_2)|\tilde{h}||\nabla^2\tilde{\psi}|\right\} dxdy.$$

In order to establish conditions for nonlinear stability. we need to establish conditions that guarantee that $\Im$ is either positive or negative definite. To establish such bounds would require that we establish conditions such that the bound on the left (right) in (5.3.21) is positive (negative) for all perturbations. Such conditions require an inequality of the form

$$\frac{\alpha_1}{2}|\tilde{h}| \geq \max(\alpha_2, \beta_2)|\nabla^2\tilde{\psi}|$$

or

$$\frac{\beta_1}{2}|\tilde{h}| \leq -\max(\alpha_2, \beta_2)|\nabla^2\tilde{\psi}|,$$

respectively. These conditions require that the perturbation to the barotropic stream function be somehow bounded by the perturbation to the upper-layer height, that is,

$$|\nabla^2\tilde{\psi}| \leq C|\tilde{h}|, \tag{5.3.22}$$

for some positive constant C. This is clearly not true for general perturbations and specifically not true as length scales become small. We can relate this condition

5. SE model

to the analysis in §5.2 by associating $\nabla^2 \tilde{\psi}$ with $k^2 \tilde{\psi}$. Then for (5.3.22) to hold, we require

$$k^2 |\tilde{\psi}| \leq C|\tilde{h}|,$$

which will only hold as $k \to \infty$ if either we do not allow perturbations to the stream function, $\tilde{\psi} = 0$, or the perturbations to the frontal layer become large, $\tilde{h} \to \infty$. The latter case is instability, unbounded growth in the perturbations. and the former is a restriction that essentially reduces the model to a single layer/reduced gravity model. Thus, it is not possible to establish nonlinear stability conditions since it is not possible to bound the small-scale growth.

5.4 Weakly Nonlinear Analysis

In the following sections, we examine the effects of nonlinear terms in the model using a weakly nonlinear analysis of the solutions found in §5.2. We begin with the gently sloping front and then follow this with the analysis of the wedge front using the transformed model. Once again. both models give rise to the same envelope equation and solutions to this equation are discussed. Since the weakly nonlinear analysis of the ST model contains many similarities, we reference §3.4 whenever possible to reduce redundancy.

5.5 Gently Sloping Front

As found in §5.2, the SE model has an exact solution for the gently sloping front basic state (3.2.22) with assumptions (3.2.24) and (3.2.25) and the dispersion relation (5.2.33). In the following analysis we will drop the tildes from the small quantities. The variables are given by the basic solution plus a smaller perturbation, that is,

$$h = \aleph + \Delta\alpha \left(y - \frac{L}{2}\right) + \Delta^2 h,$$

$$\psi = \Delta^2 \psi.$$

(5.5.1)

Substituting (5.5.1) into the nonlinear model (5.2.1) and (5.2.2) gives the fully

5. SE model

nonlinear equations

$$h_t + \alpha\psi_x = \Delta M, \tag{5.5.2}$$

$$\nabla^2\psi_t + \beta\psi_x - \aleph\mu(1 - \mu\aleph)\alpha\nabla^2 h_x = \Delta N_1 + \Delta^2 N_2 + O(\Delta^3). \tag{5.5.3}$$

where

$$M = J(h, \psi), \tag{5.5.4}$$

$$N_1 = \mu(1 - 2\aleph\mu)\left[\alpha^2 h_{xy} + \alpha^2(y - \frac{L}{2})\nabla^2 h_x\right], \tag{5.5.5}$$

$$N_2 = -\mu(1 - 2\aleph\mu)\left[\alpha(y - \frac{L}{2})J(h, \nabla^2 h) + \alpha J(h, h_y)\right.$$

$$\left. - \alpha h\nabla^2 h_x - \alpha h_x h_{xx} - \alpha h_y h_{xy}\right] \tag{5.5.6}$$

$$-\mu^2\alpha^3\left(y - \frac{L}{2}\right)^2\nabla^2 h_x - 2\mu^2\alpha^3\left(y - \frac{L}{2}\right)h_{xy},$$

and we reiterate that α, β, and t have been appropriately scaled for the gently sloping front with the tildes dropped.

We can construct an equation that eliminates ψ from the linear terms by taking $(\nabla_t^2 + \beta\partial_x)(5.5.2) - \alpha\partial_x(5.5.3)$ to give

$$\mathfrak{L}(\partial_t, \partial_x, \partial_y, \alpha)h = \Delta[(\nabla_t^2 + \beta\partial_x)M - \alpha\partial_x N_1] - \Delta^2[\alpha\partial_x N_2] + O(\Delta^3), \tag{5.5.7}$$

where

$$\mathfrak{L}(\partial_t, \partial_x, \partial_y, \alpha) = \nabla_{tt}^2 + \aleph\mu(1 - \aleph\mu)\alpha^2\nabla_{xx}^2 + \beta\partial_{xt}. \tag{5.5.8}$$

Equations (5.5.7) and (5.5.2) are the equations we will study.

The marginal stability curve (5.2.26) gives a critical value of the frontal slope α given by

$$\alpha_c = \frac{\beta}{2[\mu\aleph(1 - \mu\aleph)]^{\frac{1}{2}}K^2}, \tag{5.5.9}$$

where it is assumed that $\alpha_c > 0$ (see later discussion). If $\alpha > \alpha_c$ we have linear stability, if $\alpha < \alpha_c$ we have linear instability. To facilitate a weakly nonlinear

5. SE model

analysis, we study a front that is only marginally unstable. That is, a front where the linear instability will grow slowly allowing the nonlinear interactions to evolve and be analyzed. Therefore a value of α slightly larger than the critical value is chosen, that is,

$$\alpha = \alpha_c + \nu \Delta_1,$$

for some small Δ_1 and an order one parameter ν that allows the growth rate of the linear instability to be adjusted. The imaginary part of the linear phase speed, (5.2.33), will then be given by

$$\sqrt{2\mu\aleph(1-\mu\aleph)\alpha_c}\Delta_1^{\frac{1}{2}} + O(\Delta_1). \qquad (5.5.10)$$

In order to simplify this, $\Delta = (\Delta_1)^{\frac{1}{2}}$ is introduced so that

$$\alpha = \alpha_c + \nu\Delta^2. \qquad (5.5.11)$$

where ν is an $O(1)$ parameter that allows us to adjust the size of the linear growth rate. Figure 5.1 shows the marginal stability curve given by (5.5.9) and the value for α used in the analysis as given by (5.5.11).

Slow time and space variables as given by (3.5.1) are again introduced, although now we will need only one slow time variable and a second slow space variable, that is,

$$T = \Delta t, \quad X = \Delta x, \quad \mathfrak{X} = \Delta^2 x. \qquad (5.5.12)$$

Note that we have already scaled t accordingly for the gently sloping front analysis.

Using the slightly unstable frontal slope, (5.5.11), and the slow variables,

172

Figure 5.1: The marginal stability curve as given by (5.5.9), giving the critical value of the interface slope, α_c, versus the wavenumber K. Values of α greater than α_c represent unstable fronts, those less, stable fronts. The value of α used in the analysis as given by (5.5.11) is shown to be a small increase in the frontal slope so that the front is in the unstable regime.
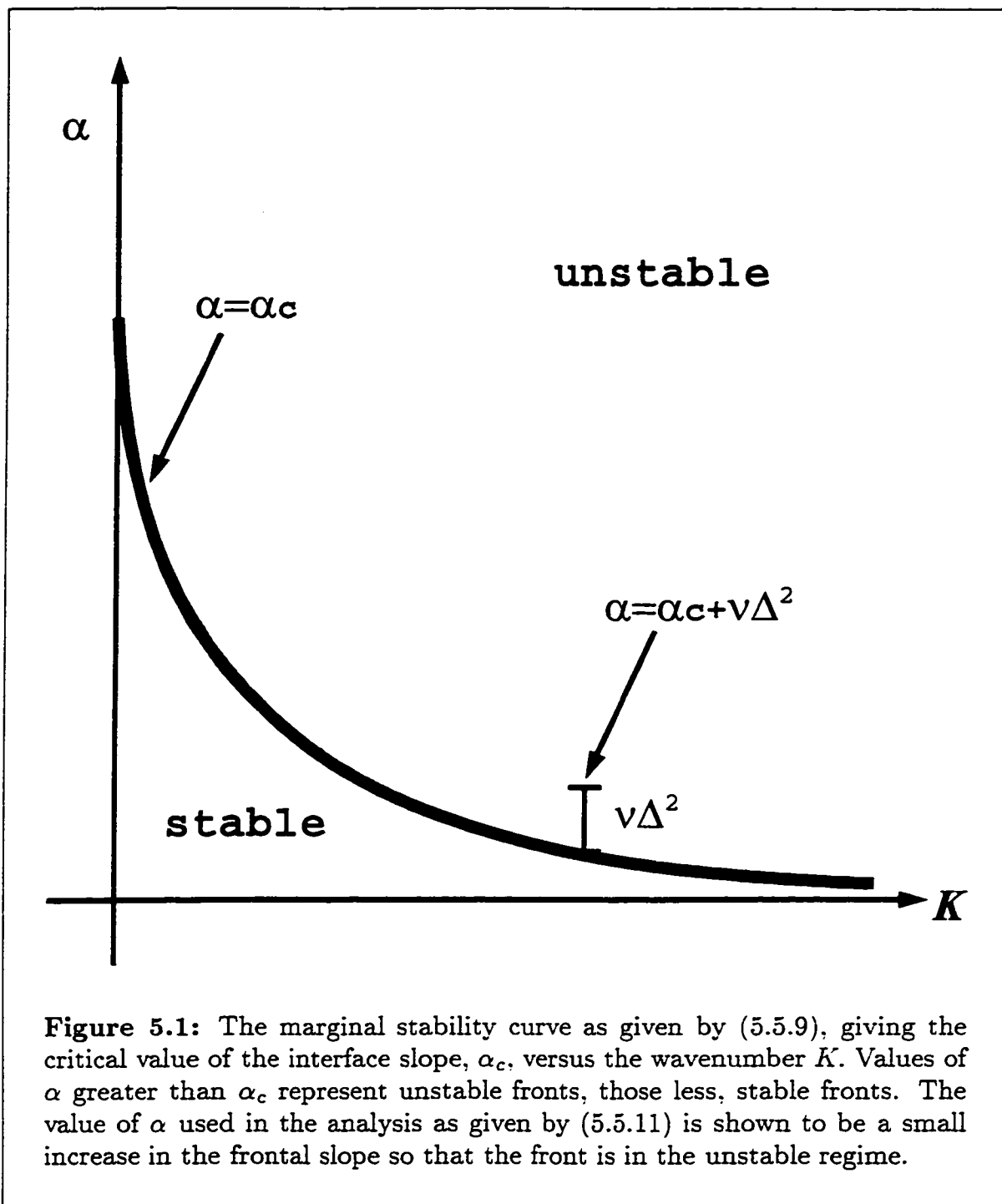
5. SE model

(5.5.12), in linear operator in (5.5.8) gives

$$\mathcal{L}(\partial_t + \Delta\partial_T, \partial_x + \Delta\partial_X + \Delta^2\partial_{\mathfrak{X}}, \partial_y, \alpha_c + \nu\Delta^2) =$$

$$\mathcal{L}(\partial_t, \partial_x, \partial_y, \alpha_c) + \Delta\left[\mathcal{L}_1(\partial_t, \partial_x, \partial_y, \alpha_c)\partial_T + \mathcal{L}_2(\partial_t, \partial_x, \partial_y, \alpha_c)\partial_X\right]$$

$$+ \Delta^2\left[\frac{1}{2}\mathcal{L}_{11}(\partial_t, \partial_x, \partial_y, \alpha_c)\partial_{TT} + \mathcal{L}_{12}(\partial_t, \partial_x, \partial_y, \alpha_c)\partial_{TX}\right.$$

$$+ \frac{1}{2}\mathcal{L}_{22}(\partial_t, \partial_x, \partial_y, \alpha_c)\partial_{XX} + \mathcal{L}_2(\partial_t, \partial_x, \partial_y, \alpha_c)\partial_{\mathfrak{X}}$$

$$\left. + \nu\mathcal{L}_4(\partial_t, \partial_x, \partial_y, \alpha_c)\right]. \tag{5.5.13}$$

As in §3.5, the quantities h and ψ are expanded in a power series in the small quantity Δ as follows:

$$(h, \psi) = (h, \psi)^{(0)} + \Delta(h, \psi)^{(1)} + \Delta^2(h, \psi)^{(2)} + \ldots. \tag{5.5.14}$$

Using this expansion in equations (5.5.7) and (5.5.4) with the slightly unstable frontal slope, (5.5.11), and the slow variables, (5.5.12), making use of (5.5.13) and setting the coefficients of terms in similar orders of Δ to zero gives a series of problems that must be solved. The solvability conditions that arise at each order according to the F.A.T. give rise to an evolution equation for the slowly varying amplitude of the linear solution.

The leading-order problem is given by

$$\mathcal{L}(\partial_t, \partial_x, \partial_y, \alpha_c)h^{(0)} = 0,$$
$$\alpha_c\psi_x^{(0)} = -h_t^{(0)}. \tag{5.5.15}$$

As in §5.2, we assume the perturbations have a wave form, that is, we let

$$h^{(0)} = A(X, \mathfrak{X}, T)\exp[i(kx - \omega t)]\widetilde{h}(y) + c.c., \tag{5.5.16}$$

$$\psi^{(0)} = B(X, \mathfrak{X}, T)\exp[i(kx - \omega t)]\widetilde{\psi}(y) + c.c., \tag{5.5.17}$$

where A, B represent the slow time and space evolution of the solution envelope.

174

5. SE model

This gives the system

$$\mathfrak{L}(-i\omega, ik, \partial_y, \alpha_c)\widetilde{h} = -2\omega^2[\partial_{yy} + \ell^2]\widetilde{h} = 0,$$

$$\widetilde{\psi} = \frac{\omega}{k\alpha_c}\widetilde{h}, \tag{5.5.18}$$

which is just system (5.2.21) with $\alpha = \alpha_c$ and has the nontrivial solution $\widetilde{h}(y.\ell)$ given by (5.2.23) provided (5.2.33) holds, that is, if

$$\omega(k.\ell) = -\frac{k\beta}{2K^2}. \tag{5.5.19}$$

The $O(\Delta^2)$ problem is given by

$$\mathfrak{L}(\partial_t, \partial_x, \partial_y, \alpha_c)h^{(1)} = [\mathfrak{L}_1(\partial_t, \partial_x, \partial_y, \alpha_c)\partial_T + \mathfrak{L}_2(\partial_t.\partial_x.\partial_y.\alpha_c)\partial_X]\,h^{(0)}$$

$$+ (\nabla_t^2 + \beta\partial_x)M^{(0)} + -\alpha\partial_x N_1^{(0)}. \tag{5.5.20}$$

$$\alpha\psi_x^{(1)} = -h_t^{(1)} - h_T^{(0)} - \alpha\psi_X^{(0)} + M^{(0)}. \tag{5.5.21}$$

where the $M^{(0)}$ and $N_1^{(0)}$ represent the leading-order terms in M and N_1, respectively, when (5.5.14), (5.5.11), and (5.5.12) are used. Using the leading-order solution (5.5.16, 5.5.17, 5.5.18, 5.2.23) gives

$$\mathfrak{L}(\partial_t, \partial_x, \partial_y, \alpha_c)h^{(1)} =$$

$$- \Big\{ [A_T\mathfrak{L}_1(-i\omega(k,\ell), ik, \partial_y, \alpha_c) + A_X\mathfrak{L}_2(-i\omega(k,\ell), ik.\partial_y, \alpha_c)]\,\widetilde{h}(y.\ell)$$

$$+ A\alpha_c^3 k^2\mu(1 - 2\aleph\mu)\left[\ell\cos(\ell y) - (k^2 + \ell^2)\left(y - \frac{L}{2}\right)\sin(\ell y)\right] \tag{5.5.22}$$

$$\Big\}\exp[i(kx - \omega t)] + c.c.,$$

$$\alpha\psi_x^{(1)} = -h_t^{(1)} - A_T\widetilde{h}(y, \ell)\exp[i(kx - \omega t)] + c.c. \tag{5.5.23}$$

Note that all quadratic terms, terms proportional to $\exp(2ik\theta)$, have cancelled each other as in §3.5 but in contrast to the analysis of §3.6. Examining the operator $\mathfrak{L}$ as given in (5.5.8) gives that

$$\mathfrak{L}_1(\partial_t, \partial_x, \partial_y, \alpha_c) = 2\nabla_t^2 + \beta\partial_x,$$

$$\mathfrak{L}_2(\partial_t, \partial_x, \partial_y, \alpha_c) = 2\partial_{ttx} + \aleph\mu(1 - \mu\aleph)\alpha_c^2(4\partial_{xxx} + 2\partial_{yyx}) + \beta\partial_t. \tag{5.5.24}$$

5. SE model

Using (5.2.23), (5.5.19), and (5.5.9) gives that

$$\mathfrak{L}_1\left(-i\omega(k,\ell), ik, \partial_y, \alpha_c\right)\widetilde{h}(y,\ell) = 0,$$

$$\mathfrak{L}_2\left(-i\omega(k,\ell), ik, \partial_y, \alpha_c\right)\widetilde{h}(y,\ell) = -i\frac{k^3\beta^2}{(k^2+\ell^2)^2}\widetilde{h}(y,\ell). \tag{5.5.25}$$

As in §3.4, it is reasonable to assume that the solution has the form

$$h^{(1)} = C(X, \mathfrak{X}, T)G(y)\exp[i(kx - \omega t)] + c.c. + \Phi(y, X, \mathfrak{X}, T). \tag{5.5.26}$$

The function Φ is a solution to the left-hand side of (5.5.22) since it is independent of x and t. Its inclusion is necessary in the next order problem where its form will be derived. Substituting (5.5.26) into (5.5.22) using (5.5.25) gives

$$G'' + \ell^2 G = \frac{1}{C(X, \mathfrak{X}, T)}\left\{ 2ikA_X\widetilde{h}(y,\ell) \right.$$

$$\left. + A\frac{\alpha_c\mu(1-2\aleph\mu)}{2\aleph\mu(1-\aleph\mu)}\left[\ell\cos(\ell y) - (k^2+\ell^2)\left(y - \frac{L}{2}\right)\sin(\ell y)\right] \right\}. \tag{5.5.27}$$

The left-hand side obviously has the homogeneous solution $G(y) = \widetilde{h}(y,\ell) = \sin(\ell y)$, and we can apply the F.A.T. as in §3.5. The form of the eigenfunction, $\widetilde{h}(y,\ell)$, is identical to that given in §3.5, and the integrals discussed there apply. The final two terms on the right-hand side in (5.5.27) integrate to zero so that the F.A.T. reduces to requiring that

$$A_X = 0, \tag{5.5.28}$$

so that $A = A(\mathfrak{X}, T)$. Similarly, all variables are now assumed to be independent of X. At first glance, this result may appear different than that obtained at the same order for the ST model in §3.5. For the ST model, the $O(\Delta^2)$ problem determined that the wave amplitude travelled at the group speed (see derivation of (3.6.23)). However, if the expression for the group speed for the SE model, (5.2.29), is examined in the limit as $\alpha \rightarrow \alpha_c$, it is determined that the group speed becomes infinite on the marginal stability curve. (Note that the two waves that coalesce on the marginal stability have equal phase speeds, but not group speeds. One tends to

176

5. SE model

positive infinity and the other to negative infinity.) The result (5.5.28) corresponds to the envelope travelling at the infinite group speed so that no variation in X is seen.

Now the solutions to (5.5.22) can be found as $C(\mathfrak{X}, T) = A(\mathfrak{X}, T)$ and

$$
G = -\alpha_c \frac{\mu(1 - 2\aleph\mu)}{2\aleph\mu(1 - \aleph\mu)} \left[\frac{(k^2 + \ell^2)^2}{4\ell} y(y - L) \cos(\ell y) \right.
$$
$$
\left. - \frac{(k^2 - \ell^2)}{4\ell^2} \left(y - \frac{L}{2} \right) \sin(\ell y) \right]. \tag{5.5.29}
$$

Given (5.5.29) the solution to (5.5.23) is given by

$$
\psi^{(1)} = \frac{i}{k\alpha_c} A_T \widetilde{h}(y, \ell) + AF(y) \exp[i(kx - \omega t)] + c.c., \tag{5.5.30}
$$

where

$$
F = -c \frac{\mu(1 - 2\aleph\mu)}{2\aleph\mu(1 - \aleph\mu)} \left[\frac{(k^2 + \ell^2)^2}{4\ell} y(y - L) \cos(\ell y) \right.
$$
$$
\left. - \frac{(k^2 - \ell^2)}{4\ell^2} \left(y - \frac{L}{2} \right) \sin(\ell y) \right]. \tag{5.5.31}
$$

Note that a function analogous to Φ could be added to (5.5.30) but this function plays no role in the final equation and so is not included.

5. SE model

The $O(\Delta^3)$ problem is given by

$$
\mathfrak{L}(\partial_t, \partial_x, \partial_y, \alpha_c) h^{(2)}
$$

$$
= \left\{ \left[A_{TT} \frac{1}{2} \mathfrak{L}_{11}(-i\omega(k,\ell), ik, \partial_y, \alpha_c) + A_{\mathfrak{X}} \mathfrak{L}_2(-i\omega(k,\ell), ik, \partial_y, \alpha_c) \right. \right.
$$

$$
\left. + A\nu \mathfrak{L}_4(-i\omega(k,\ell), ik, \partial_y, \alpha_c) \right] \widetilde{h}(y,\ell)
$$

$$
- A\alpha_c k^2 \aleph \mu (1 - \aleph \mu) \left[2(k^2 + \ell^2)\Phi_y \sin(\ell y) \right. \tag{5.5.32}
$$

$$
\left. + 2\ell \Phi_{yy} \cos(\ell y) + 2\Phi_{yyy} \sin(\ell y) \right]
$$

$$
\left. - iA\gamma(y) + A_T M_{A_\xi}(y) \right\} \exp[i(kx - \omega t)]
$$

$$
+ M_{e^2} \exp[2i(kx - \omega t)] + c.c..
$$

$$
\alpha \psi_x^{(2)} + h_t^{(2)} = -\Phi_T + \frac{\ell \sin(2\ell y)}{\alpha_c} (|A|^2)_T + P_e \exp[i(kx - \omega t)]
$$
$$
+ P_{e^2} \exp[2i(kx - \omega t)] + c.c.. \tag{5.5.33}
$$

where

$$
\gamma(y) = -\mu k^2 \alpha_c^3 (1 - 2\aleph\mu) \left[\left(y - \frac{L}{2} \right)(G'' - k^2 G) + G' \right]
$$

$$
+ \mu \alpha_c (k^2 + \ell^2) \left(y - \frac{L}{2} \right)^2 \sin(\ell y) \tag{5.5.34}
$$

$$
- \mu \alpha_c \ell \left(y - \frac{L}{2} \right) \cos(\ell y),
$$

and the terms M_{A_ξ}, M_{e^2}, P_e, and P_{e^2} are not needed in the following analysis and so are not expanded here.

It is now clear why it was necessary to add the homogeneous solution to the second order solution $h^{(1)}$. It is necessary to balance the terms that arise in (5.5.33) that are independent of x, t and, thus, are also homogeneous solutions to the LHS

5. SE model

of (5.5.33). Therefore, we choose Φ such that these terms vanish, that is,

$$\Phi_T = \frac{\ell \sin(2\ell y)}{\alpha_c} \left(|A|^2\right)_T,$$

or, after integrating,

$$\Phi = \frac{\ell}{\alpha_c} \left(|A|^2 - |A_0|^2\right) \sin(2\ell y), \tag{5.5.35}$$

where $A_0 = A_0(\mathfrak{X}) = A(\mathfrak{X}, 0)$ is the initial amplitude of the perturbation. Note that in (5.5.35) we have chosen the integration constant so that the mean flow correction Φ is initially zero. This is not necessarily required and it will be discussed later how this influences the solution. Also note that the case of the long-wave–short-wave resonance that occurred in §3.4 does not occur here. This is simply because all modes on the marginal stability curve have a finite phase speed and an infinite group speed and so the two can never be equal. The solution (5.5.35) cannot be found if $\alpha_c = 0$, but this is the case of a flat front and is of no interest.

Using (5.5.35) we have that

$$\begin{aligned} \alpha_c k^2 \aleph\mu(1 - \aleph\mu) &\left[2(k^2 + \ell^2)\Phi_y \sin(\ell y) + 2\ell\Phi_{yy}\cos(\ell y) + 2\Phi_{yyy}\sin(\ell y)\right] \\ &= -2k^2\ell^2\aleph\mu(1 - \aleph\mu)(k^2 - \ell^2)\left[\sin(\ell y) - \sin(3\ell y)\right]\left(|A|^2 - |A_0|^2\right). \end{aligned} \tag{5.5.36}$$

Assuming

$$\begin{aligned} h^{(2)} =& C_1(X, T, \tau)N_1(y)\exp[i(kx - \omega t)] \\ &+ C_2(X, T, \tau)N_2(y)\exp[2i(kx - \omega t)] + c.c., \end{aligned}$$

and considering the $\exp[i(kx - \omega t)]$ problem for the equation (5.5.32) gives

$$\begin{aligned} C_1(X,T,\tau)&\mathfrak{L}(-i\omega(k,\ell), ik, \partial_y, \alpha_c)N_1(y) \\ =& \left[(k^2 + \ell^2)A_{TT} + i\frac{k^3\beta^2}{(k^2 + \ell^2)^2}A_{\mathfrak{X}} \right.\\ &\left. - 2\nu k^2\alpha_c\aleph\mu(1 - \aleph\mu)(k^2 + \ell^2)A\right]\tilde{h}(y, \ell) \\ &- 2ik^2\ell^2\aleph\mu(1 - \aleph\mu)(k^2 - \ell^2)A\left(|A|^2 - |A_0|^2\right)\left[\sin(\ell y) - \sin(3\ell y)\right] \\ &- iA\gamma(y) + A_\xi M_{A_\xi}(y), \end{aligned} \tag{5.5.37}$$

179

5. SE model

where we've used (5.5.25) and that

$$\frac{1}{2}\mathcal{L}_{11}(-i\omega(k,\ell),ik,\partial_y,\alpha_c)\widetilde{h}(y,\ell) = -(k^2 + \ell^2)\widetilde{h}(y,\ell).$$

$$\mathcal{L}_4(-i\omega(k,\ell),ik,\partial_y,\alpha_c)\widetilde{h}(y,\ell) = 2\nu k^2\alpha_c\aleph\mu(1-\aleph\mu)(k^2 + \ell^2)\widetilde{h}(y,\ell).$$

(5.5.38)

Once again, equation (5.5.37) has the homogeneous solution $N_1(y) = \widetilde{h}(y,\ell)$. It follows from the F.A.T. that a solution exists iff it holds that

$$A_{TT} + i\chi A_{\chi} = (\sigma^2 - \Gamma)A - \Sigma\left(|A|^2 - |A_0|^2\right)A,$$

(5.5.39)

where

$$\chi = \frac{k^3\beta^2}{(k^2 + \ell^2)^3}.$$

(5.5.40)

$$\sigma^2 = 2\nu k^2\aleph\mu(1 - \aleph\mu)\alpha_c,$$

(5.5.41)

$$\Sigma = \frac{2\aleph\mu(1 - \aleph\mu)k^2\ell^2(k^2 - \ell^2)}{(k^2 + \ell^2)}.$$

(5.5.42)

$$\Gamma = -\frac{2}{L(k^2 + \ell^2)}\int_0^L \gamma(y)\widetilde{h}(y,\ell)\,dy.$$

(5.5.43)

and we've used that

$$\int_0^L M_{A_\ell}(y)\widetilde{h}(y,\ell)\,dy = 0.$$

Equation (5.5.39) is the unstable nonlinear Schrödinger equation (UNLS) derived in Pedlosky (1972) and presented in Tan and Liu (1995) for a two-layer Phillips model, derived in Reszka (1997) for the WVT model, and derived in Mooney and Swaters (1996) for the LST model. The parameter σ is the small linear growth of the marginally unstable mode (see (5.5.10)). The parameter Σ represents the nonlinear interactions. The parameter Γ represents the corrections to the linear solution growth rate as higher order, linear terms are considered. We write the equation in a slightly simpler form by introducing

$$\varsigma = \sigma^2 - \Gamma + \Sigma|A_0|^2,$$

(5.5.44)

5. SE model

giving from (5.5.39)

$$A_{TT} + i\chi A_{\bar{x}} = \varsigma A - \Sigma A|A|^2.$$ (5.5.45)

The correction term Γ arises from the approximation that the slope is small in the basic state and so certain terms in the linear equation are not included in the leading-order problem. These terms are included when we consider the higher order terms as we examine the weakly nonlinear analysis and hence the presence of Γ in the envelope equation. These correction terms can either stabilize or further destabilize the leading-order, marginally-unstable front depending on whether Γ is positive or negative. The size of Γ is very sensitive to the y structure of the linear solution and grows rapidly as meridional length scale increases. That is, the size of Γ increases with the domain width L but decreases with the meridional wavenumber. This illustrates that the error in the approximation becomes greater as the size of $y - L/2$ grows. In Figure 5.2, plots of Γ and σ^2 are given versus k/ℓ for three values of L. For small L, Γ is small compared to σ^2 and has little effect on the coefficient ς. It can be seen that as L increases Γ grows to a size where it can dominate σ^2 so that $\sigma^2 - \Gamma$ is negative for small k/ℓ. That is, the front is linearly stable for these parameter values. At higher values of k/ℓ the instability is enhanced as Γ becomes negative.

A second way of looking at this is that the correction terms will move the marginal stability curve. If this adjustment is great enough, the analysis is no longer being carried out on a marginally unstable front but on a marginally stable front. In the following analysis, we wish only to consider the nonlinear modulation of a linearly unstable front and therefore assume that $\sigma^2 - \Gamma$ is positive. We do present some brief analysis of linearly stable fronts in §5.8, and cases where $\sigma^2 - \Gamma$ is negative are included in this analysis.

Before looking at solutions of this equation, it should be noted that the assumption that $\alpha_c > 0$ is not important in the analysis. Indeed, the above analysis can be carried out with $\alpha_c < 0$ and the same evolution equation is obtained. The only change that occurs is that in this case

$$\alpha = \alpha_c - \nu\Delta^2.$$

This is reasonable as the linear results are identical for positive and negative α.
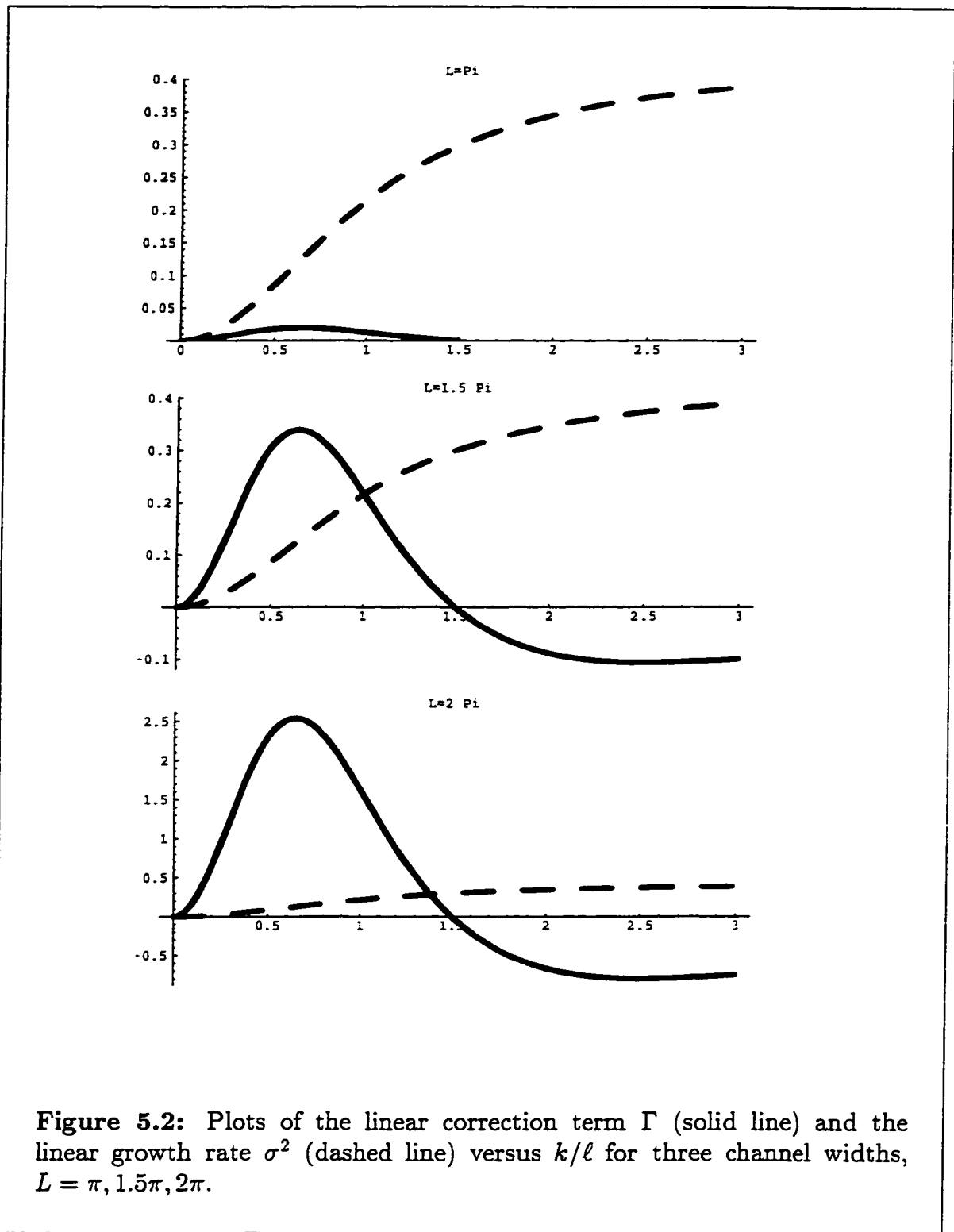
5. SE model

Figure 5.2: Plots of the linear correction term Γ (solid line) and the linear growth rate σ^2 (dashed line) versus k/ℓ for three channel widths, $L = \pi, 1.5\pi, 2\pi$.

5. SE model

5.6 Transformed Model Wedge Front

The transformed model that was used to find a solution in §5.2 will also be used in the weakly nonlinear analysis. The analysis is virtually identical to that in the previous section, and so we will be brief. The variables are given by the basic solution plus a smaller perturbation, that is,

$$\hbar = \aleph + \alpha y + \Delta \hbar,$$
$$\psi = \Delta \psi. \tag{5.6.1}$$

Substituting (5.6.1) into the transformed model (5.1.10) and (5.1.11), gives the fully nonlinear equations

$$\hbar_t + \alpha w_x = \Delta M. \tag{5.6.2}$$
$$\nabla^2 \psi_t + \beta w_x - \alpha \nabla^2 \hbar_x = \Delta N. \tag{5.6.3}$$

where

$$M = J(\hbar, w), \tag{5.6.4}$$
$$N = J(\nabla^2 w, \psi) + J(\nabla^2 \hbar, \hbar). \tag{5.6.5}$$

We can construct an equation that eliminates w from the linear terms by taking $(\nabla_t^2 + \beta \partial_x)(5.5.2) - \alpha \partial_x (5.5.3)$ to give

$$\mathfrak{L}(\partial_t, \partial_x, \partial_y, \alpha)\hbar = \Delta[(\nabla_t^2 + \beta \partial_x)M - \alpha \partial_x N], \tag{5.6.6}$$

where

$$\mathfrak{L}(\partial_t, \partial_x, \partial_y, \alpha) = \nabla_{tt}^2 + \alpha^2 \nabla_{xx}^2 + \beta \partial_{xt}. \tag{5.6.7}$$

Equations (5.6.6) and (5.6.2) are the equations we will study. The equations are very similar to those of the previous section with a small change in the linear operator, no fast-varying linear terms in the higher order problems, and some simplification in the nonlinear terms.

183

5. SE model

The analysis proceeds as before. We begin by choosing a marginally unstable curve by choosing the frontal slope as in (5.5.11) where now

$$\alpha_c = \frac{\beta}{2(k^2 + \ell^2)}.$$

(5.6.8)

We introduce the slow space and time variables (5.5.12) and the analogue of the expansion (5.5.14). We proceed to solve the leading-order problem, obtaining the linear solution given in §5.2, and second order problem, getting that the solution is independent of X. Note that we do not get a solution corresponding to (5.5.29) since there are no fast-varying linear terms in this and higher order problems. We proceed to the $O(\Delta^2)$ problem, eliminate the constant terms, apply the F.A.T. and once again obtain the envelope evolution equation (5.5.45) with

$$\chi = \frac{k^3 \beta^2}{(k^2 + \ell^2)^3},$$

(5.6.9)

$$\varsigma = 2\nu k^2 \alpha_c + \Sigma |A_0|^2,$$

(5.6.10)

$$\Sigma = \frac{2k^2 \ell^2 (k^2 - \ell^2)}{(k^2 + \ell^2)}.$$

(5.6.11)

As before the analysis can be carried out with $\alpha_c < 0$ and the same evolution equation is obtained.

The fact that the evolution equations are so similar for the two basic states is not surprising. However it should be stressed that the analysis of this section holds for fronts with no limitations on the frontal slope, while the previous section assumed the frontal slope was small. This leads to the very important conclusion that weakly nonlinear analysis that is performed under simplifying assumptions can capture the essential nonlinear aspects of the model even when these assumptions break down. However, the similarity of the evolution equations is also a result of the similarity of the eigenfunctions and hence, the expansion of the nonlinear terms. As shown in the analysis of the ST model if the structure of the eigenfunction changes a greater array of interactions can occur (see §3.6). This leaves the question open as to whether the analysis carried out here captures all the essential nonlinear effects of a basic-state front that has an outcropping.

5. SE model

5.7 Solutions to the Amplitude Equation

The amplitude equation (5.5.45) has been derived for other models similar to the SE model. It is the equation derived in Pedlosky's weakly nonlinear work for a Phillips model (Pedlosky, 1972) and also has been derived in the weakly nonlinear analysis of the LST model (Mooney and Swaters, 1996) and the WVT model (Reszka, 1997). The first term on the right-hand side in the equation represents the linear effects in the model and gives rise to linear growth. (As mentioned before, we are assuming $\sigma^2 - \Gamma$ is positive in the gently sloping front analysis and so $\varsigma > 0$, for both models.) The second term on the right represents the influence of the nonlinear terms in the model. For $\Sigma > 0$, this term will dampen the growth of the instability; for $\Sigma < 0$, this term will enhance the growth of the instability. The fact that Σ changes sign at $O(1)$ values in this model will lead to additional analysis not found in Pedlosky (1970) or Mooney and Swaters (1996) but similar to that found in Reszka (1997). On the other hand, the lack of a critical shear value, a positive critical value of α that must be exceeded for instability, results in no analysis analogous to the critical shear analysis found in Pedlosky (1982) and Mooney and Swaters (1996).

First, we analyze flows that are independent of $\mathfrak{X}$ by letting

$$A(\mathfrak{X}, T) = f(T),$$

where for simplicity, f is assumed to be real (see Pedlosky, 1970 or Mooney and Swaters, 1996). This leads to a nonlinear ordinary differential equation for f given by

$$f'' - \varsigma f + \Sigma f^3 = 0, \tag{5.7.1}$$

which is the equation examined in Appendix 5. The form of the solution depends critically on the sign of Σ as one would expect. If $\Sigma > 0$ the solution lies in region 1 or 2 and is a bounded periodic solution. The exact form of the solution depends on the sign of γ_3 as defined by (A.5.6), which when written in terms of the parameters of this section is defined by

$$\gamma_3 = A_0^4 + \frac{2}{\Sigma} \left(\sigma^2 A_0^2 - (A_0')^2 \right), \tag{5.7.2}$$

where we have ignored Γ. Therefore, γ_3 is only negative if A'_0 is sufficiently large. Two standard cases can be considered:

1. $A'_0 = 0$: the initial amplitude of the envelope is specified, and it is not assumed to be changing.

2. $A'_0 = \sigma A_0$: the initial amplitude is assumed to be growing at a rate equal to that of the linear growth rate.
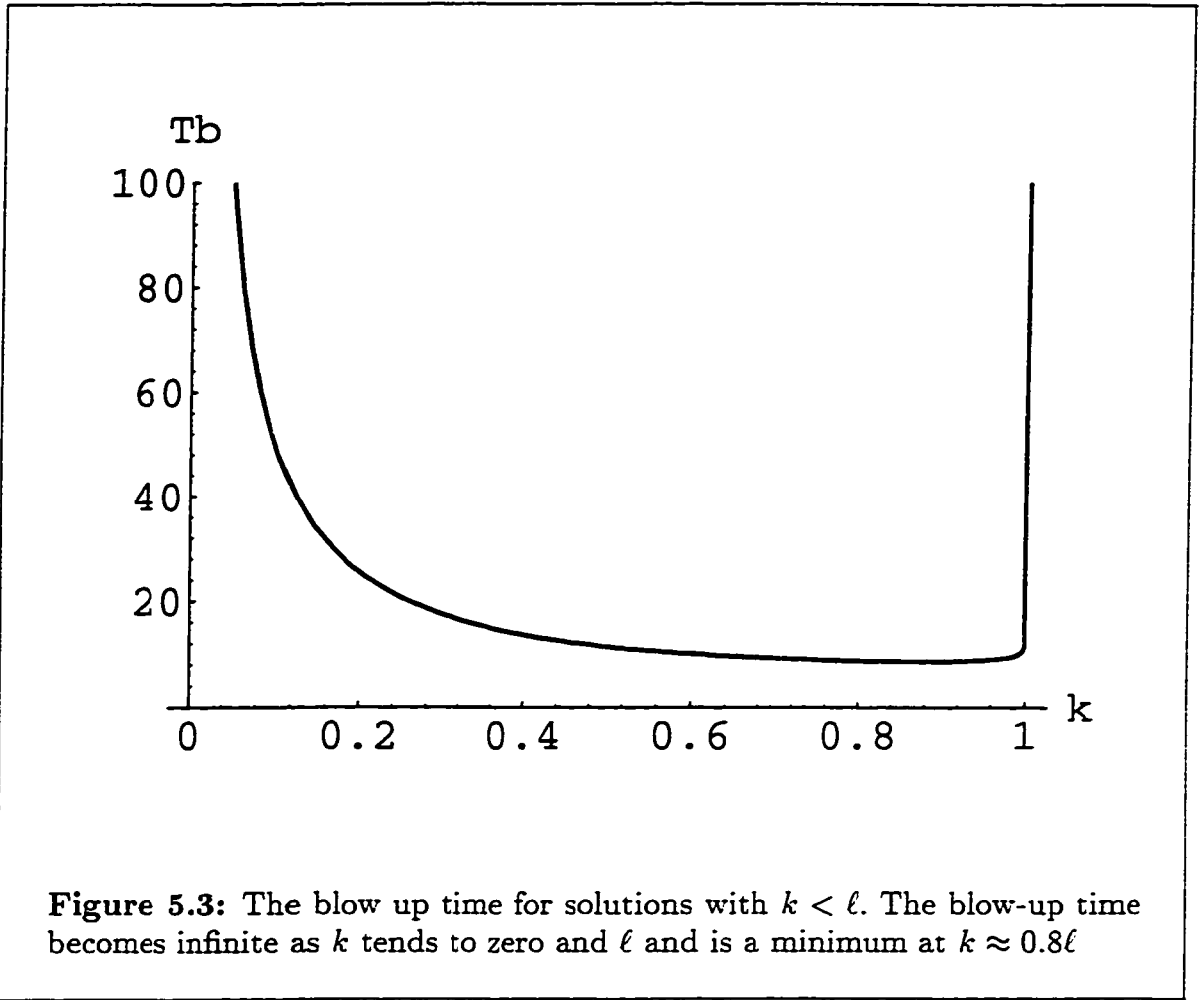
Both cases give rise to γ_3 being positive. The solution lies in region 2 and is plotted in Figure A.5.5. The two different initial conditions have no effect other than shifting the starting point of the solution. The solution grows initially due to linear instability, the instability is inhibited by nonlinear terms, and the solution reaches a maximum. The growth is reversed and the amplitude decreases until linear terms dominate once again, creating linear growth. and the process repeats itself. If A'_0 is chosen sufficiently large to make γ_3 negative, the solution lies in region 1 and oscillates through zero, that is, the wave changes phase by 180 degrees.

One can provide a detailed analysis of the characteristics of these solutions (see Mooney and Swaters, 1996) but we will only give a brief comment on the main characteristics. For solutions in region 2 the main characteristics are the period of oscillation and the maximum amplitude of the solution. As found in Reszka (1997) and Mooney and Swaters (1996) as k increases the period decreases and the maximum amplitude decreases. As $k \rightarrow \ell$, that is, as Σ tends to zero, the period and the maximum amplitude both tend to infinity.

If $\Sigma < 0$, the solution lies in region 3, 4, or 7, and becomes infinite in finite time. A typical plot of the solutions in regions 3, 4, or 7 is given in Figure A.5.5. The solutions grow initially due to the linear instability and, as the amplitude becomes finite, nonlinear terms actually enhance the growth. The growth continues to accelerate leading to the amplitude becoming infinite in finite time. This finite blow-up time can be calculated and is plotted in Figure 5.3 versus the ratio k/ℓ for $\beta = 1$ and $\mu = 0.5$. The blow-up time becomes large as k tends to ℓ and zero. The time of blow-up is a minimum at an along channel wavenumber just slightly less than the cross channel wavenumber, $k \approx 0.8737\ell$, where $T_b = 8.4143$.

In deriving the evolution equation, we considered only weak nonlinear effects by considering a wave of small amplitude. The above analysis suggests that nonlinear effects can enhance the linear growth so that the wave amplitude becomes large very quickly. Once the wave has become large, the evolution is fully nonlinear. It is

Figure 5.3: The blow up time for solutions with $k < \ell$. The blow-up time becomes infinite as k tends to zero and ℓ and is a minimum at $k \approx 0.8\ell$

expected that the fully nonlinear effects will eventually suppress the growth of the wave, since a wave of infinite amplitude is unphysical.

We now return to (5.5.45), which includes spatial variability. We have illustrated the time behaviour of the solutions and now quickly illustrate that the stable, periodic solutions found when $\Sigma > 0$ can be associated with travelling-wave and soliton solutions when slow spatial variations are included with the appropriate boundary conditions. Such solutions were also found in Pedlosky (1972), Mooney and Swaters (1996), and Reszka (1997). In order to cast (5.5.45) into the standard form examined in Appendix 5, we first make the transformation (Reszka, 1997)

$$ A(X_2, T) = \exp\left(\frac{i}{\chi} \int_0^{X_2} -\varsigma(\xi)\, d\xi \right) C(X_2, T). \qquad (5.7.3) $$

5. SE model

It is necessary to make this transformation, as opposed to the simple rearranging done previously, because A_0 now depends on $\mathfrak{X}$ and therefore cannot be included in the constant coefficients. Note that in Tan and Liu (1995) the term proportional to $|A_0|^2$ is not in their final equation. This term arises from the condition we imposed that the mean flow corrections be initially zero (see the derivation of (5.5.35)). Through this transformation, it is illustrated that whether or not this condition is imposed does not qualitatively affect the basic governing equation. Substituting (5.7.3) into (5.5.45) and simplifying gives

$$C_{TT} + i\chi C_{X_2} + \Sigma C|C|^2 = 0. \tag{5.7.4}$$

Travelling-wave and soliton solutions to (5.7.4) can be obtained by assuming

$$C = \exp\left(i\mathfrak{K}\mathfrak{X} - iVT\right) f(\mathfrak{X} - UT), \tag{5.7.5}$$

where we choose

$$V = -\frac{\chi}{2U}. \tag{5.7.6}$$

Substituting (5.7.5) into (5.5.45) gives

$$f'' - \gamma_1 f + \gamma_2 f^3 = 0, \tag{5.7.7}$$

where

$$\gamma_1 = \frac{(\chi\mathfrak{K} + V^2)}{U^2}, \quad \gamma_2 = \frac{\Sigma}{U^2}.$$

This equation is examined in Appendix 5, and the solutions found there apply. Now, since we are considering a travelling wave, the solutions must be bounded for all values of θ. Hence we must restrict ourselves to regions 1 and 2, where $\gamma_2 > 0$ and hence $\Sigma > 0$. As expected from the previous analysis, travelling-wave/soliton solutions only exist for solutions that are stabilized by nonlinear effects, that is, when $k > \ell$. The solutions in regions 1 and 2 again apply, only now they describe the evolution of the travelling wave. The characteristics of the solutions are the same as described above and are not discussed in detail here. Instead we proceed to illustrate that a limit of these solutions may lead to solitons.

5. SE model

As discussed in Appendix 5, the limit in which $\gamma_3 \to 0$ leads to a bright soliton solution, a solution that tends to zero as $\theta \to \pm\infty$. Assuming $f'(0) = A_{\mathfrak{X}}(0,0) = 0$, this solution is realized if

$$A(0,0) = A_0 = \left(\frac{2(\chi \mathfrak{K} + V^2)}{\Sigma} \right)^{\frac{1}{2}}.$$

The solution from (A.5.27) is

$$f(\mathfrak{X} - UT) = A_0 \, \mathrm{sech} \left[\mathfrak{w}(\mathfrak{X} - UT) \right], \tag{5.7.8}$$

where

$$\mathfrak{w} = \left(\frac{A_0^2 \Sigma}{U^2} \right)^{\frac{1}{2}}. \tag{5.7.9}$$

We can recast the solution (5.7.8) in terms of our original variables by first using

$$|A_0|^2 = |C(\mathfrak{X},0)|^2 = |f(\mathfrak{X})|^2 = A_0^2 \, \mathrm{sech}^2 (\mathfrak{w}\mathfrak{X}).$$

so that

$$\int_0^{\mathfrak{X}} \varsigma(\xi) \, \mathrm{d}\xi = - \int_0^{\mathfrak{X}} (\sigma + \Sigma|A_0|^2) \, \mathrm{d}\xi$$

$$= -\sigma\mathfrak{X} - \frac{\Sigma A_0^2}{\mathfrak{w}} \tanh(\mathfrak{w}\mathfrak{X}). \tag{5.7.10}$$

Using (5.7.8), (5.7.3), (5.7.5), and (5.7.10) the soliton solution is

$$\hbar(x,y,t) = A_0 \, \mathrm{sech} \left[\mathfrak{w}(\mathfrak{X} - UT) \right]$$

$$\times \left\{ \exp \left[i(\tilde{k}x - \tilde{\omega}t) - i\frac{\Sigma A_0^2}{\chi\mathfrak{w}} \tanh(\mathfrak{w}\Delta^2 x) \right] + c.c. \right\}, \tag{5.7.11}$$

where

$$\tilde{k} = k + \Delta^2 \left(\mathfrak{K} - \frac{\sigma}{\chi} \right), \tag{5.7.12}$$

$$\tilde{\omega} = \omega + \Delta V. \tag{5.7.13}$$

189

5. SE model

The relationships between the soliton amplitude, A_0, the soliton width, w, the soliton speed, U, the wavenumber shift, $\mathfrak{K}$, and the frequency shift, V, are given by (5.7.6), (5.7.7), and (5.7.9). We've given the solution here in terms of the notation for the wedge front but the solution holds identically for the gently sloping front with Γ included appropriately.

The form of the solution illustrates that the soliton acts to vary the amplitude of the linear solution. The carrier wave actually alters the form of the original wave changing its wavenumber and phase speed over the slow space and time scales. The tanh term in (5.7.11) and the extra shift term in (5.7.12) can be dropped if we allow an initial mean flow correction. Note that the solution is stable: the amplitude of the soliton does not increase with time. The result of Pedlosky (1972) that the soliton speed lies outside the range of the group speeds of the coalescing waves is not possible as the group speeds are infinite. Further analysis of soliton interaction has been examined in Tan and Liu (1995) but it is not of great importance in this work.

5.8 Stable Solutions

The possibility in §5.5 that the higher order linear terms stabilize the flow leads to the question of how the weakly nonlinear analysis applies to linearly stable flows. The above analysis can be repeated for a marginally stable flow equally well if we choose

$$\alpha = \alpha_c - \nu_s \Delta^2 \qquad (5.8.1)$$

as opposed to (5.5.11). The analysis is identical to that presented above and leads to (5.5.45) with $\nu = -\nu_s$. The only change is that the linear term in (5.5.45), which before was dominated by the contribution of the linearly unstable growth rate σ, corresponds to a linearly stable wave and is of the opposite sign. Thus, all solutions will be initially stable and their amplitude will decrease. In the analysis for unstable waves, it was found that when $k < \ell$ the nonlinear effects enhanced the instability leading to explosive growth and solution breakdown in finite time. It would seem reasonable that these effects would also act on a marginally stable flow. The question of greatest interest is whether nonlinear effects can destabilize the linearly stable flows.

5. SE model

To answer this question, one only need examine solutions to (5.5.45): when $\varsigma < 0$, the solution is linearly stable, and when $\Sigma > 0$, nonlinear terms act to destabilize the flow. So equation (5.7.1) would now correspond to an equation having solutions plotted in Figure A.5.4 and lying in region 6 or 7 as described in Appendix 5. (Solutions in regions 3 and 5 are not possible since by the definition of ς and the assumption that the solution is linearly stable, $\varsigma/\Sigma < |A_0|$.) Solutions in region 6 are stable, periodic solutions (see (A.5.20)). However solutions in region 7 are unstable solutions that become infinite in finite time as discussed previously. These solutions are possible if $\gamma_3 > (\gamma_1/\gamma_2)^2$. This is only possible if A_0' takes on sufficiently large values. For a linearly stable solution, a physical choice for A_0' would be setting it to zero to reflect the neutral growth of amplitude associated with a linearly stable solution. Giving A_0' a large positive value corresponds to giving the initial solution a large kick to get it initially growing, and may not be physical.

5.9 Numerical Solutions

We now examine the numerical solutions to the full nonlinear SE model. The numerical scheme, basic states, and diagnostics are described in §3.11. Since the model predicts linear instability at small wavenumbers, we expect the numerical simulations to illustrate large growth at small scales. We first illustrate this by examining the coupled-front and isolated-front simulations similar to those of the previous sections. Note that the SE model does not have a decoupled limit. Therefore, we do not expect the coupled-front simulation to be similar to that of the RED, ST, and WVT models. In Figure 5.4, we plot the frontal height for times $t = 6$ to 11. These illustrate the growth of small-scale waves initially. These waves begin to form smaller-scale structures until we have a turbulent current. No large-scale structures are seen and the results are independent of the form of the initial perturbation, the inclusion of friction, or the structure of the basic state. Indeed for a isolated front, the results are similar as shown in Figure 5.5. The instability takes somewhat longer to grow, but in the end we see development of small-scale turbulence. Obviously, the ultraviolet catastrophe predicted by the linear analysis is being observed. This growth is not being suppressed by nonlinear terms as the weakly nonlinear analysis suggests.

In Figures 5.6 and 5.7, we examine the energy diagnostics for these simula-
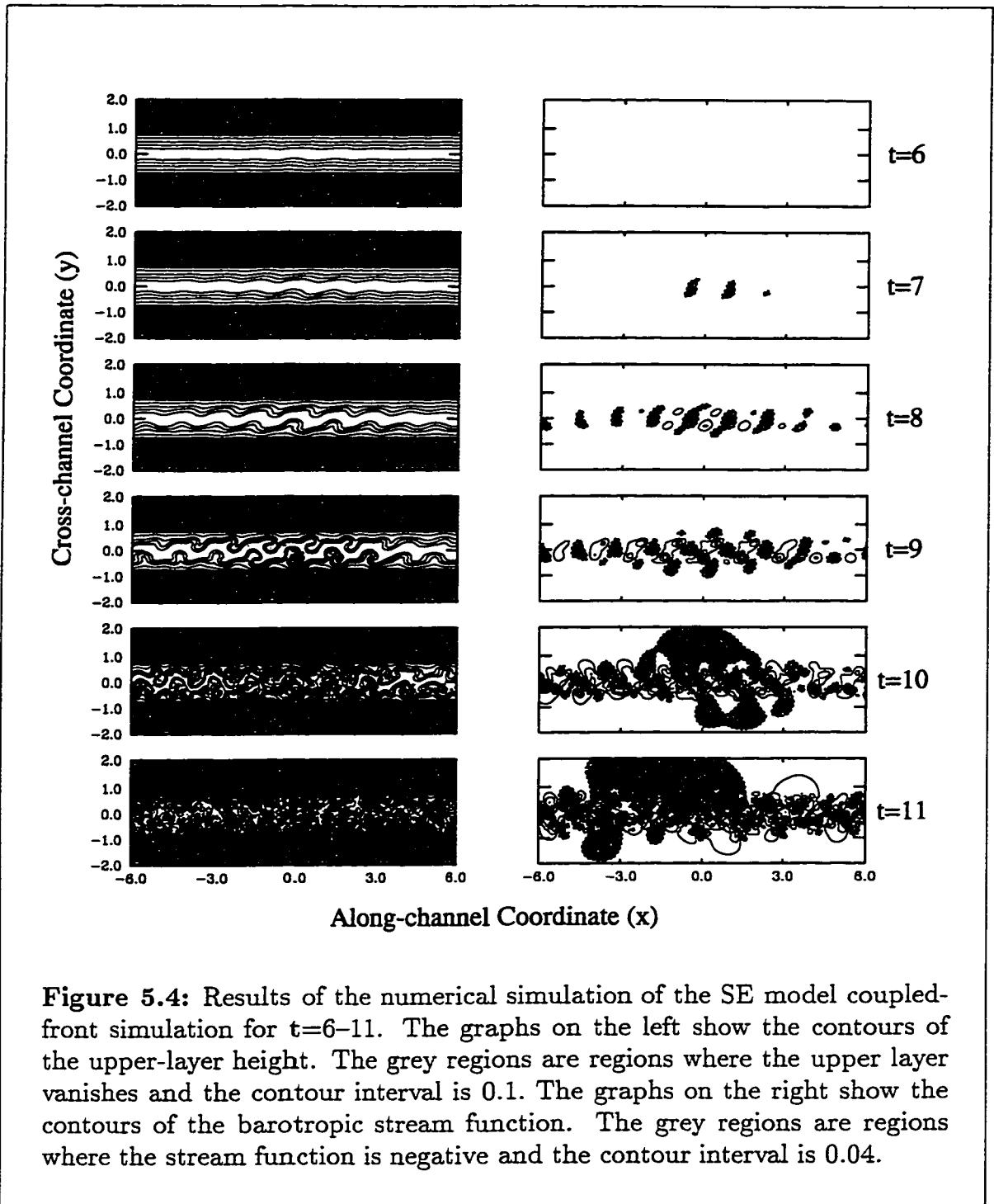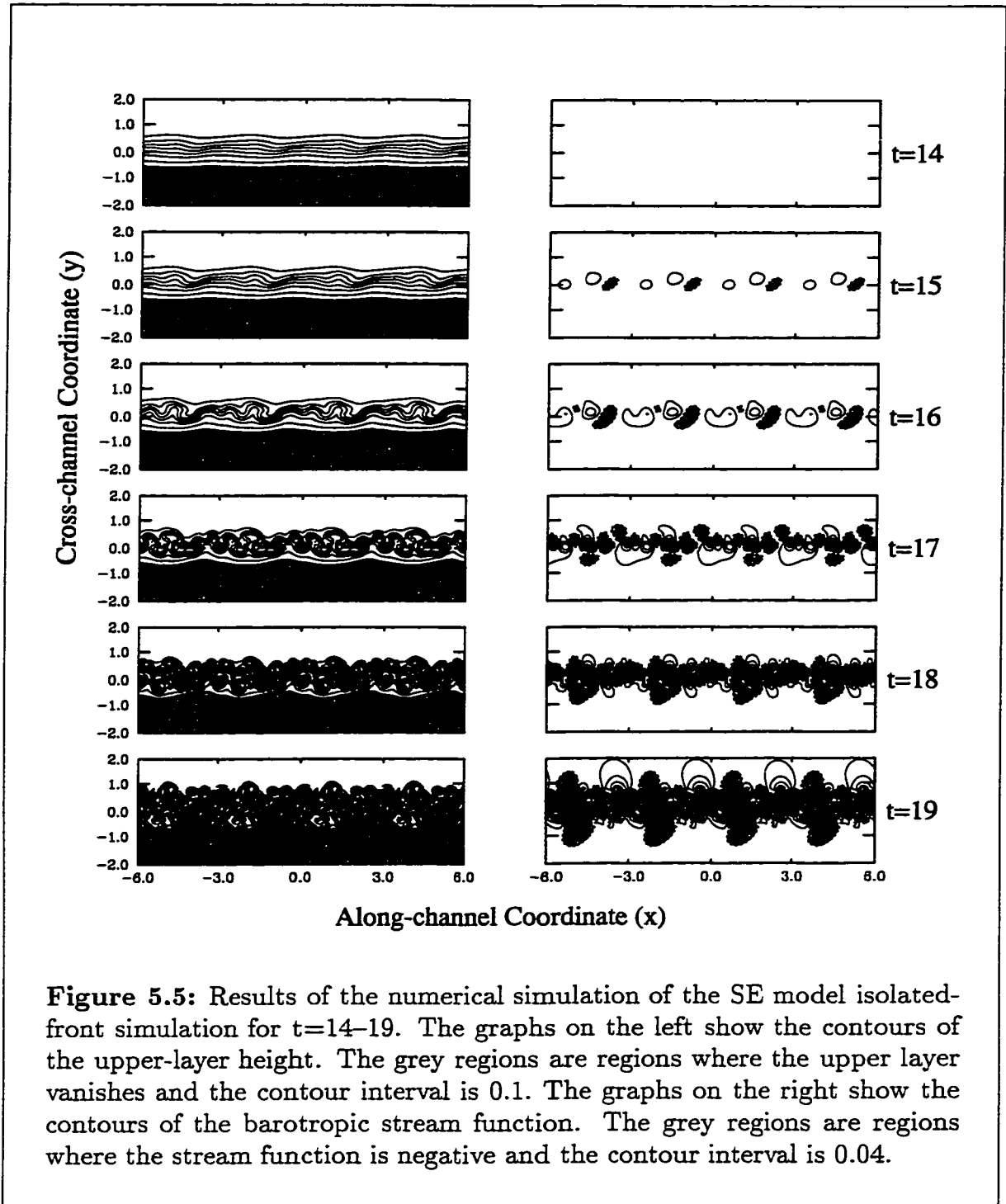
Figure 5.4: Results of the numerical simulation of the SE model coupled-front simulation for t=6–11. The graphs on the left show the contours of the upper-layer height. The grey regions are regions where the upper layer vanishes and the contour interval is 0.1. The graphs on the right show the contours of the barotropic stream function. The grey regions are regions where the stream function is negative and the contour interval is 0.04.
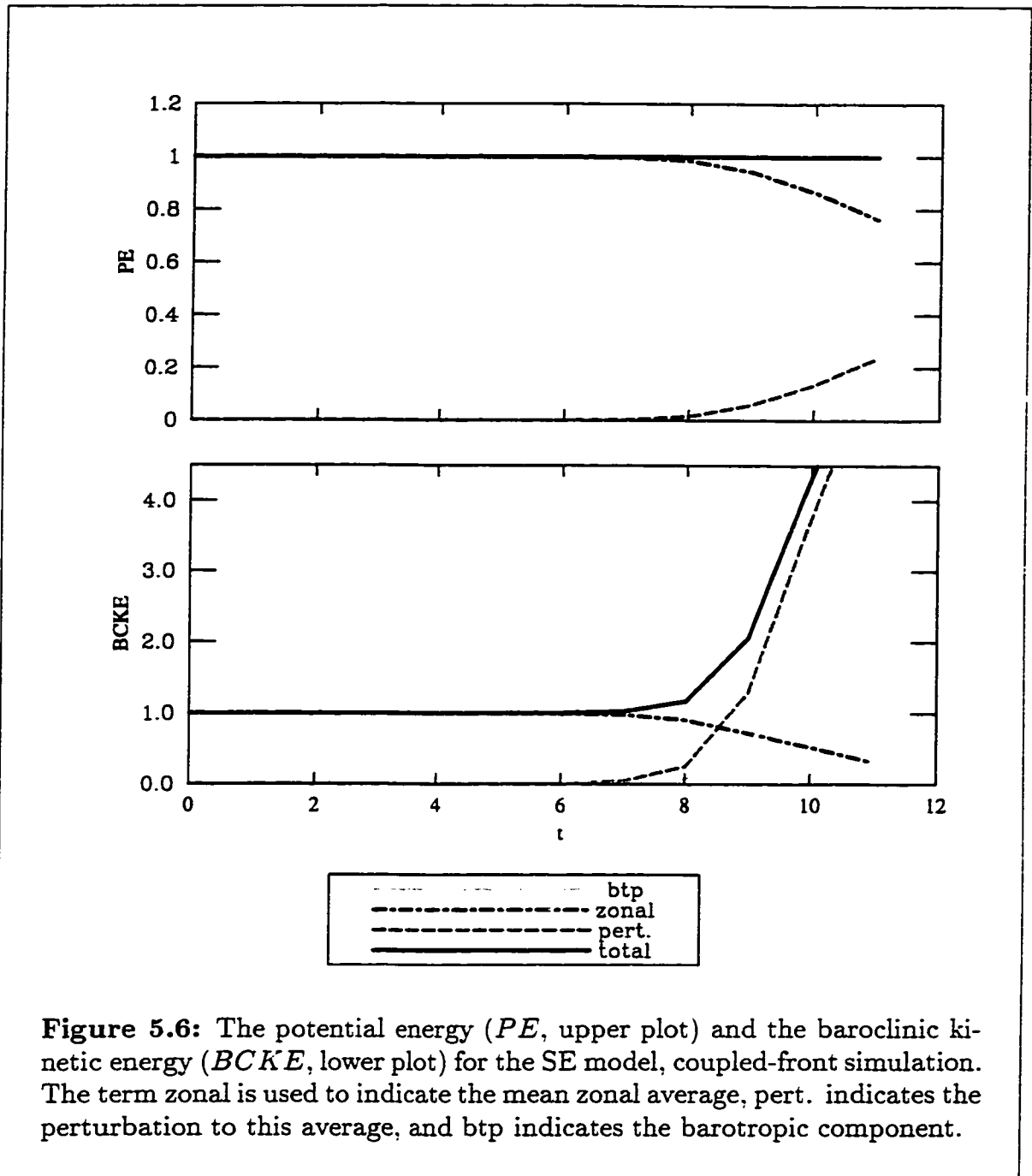
Figure 5.5: Results of the numerical simulation of the SE model isolated-front simulation for t=14–19. The graphs on the left show the contours of the upper-layer height. The grey regions are regions where the upper layer vanishes and the contour interval is 0.1. The graphs on the right show the contours of the barotropic stream function. The grey regions are regions where the stream function is negative and the contour interval is 0.04.

Figure 5.6: The potential energy (PE, upper plot) and the baroclinic kinetic energy ($BCKE$, lower plot) for the SE model, coupled-front simulation. The term zonal is used to indicate the mean zonal average, pert. indicates the perturbation to this average, and btp indicates the barotropic component.

tions. As the instability grows, we do see a release of mean potential energy and a growth of the perturbation PE. The plots of the kinetic energy are in striking contrast to those of the previous section. We see rapid growth in the total and perturbation baroclinic KE as well as the barotropic KE. There is also a small release in mean $BCKE$. The large growth is expected as small scales begin to dominate the
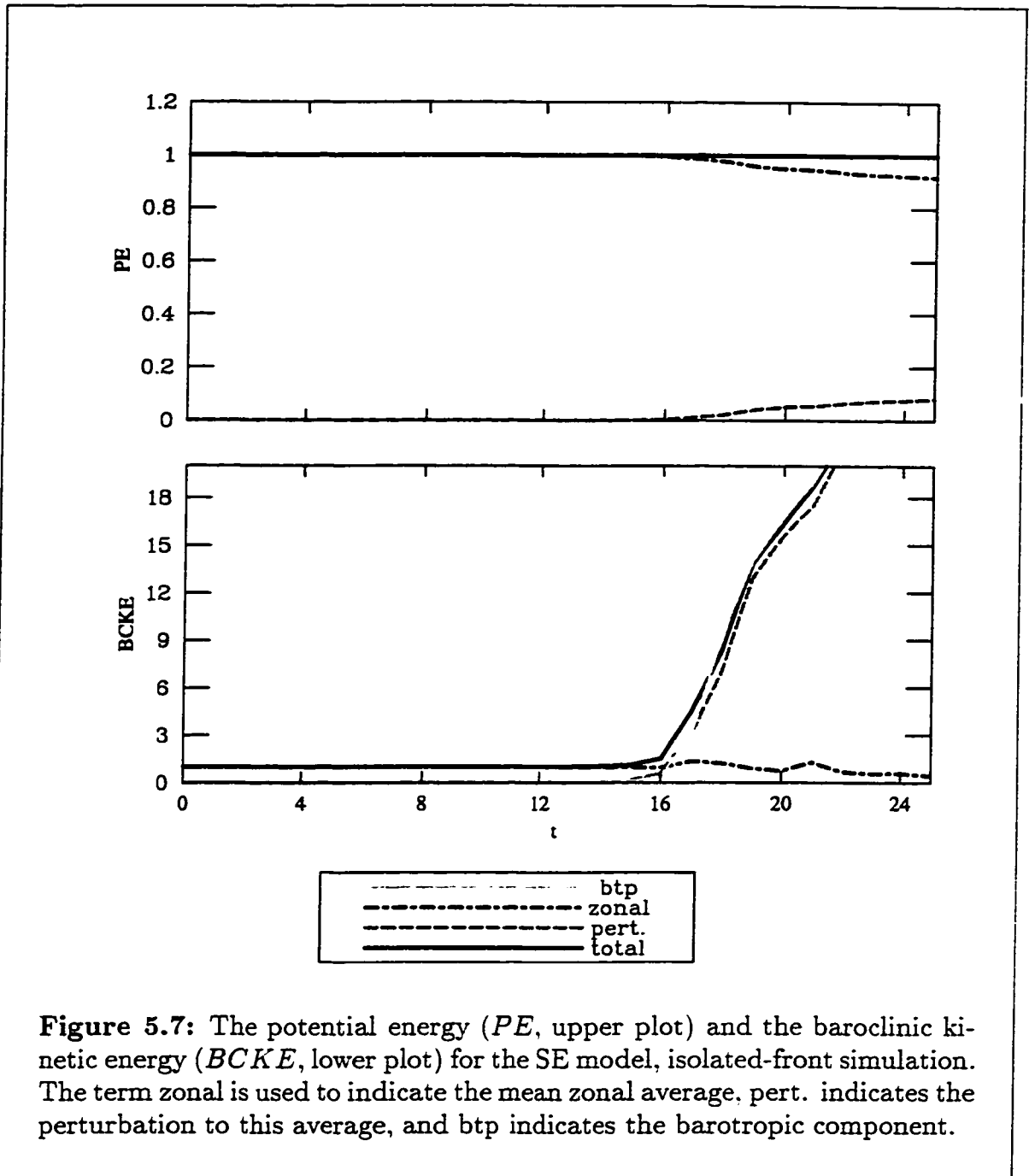
Figure 5.7: The potential energy (PE, upper plot) and the baroclinic kinetic energy ($BCKE$, lower plot) for the SE model, isolated-front simulation. The term zonal is used to indicate the mean zonal average, pert. indicates the perturbation to this average, and btp indicates the barotropic component.

flow. The fact that the baroclinic and barotropic KE grow concurrently is required by the conservation of the pseudo-energy $\mathcal{E}$. Note that in the case of the isolated front, the release of KE precedes the release of PE and we see a large growth in KE for a relatively small release of PE.

In order to examine the weakly nonlinear analysis more closely, we ran sim-
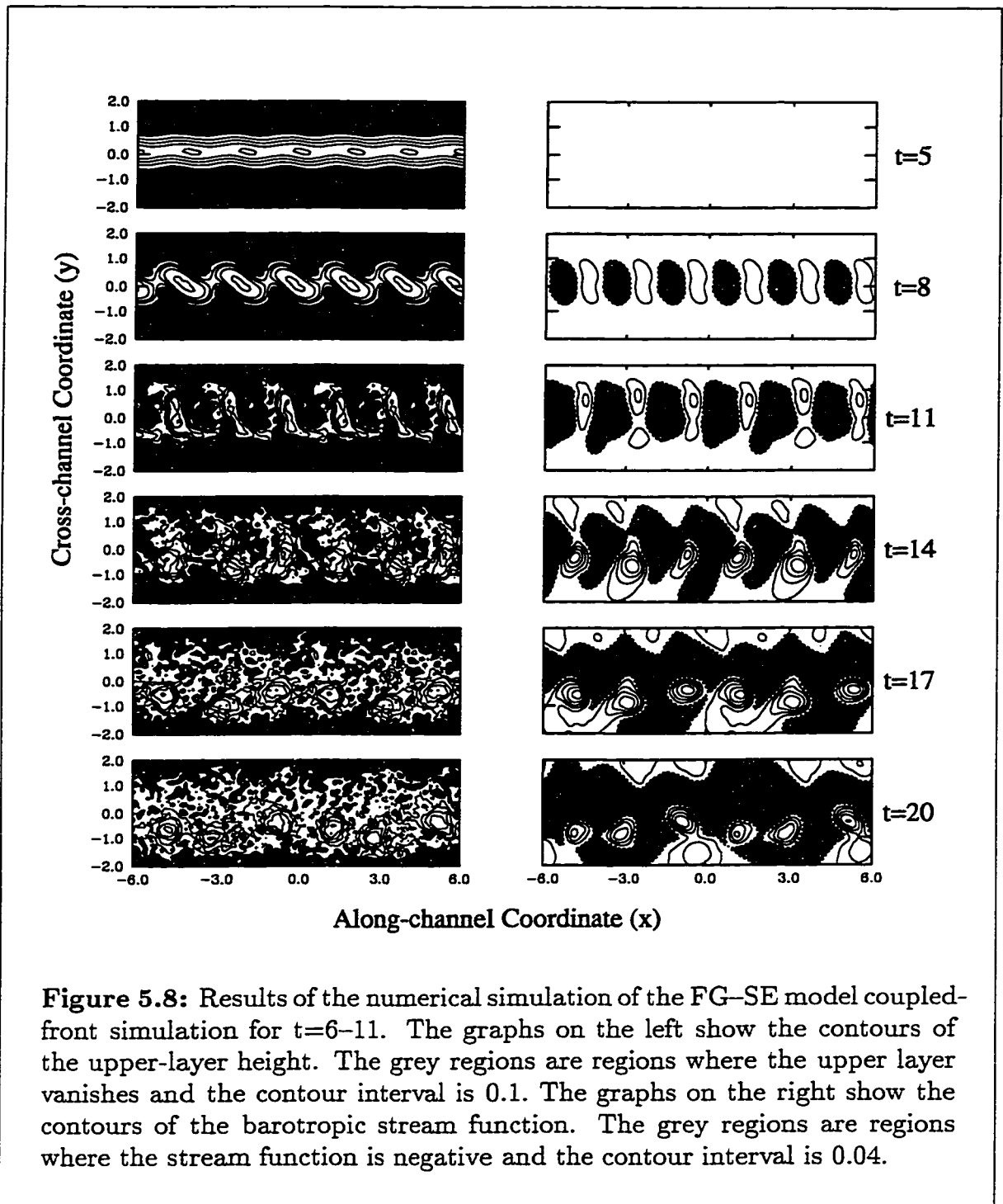
ulations with the gently sloping front. These simulations were not able to produce results that were identifiable with the analysis. The reason is simple. Small-scale growth dominates the simulations because the marginal stability curve does not have a critical value of the frontal slope for instability. While the fundamental wave may be marginally unstable. waves of smaller scale are also linearly unstable and not marginally so. Therefore, waves of smaller scale grow quickly, and we postulate that they grow at such small scales that nonlinear terms that may suppress their growth cannot develop properly due to the limitations of the numerical grid. (The nonlinear terms are necessarily of a smaller scale.) Thus, we see small-scale growth even in simulations chosen to simulate the finite amplitude analysis. (It should be noted that various forms of numerical friction were implemented in an attempt to eliminate this small-scale growth with little success.)

As discussed previously, the difficulty with the SE model is that the instability results in energy cascading to scales that are smaller than the model resolves. One way to deal with this is to choose a larger Rossby number and allow for some influence of the nonlinear terms in the baroclinic equation. That is, if we examine the general baroclinic equation (2.3.14), we see that in the SE model limit the nonlinear Jacobian term is $O(\epsilon)$ smaller than the time derivative term and the barotropic-baroclinic coupling term. Thus, in the model we've dropped these terms. But, when scales become small these terms become important as the fourth order derivatives become large. If the Rossby number is not prohibitively small. the nonlinear Jacobian will effect the evolution of the flow. Evidence that these terms will inhibit unstable growth at small scales is given by the stability observed in the RED and ST models and the high wavenumber cutoff for instabilities in the WVT model (see Appendix 2). Therefore, we solve the full FG equation (2.3.13) and (2.3.14) with the time and barotropic Rossby numbers given by the SE limit. (Note that even the final term in (2.3.14) must be included now.)

In Figures 5.8 and 5.9, we present the results of running the coupled- and isolated-front simulations when the higher order terms are included by choosing $\epsilon = 0.1$. We see that small-scale growth has been suppressed and large-scale growth dominates the flow. In the coupled-front simulation, Figure 5.8, the large-scale structures form eddies reminiscent of those produced by the RED model; see Figure 3.9. These eddies are not as stable and tend break up into smaller eddies which drift southward. However, at the end of the simulation we still have large-scale structures,

Figure 5.8: Results of the numerical simulation of the FG–SE model coupled-front simulation for t=6–11. The graphs on the left show the contours of the upper-layer height. The grey regions are regions where the upper layer vanishes and the contour interval is 0.1. The graphs on the right show the contours of the barotropic stream function. The grey regions are regions where the stream function is negative and the contour interval is 0.04.
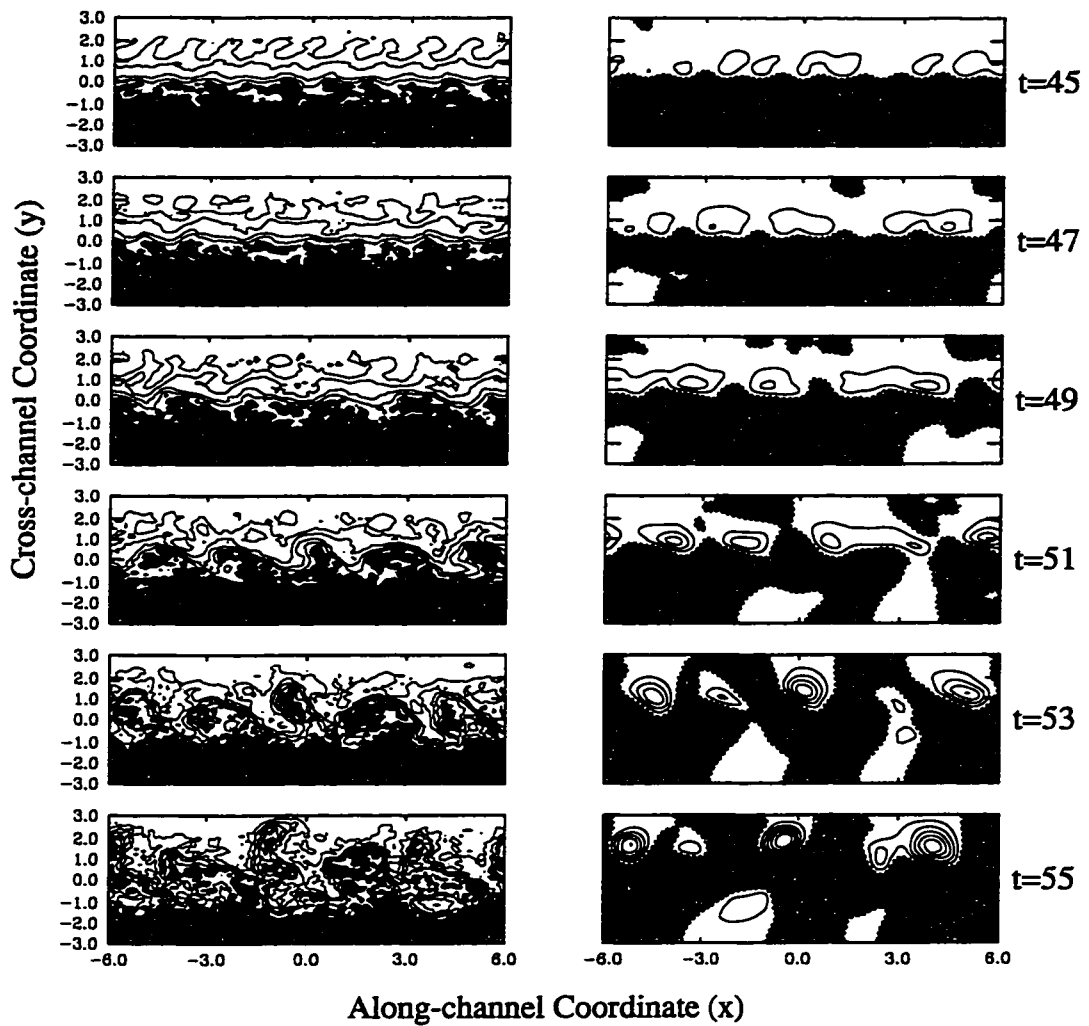
Figure 5.9: Results of the numerical simulation of the FG–SE model isolated-front simulation for t=14–19. The graphs on the left show the contours of the upper-layer height. The grey regions are regions where the upper layer vanishes and the contour interval is 0.1. The graphs on the right show the contours of the barotropic stream function. The grey regions are regions where the stream function is negative and the contour interval is 0.04.

especially in the barotropic stream function. For the isolated front. Figure 5.9, small-scale waves initially grow and then large-scale structures dominate. These large waves tend to break backwards often entrapping colder lower-layer water as a cold-core eddy or pinching off as a warm-core eddy (see $t = 51, 53, 55$). These eddies are coupled with cyclonic and anticyclonic eddies in the barotropic flow. As well, filaments of lighter fluid extend outward from the front while intrusions of lower-layer fluid (seen as a vanishing of upper-layer depth) reach across the front to the far channel wall. In different simulations, with different initial perturbations, we see different combinations of cold-core eddies, warm-core eddies, and filaments. Two things are always common, the front is always very unstable and the structures in the upper layer are always coupled to strong large-scale eddies in the barotropic stream function.

The simulations share much in common with that of the WVT model as one would expect. Both models produce eddies for both coupled and isolated fronts. However, for the SE model these structures tend to be unstable and the fronts remains dynamic after eddies have formed. In the WVT model, the waves tend to be of larger scale, the eddies tend to be better defined, and the small-scale noisiness seen in the above figures is not a feature (see A.2.1 and A.2.3). This is indicative of the greater amount of baroclinic energy available in the SE model due to the thickness of the active layer. As well, it has been shown that increasing the depth ratio and increasing the β-plane effect both lead to a shift to a higher-growth rate, smaller-scale instability (Barth, 1994). Thus, even though the inclusion of the higher order nonlinear terms may restrict growth at smaller scales, it does not eliminate it. The vigorous growing instabilities of the isolated front are indicative of the short-wave, rapidly growing meanders, eddies, and squirts common to all coastal currents (Paldor and Ghil, 1991). These active fronts with many dynamic features are similar to those shown in the works of Haidvogel *et al.* (1991), Spall (1995), Barth (1994), and Bush *et al.* (1996). As well, similar jet meandering and eddy pinch off were observed using a QG model in Flierl *et al.* (1987) and Feliks and Ghil (1996). There, they also saw the baroclinic monopole structure dominate the upper layer, coupled to barotropic dipoles. Also, nonlinear effects leading to steady meanders, jets, squirts, and cold and warm-core eddies are well documented in the above works. These features are all present in the FG–SE model simulations. For now a complete parameter space examination and comparison to specific works

and observations is not undertaken but is left to future work.

In Figures 5.10 and 5.11, we examine the energy transfers of the FG–SE simulations. We can see that the suppression of small-scale instabilities has also suppressed the unbounded growth of kinetic energy and allowed for a greater release of PE (compare to Figures 5.6 and 5.7). We conclude that large-scale structures are more efficient at releasing mean PE. The growth in baroclinic and barotropic KE is no longer balanced as $\mathcal{E}$ is no longer conserved. However, the isolated-front instability is still associated with a large growth of KE. This growth does not come at the expense of zonal KE. This form of instability, where large growth appears, but apparently not at the expense of mean energy, is discussed in Barth (1989a). There, the possibility of negative wave energy is discussed. This notion allows wave amplitudes to grow while mean flow energies remain constant or even increase. We believe that the instabilities of the isolated front shown here share this structure. Note that these energy balances are very similar to that seen in the WVT model simulations (see Figure A.2.5).

It should be noted that these simulations do reflect the results of the finite amplitude analysis of §5.4. There, it was found that nonlinear effects should result in periodic modulation of linear growth when zonal scales are smaller than meridional scales and explosive growth when zonal scales exceed meridional scales. In both the coupled- and isolated-front simulations the vigorous instabilities and eddy formation can be connected to explosive growth. If we examine the figures, especially the barotropic stream function plots, we can conclude that for the large growth instabilities zonal scales are equal to meridional scales. In Figure 5.12, we plot the zonal and meridional spectrum of the barotropic stream function. For the initial 20 time units we see the growth of initial perturbation of zonal wavenumber 10 and little structure meridionally. Over the next 20 time units the growth of this wave is modulated periodically while meridional structure at larger length scales begins to form. Then, at the times shown in Figure 5.9, growth at large zonal scales, wavenumbers 1, 3 and 5, similar to the scale of the meridional structure, grow explosively. Note that the zonal wavenumber 5 mode, which is a somewhat smaller scale than the meridional scales, is also modulated before the end of the simulation.

Once again, these results can be compared to those of Tang and Cushman-Roisin (1992) (note that their results are found using a small depth ratio). There,
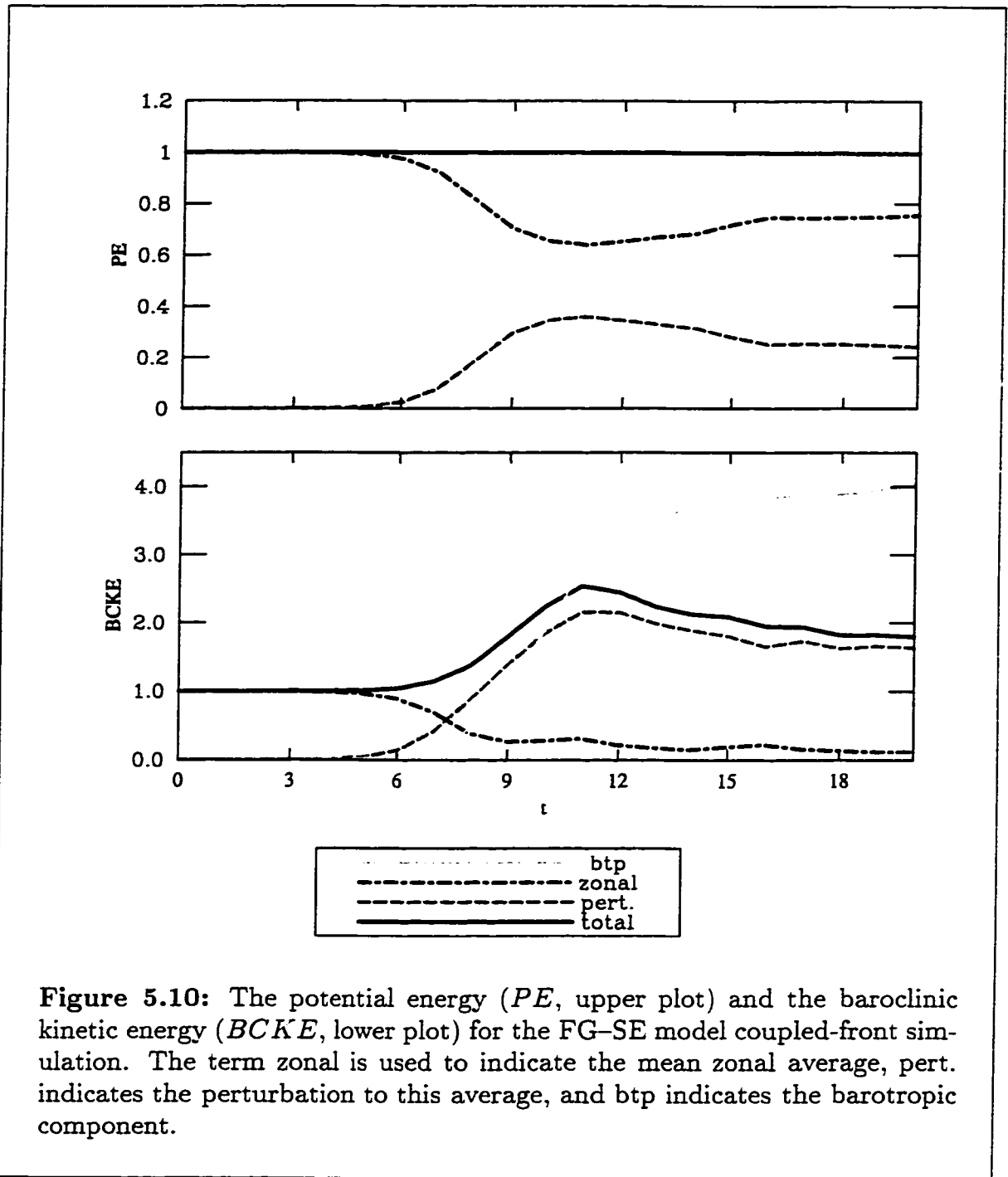
Figure 5.10: The potential energy (PE, upper plot) and the baroclinic kinetic energy ($BCKE$, lower plot) for the FG–SE model coupled-front simulation. The term zonal is used to indicate the mean zonal average, pert. indicates the perturbation to this average, and btp indicates the barotropic component.

PE

1.2
1
0.8
0.6
0.4
0.2
0

BCKE

18
15
12
9
6
3
0

0   10   20   30   40   50
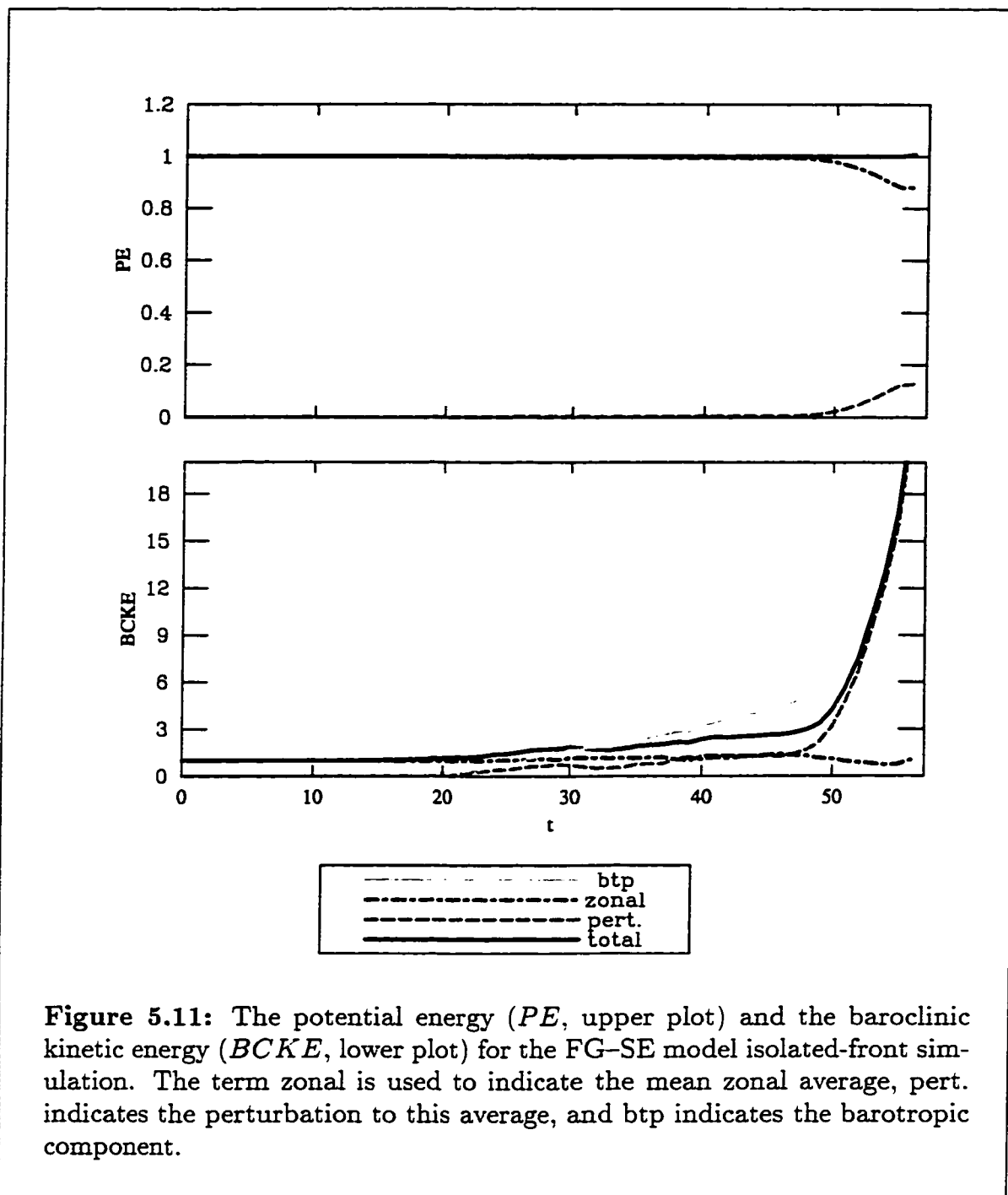
t

btp
zonal
pert.
total

Figure 5.11: The potential energy (PE, upper plot) and the baroclinic kinetic energy ($BCKE$, lower plot) for the FG–SE model isolated-front simulation. The term zonal is used to indicate the mean zonal average, pert. indicates the perturbation to this average, and btp indicates the barotropic component.
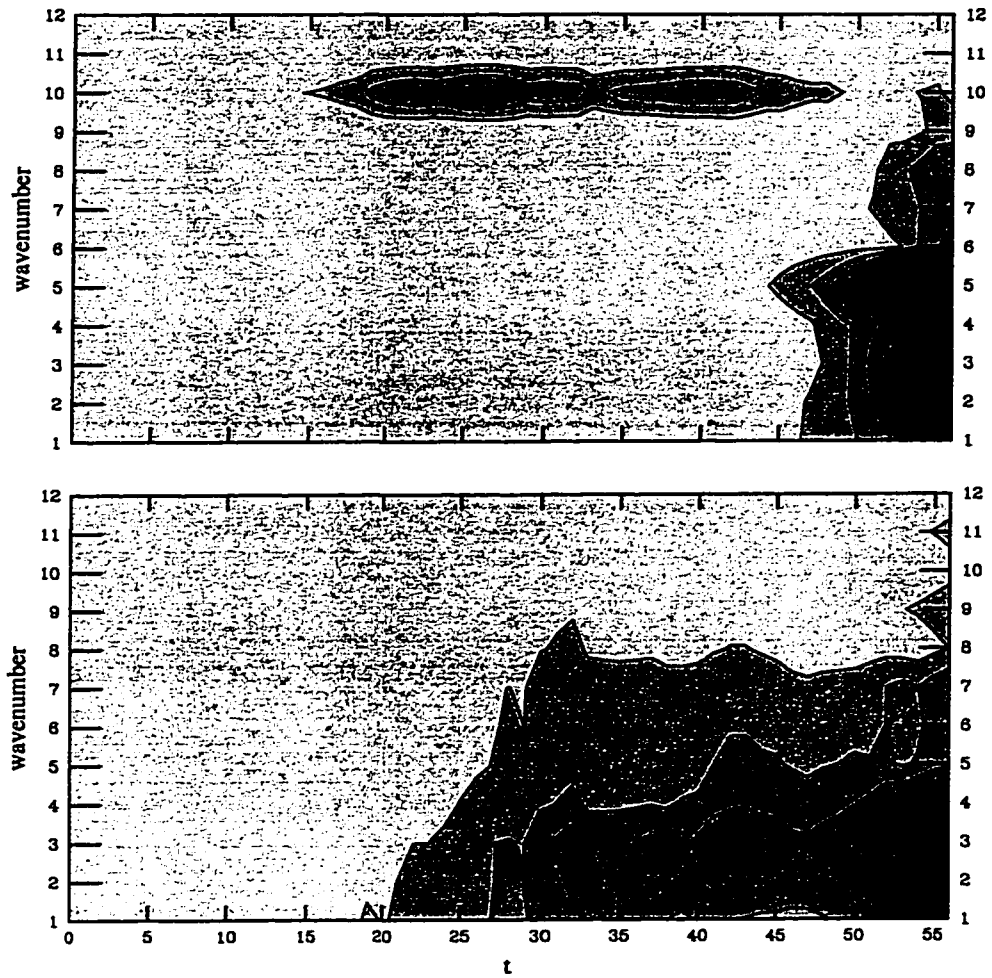
Figure 5.12: The zonal (top) and meridional (bottom) spectrum plots for the FG–SE isolated-front simulation.

it was found that in the frontal regime, a balance between frontal effects and baroclinic instability leads to stable anticyclonic eddies. The above results give further evidence of this. Without the frontal effects, baroclinic instability dominates and we see small-scale turbulence and rapid increases in the kinetic energy. In the general model of Tang and Cushman-Roisin (1992) where all QG terms are included, this leads to a barotropization of the flow.

Chapter 6

Conclusions

In this chapter we summarize the results of this thesis. We begin by comparing the structure of the four two-layer FG models. Next we discuss how this differing structure leads to the results presented in the thesis. We then compare these results to those of other models and discuss the advantages and shortcomings of the FG formulation. Finally, we discuss possible future avenues of research.

We begin by comparing the structure of the three models studied in the body of the thesis and the WVT model described in Appendix 2. For convenience, a comparison of the scaling of the models is found in Table 6.1. We also include a description of the baroclinic and barotropic equations using the terms QG, PG, FG, and β. We used these terms based on the similarity of the equations to previously derived equations that use similar nomenclature. As such, QG is applied to models that involve the evolution of relative vorticity terms, PG is applied to models that are dominated by layer depth changes and the coupling of the two layers, and FG is applied to models that include the nonlinear advection terms associated with frontal effects. The label β is used in two ways. When written in regular type it signifies a model that is dominated by the background vorticity gradient provided by the β-plane effect. When used as a subscript, it indicates that the model includes β-plane effects. The baroclinic equation can be described as one of the first three types of models. The barotropic equation, representing a balance between baroclinic and barotropic effects, is a balance of two forms of equations. In the last two columns of Table 6.1 we list the appropriate description of each equation for the given model. In the description of the barotropic equation we list the barotropic component first and then the baroclinic component.

From Table 6.1, the effect of the two parameters, δ and ϵ_β, used to determine the models is clear. As the depth ratio δ increases, the coupling between the two layers becomes more important and dominates the frontal effects. Thus, the baroclinic equation for the models where the layers are scaled equally, the VSE and SE models, are PG in form, while the models where the upper layer is thinner, the ST and WVT models, are FG in form. As the β-plane effect, ϵ_β, increases, it eventually dominates the relative vorticity terms of the barotropic flow. Thus the

6. Conclusions

Model	δ	ϵ_β	ϵ_T	ϵ_v	Baroclinic Motion	Barotropic Motion
ST	ϵ	ϵ	ϵ^2	ϵ^2	FG_β	β-FG
VSE	1	$\epsilon^{\frac{1}{2}}$	$\epsilon^{\frac{3}{2}}$	$\epsilon^{\frac{3}{2}}$	PG_β	β-FG
SE	1	ϵ	ϵ	ϵ	PG	QG_β-FG
WVT	ϵ^2	ϵ^2	ϵ^2	ϵ^2	FG	QG_β-FG

TABLE 6.1.   A comparison of the model scalings. Each term is given in relation to the baroclinic Rossby number of the flow. The final two columns give the classification of the two equations.

barotropic equation for the models where the β-plane effect is relatively strong, the VSE and ST models, are β-FG in form, while the models where the β-plane effect is relatively weak, the SE and WVT models, are QG-FG in form.

These models can be classified as strong-β and weak-β models based on a critical length scale

$$ L_c = \left(R_I{}^4 L_\beta{}^2 \frac{H_1}{H} \right)^{1/6} . $$

L_c is the scale at which the β-plane effects and the QG effects balance each other in the barotropic equation. Using the notation of §2, it is the scale where $\epsilon_T = \epsilon_v = \epsilon_\beta$. It can be derived using the parameter definitions given by (2.3.7) and that for all the two-layer, FG models $\epsilon_T = \epsilon_v = \delta\epsilon^2/\epsilon_\beta$ (see Figure 2.3). When the length scale of the model exceeds L_c, β-plane effects dominate the barotropic equation and the models are called strong-β models. Such is the case for the ST and VSE models, where $(L_c/L)^6 = \epsilon$. On the other hand, if the length scale of the model is less than or equal to L_c, QG effects dominate the barotropic equation and the models are called weak-β models. Such is the case for the SE and WVT models, where $L_c = L$. As such, L_c is analogous to the Rhines scale for QG models (see §3.11 for definition and discussion). Note that in Benilov and Reznik (1996) the parameter $\alpha = R_{I_H}/L_\beta = \epsilon_\beta \epsilon^{\frac{1}{2}} \delta^{-\frac{1}{2}}$ is introduced to make a more accurate assessment of the relative importance of the β-plane effect. The VSE and ST models both have $\alpha = \epsilon$ and are called strong-β models, while the SE and WVT models have $\alpha = \epsilon^{3/2}$ and are called weak-β models. (It should be noted that a

6. Conclusions

similar parameter is introduced in Cushman-Roisin and Tang (1990) and Cushman-Roisin *et al.* (1992) with $\alpha = R_I/L_\beta$. However, this choice of parameter does not give the clear distinction between strong and weak β-plane models as discussed above.)

The classification above can also lead to insight into the stability of fronts described by a given model. In general, PG models are unstable. with the possibility of ultraviolet catastrophe (de Verdiére, 1986) and therefore increasing the depth ratio increases the possibility of instability. This is reasonable because increasing the depth ratio increases the vertical scale of the front and thus increases the available energy stored in the front. QG models are also subject to instability but the inclusion of relative vorticity terms provides the apparatus to eliminate growth at small scales. Thus, QG models give rise to large-scale. unstable. baroclinic waves. On the other hand, the background vorticity gradient of the β-plane is generally a stabilizing force. A stronger β-plane is the result of increasing the horizontal length scale. This has the effect of reducing isopycnal slopes and diminishing the relative vorticity terms. thus stabilizing the front.

To classify the FG influences as stabilizing or destabilizing we examine the RED model results. As the RED model is strictly an FG model we can attribute the processes seen there to FG influences. Under the RED model. monotonic fronts are stable, while coupled fronts are unstable. Generally, we associate frontal effects with small-scale motions. Only when streamlines are coupled do these motions progress to larger scales resulting in the forms of instabilities seen for coupled fronts. This does not occur in isolated fronts and we do not see instability. In general, frontal effects tend to steepen the front favouring the formation of robust, coherent structures (see Cushman-Roisin and Tang, 1990 and Tang and Cushman-Roisin, 1992). In summary, we expect PG and QG effects to be destabilizing at smaller and larger scales, respectively, and β-plane effects and FG effects to be stabilizing.

Given the classification of the models, and the stability considerations, we now summarize the results of the nonlinear examination of the body of the thesis. The results of the analysis of the previous chapters, and those given in Appendix 2, are summarized in Table 6.2. The results listed apply to isolated fronts and the results for the RED model and LST model are also included (see Table 1.1 for where these results are derived). All models gave unstable growth for coupled fronts leading to eddy formation. The effect of the lower-layer on the evolution of

206

6. Conclusions

Model	Linear Stability Analysis	Nonlinear Stability Analysis	Finite Amplitude Analysis	Numerical Solutions (isolated front)
ST	fronts where PV gradients do not vanish are stable	**linearly sloping fronts are stable**	**wave packet formation**	**stability, long waves**
VSE	monotonic fronts are stable	**linearly sloping fronts are stable**	**wave packet formation**	**stability, long waves**
SE	unstable to small-scale disturbances	**impossible to prove stability**	**saturation or explosive growth**	**explosive growth at small scales**
WVT	instability for finite, bounded region of wavenumbers	nonlinear stability possible	saturation or explosive growth	eddy formation
RED	monotonic fronts are stable	linearly sloping fronts are stable	wave packet formation	stability, long waves
LST	instability for finite, bounded region of wavenumbers	nonlinear stability possible	saturation (critical layer dominates)	instability leading to vorticity wrap up and eddy formation

TABLE 6.2.   A comparison of the model results as determined in this thesis, in bold, and from previous works. Numerical results are for isolated fronts.

coupled fronts was determined to be small. The differences between the models occurred chiefly because of the differences in the uncoupled forms of the models. Thus, while the eddy evolution in the ST and WVT models was almost identical to that of the RED model, the VSE model illustrated hyperbolic behaviour as seen in the BCHY model. The SE model coupled-front simulation, which does not have an analogous uncoupled model, simply illustrated the small-scale growth associated with ultraviolet catastrophe. The existence of this unstable growth for coupled fronts points to the importance of the singular point of the models where the PV gradient vanishes (see Benilov, 1995a).

6. Conclusions

The ST and VSE models produce similar results. Both models are dominated by the β-plane effect. Each has a diagnostic barotropic equation, which leads to difficulties when discussing outcrops. For both models all fronts are linearly stable unless the PV gradients vanish and all linearly sloping fronts are nonlinearly stable. This indicates the baroclinic nature of the instability of a monotonic front and that FG effects in the barotropic equations do not destabilize fronts. The finite-amplitude analysis suggests that stable waves should form wave packet/soliton structures. The analysis also found that wave resonances are important in the initialization and evolution of these packets. Numerical simulations illustrate that large-scale perturbations do develop but they are small in amplitude. Resonances can play a role in determining long term evolution, as the simulations indicated that long-wave-short-wave resonances allowed the development of a meridional wave perturbation to the basic-state flow. Although small in amplitude, such a structure may play a role in determining the long time evolution and structure of stable fronts. Finally, the development of finite amplitude long-waves can result from a front that has some shear in it. The shear provides the kinetic energy to feed an instability that flattens out the front. The long waves that result can persist for long times. In conclusion, FG models that are dominated by the β-plane effect produce stable fronts with nonlinear effects shifting energy to larger scales. This result implies that as the β-plane effect becomes strong and begins to dominate frontal effects we see a transition to the Rossby wave regime discussed in Tang and Cushman-Roisin (1992). In this regime, there is "little vertical energy transfer" and the flow "amounts to no more than the dispersion of linear Rossby waves" (Tang and Cushman-Roisin, 1992).

The SE model is dominated by its PG baroclinic equation. This leads to large growth at small scales or what is called ultraviolet catastrophe. The balance of terms in the barotropic equation does not suppress growth at small scales because the barotropic relative vorticity terms are balanced by the baroclinic FG terms. As expected, we see the ultraviolet catastrophe predicted by the linear analysis in the numerical simulations. Note that energy considerations do not rule out this growth, as the pseudo-energy invariant $\mathcal{E}$ requires equivalent growth in both the barotropic and baroclinic kinetic energy. The nonlinear stability analysis was unable to establish stability results as it was not possible to bound growth at small scales. Furthermore, the finite amplitude analysis suggests large-scale waves are subject

6. Conclusions

to an explosive nonlinear instability. In the numerical simulations, all fronts were dominated by unbounded small-scale growth. This led to running simulations that included appropriately scaled FG terms in the baroclinic equations. These terms do suppress small-scale growth, indicating that FG terms in the baroclinic equations are a stabilizing effect at small scales. The result is the development of large-scale structures within a highly unstable front. These results are similar to many coastal models that have illustrated the highly unstable nature of fronts using primitive equation analysis (see Haidvogel *et al.*, 1991 and Barth, 1994).

The WVT model shares characteristics of the ST model and the SE model (see Appendix 2 for details). The baroclinic equation is of FG form, though there is no influence of the β-plane. From the analysis of the ST and RED models, we do not expect this equation to be a source of instability. The QG-FG balance in the barotropic equation allows the possibility of instability at the large scales QG favours. This is seen in the linear analysis which predicts instability for a finite band of wavenumbers. The finite amplitude analysis suggests a suppression of small-scale growth but explosive nonlinear instability at large scales as seen in the SE model. We suggest that it is this explosive nonlinear growth that leads to the coherent eddy formation seen in the numerical solutions of Reszka (1997) and Appendix 2. It should be noted that while the instabilities of the WVT model occur at larger scales nondimensionally, the length scale of the model is smaller than the length scale of the SE model. Therefore, in reality, the instabilities have similar scales. It should be noted that the numerical results for the SE and WVT models reiterate the results of Tang and Cushman-Roisin (1992). If frontal effects are important, as in the WVT model and the FG-SE model, we see stable anticyclonic eddies form. However, if baroclinic instability dominates frontal effects, as in the original SE model, we see the destruction of large-scale features.

In comparison to the RED model, it was made clear in the analysis of the ST model that a weakly coupled barotropic flow does not greatly change the evolution of a front. On the other hand, coupling a stronger, independent barotropic flow as seen in the WVT model can destabilize isolated fronts. This leads to the conclusion that the RED model is generally more applicable than the strict bounds found in §2. There, the RED model was determined to be applicable when no coupling occurred. The analysis of this thesis suggests that the RED model still provides accurate results when only weak coupling occurs. Thus, the RED model is applicable if

6. Conclusions

the equations decouple, which occurs under the condition determined in §2. or the β-plane effect dominates the barotropic equation, that is, $\epsilon_v \ll \epsilon_\beta$. Using the solutions presented in Figure 2.3, this gives the condition

$$\delta \ll \frac{\epsilon_\beta^2}{\epsilon^2}.$$

This condition allows for the RED model to describe fronts with much thicker upper layers provided the length scale of motion is long enough.

It is also interesting to compare the results of the two-layer FG models to the analysis of the LST model. As illustrated in Appendix 1, the LST model is derived in the FG limit when considering bottom-trapped flow over topography. The SE and WVT models also have corresponding forms for such flows provided the topography is scaled appropriately. The baroclinic equation for the LST model has a PG structure with topographic influences. The barotropic equation is a QG-topography balance. Despite being derived in the large-amplitude limit. there are no highly nonlinear FG terms seen in the other FG models. Due to its simplicity, the LST model allows for greater analysis (see Swaters. 1991. Mooney and Swaters, 1996. Poulin, 1997, Karsten *et al.* 1995, Karsten and Swaters, 1996b, and Swaters, 1998). A couple of important differences arise between the results of the LST model and the FG models discussed here. The predominant difference is that the strong bottom topography in the LST model allows for a release of potential energy that drives the instability (see discussion in Swaters. 1991 and Swaters, 1993b). Thus, the instability is asymmetric and is seen as a slumping of fluid down the sloping bottom. The fact that the barotropic motion is primarily QG means that this instability occurs for a finite band of length scales and we do not see the ultraviolet catastrophe of the SE model. The finite amplitude analysis of the LST model illustrates that nonlinear terms suppress the linear growth (Mooney and Swaters, 1996) at all scales. This effect can be clearly seen in the numerical simulations of a coupled front in Swaters (1998) where linear instabilities grow to form filaments that are then rolled up into eddy-like structures. This instability is fundamentally different from the instability seen in the two-layer FG models examined here. The instability that develops in the two-layer FG models examined here is symmetric and the eddies form not as a result of a roll up of filaments but as the growth and pinch off of a single wave. This eddy formation is present in both coupled and

6. Conclusions

isolated fronts for the WVT and SE models. We suggest that it is this explosive nonlinear growth, predicted in the finite amplitude analysis for the SE and WVT models, that leads to the coherent eddy formation seen in the numerical solutions of Reszka (1997) and this thesis.

In the numerical solutions for all the FG models one important advantage is revealed. All the FG models handle outcroppings with ease, with no additional code to specify the location of the outcropping. This advantage results from the fact that the baroclinic equation is given in terms of the upper-layer depth h and is trivially satisfied when $h = 0$. Thus, as long as the frontal height is continuous across an outcropping, the baroclinic equation applies equally well on either side of the outcropping. It is this feature of the FG models that allows for the dramatic visualization of the eddies and meanders seen here and in Reszka (1997).

However, it should be noted that the inclusion of the highly nonlinear frontal terms seen in the four FG models studied here requires small time steps in the numerical code. Thus, even though the vertical resolution is low (only two layers) and the horizontal length scale is large (greater than the internal Rossby deformation) the time step in the code remains small. For example, with the SE model a nondimensional horizontal grid size of 0.1 requires a time step of 1×10^{-4} to run simulations. In dimensional terms, assuming a Rossby number of 0.1 and an internal Rossby deformation radius of 10 km, this gives a horizontal grid of roughly 3 km and a time step of roughly 10 seconds. This is a limitation of these models not seen in the LST model where the nonlinear terms do not arise. However, it does appear that if the large inertial terms associated with a front are to be included in a model, even with the reduced structure of the two-layer FG model, that numerical simulations will be costly.

It is also of interest to compare our results to those of other works. For example, in Barth (1989a) and Barth (1989b) a coastal front over large topography was studied using a two-layer model that employed the geostrophic momentum approximation. It was shown that a zero-energy instability existed; an instability that grew without a release of energy from the mean state. This instability is similar in form to that seen in the SE and WVT models where unstable growth can occur with both the baroclinic and barotropic kinetic energy increasing and little release of PE. The fact that both baroclinic and barotropic kinetic energy increase together is in fact required by the conservation of the pseudo-energy $\mathcal{E}$.

6. Conclusions

The linear analysis and numerical simulations using primitive-equation models of McCreary *et al.* (1991), Haidvogel *et al.* (1991), and Barth (1994) provide further insight. Here, both a long and short wave instability were observed and classified as baroclinic and frontal instabilities. We believe that the results here show that FG models capture these two forms of instabilities. Indeed, the numerical simulations of the WVT model show the development of large-scale structures comparable to the baroclinic instability. Yet, within the simulations of the SE model, and even some simulations of the WVT model (personal communication from M. Reszka) small-scale structures develop, grow, and play important roles in the development of the large-scale structures. In comparing the results to the simulations using primitive equations, it is clear that the FG models capture the major characteristics of frontal instabilities.

Although we have attempted to examine a great deal of the nature of FG models, there still remain many open areas of research. Further examination of the linear FG models using numerical techniques could provide a more accurate picture of the form of the instability that develops on coupled and isolated fronts. Detailed comparison and analysis of specific fronts and currents could be carried out to see how well the models predict the observed features (see for example Barth. 1989b).

An obvious extension of this work is the examination of several-layer models. The addition of more layers allows for the examination of more complicated physical processes and the modelling of more realistic situations (see Spall. 1995). In Benilov and Sakov (1997), the two-layer LST model description of a bottom-trapped current is extended to a three-layer model by coupling the LST description of a bottom-trapped flow to the WT model for a thin, upper-layer front. The analysis there immediately points out some difficulties. First, one cannot simply match any models together, as the middle layer must describe dynamics at equivalent scales for both models. Second, the stability characteristics of one model may dominate the other. In Benilov and Sakov (1997), the linear stability analysis illustrated that the model was also subject to ultraviolet catastrophe as the characteristic of the WT model dominated that of the LST model (the WT model has the same linear characteristics as the SE model). The question of how three- or possibly four-layer FG models can be used to accurately describe systems with both surface and bottom currents is one that requires further investigation.

Finally, a study of how two-layer, FG models could be used to improve ocean

6. Conclusions

circulation models could be undertaken. A detailed examination of the numerical simulations, including the effects of the ageostrophic velocities, would allow for estimates of the mixing and transport that occur as a front destabilizes. These could be used to test eddy parametrization schemes. In Greatbatch (1998), it is proposed that the eddy parametrization of the isopycnal flux potential vorticity be derived from a thickness-averaged, isopycnal-averaged, potential-vorticity equation. The FG models studied here allow the simple, two-layer analogue of this equation to be studied both analytically and numerically. As well, the FG models allow for measurements of the inertial terms associated with the frontal effects not present in analysis based on a QG assumption. Finally, the ease with which outcropping can be numerically modelled allows the details of eddy mixing and transport when outcroppings are included to be fully examined. Alternatively, the knowledge of the two-layer FG models could be used to include schemes to resolve the necessary scales needed to model frontal instabilities with limited vertical resolution. Further work continues in these areas, and the results will doubtlessly prove very interesting.

References

[1] Arakawa, A., 1966: Computational design for long-term numerical integration of the equations of fluid motion: two dimensional incompressible flow. Part 1. *J. Comp. Phys.*, **1**, 119-143.

[2] Arnol'd, V. I., 1965: Conditions for nonlinear stability of stationary plane curvilinear flows of an ideal fluid: English. transl. *Sov. Math.*, **6**, 773-777.

[3] Arnol'd, V. I., 1966: On an a priori estimate in the theory of hydrodynamical stability: English. transl. *Am. Math. Soc. Transl., Ser. 2*, **79**, 267-269.

[4] Barth J. A., 1989a: Stability of a coastal upwelling front. 1. Model development and a stability theorem. *J. Geophys. Res.*, **94**, 10844-10856.

[5] Barth J. A., 1989b: Stability of a coastal upwelling front. 1. Model results and comparison with observations. *J. Geophys. Res.*, **94**, 10857-10883.

[6] Barth J. A., 1994: Short-wavelength instabilities on coastal jets and fronts. *J. Geophys. Res.*, **99**, 16095-16115.

[7] Benilov, E. S., 1992a: Large-amplitude geostrophic dynamics: the two-layer model. *Geophys. Astrophys. Fluid Dyn.*, **66**, 67-79.

[8] Benilov, E. S., 1992b: A note on the stability of one-layer geostrophic fronts. *Geophys. Astrophys. Fluid Dyn.*, **66**, 81-86.

[9] Benilov, E. S., 1993: Baroclinic instability of large-amplitude geostrophic flows. *J. Fluid Mech.*, **251**, 501-514.

[10] Benilov, E. S., 1994: Dynamics of large-amplitude geostrophic flows: the case of 'strong' beta effect. *J. Fluid Mech.*, **262**, 157-169.

[11] Benilov, E. S., 1995a: On the stability of large-amplitude geostrophic flows: the case of 'strong' beta effect. *J. Fluid Mech.*, **284**, 137-158.

[12] Benilov, E. S., 1995b: Stability of large-amplitude geostrophic flows localized in a thin layer. *J. Fluid Mech.*, **288**, 157-174.

[13] Benilov, E. S., 1995c: Baroclinic instability of a quasigeostrophic flow localized in a thin layer. *J. Fluid Mech.*, **288**, 175-199.

References

[14] Benilov, E. S. and B. Cushman-Roisin, 1994: On the stability of two-layered large-amplitude geostrophic flows with thin upper layer. *Geophys. Astrophys. Fluid Dyn.*, **76**, 29-41.

[15] Benilov, E. S. and G. M. Reznik, 1996: The complete classification of large-amplitude geostrophic flows in a two-layer fluid. *Geophys. Astrophys. Fluid Dyn.*, **82**, 1-22.

[16] Benilov, E. S. and P. V. Sakov, 1997: Dynamics of large-amplitude flows over bottom topography. *Nonlinear Proc. in Geophys.*, **4**, 55-62.

[17] Boss, E., N. Paldor and L. Thompson, 1996: Stability of a potential vorticity front from quasi-geostrophy to shallow water. *J. Fluid Mech.*, **315**, 65-84.

[18] Bush, A. B. G., J. C. McWilliams and W. R. Peltier, 1995: The formation of oceanic eddies in symmetric and asymmetric jets. Part 1: Early time development and bulk eddy transports. *J. Phys. Oceanogr.*, **25**, 1959-1979.

[19] Bush, A. B. G., J. C. McWilliams and W. R. Peltier, 1996: The formation of oceanic eddies in symmetric and asymmetric jets. Part 2: Late time evolution and coherent vortex formation. *J. Phys. Oceanogr.*, **26**, 1825-1848.

[20] Craik, A. D. D., 1985: *Wave Interactions in Fluid Flows*, Cambridge University Press, Cambridge.

[21] Chassignet, E. P. and B. Cushman-Roisin, 1991: On the influence of a lower layer on the propagation of nonlinear oceanic eddies. *J. Phys. Oceanogr.*, **21**, 939-957.

[22] Cushman-Roisin,B., 1986: Frontal geostrophic dynamics. *J. Phys. Oceanogr.*, **16**, 132-114.

[23] Cushman-Roisin,B., E. P. Chassignet and B. Tang, 1990: Westward Motion of Mesoscale Eddies. *J. Phys. Oceanogr.*, **20**, 2011-2024.

[24] Cushman-Roisin,B. and S. Merchant-Both, 1995: Elliptical warm-core rings in a two-layer ocean with ambient shear. *J. Phys. Oceanogr.*, **25**, 2011-2024.

[25] Cushman-Roisin, B., G. G. Sutyrin and B. Tang, 1992: Two-Layer geostrophic dynamics. Part I: Governing Equations. *J. Phys. Oceanogr.*, **22**, 117-127.

[26] Cushman-Roisin,B. and B. Tang, 1990: Geostrophic turbulence beyond and the

References

emergence of eddies beyond the radius of deformation. *J. Phys. Oceanogr.*, **20**, 97-113.

[27] de Verdiére, A. C., 1986: On mean flow instabilities within the planetary geostrophic equations.. *J. Phys. Oceanogr.*, **16**, 1981-1984.

[28] Dewar W. K., 1992: Spontaneous Shocks. *J. Phys. Oceanogr.*, **22**, 505-522.

[29] Djordjevic, V. D. and L. G. Redekopp, 1977: On two-dimensional packets of capillary-gravity waves. *J. Fluid Mech.*, **79**, 703-714.

[30] Drazin, P. G. and W. H. Reid, 1981: *Hydrodynamic Stability*, Cambridge University Press, Cambridge, U. K.

[31] Eady, E. T., 1949: Long waves and cyclone waves.. *Tellus*, **1**, 33-52.

[32] Feliks, Y. and M. Ghil, 1996: Mixed barotropic-baroclinic eddies growing on an eastward mid-latitude jet. *Geophys. Astrophys. Fluid Dynamics*, **82**, 137-171.

[33] Flierl, G. R., P Malanotte-Rizzoli and N. J. Zabusky. 1987: Nonlinear waves and coherent vortex structures in barotropic β-plane jets. *J. Phys. Oceanogr.*, **17**, 1408-1438.

[34] Ghil, M. and N. Paldor, 1994: A model Equation for nonlinear wavelength selection and amplitude evolution of frontal waves. *J. Nonlinear Sci.*. **4**, 471-496.

[35] Greatbatch. R. J, 1998: Exploring the relationship between eddy-induced transport velocity, vertical momentum transfer, and the isopycnal flux of potential vorticity. *J. Phys. Oceanogr.*, **28**, 422-432.

[36] Griffiths, R. W., P. D. Killworth and M. E. Stern, 1982: Ageostrophic instability of ocean currents. *J. Fluid Mech.*, **117**, 343-377.

[37] Griffiths, R. W. and P. F. Linden, 1981: The stability of buoyancy-driven coastal currents. *Dyn. Atmos. Oceans*, **5**, 281-306.

[38] Grimshaw, R. H. J., 1977: The modulation of an internal gravity-wave packet, and the resonance with the mean motion. *Studies Appl. Math.*, **56**, 241-266.

[39] Haidvogel, D. B., A. Beckmann and K. S. Hedström, 1991: Dynamical simu-

References

lations of filament formation and evolution in the coastal transition zone. *J. Geophys. Res.*, **96**, 15017-15040.

[40] Holm, D. D., J. E. Marsden, T. Ratiu and A. Weinstein, 1985: Nonlinear stability of fluid and plasma equilibria. *Phys. Rep.*, **123**, 1-116.

[41] Ikeda, M.and W. J. Emery, 1984: Satellite observations and modeling of meanders in the California current system off Oregon and Northern California. *J. Phys. Oceanogr.*, **14**, 1434-1450.

[42] Ikeda, M., W. J. Emery and L. A. Mysak. 1984: Seasonal variability in meanders of the California current system off Vancouver Island. *J. Geophys. Res.*, **89**, 3487-3505.

[43] Karsten, R. H. and G. E. Swaters, 1996a: Nonlinear Stability of baroclinic fronts in a channel with variable topography. *Studies Appl. Math.*, **96**, 183-199.

[44] Karsten, R. H. and G. E. Swaters, 1996b: A note on the stability theory of buoyancy-driven ocean currents over a sloping bottom. *ZAMP.* **47**, 28-38.

[45] Karsten, R. H., G. E. Swaters and R. E. Thomson, 1995: Stability characteristics of deep water replacement in the Strait of Georgia. *J. Phys. Oceanogr.*, **25**, 2391-2403.

[46] Killworth, P. D., 1983: Long wave instability of an isolated front. *Geophys. Astrophys. Fluid Dyn.*, **25**, 235-258.

[47] Killworth, P. D., N. Paldor and M. E. Stern. 1984: Wave propagation and growth on a surface front in a two-layer geostrophic current. *J. Mar. Res.*, **42**, 761-785.

[48] Killworth, P. D. and M. E. Stern, 1982: Instabilities on density-driven boundary currents and fronts. *Geophys. Astrophys. Fluid Dyn.*, **22**, 1-28.

[49] Kundu, P. K., 1990: *Fluid Dynamics*, Academic Press, Inc., San Diego.

[50] LeBlond, P. H. and L. A. Mysak, 1978: *Waves in the Ocean*, Elsevier, New York.

[51] Ma, Yan-Chow, 1978: The Complete Solution of the Long-Wave–Short-Wave Resonance Equations. *Studies Appl. Math.*, **59**, 201-221.

References

[52] Marsden, J. E. and T. S. Ratiu , 1994: *Introduction to Mechanics and Symmetry*, Springer-Verlag, New York.

[53] McCreary, J. P., Y. Fukamachi and P. K. Kundu. 1991: A numerical investigation of jets and eddies near an eastern ocean boundary. *J. Geophys. Res.*, **96**, 2515-2534.

[54] McIntyer, M. E. and T. G. Shepherd, 1987: An exact local conservation theorem for finite-amplitude disturbances to non-parallel shear flows, with remarks on Hamiltonian structure and Arnol'd's stability theorems. *J. Fluid Mech.*, **181**, 527-565.

[55] Milne-Thomson, L. M., 1950: *Jacobian Elliptic Function Tables*, Dover Publications, New York.

[56] Mooney, C. J. and G. E. Swaters, 1996: Finite amplitude baroclinic instability of a mesoscale gravity current in a channel. *Geophys. Astrophys. Fluid Dynamics*, **82**, 173-205.

[57] Nowlin, W. D. and J. M. Klink, 1986: The physics of the Antarctic Circumpolar current. *Rev. Geophys.*, **24**, 469-491.

[58] Newell, A. C., 1974: *"Envelope Equations," Nonlinear Wave Motion: Lectures in Applied Math, Volume 15*, American Mathematical Society, 171-191.

[59] Paldor. N., 1983a: Linear stability and stable modes of geostrophic fronts. *Geophys. Astrophys. Fluid Dyn.*. **24**, 299-326.

[60] Paldor, N., 1983b: Stability and stable modes of coastal fronts. *Geophys. Astrophys. Fluid Dyn.*, **27**, 217-228.

[61] Paldor, N., 1987: Nonlinear waves on a coupled density front. *Geophys. Astrophys. Fluid Dyn.*, **37**, 171-191.

[62] Paldor, N. and M. Ghil, 1990: Finite-wavelength instabilities of a coupled density front. *J. Phys. Oceanogr.*, **20**, 114-123.

[63] Paldor, N. and M. Ghil, 1991: Shortwave instabilities of coastal currents. *Geophys. Astrophys. Fluid Dyn.*, **58**, 225-241.

[64] Paldor, N. and P. D. Killworth, 1987: Instabilities of a two-layer coupled front. *Deep Sea Res.*, **34**, 1525-1539.

References

[65] Pavia, N., 1992: The breakup of frontal filaments. *J. Phys. Oceanogr.*, **22**, 399-403.

[66] Phillips, N. A., 1954: Energy transformations and meridional circulations associated with simple baroclinic waves in a two level. quasi-geostrophic model. *Tellus*, **6**, 273-286.

[67] Pedlosky, J., 1970: Finite amplitude baroclinic waves. *J. Atmos. Sci.*, **27**, 15-30.

[68] Pedlosky, J., 1972: Finite amplitude baroclinic wave packets. *J. Atmos. Sci.*, **29**, 680-686.

[69] Pedlosky, J., 1982: Finite-amplitude baroclinic waves at minimum critical shear. *J. Atmos. Sci.*, **39**, 555-562.

[70] Pedlosky. J., 1987: *Geophysical fluid Dynamics: 2nd edition*. Springer-Verlag, New York.

[71] Poulin. F., 1997: Mesoscale gravity currents and cold-pools within a continuously stratified fluid overlying gently sloping topography. *M.SC. Thesis, University of Alberta.*

[72] Reszka, M., 1997: Finite Amplitude waves and eddy development on a baroclinically unstable front over a sloping bottom. *M.SC. Thesis, University of Alberta.*

[73] Rhines P. B., 1975: Waves and turbulence on a beta-plane. *J. Fluid Mech.*, **69**, 417-443.

[74] Robinson, A. R. (ed), 1983: *Eddies in Marine Science.* Springer-Verlag, New York.

[75] Roden G. I., 1975: On North Pacific temperature, salinity, sound velocity and density fronts and their relation to the wind energy flux fields. *J. Phys. Oceanogr.*, **5**, 557-571.

[76] Shepherd, T. G., 1990: Symmetries, Conservation Laws, and Hamiltonian Structure in Geophysical Fluid Dynamics. *Advances in Geophysics*, **32**, 287-335.

[77] Slomp, C. G., 1995: On the hamiltonian structure, stability characteristics and

finite amplitude evolution of geostrophic fronts.. *M.SC. Thesis. University of Alberta.*

[78] Slomp, C. G. and G. E. Swaters, 1997: On the Finite Amplitude Evolution of Geostrophic Fronts.. *Geophys. Astrophys. Fluid Dyn.* . **86**, 149-172.

[79] Spall, M. A., 1995: Frontogenesis, subduction, and cross front exchange at upper ocean fronts. *J. Geophys. Res.*, **100**, 2543-2557.

[80] Stern, Melvin E., 1986: On the amplification of convergences in coastal currents and the formation of "squirts". *J. Mar. Res.*, **44**, 403-421.

[81] Stern, Melvin E., 1987: Large-scale lateral entrainment and detrainment at the edge of a geostrophic shear layer. *J. Phys. Oceanogr.*, **17**, 1680-1687.

[82] Swaters, G. E., 1991: On the baroclinic instability of cold-core coupled density fronts on a sloping continental shelf. *J. Fluid Mech.*, **224**, 361-382.

[83] Swaters, G. E., 1993a: Nonlinear stability of intermediate baroclinic flow on a sloping bottom. *Proc. R. Soc. Lond.A*, **442**, 249-272.

[84] Swaters, G. E., 1993b: On the baroclinic dynamics, hamiltonian formulation and general stability characteristics of density-driven surface currents and fronts over a sloping continental shelf. *Phil. Trans. R. Soc. Lond.* **A 345**, 295-325.

[85] Swaters, G. E., 1998: Numerical simulations of baroclinic dynamics of density-driven coupled fronts and eddies on a sloping bottom. *J. Geophys. Res.*, **103**, 2945-2961.

[86] Swaters, G. E., and G. R. Flierl, 1991: Dynamics of ventilated coherent cold eddies on a sloping bottom.. *J. Fluid Mech.*, **223**, 565-587.

[87] Tan, B. and S. Liu, 1995: Collisions and interactions of solitons in a baroclinic atmosphere. *J. Phys. Oceanogr.*, **52**, 1501-1512.

[88] Tang, B. and B. Cushman-Roisin, 1992: Two-Layer geostrophic dynamics. Part II: Governing turbulence. *J. Phys. Oceanogr.*, **22**, 128-138.

[89] Visbeck, M., J. Marshall, T. Haines, and M. Spall, 1997: On the specification of eddy transfer coefficients in coarse resolution ocean circulation models. *J. Phys. Oceanogr.*, **27**, 381-402.

References

[90] Whitham, G. B., 1974: *Linear and Nonlinear Waves*, John Wiley and Sons, New York.

[91] Zwillinger, D, 1989: *Handbook of Differential Equations*, Academic Press, New York.

Appendices

Appendix 1.   Derivation of General Two-layer Geostrophic Models

In this section we generalize the derivation found in §2 by including bottom topography and by not expliciting making the FG approximation. This allows us to explore the relationship between QG and FG models, as well as the relationship between the β-plane effect and bottom topography. Finally, through this derivation the clear distinction between surface buoyancy fronts and bottom-trapped fronts is illustrated.

Most of the assumptions of §2 are retained but now we allow the ocean bottom to vary and introduce a variable to describe the interface deflections. As shown in Figure A.1.1 the model geometry now includes bottom topography h_B and interface deflections η. A variable describing interface deflections separate from layer depths is necessary if QG dynamics are to be described. From Figure A.1.1, it follows that

$$h_1 + h_2 + h_B = H.$$
$$h_1 = H_1 + \eta.$$
$$h_2 = H - H_1 - h_B - \eta = H_2 - h_B - \eta. \tag{A.1.1}$$
$$H_1 + H_2 = H.$$

The inclusion of bottom topography in the shallow water equations is straight forward. in fact there is no change. Equations (2.1.5-2.1.9) still hold, with the effects of bottom topography seen through the new relationships governing the depths of the layers as given by (A.1.1). There is a slight change in equation (2.1.9). We now write pressure continuity as

$$\widetilde{p}_1(x,y,t) = g'\eta + \widetilde{p}_2(x,y,t). \tag{A.1.2}$$

This redefines the upper-layer pressure p_1 by subtracting a constant value, $g'H_1$, from it. This has no effect on the model derivations as the pressure is only determined up to a constant.

As before we introduce the barotropic and baroclinic velocities given by (2.2.1) and (2.2.2), respectively, with the barotropic velocity divergent free. The layer

Figure A.1.1: The general model configuration with bottom topography h_B and interface deflections η.
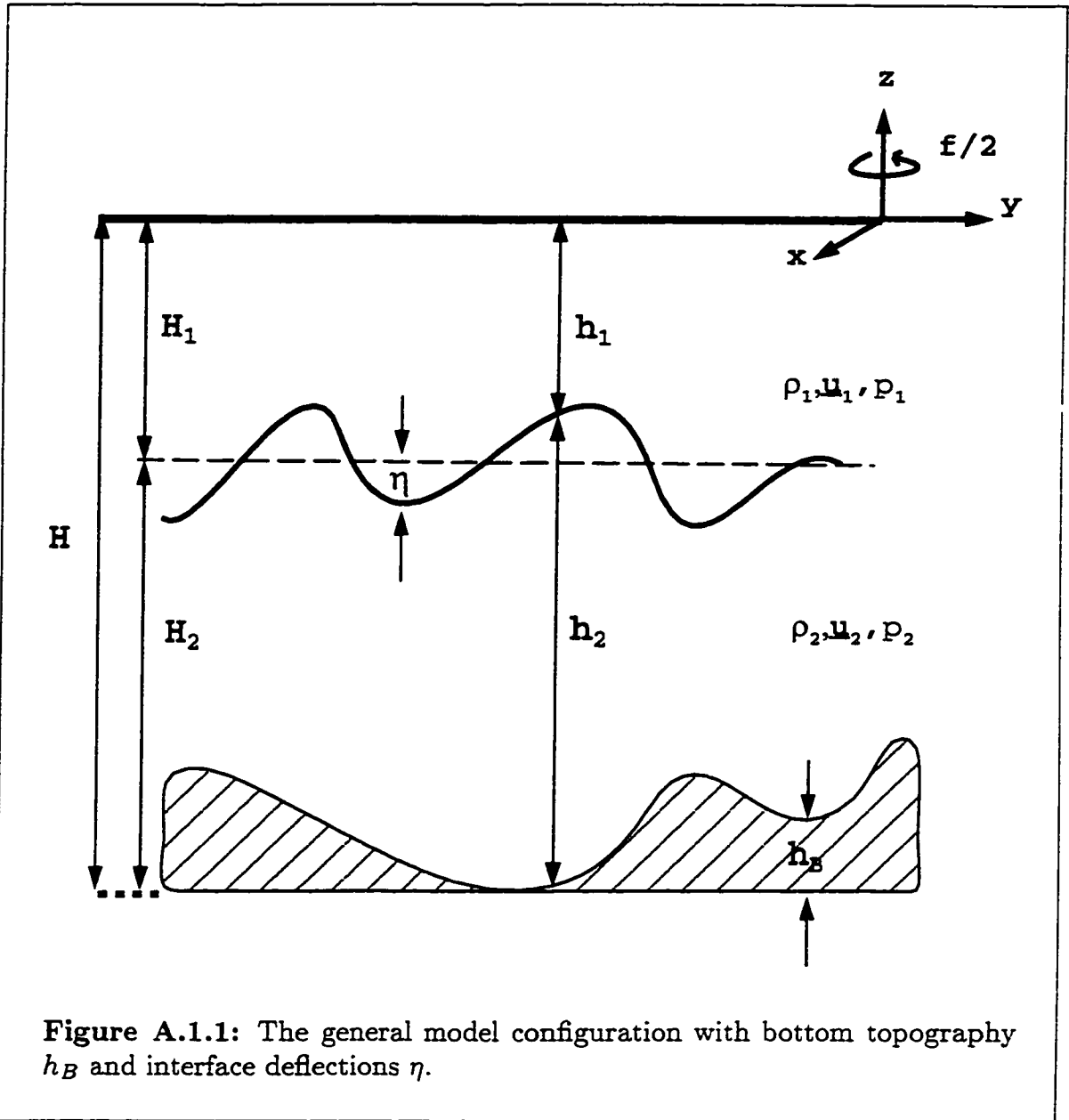
velocities can be expressed in terms of these new velocities, that is,

$$u_1 = \frac{H}{h_1 + h_2}\left(u_{bt} + \frac{h_2}{H}u_{bc}\right), \tag{A.1.3}$$

$$u_2 = \frac{H}{h_1 + h_2}\left(u_{bt} - \frac{h_1}{H}u_{bc}\right). \tag{A.1.4}$$

Appendices

Note that these expressions are not equivalent to (2.2.4) and (2.2.5) as $h_1 + h_2$ is no longer equivalent to H (see (A.1.1)). Since the barotropic velocity is divergent free we again introduce the stream function given by (2.2.12). We form the barotropic equation by taking $\nabla \times [h_1 * (2.1.5) + h_2 * (2.1.7)]$ and divide by H and the baroclinic equation by taking (2.1.5) -(2.1.7). After some simplification and the use of (A.1.3), (A.1.4), (2.1.6), and (2.1.8) we obtain the barotropic, baroclinic and continuity equations given by

$$
\frac{\partial \nabla^2 \psi}{\partial t} + \gamma_H J(\psi, \nabla^2 \psi) + \beta_0 \psi_x
$$
$$
+ \frac{1}{2} J(\nabla \psi \cdot \nabla \psi, \gamma_H) + \left[\psi_x \psi_y (\partial_{yy} - \partial_{xx}) + (\psi_x^2 - \psi_y^2)\partial_{xy} \right] \gamma_H
$$
$$
+ (\gamma_{h*} uv)_{xx} - (\gamma_{h*} uv)_{yy} - \left[\gamma_{h*}(u^2 - v^2) \right]_{xy}
$$
$$
- \frac{J(h_B, p_2)}{H} = 0, \tag{A.1.5}
$$

$$
\frac{\partial u}{\partial t} + \gamma_{h-} (u \cdot \nabla) u + \frac{1}{2} u (u \cdot \nabla \gamma_{h-}) + \gamma_H J(\psi, u)
$$
$$
+ (u \cdot \nabla)(\gamma_H e_3 \times \psi) + (f_0 + \beta_0 y) e_3 \times u + g' \nabla \eta = 0, \tag{A.1.6}
$$

$$
\frac{\partial \eta}{\partial t} + J(\psi, \gamma_H \eta) + H_1 J(\psi, \gamma_H) + \nabla \cdot (H \gamma_{h*} u) = 0. \tag{A.1.7}
$$

respectively, where we have introduced the shorthand notation given by

$$
\gamma_{h*} = \frac{h_1 h_2}{H(h_1 + h_2)} = \frac{h_1 h_2}{H(H - h_B)}, \tag{A.1.8}
$$

$$
\gamma_H = \frac{H}{h_1 + h_2} = \frac{H}{H - h_B}, \tag{A.1.9}
$$

$$
\gamma_{h-} = \frac{h_2 - h_1}{h_1 + h_2} = \frac{h_2 - h_1}{H - h_B}, \tag{A.1.10}
$$

$$
\gamma_{h_B} = \frac{h_B}{h_1 + h_2} = \frac{h_B}{H - h_B}. \tag{A.1.11}
$$

As before, we introduce typical scales as in (2.3.1) with the addition of the

Appendices

scales

$$\eta = \Delta H \eta^*, \quad h_B = h_{B*} h_B^*, \quad \tilde{p}_1 = P_1 p_1^*, \quad \tilde{p}_2 = P_2 p_2^*, \qquad (A.1.12)$$

where ΔH, h_{B*}, P_1, and P_2, are typical interfacial displacement amplitude, bottom variations, upper-layer and lower-layer pressure, respectively.

Applying the scaling (2.3.1) and (A.1.12) to the governing equations, (A.1.5), (A.1.6) and (A.1.7), and dropping the asterisks, gives

$$\begin{aligned}
\epsilon_T \epsilon_\psi \frac{\partial \nabla^2 \psi}{\partial t} &+ \epsilon_\psi^2 \gamma_H J(\psi, \nabla^2 \psi) + \epsilon_\beta \epsilon_\psi \psi_x + \epsilon_\psi^2 J(\frac{1}{2} \nabla \psi \cdot \nabla \psi . \gamma_{h_B}) \\
&+ \epsilon_\psi^2 \left[\psi_x \psi_y (\partial_{yy} - \partial_{xx}) + (\psi_x^2 - \psi_y^2) \partial_{xy} \right] \gamma_{h_B} \\
&+ \epsilon^2 \left[(\gamma_{h*} uv)_{xx} - (\gamma_{h*} uv)_{yy} - \left[\gamma_{h*} (u^2 - v^2) \right]_{xy} \right] \\
&- \delta_B \epsilon_2 J(h_B, p_2) = 0.
\end{aligned} \qquad (A.1.13)$$

$$\begin{aligned}
\epsilon_T \frac{\partial u}{\partial t} &+ \epsilon \gamma_{h-} (u \cdot \nabla) u + \epsilon \frac{1}{2} u (u \cdot \nabla \gamma_{h-}) + \epsilon_\psi \gamma_H J(\psi . u) \\
&+ \epsilon_\psi (u \cdot \nabla)(\gamma_H e_3 \times \nabla \psi) + (1 + \epsilon_\beta y) e_3 \times u + + \frac{\delta_\Delta \epsilon}{F^2} \nabla \eta = 0,
\end{aligned} \qquad (A.1.14)$$

$$\epsilon_T \delta_\Delta \frac{\partial \eta}{\partial t} + \epsilon_\psi \delta_\Delta J(\psi, \gamma_H \eta) + \epsilon_\psi \delta_U J(\psi, \gamma_H) + \epsilon \nabla \cdot (\gamma_{h*} u) = 0, \qquad (A.1.15)$$

where now from (A.1.8), (A.1.17) (A.1.10) and (A.1.11) we have

$$\gamma_{h*} = \frac{(\delta_U + \delta_\Delta \eta)(\delta_L - \delta_\Delta \eta - \delta_B h_B)}{(1 - \delta_B h_B)}, \qquad (A.1.16)$$

$$\gamma_H = \frac{1}{1 - \delta_B h_B}, \qquad (A.1.17)$$

$$\gamma_{h-} = \frac{\delta_L - \delta_U - 2\delta_\Delta \eta - \delta_B h_B}{1 - \delta_B h_B}, \qquad (A.1.18)$$

$$\gamma_{h_B} = \frac{\delta_B h_B}{1 - \delta_B h_B}. \qquad (A.1.19)$$

Appendices

We have introduced the nondimensional parameters given in (2.3.7) and

$$F = \frac{U}{\sqrt{g'H}}, \quad \epsilon_1 = \frac{U_1}{f_0 L}, \quad \epsilon_2 = \frac{U_2}{f_0 L}, \quad \delta_\Delta = \frac{\Delta H'}{H} \quad \delta_B = \frac{h_B \cdot}{H}. \tag{A.1.20}$$

where F is the Froude number associated with the total depth of the ocean, ϵ_1 and ϵ_2 are the Rossby numbers associated with the layer velocities, and δ_Δ and δ_B are depth ratios associated with the motion amplitude and the bottom topography. Also, assuming the scales (2.3.1) satisfy (2.2.4) and (2.2.5) gives the relations

$$\epsilon_1 = \max(\epsilon_\psi, \delta_L \epsilon), \tag{A.1.21}$$

$$\epsilon_2 = \max(\epsilon_\psi, \delta_U \epsilon). \tag{A.1.22}$$

From (A.1.1) it follows that

$$\begin{aligned}
\delta_U h_1 + \delta_L h_2 + \delta_B h_B &= 1, \\
h_1 &= 1 + \frac{\delta_\Delta}{\delta_U} \eta, \\
h_2 &= 1 - \frac{\delta_B}{\delta_L} h_B - \frac{\delta_\Delta}{\delta_L} \eta, \\
\delta_U + \delta_L &= 1.
\end{aligned} \tag{A.1.23}$$

We have written all height variations in terms of η to allow the possibility that changes in layer depth may be scaled differently than the layer depth itself.

We assume that the baroclinic velocity and the velocity in each layer is in *geostrophic balance* with the appropriate pressure gradient. For the geostrophic balance to hold we require $F^2 = \delta_\Delta \epsilon$, or in terms of the velocity scales

$$U = \frac{g' \Delta H}{f_0 L}, \quad U_1 = \frac{P_1}{f_0 L}, \quad U_2 = \frac{P_2}{f_0 L}. \tag{A.1.24}$$

Then, to leading order, equation (A.1.14) gives that the baroclinic velocity is determined *geostrophically* by

$$\boldsymbol{u} = \mathbf{e}_3 \times \nabla \eta + O(\epsilon, \epsilon_T, \epsilon_\beta, \epsilon_\psi). \tag{A.1.25}$$

226

Appendices

The expression (A.1.25) can be used to simplify the next order terms in (A.1.14) to obtain

$$\boldsymbol{u} = (1 - \epsilon_\beta y)\mathbf{e}_3 \times \nabla\eta - \epsilon_T \nabla\eta_t - \epsilon\gamma_{h-} J(\eta, \nabla\eta) - \epsilon\frac{\nabla\eta}{2} J(\gamma_{h-}, \eta)$$
$$- \epsilon_\psi \gamma_H J(\psi, \nabla\eta) - \epsilon_\psi J(\eta, \gamma_H \nabla\psi) + O(\epsilon_\beta, \epsilon, \epsilon_\psi, \epsilon_T)^2. \tag{A.1.26}$$

Substituting this expression into (A.1.13) and (A.1.15) gives

$$\epsilon_T \epsilon_\psi \frac{\partial \nabla^2 \psi}{\partial t} + \epsilon_\psi^2 \gamma_H J(\psi, \nabla^2\psi) + \epsilon_\beta \epsilon_\psi \psi_x + \frac{\epsilon_\psi^2}{2} J(\nabla\psi \cdot \nabla\psi, \gamma_{h_B})$$
$$+ \epsilon_\psi^2 \left[\psi_x \psi_y (\partial_{yy} - \partial_{xx}) + (\psi_x^2 - \psi_y^2)\partial_{xy} \right] \gamma_{h_B} \tag{A.1.27}$$
$$+ \epsilon^2 \nabla \cdot J(\eta, \gamma_{h*} \nabla\eta) - \delta_B \epsilon_2 J(h_B, p_2) = h.o.t..$$

$$\epsilon_T \delta_\Delta \frac{\partial\eta}{\partial t} + \epsilon_\psi \delta_\Delta J(\psi, \gamma_H \eta) + \epsilon_\psi \delta_U J(\psi, \gamma_H)$$
$$- \epsilon\gamma_{h*} \left[\epsilon_\beta \eta_x + \epsilon_T \nabla^2 \eta_t + \epsilon\nabla \cdot [\gamma_{h-} J(\eta, \nabla\eta)] \right.$$
$$+ \epsilon\frac{\nabla\eta}{2} \cdot \nabla J(\gamma_{h-}, \eta) + \epsilon\frac{\nabla^2\eta}{2} J(\gamma_{h-}, \eta)$$
$$\left. + \epsilon_\psi \nabla \cdot [\gamma_H J(\psi, \nabla\eta) + J(\eta, \gamma_H \nabla\psi)] \right] \tag{A.1.28}$$
$$+ \epsilon\delta_B \gamma_H \left[\gamma_{h*} - (\delta_U + \delta_\Delta \eta) \right] J(\eta, h_B)$$
$$- \epsilon \left[+ \epsilon_T \nabla\eta_t + \epsilon\gamma_{h-} J(\eta, \nabla\eta) + \epsilon\frac{\nabla\eta}{2} J(\gamma_{h-}, \eta) \right.$$
$$\left. + \epsilon_\psi \gamma_H J(\psi, \nabla\eta) + \epsilon_\psi J(\eta, \gamma_H \nabla\psi) \right] \cdot \nabla\gamma_{h*} = h.o.t.$$

The relation (A.1.2) reduces to

$$\epsilon_1 p_1 = \epsilon\eta + \epsilon_2 p_2. \tag{A.1.29}$$

The final term in (A.1.27) contains a term in p_2 that we wish to write in terms of ψ and η. To do so we consider the expanded versions of the layer velocities

227

analogous to (A.1.26), given by

$$u_1 = e_3 \times \nabla p_1 - \epsilon_T(\nabla p_1)_t - \epsilon_1 J(p_1, \nabla p_1)$$
$$- \epsilon_\beta y e_3 \times \nabla p_1 + [O(\epsilon_T, \epsilon_1, \epsilon_\beta)]^2, \tag{A.1.30}$$

$$u_2 = e_3 \times \nabla p_2 - \epsilon_T(\nabla p_2)_t - \epsilon_2 J(p_2, \nabla p_2)$$
$$- \epsilon_\beta y e_3 \times \nabla p_2 + [O(\epsilon_T, \epsilon_2, \epsilon_\beta)]^2. \tag{A.1.31}$$

Using these expressions and using ΨL as a barotropic velocity scale, it follows from (2.2.1) that

$$\epsilon_\psi u_{bt} = e_3 \times \nabla \left(\delta_U \epsilon \eta + \frac{1}{2} \epsilon \delta_\Delta \eta^2 + \epsilon_2 p_2 \right)$$
$$- \epsilon_2 \delta_B h_B e_3 \times \nabla p_2 + O[\epsilon_1(\epsilon_T, \epsilon_1, \epsilon_\beta), \epsilon_2(\epsilon_T, \epsilon_2, \epsilon_\beta)]. \tag{A.1.32}$$

Now, the fact that the barotropic velocity is divergent free places a restriction on the final term of (A.1.32). Taking the divergence of (A.1.32) gives

$$\epsilon_2 \delta_B J(h_B, p_2) = O[\epsilon_1(\epsilon_T, \epsilon_1, \epsilon_\beta), \epsilon_2(\epsilon_T, \epsilon_2, \epsilon_\beta)].$$

Since h_B and p_2 are presumed to be $O(1)$ quantities, it follows that either

$$J(h_B, p_2) = 0, \tag{A.1.33}$$

or

$$\delta_B = \max\left(\frac{\epsilon_1}{\epsilon_2}, 1 \right) O(\epsilon_T, \epsilon_\beta, \epsilon_1, \epsilon_2). \tag{A.1.34}$$

In the former case, the general solution to (A.1.33) is that the lower-layer pressure is a function of bottom topography, that is, $p_2 = F(h_B)$. Therefore lines of constant pressure p_2 are parallel to lines of constant bathymetry, h_B. Since, to leading order, p_2 is the lower-layer stream function (see (A.1.31)) it follows that the flow is topographically steered; the flow follows lines of constant bathymetry. This is not a case that is of interest in this thesis since it is obviously not the front that is driving the flow in the lower layer but the strong topography.

Appendices

In the latter case, in order that (A.1.34) hold even when $\epsilon_2 \simeq \epsilon_1$, it is necessary that

$$\delta_B \ll 1. \tag{A.1.35}$$

This assumption simply states that the bottom topography we consider is weak in order to avoid flow that are strongly influenced by topography. This allows (A.1.16–A.1.19) to be simplified , giving

$$\gamma_{h*} = (\delta_U + \delta_\Delta \eta)(\delta_L - \delta_\Delta \eta - \delta_B h_B), \tag{A.1.36}$$

$$\gamma_H = 1 + \delta_B h_B, \tag{A.1.37}$$

$$\gamma_{h-} = (\delta_L - \delta_U - 2\delta_\Delta \eta - \delta_B h_B). \tag{A.1.38}$$

$$\gamma_{h_B} = \delta_B h_B. \tag{A.1.39}$$

It follows from (A.1.34) that (A.1.32) can be reduced to

$$\epsilon_2 p_2 = \epsilon_\psi \psi - \epsilon \delta_U \eta - \frac{1}{2}\epsilon \delta_\Delta \eta^2 + O(\epsilon_T, \epsilon_1, \epsilon_2, \epsilon_3). \tag{A.1.40}$$

This can be used to eliminate p_2 in the final term of (A.1.27) and using (A.1.36–A.1.39) in both (A.1.27) and (A.1.28) gives

$$\epsilon_T \epsilon_\psi \frac{\partial \nabla^2 \psi}{\partial t} + \epsilon_\psi^2 \gamma_H J(\psi, \nabla^2 \psi) + \epsilon_3 \epsilon_\psi \psi_x + \epsilon^2 \nabla \cdot J(\eta, \gamma_{h*} \nabla \eta)$$
$$- \delta_B J\left(h_B, \epsilon_\psi \psi - \epsilon \delta_U \eta - \frac{1}{2}\epsilon \delta_\Delta \eta^2\right) = 0, \tag{A.1.41}$$

$$\epsilon_T \delta_\Delta \frac{\partial \eta}{\partial t} + \epsilon_\psi \delta_\Delta J(\psi, \eta) + \epsilon_\psi \delta_B \delta_U J(\psi, h_B) - \epsilon \epsilon_3 \gamma_{h*} \eta_x$$
$$- \epsilon \nabla \cdot \left[\epsilon_T \gamma_{h*} \nabla \eta_t + \epsilon \gamma_{h*} \gamma_{h-} J(\eta, \nabla \eta)\right.$$
$$\left. + \epsilon_\psi \gamma_{h*} [J(\psi, \nabla \eta) + J(\eta, \nabla \psi)]\right] \tag{A.1.42}$$
$$- \epsilon \delta_B \left[(\delta_U + \delta_\Delta \eta)(\delta_U + \delta_\Delta \eta + \delta_B h_B)\right] J(\eta, h_B) = h.o.t.,$$

respectively. These are the general barotropic and baroclinic equations analogous to (2.3.13) and (2.3.14) but now including QG effects and bottom topography.

Appendices

We define

$$\delta = \min(\delta_U, \delta_L),$$ (A.1.43)

so that $\delta \leq \frac{1}{2}$. We also assume that $\delta_\Delta \leq \delta$, that is, the motion amplitude can be at most the size of the thinnest layer (see Cushman-Roisin *et al.*, 1992). This allows us to define the internal Froude number in terms of the thinner layer, $F_I = \delta^{1/2} F$, which satisfies,

$$F_I^2 = \frac{\delta_\Delta}{\delta} \epsilon.$$ (A.1.44)

With the assumption that $\epsilon_1 = \epsilon$, that is, the upper-layer velocity scales the same as the baroclinic velocity, substitution of ψ into (A.1.41) and (A.1.42) gives equations similar to the barotropic and baroclinic equations found in Cushman-Roisin *et al.* (1992) (equations 23 and 31, respectively).

As before, we argue that the secondary parameters, ϵ_T and ϵ_ψ, are functions of the other parameters. The ϵ_T parameter is determined by enforcing that a balance exists between prognostic terms and diagnostic terms in the baroclinic equations. The ϵ_ψ parameter is determined by enforcing that a balance exists between barotropic terms and baroclinic terms in the barotropic equations. The addition of bottom topography makes the flow asymmetric with respect to the layer depths as seen in the equations (A.1.16–A.1.19). When bottom topography is removed, as in the body of the thesis, the model is symmetric and one can without loss of generality choose $H_1 \leq H_2$, and thus $\delta = \delta_U$. Simply stated, with a rigid lid and flat bottom, a thin-upper-layer model is identical to a thin-lower-layer model. But, as we have chosen to include bottom topography, we must examine these two cases separately. We will discuss the thin-upper-layer case first and then the thin-lower-layer case.

We begin by examining the case where $H_1 \leq H_2$, so that $\delta_U = \delta$ and $\delta_L = 1 - \delta$. Using these expressions in (A.1.36, A.1.38) gives

$$\begin{aligned}
\gamma_{h*} &= (\delta + \delta_\Delta \eta)(1 - \delta - \delta_\Delta \eta - \delta_B h_B), \\
\gamma_{h-} &= 1 - 2(\delta + \delta_\Delta \eta) + O(\delta, \delta_\Delta, \delta_B)^2.
\end{aligned}$$ (A.1.45)

Appendices

Examining (A.1.42) and (A.1.41) gives that

$$\epsilon_T = \frac{\max(\delta_\Delta \epsilon_\psi, \delta\delta_B\epsilon_\psi, \delta\epsilon\epsilon_\beta, \delta\epsilon^2, \delta^2\delta_B\epsilon, \delta\delta_B^2\epsilon)}{\max(\delta_\Delta, \delta\epsilon)}. \tag{A.1.46}$$

$$\epsilon_\psi = \frac{\delta\epsilon\max(\epsilon, \delta_B)}{\max(\epsilon_T, \epsilon_\beta, \delta_B)}, \tag{A.1.47}$$

where we have used that (2.4.4) and (2.4.3) again hold.

From (A.1.46), it becomes evident that an important relation is which term dominates the numerator, that is, whether $\delta_\Delta \geq \epsilon\delta$ or not. In order to examine the essential role this inequality plays, we examine the very simple case of no bottom topography or β-plane, that is, $\delta_B = \epsilon_\beta = 0$. In this limit, (A.1.46, A.1.47) reduce to

$$\epsilon_T = \frac{\max(\frac{\delta_\Delta \delta\epsilon^2}{\epsilon_T}, \delta\epsilon^2)}{\max(\delta_\Delta, \delta\epsilon)}, \tag{A.1.48}$$

$$\epsilon_\psi = \frac{\delta\epsilon^2}{\epsilon_T}.$$

The solution to (A.1.48) can be plotted graphically and is shown in Figure A.1.2 (see §2 for a description of this type of graph). The graph suggests that a single limit, that found at the X marked QG, embodies the characteristics of all the regions in the graph. This point is given by

$$\delta_\Delta = \epsilon\delta, \quad \delta = O(1), \tag{A.1.49}$$

that is, the motion amplitude is an order Rossby number smaller than the layer depth and the layer depths are on the order of the total ocean depth. This is the classical QG limit (see Pedlosky, 1987).

Upon closer examination, it becomes apparent that this limit cannot describe the δ axis where $\delta_\Delta = O(\delta)$. This limit, where motion amplitude has the same scale as the layer depth, is the FG limit (Cushman-Roisin, 1986 and Cushman-Roisin *et al.*, 1992). From the graph, the X marked FG where

$$\delta_\Delta = \delta, \quad \delta = O(\epsilon^2), \tag{A.1.50}$$

Figure A.1.2: The solution to (A.1.48) is plotted in the $\delta - \delta_\Delta/\delta$ plane. The shaded regions mark area in which solutions do not exist. The values for ϵ_T and ϵ_ψ are given, with the lines marking the boundaries where these change. Important models occur at the vertices of these lines and are marked with Xs and labelled.

is the 'most important' of these models. It corresponds to a model where the 'active' layer is very thin compared to the total ocean, $H_*/H = O(\epsilon^2) \ll 1$. Note that this scaling gives the WVT model with $\beta = 0$.

This simple limit of no bottom topography or β-plane leads us to consider two important limits, QG where $\delta_\Delta \sim \epsilon\delta$ and FG where $\delta_\Delta \sim \delta$. Obviously other relationships between δ and δ_Δ could be studied but it can be shown that these are the only limits worth discussing even in the presence of bottom topography and β-plane effects. Note that these two limits differ in the choice of the internal Froude number as given by the relation (A.1.44). For the QG limit, $F_I = \epsilon$ while for the FG limit, $F_I = \epsilon^{1/2}$. Since the Froude number is a ratio of inertial effects to buoyancy effects, we see that inertial terms are indeed more important in the FG limit.

We begin by examing the full equations with bottom topography and β-plane in the QG limit where $\delta_\Delta = \epsilon\delta$. For this limit, (A.1.46) and (A.1.47) reduce to

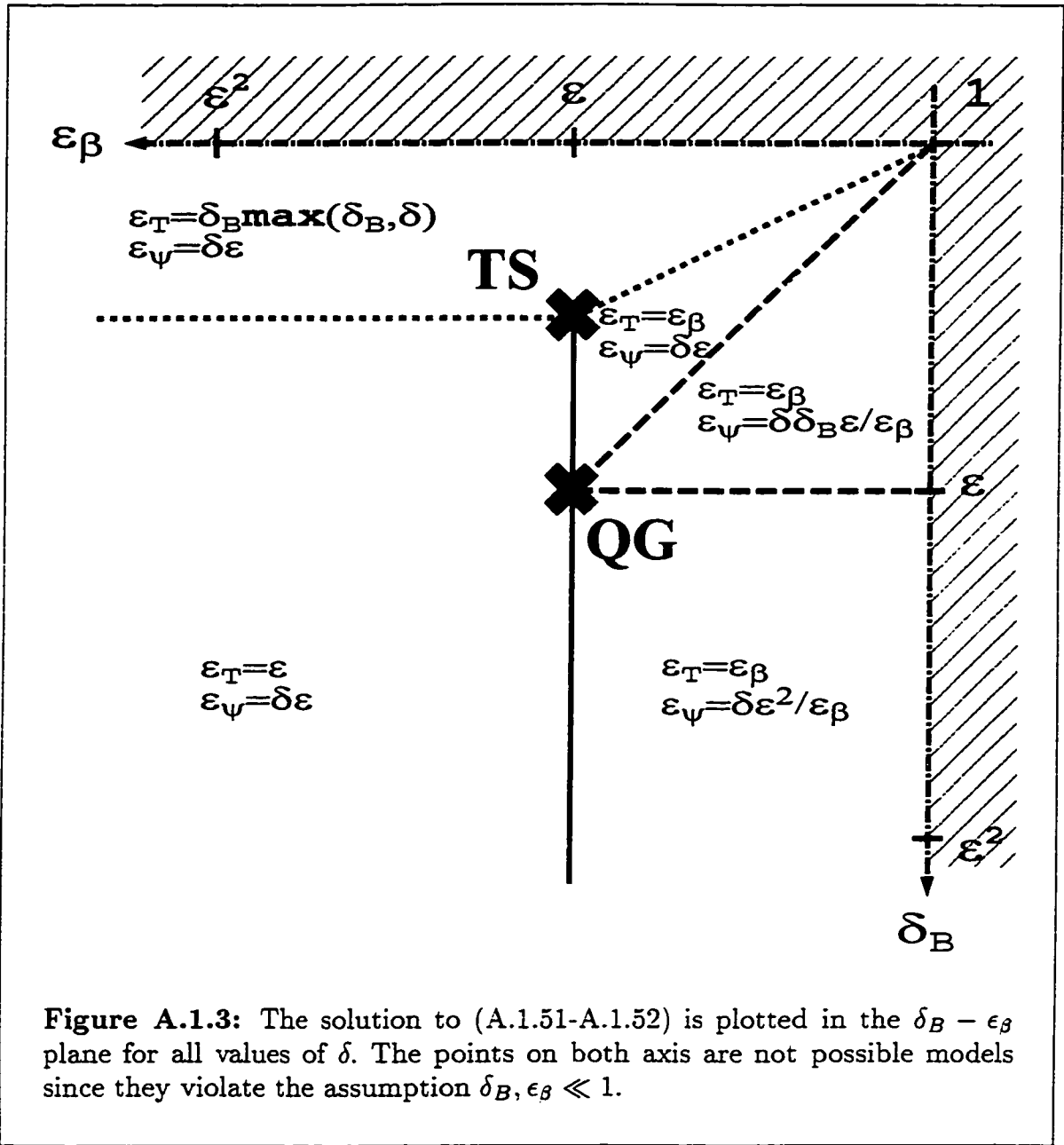$$\epsilon_T = \max(\epsilon_\beta, \epsilon. \delta\delta_B. \delta_B^2). \qquad (A.1.51)$$

$$\epsilon_\psi = \frac{\delta\epsilon \max(\epsilon. \delta_B)}{\max(\epsilon, \epsilon_\beta, \delta_B)}. \qquad (A.1.52)$$

where we have used (A.1.51) and (2.4.4) in (A.1.52) and in turn used the fact that (A.1.52) implies that $\epsilon_\psi \leq \delta\epsilon$ in (A.1.51). The solution is plotted in Figure A.1.3. In the figure, the axes are dashed to indicate that they are not attainable points, that is, points on the axis violate the assumption that $\epsilon_\beta. \delta_B \ll 1$.

Examining the solution, one finds there are two important points. The first, labelled as QG, occurs when $\epsilon_\beta = \delta_B = \epsilon$. At this scaling, where β-plane effects and topographic effects are of a similar order, the standard QG model is obtained. For the most comprehensive model we choose $\delta = O(1)$, all models with a thinner upper layer are limits of this model. The scaling for this point is given by

$$\delta = \mu, \quad \delta_\Delta = \mu\epsilon, \quad \epsilon_\beta = \beta\epsilon, \quad \delta_B = \kappa\epsilon,$$
$$\epsilon_T = \epsilon_\psi = \epsilon, \quad \epsilon_1 = \epsilon_2 = \epsilon, \qquad (A.1.53)$$

where μ, β, and κ are the $O(1)$ variations of the upper-layer depth, the β-plane effect, and the bottom topography, respectively. The governing equations (A.1.41)

Figure A.1.3: The solution to (A.1.51-A.1.52) is plotted in the $\delta_B - \epsilon_\beta$ plane for all values of δ. The points on both axis are not possible models since they violate the assumption $\delta_B, \epsilon_\beta \ll 1$.

Appendices

and (A.1.42) reduce to

$$\nabla^2\psi_t + J(\psi, \nabla^2\psi) + \beta\psi_x$$
$$+ \mu(1-\mu)J(\eta, \nabla^2\eta) - \kappa J(h_B, \psi - \mu\eta) = 0. \tag{A.1.54}$$

$$\eta_t - (1-\mu)\nabla^2\eta_t + J(\psi, \eta) - \beta(1-\mu)\eta_x$$
$$- (1-\mu)\left[(1-2\mu)J(\eta, \nabla^2\eta) + J(\psi, \nabla^2\eta) + J(\eta, \nabla^2\psi)\right] \tag{A.1.55}$$
$$- \kappa J(h_B, \psi - \mu\eta) = 0,$$

and the relations (A.1.40) and (A.1.29) reduce to

$$\psi = \mu\eta + p_2, \tag{A.1.56}$$

$$p_1 = \eta + p_2, \tag{A.1.57}$$

respectively.

The second model of importance corresponding to point TS in Figure A.1.3, occurs at the scaling $\epsilon_\beta = \epsilon$ and $\delta_B \max(\delta, \delta_B) = \epsilon$. When $\delta = O(1) > \delta_B$, this point coincides with the QG model above and is identical. We only need consider the case when $\delta \ll 1$, which in turn implies that $\delta_B \gg \epsilon$. The scaling is given by

$$\delta_\Delta = \delta\epsilon, \quad \epsilon_\beta = 3\epsilon, \quad \delta_B = \frac{\kappa\epsilon}{\max(\delta, \epsilon^{\frac{1}{2}})}, \quad \epsilon_T = \epsilon, \quad \epsilon_\nu = \delta\epsilon.$$

The governing equation (A.1.41) and (A.1.42) reduces to

$$J(h_B, \psi - \eta) = 0, \tag{A.1.58}$$

$$\eta_t - \nabla^2\eta_t - \beta(1-\mu)\eta_x - \kappa(1 + \kappa h_B)J(h_B, \eta) = 0, \tag{A.1.59}$$

and the relation (A.1.40) reduces to

$$\psi = \eta + p_2.$$

So that from (A.1.58) we have $J(h_B, p_2) = 0$, which is the case of topographic steering discussed before and is not of interest in this work.

Appendices

The FG limit scales the motion amplitude equal to the scale of the thinner layer, that is, $\delta_\Delta = \delta$. This assumption reduces the scaling equations (A.1.46) and (A.1.47) to

$$\epsilon_T = \max(\epsilon_\psi, \epsilon\epsilon_\beta, \epsilon^2, \delta\delta_B\epsilon, \delta_B^2\epsilon), \qquad (A.1.60)$$

$$\epsilon_\psi = \frac{\delta\epsilon\max(\epsilon, \delta_B)}{\max(\epsilon_\psi, \epsilon_\beta, \epsilon^2, \delta_B)}, \qquad (A.1.61)$$

where (A.1.60) has been used in (A.1.61). It is not as easy to plot the solution to these equations as in the case of QG since the solutions depend strongly on three parameters, δ, δ_B, and ϵ_β. For that reason we plot some simplified solutions.

From past experience and physical models, it has becomes evident that bottom topography and the β-plane play a similar role. The limits of one of these factors being dominant is interesting as they allow comparison to previous works and allow simplified solutions to exist. In the limit that

$$\max(\epsilon, \delta_B^2, \delta\delta_B) \geq \epsilon_\beta, \quad \text{and} \quad \max(\epsilon^2, \delta_B) \geq \epsilon_\beta, \qquad (A.1.62)$$

all terms related to ϵ_β are dropped from (A.1.60) and (A.1.61). The solution can then be plotted in the $\delta - \delta_B$ plane as shown in Figure A.1.4.

The graph indicates there are four important models labelled TS, SE, ST, and WVT. The TS model, where $\delta_B = \epsilon^{\frac{1}{2}}$ and $\delta = \epsilon$ reduces to similar equations given by the case of topographic steering discussed previously for the QG model and will not be discussed here. The remaining models correspond to the models discussed in the body of the thesis provided the value for ϵ_β is chosen to be the largest value allowed under the restrictions (A.1.62). The SE model corresponds to the scaling (5.1.1) with $\delta_B = \kappa\epsilon$, the ST model corresponds to the scaling (3.1.1) with $\delta_B = \kappa\epsilon$, and the WVT model corresponds to the scaling (A.2.1) with $\delta_B = \kappa\epsilon^2$.

On the other hand, in the limit that

$$\epsilon \geq \delta_B, \quad \text{and} \quad \max(\epsilon^2, \epsilon_\beta) \geq \delta_B, \qquad (A.1.63)$$

all terms related to δ_B are dropped from (A.1.60) and (A.1.61). The solution can then be plotted in the $\delta - \epsilon_\beta$ plane as shown in the body of the thesis in Figure 2.3. The graph indicates there are four important models namely the four models

δ ε^2 ε 1

$\varepsilon_T = \varepsilon \delta_B{}^2$
$\varepsilon_\psi = \delta \varepsilon$

TS

$\varepsilon_T = \varepsilon^2$
$\varepsilon_\psi = \delta \varepsilon$

$\varepsilon_T = \delta \varepsilon$
$\varepsilon_\psi = \delta \varepsilon$

ST   **SE**

$\varepsilon_T = \delta \varepsilon^2 / \delta_B$
$\varepsilon_\psi = \delta \varepsilon^2 / \delta_B$

$\varepsilon_T = \varepsilon^2$
$\varepsilon_\psi = \delta \varepsilon^2 / \delta_B$

ε

WT

$\varepsilon_T = \delta^{1/2} \varepsilon$
$\varepsilon_\psi = \delta^{1/2} \varepsilon$

ε^2

WVT

$\varepsilon_T = \varepsilon^2$
$\varepsilon_\psi = \delta$

δ_B

Figure A.1.4: The solution to (A.1.60-A.1.61) when ϵ_β is not important is plotted in the $\delta - \delta_B$ plane.
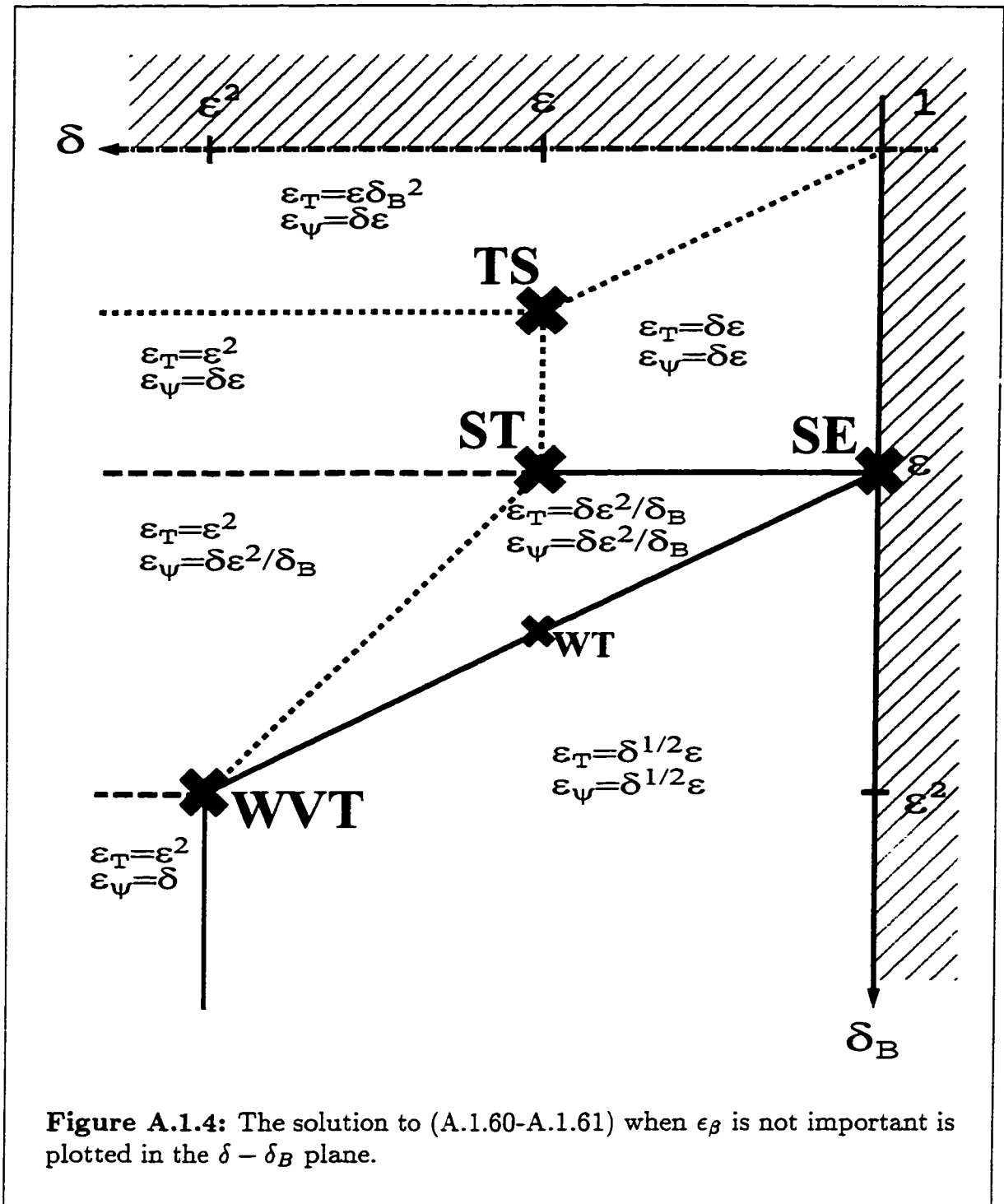
examined in the body of this thesis. For the models, bottom topography can be included by choosing the value for δ_B to be the largest value allowed under the restrictions (A.1.63). The SE, ST, and WVT models give the scalings and models found above. The VSE model scales the bottom topography as $\delta_B = \kappa\epsilon^{\frac{1}{2}}$. Note that $\delta_B = \epsilon_\beta$ in all these models emphasizing that in thin-upper-layer models bottom topography is very similar to the β-plane effect.

The range in between these two limits, where both δ_B and ϵ_β determine the scaling can be examined by plotting solutions for chosen layer depths. For example, if we choose $\delta = \delta_\Delta = \epsilon$ the solution can be plotted in the $\delta_B - \epsilon_\beta$ plane as shown in Figure A.1.5. The graph indicates there are three important models labelled TS, ST, and WT. The TS model is the topographic steering model and the ST model is the strong thin model found previously.

The WT model corresponds to the scaling

$$\delta = \delta_\Delta = \mu\epsilon, \quad \epsilon_\beta = \beta\epsilon^{\frac{3}{2}}, \quad \delta_B = \kappa\epsilon^{\frac{3}{2}}, \quad \epsilon_T = \epsilon_{\psi} = \epsilon_2 = \epsilon^{\frac{3}{2}}, \quad \epsilon_1 = \epsilon, \quad \text{(A.1.64)}$$

and corresponds to a model where the effect of topography and the β-plane are weak (W) and the upper-layer depth is thin (T). This model is not a 'unique' model from those discussed previously. Indeed, the scaling corresponds to the point labelled WT on Figure A.1.4, which is not a vertex in this graph. The model exists midway between the SE and WVT models and the model equations consist of the terms common to both these models. As such, this model is not as important as the others discussed so far. However, this is not to say it is not of use. Since the model equations are somewhat simpler than those of the SE and WVT models, and since it marks a transition between these models, this model may allow a greater amount of analysis to be done providing insight into the differences of the two models. (For example Benilov and Cushman-Roisin (1994) examined the linear stability characteristics of the WT model.) Obviously, such a 'mid-model' exists between any two of the key models discussed previously.

A final note here. It appears that important points on a solution graph in the $\epsilon_\beta - \delta_B$ plane are not always fundamental models as illustrated by the WT model. These models may mark only a shift in the importance of the bottom topography relative to the β-plane and not a fundamental shift in the dynamics a model describes.

Appendices

Figure A.1.5: The solution to (A.1.60-A.1.61) when $\delta = \epsilon$ plotted in the $\delta_B - \epsilon_\beta$ plane.

239
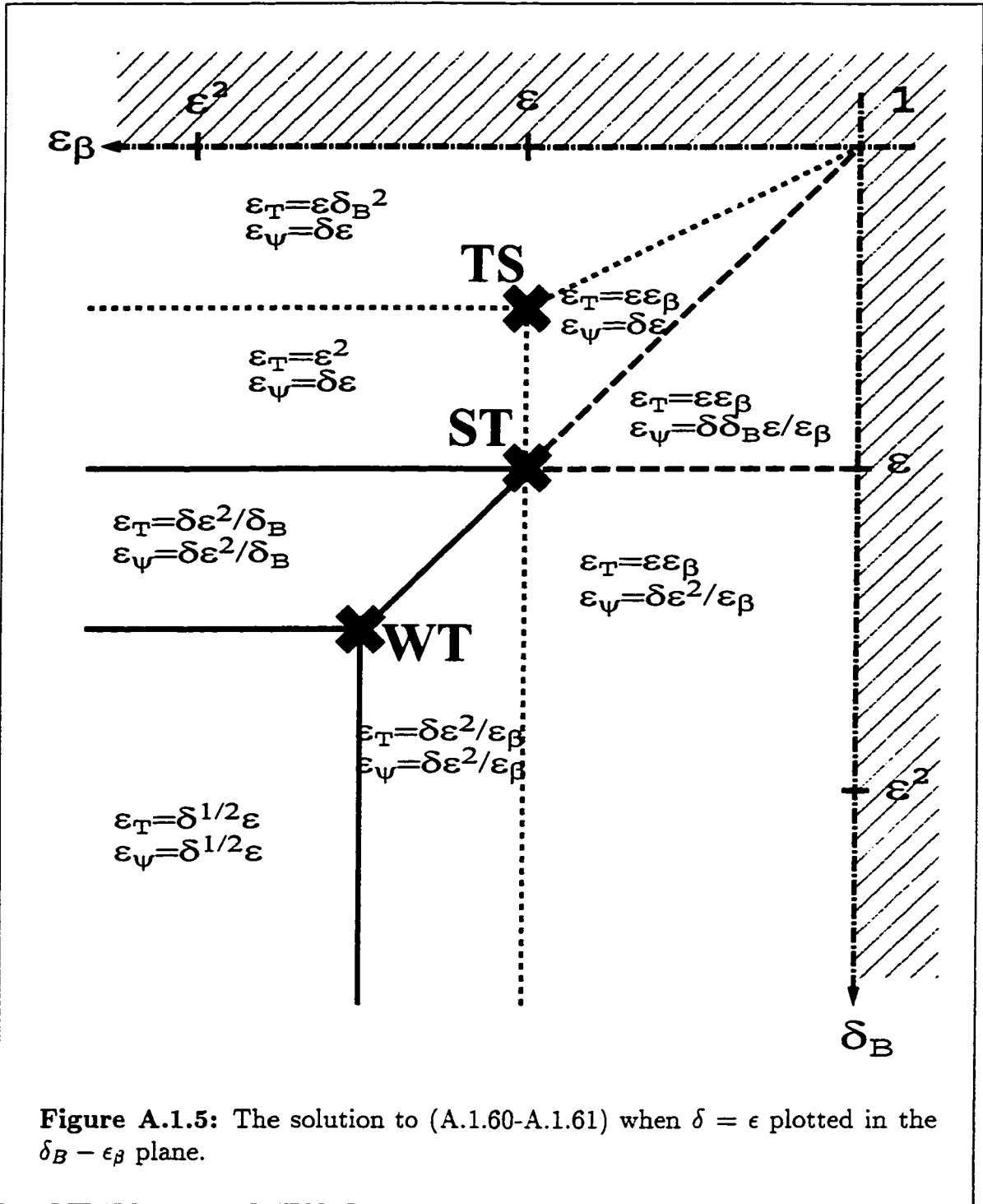
Appendices

We can now repeat the previous analysis but in the limit where the lower is the thinner layer. In this case, $H_2 \leq H_1$ and we have that $\delta_L = \delta$ and $\delta_U = 1 - \delta$. Using these expressions in (A.1.16-A.1.19) gives

$$
\begin{aligned}
\gamma_{h*} &= (1 - \delta + \delta_\Delta \eta)(\delta - \delta_\Delta \eta - \delta_B h_B), \\
\gamma_{h-} &= -1 + 2(\delta - \delta_\Delta \eta) + O(\delta, \delta_\Delta, \delta_B)^2.
\end{aligned}
\tag{A.1.65}
$$

Using the expression (A.1.65), we repeat the previous procedure to find that

$$
\epsilon_T = \frac{\max(\delta_\Delta \epsilon_\psi, \delta_B \epsilon_\psi, \delta \epsilon \epsilon_\beta, \delta \epsilon^2, \delta \epsilon \epsilon_\psi, \delta_B \epsilon)}{\max(\delta_\Delta, \delta \epsilon, \delta_B \epsilon)}.
\tag{A.1.66}
$$

$$
\epsilon_\psi = \frac{\epsilon \max(\delta \epsilon, \delta_B)}{\max(\epsilon_T, \epsilon_\psi, \epsilon_\beta, \delta_B)}.
\tag{A.1.67}
$$

It can be easily shown that (2.4.4) and (2.4.3) also hold in the case of a thin lower layer. As well, in (A.1.66) if $\delta_B \epsilon \geq \max(\delta_\Delta, \delta \epsilon)$ then it follows that

$$
\begin{aligned}
\epsilon_T &= \frac{\max(\delta_\Delta \epsilon_\psi, \delta \epsilon \epsilon_\beta, \delta \epsilon^2, \delta_B \epsilon)}{\delta_B \epsilon} \\
&\geq \frac{\delta_B \epsilon}{\delta_B \epsilon} \\
&= 1.
\end{aligned}
$$

This contradicts our assumption (2.3.8) and we therefore have that

$$
\delta_B \leq \max(\frac{\delta_\Delta}{\epsilon}, \delta).
\tag{A.1.68}
$$

Using (2.4.4), (2.4.3) and (A.1.68), (A.1.66) and (A.1.67) reduce to

$$
\epsilon_T = \frac{\max(\delta_\Delta \epsilon_\psi, \delta \epsilon \epsilon_\beta, \delta \epsilon^2, \delta_B \epsilon)}{\max(\delta_\Delta, \delta \epsilon)},
\tag{A.1.69}
$$

$$
\epsilon_\psi = \frac{\epsilon \max(\delta \epsilon, \delta_B)}{\max(\epsilon_T, \epsilon_\beta, \delta_B)}.
\tag{A.1.70}
$$

In the case of no bottom topography or β-plane, that is, $\delta_B = \epsilon_\beta = 0$, (A.1.69) and (A.1.70) reduce to (A.1.48) with the solution given in Figure A.1.2. Therefore,

240

it is once again pertinent to discuss the QG and FG limits. In the QG limit where $\delta_\Delta = \epsilon\delta$, one obtains a model equivalent to thin-upper-layer model (A.1.54–A.1.57). The FG assumption, $\delta_\Delta = \delta$, reduces the scaling equations (A.1.69) and (A.1.70) to

$$\epsilon_T = \max(\epsilon_\psi, \epsilon\epsilon_\beta, \epsilon^2, \frac{\delta_B\epsilon}{\delta}), \qquad (A.1.71)$$

$$\epsilon_\psi = \frac{\epsilon\max(\delta\epsilon, \delta_B)}{\max(\epsilon_\psi, \epsilon_\beta, \epsilon^2, \delta_B, \frac{\delta_B\epsilon}{\delta})}, \qquad (A.1.72)$$

where (A.1.71) has been used in (A.1.72).

Once again we look at the limits where either the bottom topography or β-plane dominates. In the limit that

$$\max\left(\epsilon, \frac{\delta_B\epsilon}{\delta}\right) \geq \epsilon_\beta, \quad \text{and} \quad \max(\epsilon^2, \delta_B, \frac{\delta_B\epsilon}{\delta}) \geq \epsilon_\beta. \qquad (A.1.73)$$

all terms related to ϵ_β are dropped from (A.1.71) and (A.1.72). The solution can then be plotted in the $\delta - \delta_B$ plane as shown in Figure A.1.6. The graph indicates there are three important models labelled SE, WVT, and LST. The value for ϵ_β is chosen to be the largest value allowed under the restrictions (A.1.73). The SE model corresponds to the scaling (5.1.1) with $\delta_B = \kappa\epsilon$. and the WVT model corresponds to the scaling (A.2.1) except that now the bottom topography is weaker. that is. $\delta_B = \kappa\epsilon^3$. Note that the governing equation differ slightly when considering the case of a thin lower layer versus a thin upper layer as will be illustrated at the end of this section.

The LST model corresponds to the scaling

$$\delta = \delta_\Delta = \mu\epsilon, \quad \epsilon_\beta = \beta\epsilon, \quad \delta_B = \kappa\epsilon, \quad \epsilon_T = \epsilon_\psi = \epsilon, \qquad (A.1.74)$$

and corresponds to a unique lower-layer model (L) where the effect of topography and the β-plane are strong (S) and the lower-layer depth is thin (T). This is the model derived and examined in Swaters (1991), with further work in Karsten and Swaters (1996a), Mooney and Swaters (1996), and Swaters (1998). The model equations are presented at the end of this section.

In the limit that

$$\delta\epsilon \geq \delta_B, \quad \text{and} \quad \max(\epsilon^2, \epsilon_\beta) \geq \max(\delta_B, \frac{\delta_B\epsilon}{\delta}), \qquad (A.1.75)$$
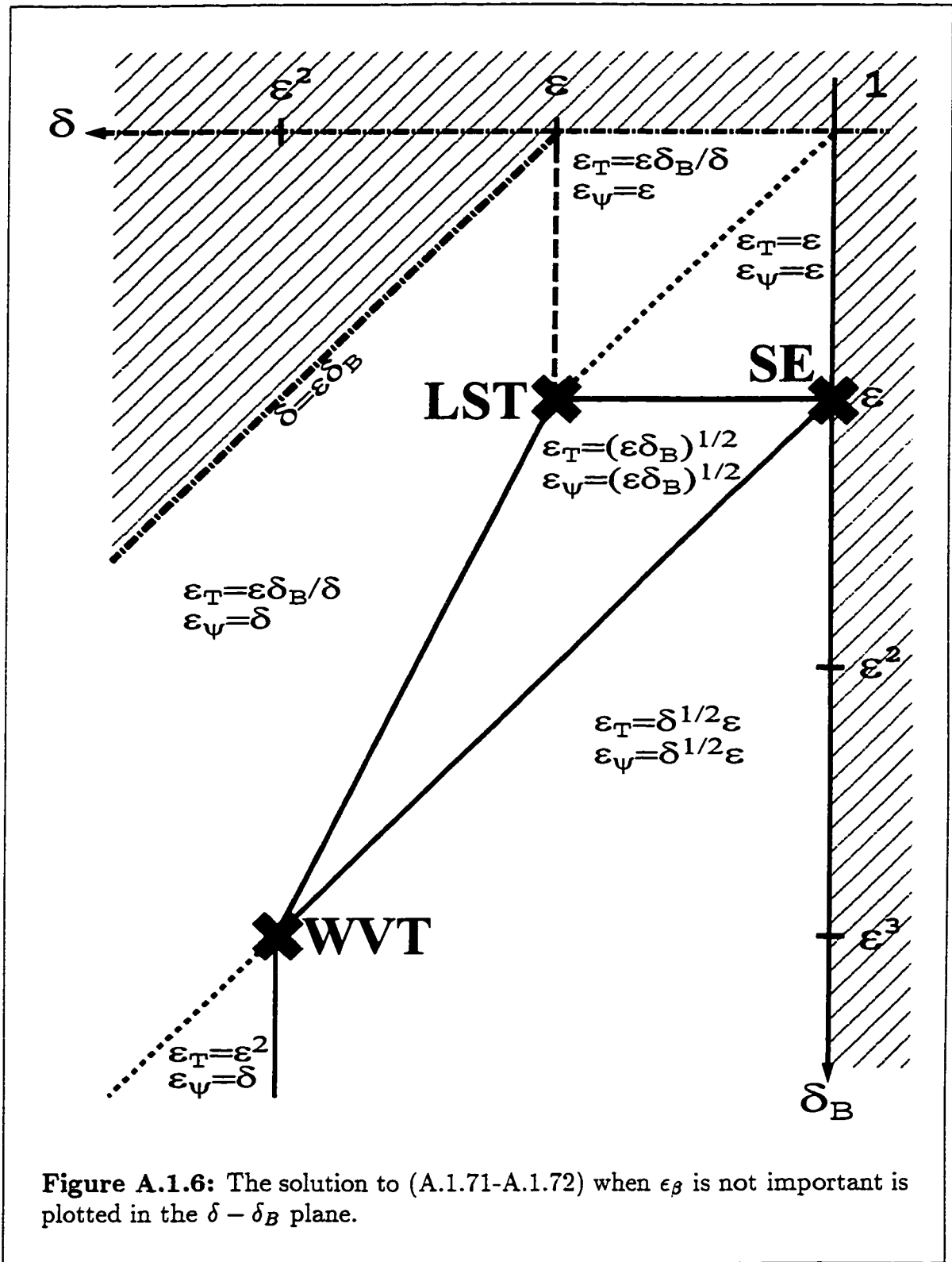
Figure A.1.6: The solution to (A.1.71-A.1.72) when ϵ_β is not important is plotted in the $\delta - \delta_B$ plane.

all terms related to δ_B are dropped from (A.1.71) and (A.1.72). The solution is then identical to the upper-layer solution under the restrictions (A.1.63) and is given in Figure 2.3. Now however, the value for δ_B is chosen to be the largest value allowed under the restrictions (A.1.75) which differ from (A.1.63). The SE and WVT models give the scalings and models found above. The VSE model corresponds to the scaling (4.1.1) $\delta_B = \kappa \epsilon^{\frac{1}{2}}$ and the ST model corresponds to the scaling (3.1.1) except that now the bottom topography again is weaker, that is, $\delta_B = \kappa \epsilon^2$. Note that in the thin-lower-layer models, the WVT and ST models, bottom topography must be scaled an order smaller than the β-plane effect. If the bottom topography is stronger, it dominates the evolution of the thin layer and we get the LST model. As with the thin-upper-layer analysis, there exist models lying between the main models, such as the WT model with the necessary change in the scaling of the bottom topography, $\delta_B = \kappa \epsilon^2$ as opposed to (A.1.64).

For the FG models, we write the model equations in terms of the layer depth, h, as opposed to the interface deflections, η. In the case of a thin upper layer, $h = 1 + \eta$ while in the case of a thin lower layer, $h = 1 - \eta - (\delta_B/\delta)h_B$. The equations for both cases are written below using the notation Θ_U and Θ_L to signify that a term is present in only the thin-upper-layer or thin-lower-layer model, respectively. The pressure in the thicker layer is given by p. For each of the five FG models derived above the barotropic equation, baroclinic equation, and stream function relation are given below.

VSE model:

$$\beta\psi_x + \mu J\left[h, h(1 - \mu h)\nabla h + \frac{1}{2}(1 - 2\mu h)|\nabla h|^2\right]$$
$$- \kappa J\left(h_B, \Theta_L h - \frac{\mu}{2}h^2\right) = 0, \tag{A.1.76}$$
$$h_t + J(\psi, h) - \beta h(1 - \mu h)h_x = 0,$$
$$\epsilon^{\frac{1}{2}}\psi = \frac{\mu}{2}h^2 + p.$$

Appendices

SE model:

$$\nabla^2 \psi_t + J(\psi, \nabla^2 \psi) + \beta \psi_x + \mu J \left[h, h(1 - \mu h)\nabla h + \frac{1}{2}(1 - 2\mu h)|\nabla h|^2 \right]$$

$$- \kappa J(h_B, \psi + \Theta_L h - \frac{\mu}{2} h^2) = 0, \qquad (A.1.77)$$

$$h_t + J(\psi, h) = 0,$$

$$\psi = \frac{\mu}{2} h^2 + p.$$

ST model:

$$\beta \psi_x + \mu J \left(h, h\nabla h + \frac{1}{2}|\nabla h|^2 \right) - \kappa J \left[h_B, \Theta_U (\psi - \frac{\mu}{2} h^2) + \Theta_L h \right] = 0.$$

$$h_t + J(\psi, h) - J \left(h, h\nabla h + \frac{1}{2}|\nabla h|^2 \right) - \beta h h_x$$

$$\qquad (A.1.78)$$

$$+ \Theta_L \frac{\kappa}{\mu} J(h_B, h) = 0.$$

$$\psi = \frac{\mu}{2} h^2 + p.$$

WVT model:

$$\nabla^2 \psi_t + J(\psi, \nabla^2 \psi) + \beta \psi_x + \mu J \left(h, h\nabla h + \frac{1}{2}|\nabla h|^2 \right)$$

$$- \kappa J(h_B, \Theta_U \psi + \Theta_L h) = 0, \qquad (A.1.79)$$

$$h_t + J(\psi, h) - J \left(h, h\nabla h + \frac{1}{2}|\nabla h|^2 \right) + \Theta_L \frac{\kappa}{\mu} J(h_B, h) = 0,$$

$$\psi = p.$$

LST model (Only for a thin lower layer.):

$$\nabla^2 \psi_t + J(\psi, \nabla^2 \psi) + \beta \psi_x - \kappa J(h_B, \psi + h) = 0,$$

$$\mu h_t + \mu J(\psi, h) + \kappa J(h_B, h) = 0, \qquad (A.1.80)$$

$$\psi = p.$$

A couple of notes on these models. First, linearly sloping, meridional topography is often assumed equivalent to a β-plane due to their similarity in the PV

244

Appendices

description of shallow water flow. From the above equations it is clear that they are similar but not identical. Especially when the lower layer is thinner than the upper layer (WVT and ST models), the baroclinic dynamics are directly affected by the bottom topography in a manner different from the β-plane. It should also be noted that models that include bottom topography and use the f-plane approx allow for smaller length scales than the β-plane models. As shown in 2.4, length scales become large in the β-plane models if the effects of the β-plane are to be included at significant levels. However, bottom topography may have relatively large-scale variations over smaller length scales. Thus, the effect of bottom topography may be strong without the length scales becoming large.

Appendix 2.   WVT Model

In this appendix we briefly present results for the WVT model. Most of these results have been established before in the papers Swaters (1993b), Karsten and Swaters (1996b), and Reszka (1997) and are therefore presented here rather than the body of the thesis.

The WVT model corresponds to the scaling

$$\delta = \mu\epsilon^2, \quad \epsilon_\beta = \beta\epsilon^2, \quad \epsilon_T = \epsilon_\psi = \epsilon^2. \tag{A.2.1}$$

and corresponds to a model where the effect of the β-plane is weak (W) and the upper-layer depth is very thin (VT). The model equations (2.3.13) and (2.3.14) reduce to

$$\nabla^2\psi_t + J(\psi, \nabla^2\psi) + \beta\psi_x + \mu J\left(h, h\nabla^2 h + \frac{1}{2}|\nabla h|^2\right) = 0, \tag{A.2.2}$$

$$h_t + J(\psi, h) - J\left(h, h\nabla^2 h + \frac{1}{2}|\nabla h|^2\right) = 0, \tag{A.2.3}$$

$$\psi = p. \tag{A.2.4}$$

Usually, the cubic nonlinear terms are eliminated from (A.2.2) by forming $(A.2.2) + \mu \times (A.2.3)$ to give

$$(\nabla^2\psi + \mu h)_t + J(\psi, \nabla^2\psi + \mu h + \beta y) = 0. \tag{A.2.5}$$

245

Appendices

The potential vorticities are given by

$$q_1 = q_1^{(0)} + \epsilon q_1^{(1)} + O(\epsilon^2) = \frac{1}{h} + \epsilon \frac{\nabla^2 h}{h} + O(\epsilon^2), \qquad \text{(A.2.6)}$$

$$\begin{aligned} q_2 &= 1 + \epsilon^2 q_2^{(0)} + O(\epsilon^4) \\ &= 1 + \epsilon^2 \left[\nabla^2 \psi + \mu h + \beta y \right] + O(\epsilon^4). \end{aligned} \qquad \text{(A.2.7)}$$

This linear stability analysis for the WVT model was presented in Swaters (1993b), where it was established that the model is linearly stable if

$$\psi_0''' - \beta > h_0' > 0, \quad \forall \ y,$$

or

$$\psi_0''' - \beta < h_0' < 0, \quad \forall \ y.$$

These conditions establish that the leading-order PV gradients in the two layers are everywhere of the same sign (see (A.2.6) and (A.2.7)). In Reszka (1997), a linear solution for the gently sloping front basic state (3.2.22) was found with $\tilde{h}$ given by (3.2.27), the frequency satisfying the dispersion relationship given by

$$\tilde{c}(k,\ell) = -\aleph \left[\frac{\tilde{\beta} + \tilde{\alpha} K^4 \pm \sqrt{\left(\tilde{\beta} + \tilde{\alpha} K^4 \right)^2 - 4\tilde{\alpha}(\mu\tilde{\alpha} + \tilde{\beta}) K^4}}{2\tilde{\beta} K^2} \right]. \qquad \text{(A.2.8)}$$

where $K^2 = k^2 + \ell^2$, and the barotropic stream function given by

$$\tilde{\psi} = \left[K^4 + \frac{\mu\tilde{\alpha} + \tilde{\beta}}{\tilde{c}} \right] \tilde{h}.$$

The waves are unstable, $\tilde{c}$ is complex, whenever

$$(\tilde{\beta} - \tilde{\alpha} K^4)^2 - 4\mu\tilde{\alpha}^2 K^4 < 0.$$

246

Appendices

This gives rise to two marginal stability curves,

$$\tilde{\alpha}_{c_1} = \frac{\tilde{\beta}}{K^2(K^2 + 2\mu^{\frac{1}{2}})}, \qquad (A.2.9)$$

$$\tilde{\alpha}_{c_2} = \frac{\tilde{\beta}}{K^2(K^2 - 2\mu^{\frac{1}{2}})}, \qquad (A.2.10)$$

where the first curve corresponds to the lower branch and the second to the upper branch of the marginal stability curve given in Reszka (1997). Note that the inclusion of the nonlinear Jacobian terms in the baroclinic equation has established a high wavenumber cutoff for instability. That is, instability occurs for

$$-\tilde{\alpha}\mu^{\frac{1}{2}} + \sqrt{\tilde{\alpha}^2\mu + \tilde{\alpha}\tilde{\beta}} \leq K^2 \leq \tilde{\alpha}\mu^{\frac{1}{2}} + \sqrt{\tilde{\alpha}^2\mu + \tilde{\alpha}\tilde{\beta}},$$

$$-\tilde{\alpha}\mu^{\frac{1}{2}} - \sqrt{\tilde{\alpha}^2\mu + \tilde{\alpha}\tilde{\beta}} \leq K^2 \leq -\tilde{\alpha}\mu^{\frac{1}{2}} + \sqrt{\tilde{\alpha}^2\mu + \tilde{\alpha}\tilde{\beta}}. \qquad (A.2.11)$$

for $\tilde{\alpha} > 0$ and $\tilde{\alpha} < 0$, respectively. Thus, the 'ultraviolet catastrophe' seen for the SE model does not occur here. It also gives analytical justification for the inclusion of these terms to suppress growth at small scales as was done in §5.9. Note that as μ and β become large, the high wavenumber cutoffs given in (A.2.11) both become large. In this limit the results tend to those of the SE model as one would expect.

The nonlinear invariants and nonlinear stability have been discussed using the structure of the Hamiltonian formulation presented in Swaters (1993b) and Karsten and Swaters (1996b). Here we simply list the invariants as derived in §2.7. They are

$$\mathcal{E} = \frac{1}{2} \iint_\Omega |\nabla\psi|^2 \, dxdy - \frac{1}{2} \iint_{FR} h|\nabla h|^2 \, dxdy, \qquad (A.2.12)$$

$$\mathfrak{C} = \iint_\Omega \Phi_2(\nabla^2\psi + \mu h + \beta y) \, dxdy + \iint_{FR} \Phi_1(h) \, dxdy, \qquad (A.2.13)$$

$$\mathfrak{M} = \iint_\Omega y\nabla^2\psi \, dxdy, \qquad (A.2.14)$$

representing the Hamiltonian or pseudo-energy invariant, the Casimir associated with the leading-order PV for the lower and upper layer and the zonal momentum invariant, respectively. Using the Hamiltonian (see Swaters, 1993b) or the zonal

247

momentum invariant (see Karsten and Swaters, 1996b) is is possible to establish linear and nonlinear stability theorems.

A weakly nonlinear analysis was carried out in Reszka (1997)resulting in an evolution equation identical to (5.5.45) where now

$$\chi = \pm \frac{4k^3(K^2 \mp 1)}{K^6(K^2 \mp 2)}, \qquad (A.2.15)$$

$$\sigma^2 = \frac{\nu k^2}{K^2}, \qquad (A.2.16)$$

$$\Sigma = 2k^2\ell^2 \left[2 \pm K^2 \mp 4\frac{\ell^2(K^2 \pm 1)}{K^2}\right]. \qquad (A.2.17)$$

where the upper sign corresponds to the marginal stability curve (A.2.10) and the lower sign to (A.2.9). The term Γ has a very complicated form (see Reszka, 1997). Note that these results were derived assuming that $\tilde{\beta} = 1$, $\aleph = 1$, and $\mu = 1$. These results can be generalized to reflect arbitrary values of these parameters but this has not been completed at this time. Solutions follow as in §5.4 or Reszka (1997). There are again two basic forms of solutions: periodic modulation of the linear instability when $\Sigma > 0$ and explosive nonlinear instability when $\Sigma < 0$. The parameter Σ changes sign when

$$k^2 = \ell^2 \left[1 \mp \frac{1 + \sqrt{1 + 4\ell^2}}{\ell^2}\right].$$

Thus, the critical zonal wavenumber where nonlinear terms change from a destabilizing effect to a stabilizing effect is slightly smaller than the meridional wavenumber for the upper branch of the marginal stability curve and slightly larger than the meridional wavenumber for the lower branch.

In Reszka (1997), numerical solutions for the WVT model were also presented. It was shown that a coupled front would break up into a series of stationary eddies. As suggested previously, for a coupled front the evolution of the front under the WVT model is very similar to that given by the RED model in the f-plane limit. In Figure A.2.1, we plot the results of a coupled-front simulation using the WVT model. The upper-layer height evolves very similarly to the simulations using the
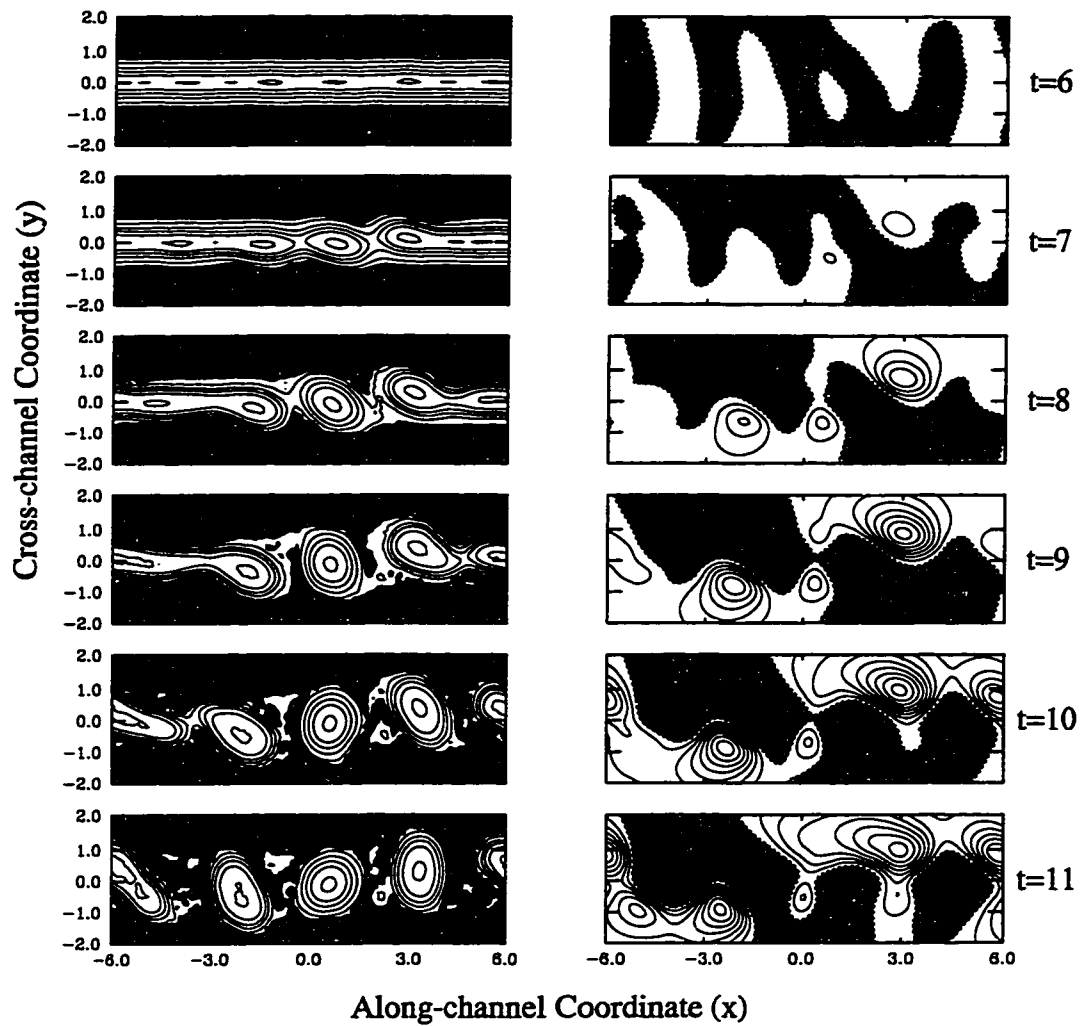
Figure A.2.1: Results of the numerical simulation of the WVT model coupled-front simulation for t=6–11. The graphs on the left show the contours of the upper-layer height. The grey regions are regions where the upper layer vanishes and the contour interval is 0.1. The graphs on the right show the contours of the barotropic stream function. The grey regions are regions where the stream function is negative and the contour interval is 0.005.
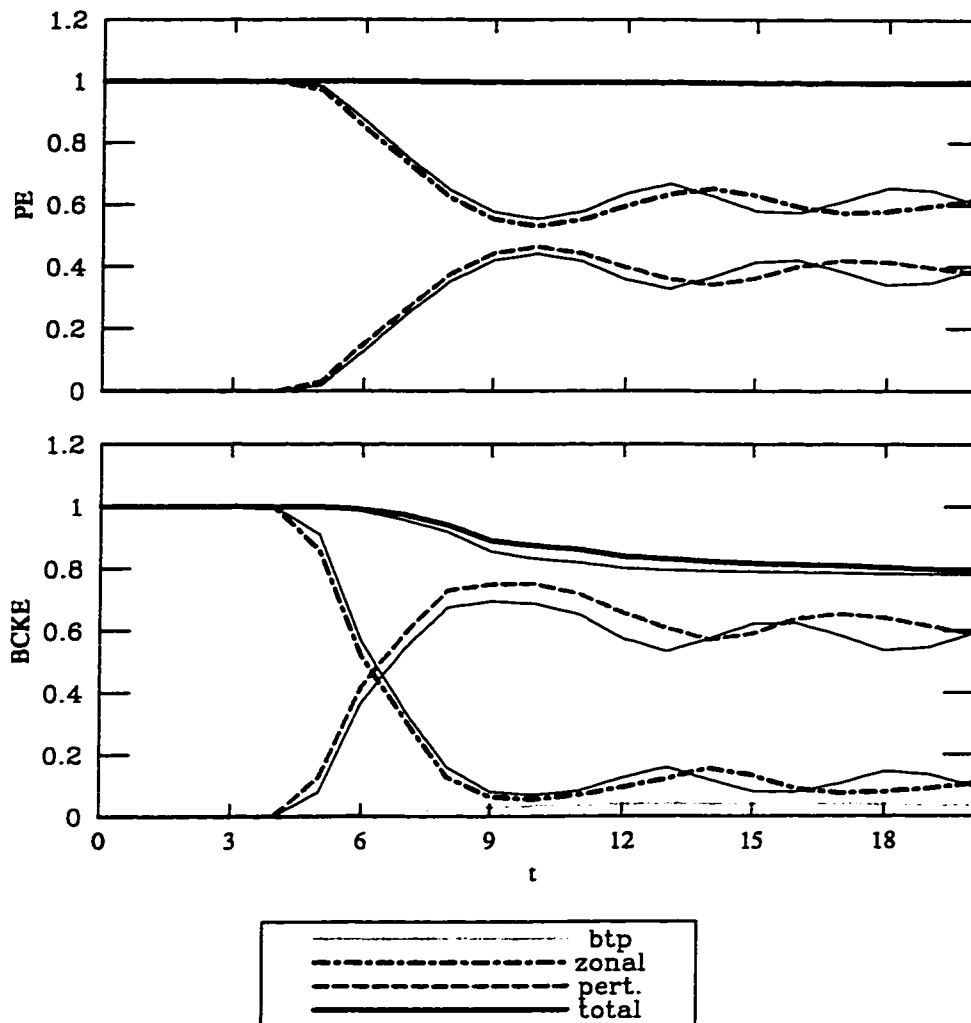
Figure A.2.2: The potential energy (PE, upper plot) and the baroclinic kinetic energy ($BCKE$, lower plot) for the WVT model simulation. The term zonal is used to indicate the mean zonal average, pert. indicates the perturbation to this average and btp indicates the barotropic component. The thin lines are the plots for the corresponding RED model simulation.

RED and ST models as expected. The barotropic stream function develops cells beneath the eddies, which are very weak. The eddies do not drift westward, which is reasonable since the reduced form of the WVT model is the RED model with $\beta = 0$. In Figure A.2.2, we compare the energy diagnostics for the WVT model to the corresponding run of the RED model. Though very similar, two differences occur. First, the instability grows somewhat quicker, indicating that even though the coupling of the lower layer is weak it does enhance instability. Secondly, the total $BCKE$ is larger as it is no longer a conserved quantity but can grow as the barotropic KE grows (see the formulation of $\mathcal{E}$).

For isolated fronts, Reszka (1997) demonstrated that large-scale waves can grow to finite size, often pinching off into warm-core eddies or enclosing cold-core eddies. These large-scale waves can also be nonlinearly modulated with amplitudes that oscillate in time. The conditions that separate these two forms of solutions are not fully understood (M. Reszka, personal communication) but there is no doubt that they are related to the two forms of nonlinear effects seen in the finite amplitude analysis. The development of a barotropic Rossby wave in the lower layer is essential in the instability process. It is the coupling of this wave to the baroclinic dynamics that initiates the instability (Reszka, 1997).

For our purpose we present an example simulation for an isolated front for comparison to the simulations run for the SE model. The results are shown in Figures A.2.3, A.2.4, and A.2.5. The first figure shows the development of a large-scale wave and corresponding barotropic cells. These cells cause the waves to break backwards and eventually pinch off eddies. Note that the growth is seen as the continual growth at a single scale. In the second figure, A.2.4, we concentrate on the process of eddy pinch off and reabsorption. We also illustrate that the instability acts to level out the zonally averaged profile of the front (compare the profile at $t = 83$ to the profile at $t = 0$). By $t = 83$, the instability has developed into large meanders of a sharper front. The zonal and meridional length scales of these meanders are almost equal. Note that longer simulations see the development of further eddies and even cold-core eddies (see Reszka, 1997).

The final figure, A.2.5, plots the energy balances for the simulation. As the large wave begins to grow we see an initial release of zonal $BCKE$ combined with an increase in total and perturbation $BCKE$ as well as barotropic KE. This initiates a release of zonal PE and the instability grows rapidly with large increases in
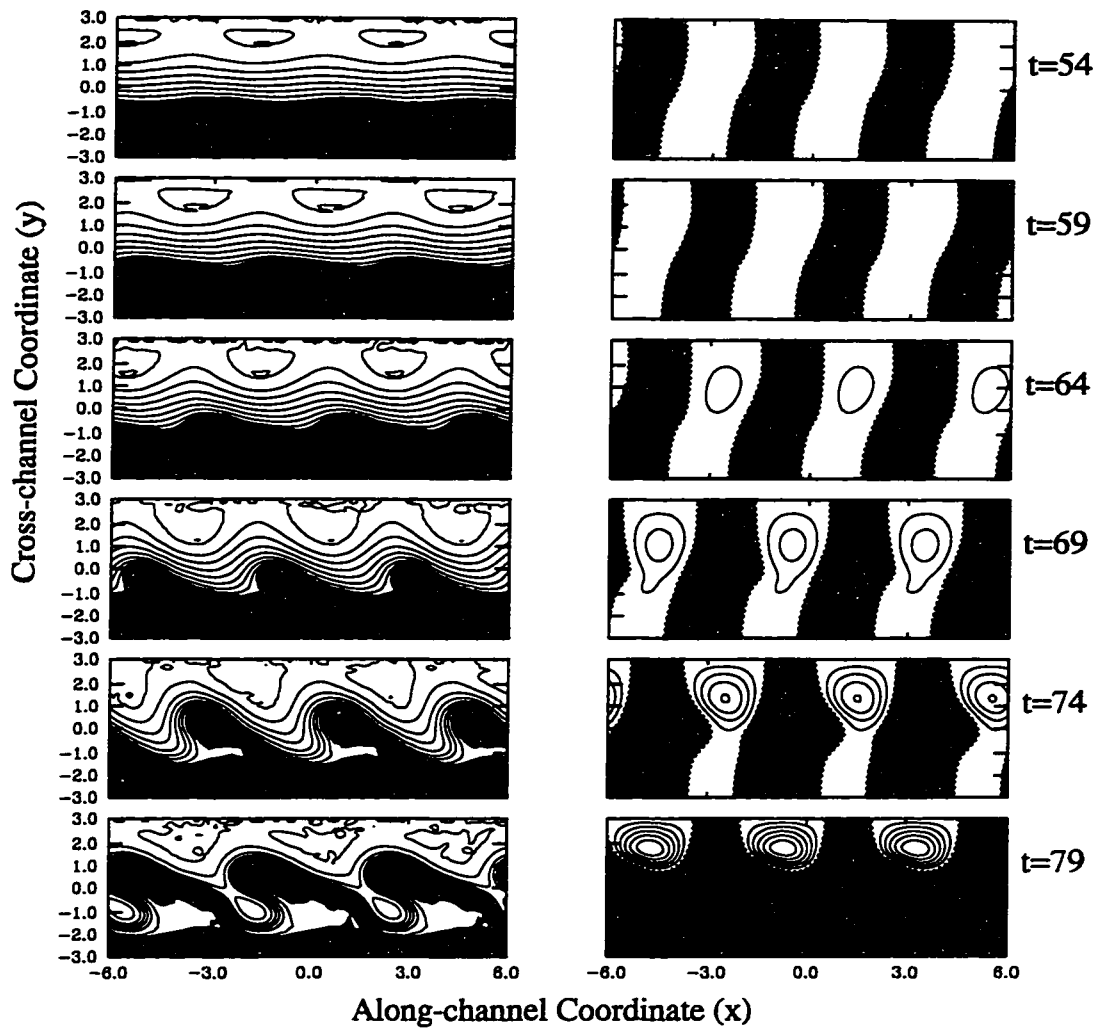
Figure A.2.3: Results of the numerical simulation of the WVT model isolated-front simulation for t=54–79. The graphs on the left show the contours of the upper-layer height. The grey regions are regions where the upper layer vanishes and the contour interval is 0.1. The graphs on the right show the contours of the barotropic stream function. The grey regions are regions where the stream function is negative and the contour interval is 0.04.
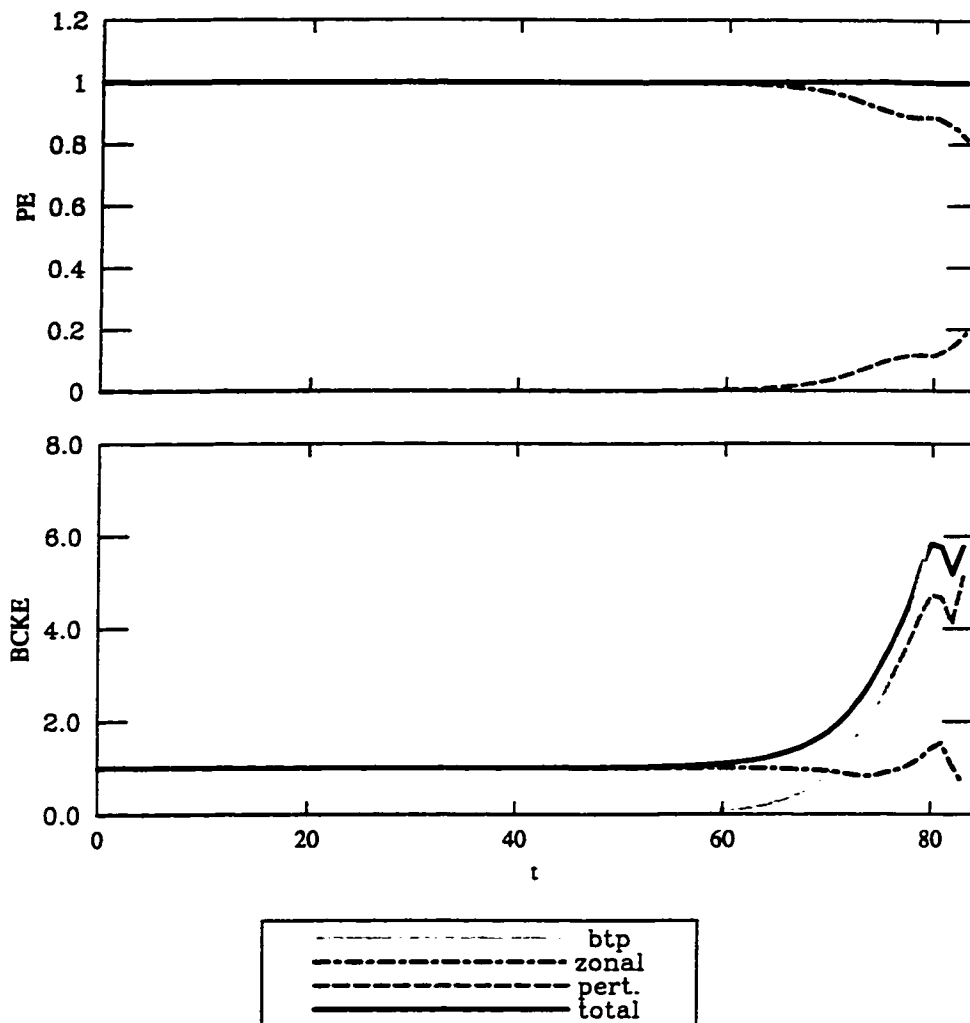
Figure A.2.4: Results of the numerical simulation of the WVT model for an isolated front. The graphs on the left show the contours of the upper-layer height. The grey regions are regions where the upper layer vanishes and the contour interval is 0.1. The plots on the right show the zonally averaged upper-layer height versus y.
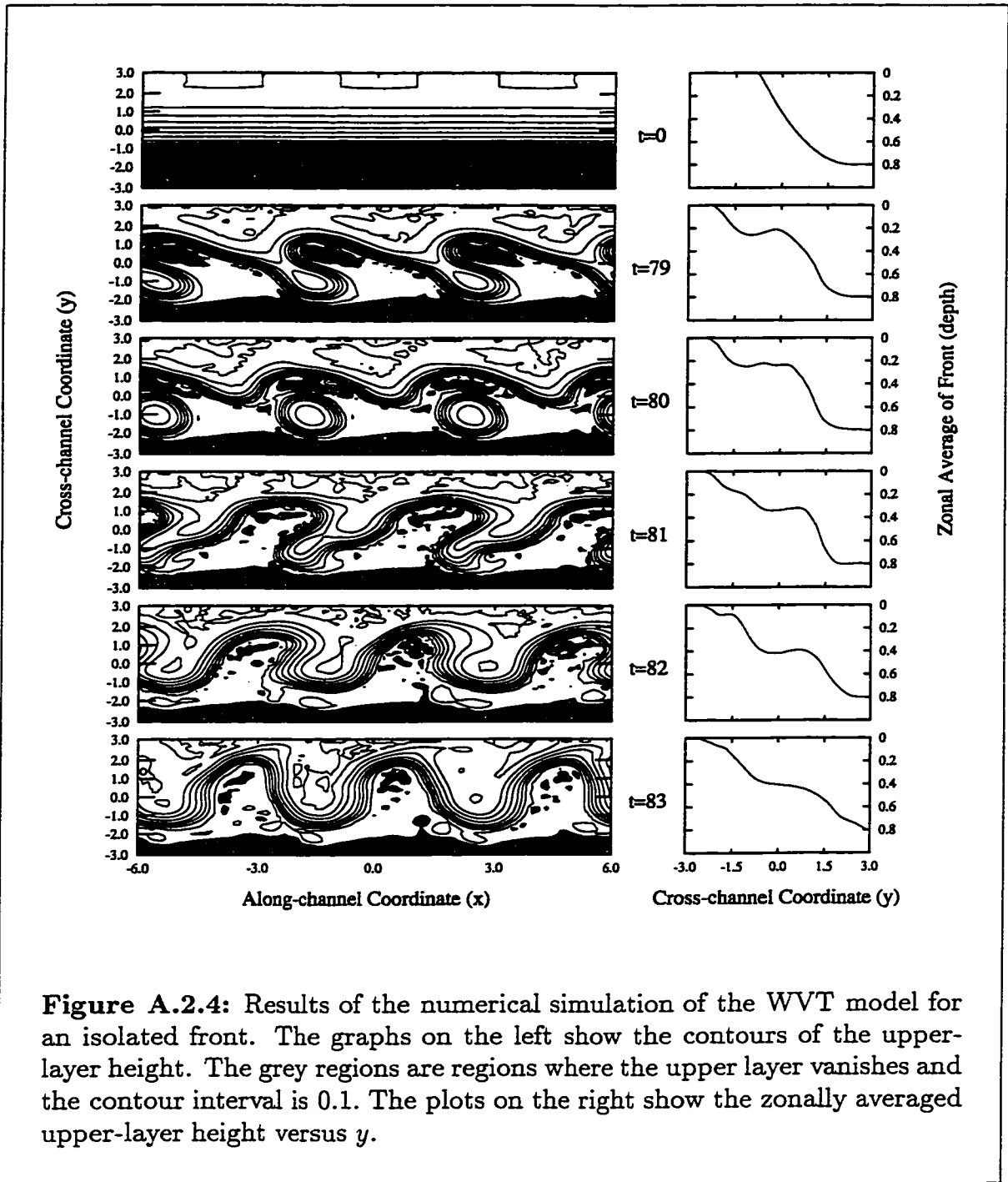
Figure A.2.5: The potential energy (PE, upper plot) and the baroclinic kinetic energy ($BCKE$, lower plot) for the WVT model isolated-front simulation. The term zonal is used to indicate the mean zonal average, pert. indicates the perturbation to this average and btp indicates the barotropic component.

Appendices

baroclinic and barotropic KE. Again, this behaviour is predicted by the pseudo-energy $\mathcal{E}$ as it requires equivalent growth in baroclinic and barotropic KE. As well, note that PE is only released when large-scale structures have formed after $t = 60$. It is the large-scale structures that rapidly flatten out the front (see Figure A.2.4).

Appendix 3.   Calculation of Nonlinear Terms for the ST Model

In this appendix we present the form of the nonlinear terms in the ST model for the wedge front weakly nonlinear analysis. The nonlinear terms in equation (3.2.5) with basic state (3.2.32, 3.2.33) are given by

$$
\begin{aligned}
M(\partial_x, \partial_y, y)\{h, \psi\} = &-(\beta + \mu\alpha)J(h\nabla^2 h + \frac{1}{2}\nabla h \cdot \nabla h.h) - \beta J(p.h) \\
&+ \beta^2 h h_x - (\beta + \mu\alpha)\alpha \left[yJ(\nabla^2 h, h) + J(h_y.h) \right. \\
&\left. + h\nabla^2 h_x + h_x h_{xx} + h_y h_{xy} \right].
\end{aligned}
\tag{A.3.1}
$$

In order to examine the full range of interactions studied in this paper, we examine the result of the nonlinear operator applied to a solution consisting of a superposition of various wavetrains. That is, we let

$$
\{h, \psi\} = \sum_{j=1}^{N} A_j \{\widetilde{h}_j(y), \widetilde{\psi}_j(y)\} \exp(i\theta_j) + c.c.,
\tag{A.3.2}
$$

where A_j represents the slowly varying amplitude of the wave, $\{\widetilde{h}_j(y), \widetilde{\psi}_j(y)\}$ are arbitrary functions, and $\theta_j = k_j x - \omega_j t$. Substituting (A.3.2) into (A.3.1) gives

$$
\begin{aligned}
M(\partial_x, \partial_y, y)\{h, \psi\} = & \\
\sum_{m,n=1}^{N} & iA_m A_n \Gamma(\pm k_m, \widetilde{h}_m, \widetilde{\psi}_m, \pm k_n, \widetilde{h}_n, \widetilde{\psi}_n) \exp[i(\pm\theta_m \pm \theta_n)] \\
+ \sum_{m,n,l=1}^{N} & iA_m A_n A_l \widetilde{\Phi}(\pm k_m, \widetilde{h}_m, \pm k_n, \widetilde{h}_n, \pm k_l, \widetilde{h}_l) \exp[i(\pm\theta_m \pm \theta_n \pm \theta_l)],
\end{aligned}
\tag{A.3.3}
$$

where Γ represents quadratic interactions while $\widetilde{\Phi}$ represents cubic interactions.

255

Appendices

From (A.3.1) it follows that

$$\Gamma(k_m, \widetilde{h}_m, \widetilde{\psi}_m, k_n, \widetilde{h}_n, \widetilde{\psi}_n) =$$

$$(\beta + \mu\alpha)\alpha y \left[k_n \widetilde{h}_m''' \widetilde{h}_n - k_m \widetilde{h}_m'' \widetilde{h}_n \right.$$

$$\left. + k_m^3 \widetilde{h}_m \widetilde{h}_n' - k_n k_m^2 \widetilde{h}_m' \widetilde{h}_n \right]$$

$$+ (\beta + \mu\alpha)\alpha \left[k_n \widetilde{h}_m'' \widetilde{h}_n - k_n \widetilde{h}_m \widetilde{h}_n'' - \frac{1}{2}(3k_m + k_n)\widetilde{h}_m' \widetilde{h}_n' \right. \qquad \text{(A.3.4)}$$

$$\left. + (\frac{k_m^2 k_n + k_m k_n^2}{2} + k_n^3)\widetilde{h}_m \widetilde{h}_n \right]$$

$$+ \beta^2 k_n \widetilde{h}_m \widetilde{h}_n + \beta \left[k_n \widetilde{\psi}_m' \widetilde{h}_n - k_m \widetilde{\psi}_m \widetilde{h}_n' \right].$$

It follows from the form of Γ that

$$\Gamma(y, -k_m, \widetilde{h}_m, \widetilde{\psi}_m, -k_n, \widetilde{h}_n, \widetilde{\psi}_n) = -\Gamma(y, k_m, \widetilde{h}_m, \widetilde{\psi}_m, k_n, \widetilde{h}_n, \widetilde{\psi}_n), \quad \text{(A.3.5)}$$

$$\Gamma(y, k, \widetilde{h}, \widetilde{\psi}, -k, \widetilde{h}, \widetilde{\psi}) + \Gamma(y, -k, \widetilde{h}, \widetilde{\psi}, k, \widetilde{h}, \widetilde{\psi}) = 0. \qquad \text{(A.3.6)}$$

For the cubic terms, we only need self interaction terms that give rise to of the same structure as the wave itself, that is. terms given by

$$\Phi(k, \widetilde{h}) = \widetilde{\Phi}(k, \widetilde{h}, k, \widetilde{h}, -k, \widetilde{h}) + \widetilde{\Phi}(k, \widetilde{h}, -k, \widetilde{h}, k, \widetilde{h}) + \widetilde{\Phi}(-k, \widetilde{h}, k, \widetilde{h}, k, \widetilde{h})$$
$$= k[\widetilde{h}''' \widetilde{h}^2 - (\widetilde{h}')^3 + 4k^2 \widetilde{h}' \widetilde{h}^2]. \qquad \text{(A.3.7)}$$

We also require the slow derivative terms given by

$$M_1(\partial_x, \partial_X, \partial_y, y)\{h, \psi\} =$$

$$-(\beta + \mu\alpha)J_1 \left(h\nabla^2 h + \frac{1}{2}\nabla h \cdot \nabla h, h \right) - \beta J_1(\psi, h) + \beta^2 h h_X$$

$$-(\beta + \mu\alpha) \left[J(2h h_{xX} + h_x h_X, h) - \alpha y J_1(\nabla^2 h, h) \right.$$

$$+ 2\alpha y J(h_x X, h) + \alpha \nabla^2 h h_X - 2\alpha h_{xX} h_x \qquad \text{(A.3.8)}$$

$$- \alpha J_1(h_y, h) - \alpha(h\nabla^2 h + \frac{1}{2}\nabla h \cdot \nabla h)_X$$

$$\left. - \alpha(2h h_{xX} + h_x h_X)_x \right].$$

Appendices

Using the substitution (A.3.2) in (A.3.8) gives

$$M_1(\partial_x, \partial_X, \partial_y, y)\{h, \psi\} =$$
$$\sum_{m,n=1}^{N} A_m(A_n)_\xi \Gamma_1(\pm k_m, \widetilde{h}_m, \widetilde{\psi}_m, \pm k_n, \widetilde{h}_n, \widetilde{\psi}_n) \exp[i(\pm\theta_m \pm \theta_n)]$$
$$+ \sum_{m,n,l=1}^{N} A_m A_n (A_l)_\xi \Phi_1(\pm k_m, \widetilde{h}_m, \pm k_n, \widetilde{h}_n, \pm k_l, \widetilde{h}_l) \exp[i(\pm\theta_m \pm \theta_n \pm \theta_l)],$$

(A.3.9)

where once again Γ_1 represents quadratic interactions while Φ_1 represents cubic interactions. For our analysis we require only the form of quadratic terms that lead to long-wave terms. those that are independent of x and t. These terms have the coefficient

$$\Gamma_1(k, \widetilde{h}, \widetilde{\psi}, -k, \widetilde{h}, \widetilde{\psi}) = \Gamma_1(-k, \widetilde{h}, \widetilde{\psi}, k, \widetilde{h}, \widetilde{\psi}) =$$
$$(\beta + \mu\alpha)\left[\alpha y \left(\widetilde{h}'''\widetilde{h} - \widetilde{h}''\widetilde{h}' + 4k^2\widetilde{h}'\widetilde{h}\right) - \alpha \left[2(\widetilde{h}')^2 - 2k^2\widetilde{h}^2\right]\right]$$
$$+ \beta^2\widetilde{h}^2 + \beta(\widetilde{\psi}'\widetilde{h} - \widetilde{\psi}\widetilde{h}').$$

(A.3.10)

Using these formulations, we can write down the forms of the nonlinear terms found in the weakly nonlinear analysis. First we examine the terms present in §3.6. For the $O(\Delta)$ problem the term M_{e^2} in equations (3.6.15) and (3.6.27) represents the quadratic interactions of the leading-order solutions and is therefore given by

$$M_{e^2} = \Gamma\left(y, k, \widetilde{h}(y, k, n), \widetilde{\psi}(y, k, n), k, \widetilde{h}(y, k, n), \widetilde{\psi}(y, k, n)\right).$$

(A.3.11)

For the $O(\Delta^2)$ problem the term M_0 in equations (3.6.31) and (3.6.36) represents the quadratic interactions of the leading-order solution with the second order solution and the slow quadratic interaction of the leading-order solution that give rise to

257

Appendices

terms independent of the fast phase. Therefore we have.

$$M_0 = \Gamma \left(y, k, \frac{\partial \widetilde{h}(y,k,n)}{\partial k}, \widetilde{\psi}_2(y), -k, \widetilde{h}(y,k,n), \widetilde{\psi}(y,k,n) \right)$$

$$+ \Gamma \left(y, -k, \widetilde{h}(y,k,n), \widetilde{\psi}(y,k,n), k, \frac{\partial \widetilde{h}(y,k,n)}{\partial k}, \widetilde{\psi}_2(y) \right) \qquad (A.3.12)$$

$$+ \Gamma_1 \left(y, k, \widetilde{h}(y,k,n), \widetilde{\psi}(y,k,n), -k, \widetilde{h}(y,k,n), \widetilde{\psi}(y,k,n) \right),$$

where we've made use of (A.3.5) and (A.3.10). The term $\mathfrak{M}$ in equations (3.6.40) represents the quadratic interactions of the leading-order solution with the second order solution and the cubic interactions of the leading-order solution with itself that give rise to terms with the phase of the leading-order solution. Therefore we have,

$$\mathfrak{M} = \frac{1}{2\beta} \left[\Gamma \left(y, 2k, 3(y), \widetilde{\psi}_3(y), -k, \widetilde{h}(y,k,n), \widetilde{\psi}(y,k,n) \right) \right.$$

$$+ \Gamma \left(y, -k, \widetilde{h}(y,k,n), \widetilde{\psi}(y,k,n), 2k, 3(y), \widetilde{\psi}_3(y) \right)$$

$$+ \Gamma \left(y, k, \widetilde{h}(y,k,n), \widetilde{\psi}(y,k,n), 0, \Phi(y), \widetilde{h}'(y) \right) \qquad (A.3.13)$$

$$+ \Gamma \left(y, 0, \Phi(y), \widetilde{h}'(y), k, \widetilde{h}(y,k,n), \widetilde{\psi}(y,k,n) \right)$$

$$\left. + \Phi \left(k, \widetilde{h}(y,k,n) \right) \right].$$

In §3.8, the term Φ_1 and Φ_2 represent quadratic interactions that have had the F.A.T. applied to them. The term Φ_1 represents the quadratic interaction of the short and long wave that give rise to terms in phase with the short wave and is given by

$$\Phi_1 = \int_0^\infty \frac{2\kappa(k)}{\beta} \widetilde{h}(y,k,n)$$

$$\times \left[\Gamma \left(y, k, \widetilde{h}(y,k,n), \widetilde{\psi}(y,k,n), 0, \widetilde{h}(y,0,m), \widetilde{\psi}(y,0,m) \right) \right. \qquad (A.3.14)$$

$$\left. + \Gamma \left(y, 0, \widetilde{h}(y,0,m), \widetilde{\psi}(y,0,m), k, \widetilde{h}(y,k,n), \widetilde{\psi}(y,k,n) \right) \right] dy.$$

258

Appendices

The term Φ_2 once again represents the quadratic interactions of the short wave with itself that produce waves independent of the fast phase. that is in phase with the long wave, and is given by

$$\Phi_2 = \int_0^\infty \frac{2\kappa(0)}{\beta} \tilde{h}(y, 0, m) M_0(y)\, dy,$$ (A.3.15)

where M_0 is given above in (A.3.12).

In §3.9, the term $\mathfrak{J}_{abc}$ represent the quadratic interactions of waves a and b that are in phase with wave c appropriately weighted and integrated according to an applications of the F.A.T. Therefore $\mathfrak{J}_{abc}$ is given by

$$
\begin{aligned}
\mathfrak{J}_{abc} = \int_0^\infty \frac{2\kappa(k_c)}{\beta} \\
\times \Big[\Gamma\left(y, -k_a, \tilde{h}(y, k_a, n_a), \tilde{\psi}(y, k_a, n_a), -k_b, \tilde{h}(y, k_b, n_b), \tilde{\psi}(y, k_b, n_b)\right) \\
+ \Gamma\left(y, -k_b, \tilde{h}(y, k_b, n_b), \tilde{\psi}(y, k_b, n_b), -k_a, \tilde{h}(y, k_a, n_a), \tilde{\psi}(y, k_a, n_a)\right) \Big] \\
\times \tilde{h}(y, k_c, n_c)\, dy.
\end{aligned}
$$ (A.3.16)

Finally, in §3.10, the term ϕ_B represents the slow quadratic interactions of the long wave with itself and is given by

$$\phi_B = \Gamma_1\left(y, 0, \tilde{h}(y, 0, n), \tilde{\psi}(y, 0, n), 0, \tilde{h}(y, 0, n), \tilde{\psi}(y, 0, n)\right).$$ (A.3.17)

Appendix 4.   The SE Model Hamiltonian Formulation

It is a useful endeavor in fluid mechanics to recast governing equations into what is referred to as Hamiltonian formulation. There is a plethora of material on Hamiltonian formulations for geophysical flows with good general overviews given in Holm *et al.* (1985) and Shepherd (1990). There are several advantages of being able to recast the governing equations in this formulation as pointed out in Shepherd (1990).

Hamiltonian structure has been established for several FG models: the WVT-model in Swaters (1993b) and Karsten and Swaters (1996b), the LST model in Swaters (1993a) and Karsten and Swaters (1996a), and the RED model in Slomp (1995).

259

Appendices

The SE model given by (5.1.2) and (5.1.3) can also be expressed in noncanonical Hamiltonian form.

The system (5.1.3, 5.1.2) is Hamiltonian and can be written as

$$q_t = \mathfrak{J} \frac{\delta \mathfrak{H}}{\delta q}. \tag{A.4.1}$$

with

$$\mathfrak{H}(q) = \mathfrak{H}(\psi, h) \equiv \frac{1}{2} \iint_\Omega \nabla \psi \cdot \nabla \psi \, dx dy$$
$$- \frac{\mu}{2} \iint_{FR} h(1 - \mu h) \nabla h \cdot \nabla h \, dx dy. \tag{A.4.2}$$

where $q = (q_1, q_2)^T$ with

$$q_1 \equiv \mu h, \tag{A.4.3}$$
$$q_2 \equiv \nabla^2 \psi + \beta y, \tag{A.4.4}$$

and the operator $\mathfrak{J} = [\mathfrak{J}_{ij}]$ is a 2×2 matrix whose components are given by

$$\mathfrak{J}_{ij} = -\delta_{i1}\delta_{j1} J(q_1, *) - \delta_{i2}\delta_{j1} J(q_1, *) - \delta_{i2}\delta_{j2} J(q_2, *), \tag{A.4.5}$$

where δ_{mn} is the Kronecker delta function, in FR and

$$\mathfrak{J} = -J(q_2, *), \tag{A.4.6}$$

in NF. The associated Poisson bracket is given by

$$[\mathfrak{F}, \mathfrak{G}] = \iint_\Omega \frac{\delta \mathfrak{F}}{\delta q} \cdot \mathfrak{J} \frac{\delta \mathfrak{G}}{\delta q} \, dx dy. \tag{A.4.7}$$

The proof that the Poisson bracket satisfies the required properties is lengthy and does not provide great insight for our purposes. The main difficulty is establishing the validity of the Jacobi identity. For similar proofs see Karsten and Swaters (1996b),, Swaters (1993a), Swaters (1993b), Mooney and Swaters (1996), or Slomp (1995).

Appendices

The Hamiltonian (A.4.2) is the pseudo-energy invariant as discussed in §5.3. Note that the state variables q_2 and q_1 are related to the expressions for potential vorticity. The connection here is more complicated than for other models (see for example Swaters (1993a) and Swaters (1993b) where the leading-order PV for each layer and the state variables are directly correlated). In the upper layer, q_1 is the inverse of the leading order potential vorticity given by (5.1.6) but q_1 is also the leading-order potential vorticity of the lower layer as given by (5.1.7). The second state variable, q_2, is a relation between the next order potential vorticities, as the second equation in the model is a balance between the two layers.

A Casimir functional is a functional that *Poisson commutes* with all other functionals that is,

$$[\mathfrak{F}, \mathfrak{C}] = 0. \tag{A.4.8}$$

for all sufficiently smooth functionals $F(q)$. Using the definition of a Casimir, (A.4.8), and Poisson bracket, (A.4.7), the Casimirs for the SE model are found to be the PV invariant (5.3.8) found in §5.3. Noether's theorem (see Shepherd, 1990) can be used with the fact that $\mathfrak{H}$ and $\mathfrak{J}$ are invariant under translations in t and x. The invariant associated with the time symmetry of the model is the Hamiltonian. (Application of Noether's Theorem actually gives $-\mathfrak{H}$.) The invariant associated with zonal symmetry, is just the zonal momentum invariant (5.3.11) found in §5.3. In the special case where $\beta = 0$, the model, Hamiltonian and operator, are also independent of y. Therefore a similar meridional momentum invariant can be derived and an invariant analogous to angular momentum can be derived.

One of the great uses of the Hamiltonian structure is the derivation of linear and nonlinear stability theorems following the pioneering work of Arnol'd, (Arnol'd, 1965 and Arnol'd, 1966). Arnol'd stability theorems have been demonstrated for a wide range of hydrodynamic flows (see Shepherd, 1990 and Holm *et al.*, 1985). Both linear and nonlinear theorems have been established for the WVT model (see Swaters, 1993b and Karsten and Swaters, 1996b), the LST model (see Swaters, 1993a and Karsten and Swaters, 1996a) and the RED model (see Slomp, 1995). Developing the stability theorems follows from working with a constrained invariant of the flow, usually the Hamiltonian, momentum invariant, or some combination of the two, plus an arbitrary Casimir. If conditions on a basic-state flow can be found such that the first variation of the constrained invariant is zero and the second vari-

ation is definite, one has established formal stability. This procedure is equivalent to illustrating that the invariant has an extreme point in finite dimensions. Linear stability usually follows from formal stability and considerations of the linear dynamics. Then by considering the fully nonlinear dynamics it is often possible to extend these results to nonlinear stability theorems. For examples of this process see any of Swaters (1993a), Swaters (1993b), Karsten and Swaters (1996a), or Karsten and Swaters (1996b). The process is virtually identical to that used to establish nonlinear stability theorems for the ST and VSE models. In §5.3, the same process was shown to break down due to an inability to bound small-scale terms. Such a difficulty remains even if the structure of the Hamiltonian formulation is used. Therefore, it is not possible to establish formal, linear, or nonlinear stability theorems for the SE model.

Appendix 5.   The NLS Equation

In this appendix we present the solutions $f(\theta)$ to the equation

$$\frac{d^2 f}{d\theta^2} - \gamma_1 f + \gamma_2 f^3 = 0, \tag{A.5.1}$$

with arbitrary initial conditions,

$$f(0) = C, \\ f'(0) = D. \tag{A.5.2}$$

When the coefficient of the linear term, γ_1, is positive (negative) we have linear instability (stability). When the coefficient of the nonlinear term, γ_2, is positive (negative) this term acts to enhance (suppress) the linear growth.

First we examine the equation by writing it as a system by letting $x_1 = f$ and $x_2 = f'$ so that we have

$$x_1' = x_2, \\ x_2' = \gamma_1 x_1 - \gamma_2 x_1^3. \tag{A.5.3}$$

The system has the equilibrium points

$$(x_1, x_2) = (0, 0), \quad \left(\pm \sqrt{\frac{\gamma_1}{\gamma_2}}, 0 \right),$$

Appendices

where the second and third points are real only when $\gamma_1/\gamma_2 \geq 0$. The system (A.5.3) conserves the quantity

$$V(x_1, x_2) = x_2^2 + \frac{\gamma_2}{2}\left[x_1^4 - 2\frac{\gamma_1}{\gamma_2}x_1^2\right], \qquad \text{(A.5.4)}$$

that is,

$$\frac{dV}{dT} = \frac{\partial V}{\partial x_1}x_1' + \frac{\partial V}{\partial x_2}x_2' = 0.$$

The solutions can be easily illustrated for arbitrary initial conditions by plotting the phase portraits using (A.5.4). Since V is conserved following the flow, curves of constant V trace out solutions in the $x_1 - x_2$ plane. Obviously these phase portraits depend critically on the signs of parameters γ_1 and γ_2. The combination of different signs leads to four cases. The phase portraits for these four cases are plotted in Figures A.5.1, A.5.2, A.5.3, and A.5.4. These portraits illustrate that three types of solutions exists: periodic solutions, solutions that become infinitely large or special solutions that tend to equilibrium points. If $\gamma_2 > 0$, solutions are periodic and nonlinearly stable (see Figures A.5.1, A.5.2) as the nonlinear terms stablize any initial growth. If $\gamma_2 > 0$, most solutions tend to infinity and are nonlinearly unstable as the nonlinear terms destabilize the solution (see Figures A.5.3, A.5.4). Solutions are bounded and periodic when $\gamma_2 > 0$ only if the solution is linearly stable, $\gamma_1 < 0$, and initial conditions are small enough that we are near the origin (see Figure A.5.4). The phase portraits are labelled with various regions that correspond to solutions given below. The solid black and dashed black lines represent the boundaries of these regions and are given by $\gamma_3 = 0$ and $\gamma_3 = (\gamma_1/\gamma_2)^2$, respectively, where these parameters are defined below.
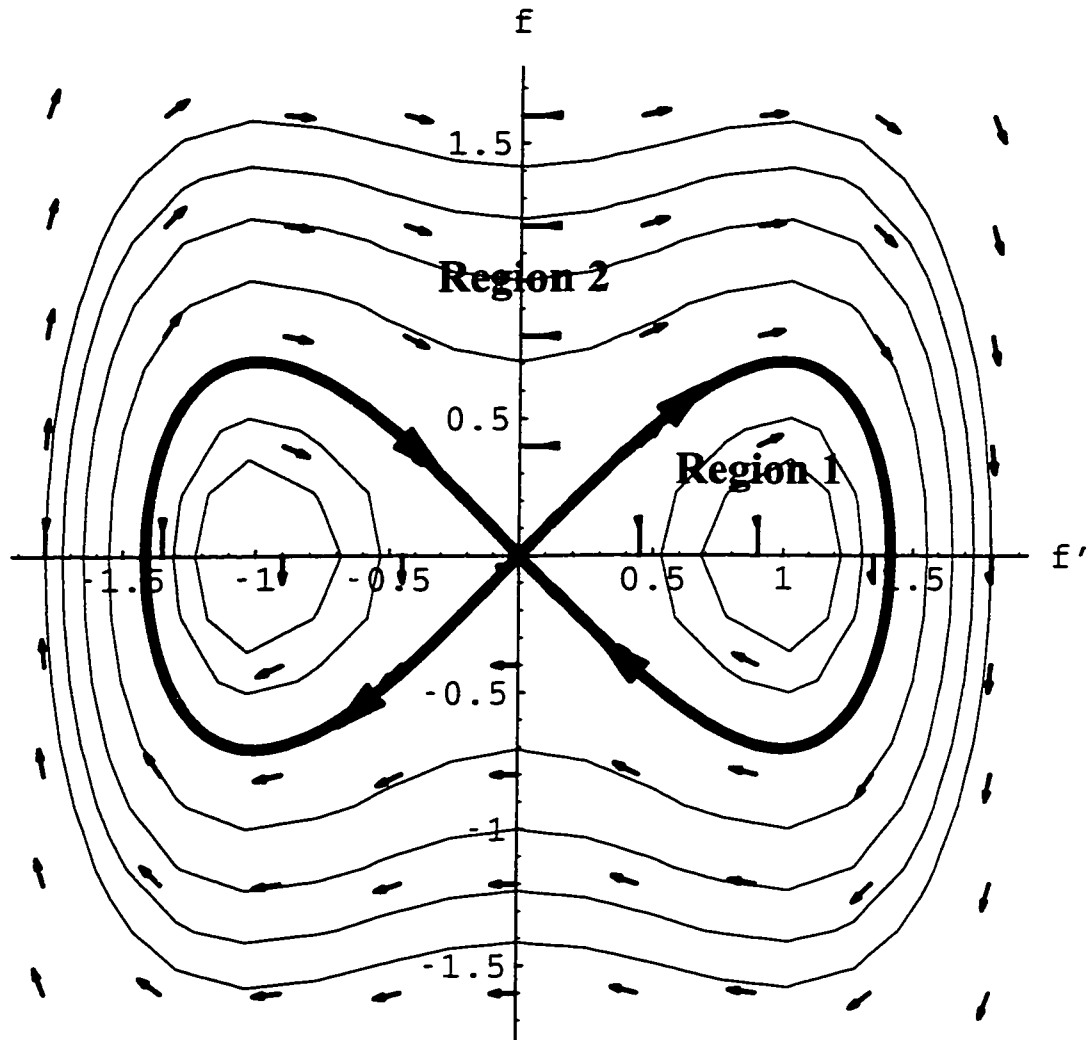
Figure A.5.1: The phase portraits for $\gamma_1 > 0$ and $\gamma_2 > 0$. The solutions are clearly periodical. Two solution regions exist separated by the separatrix (solid black line) given by the curve $\gamma_3 = 0$ along which solutions tend to the equilibrium point $(0,0)$.
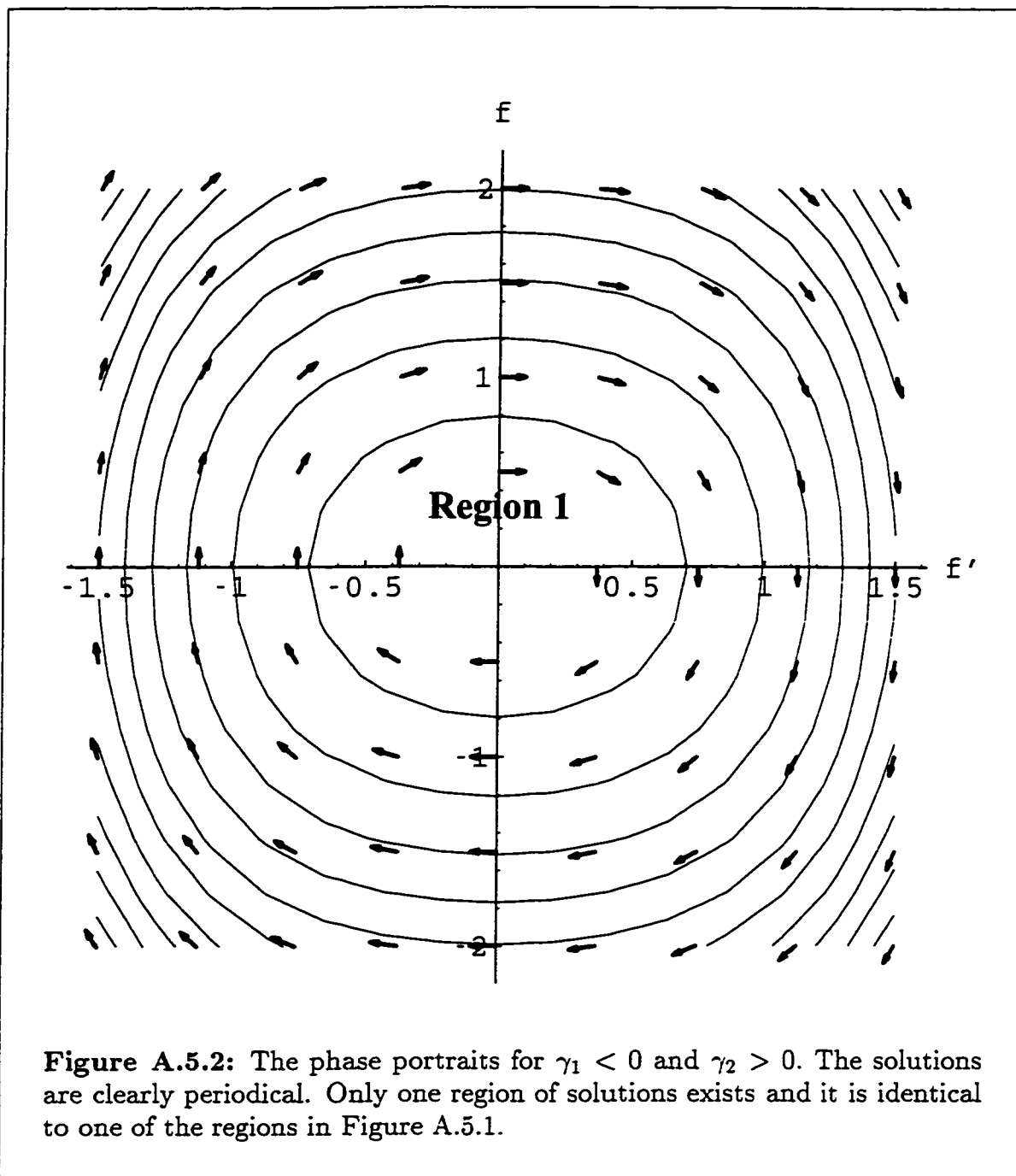
Figure A.5.2: The phase portraits for $\gamma_1 < 0$ and $\gamma_2 > 0$. The solutions are clearly periodical. Only one region of solutions exists and it is identical to one of the regions in Figure A.5.1.
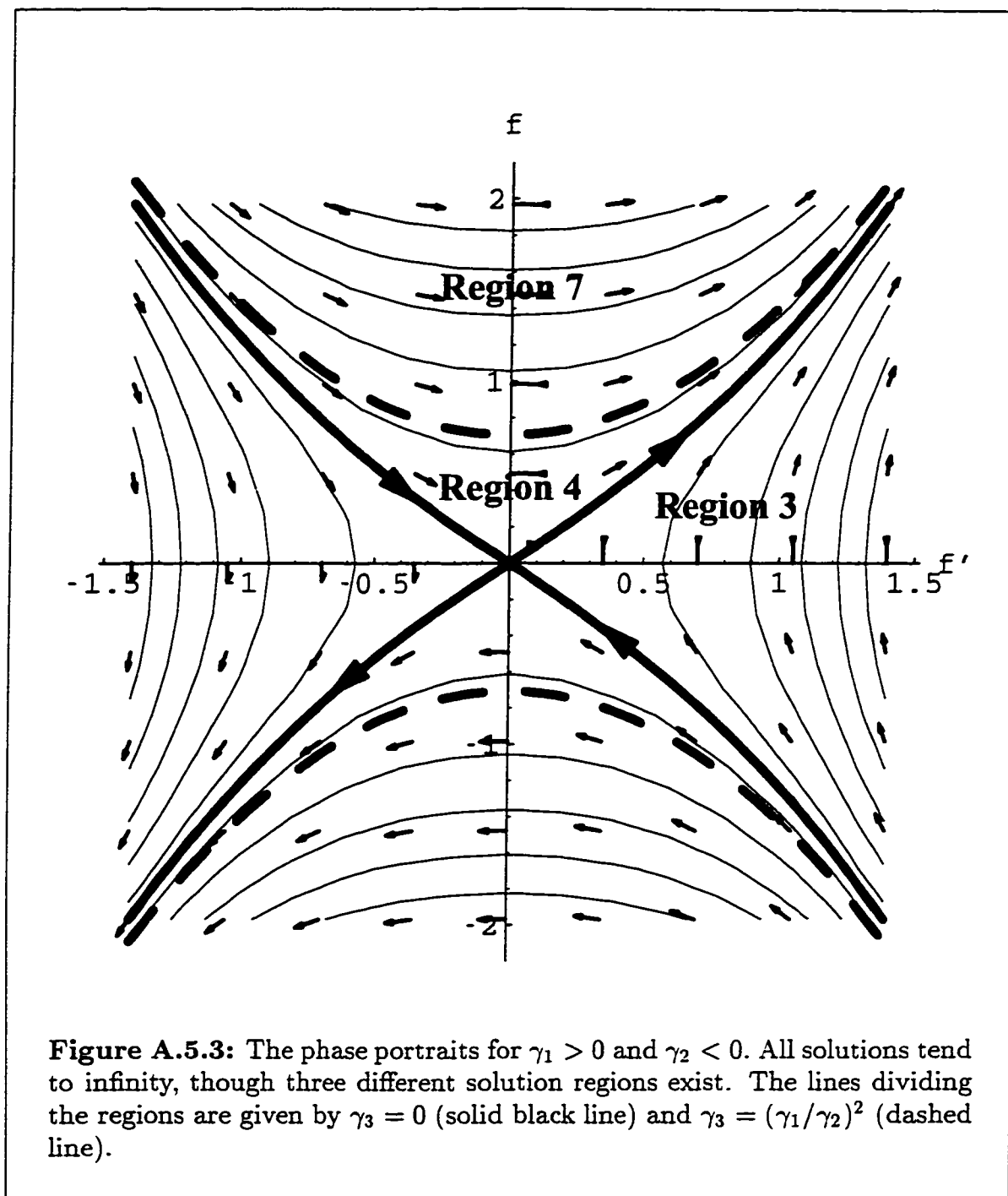
Figure A.5.3: The phase portraits for $\gamma_1 > 0$ and $\gamma_2 < 0$. All solutions tend to infinity, though three different solution regions exist. The lines dividing the regions are given by $\gamma_3 = 0$ (solid black line) and $\gamma_3 = (\gamma_1/\gamma_2)^2$ (dashed line).
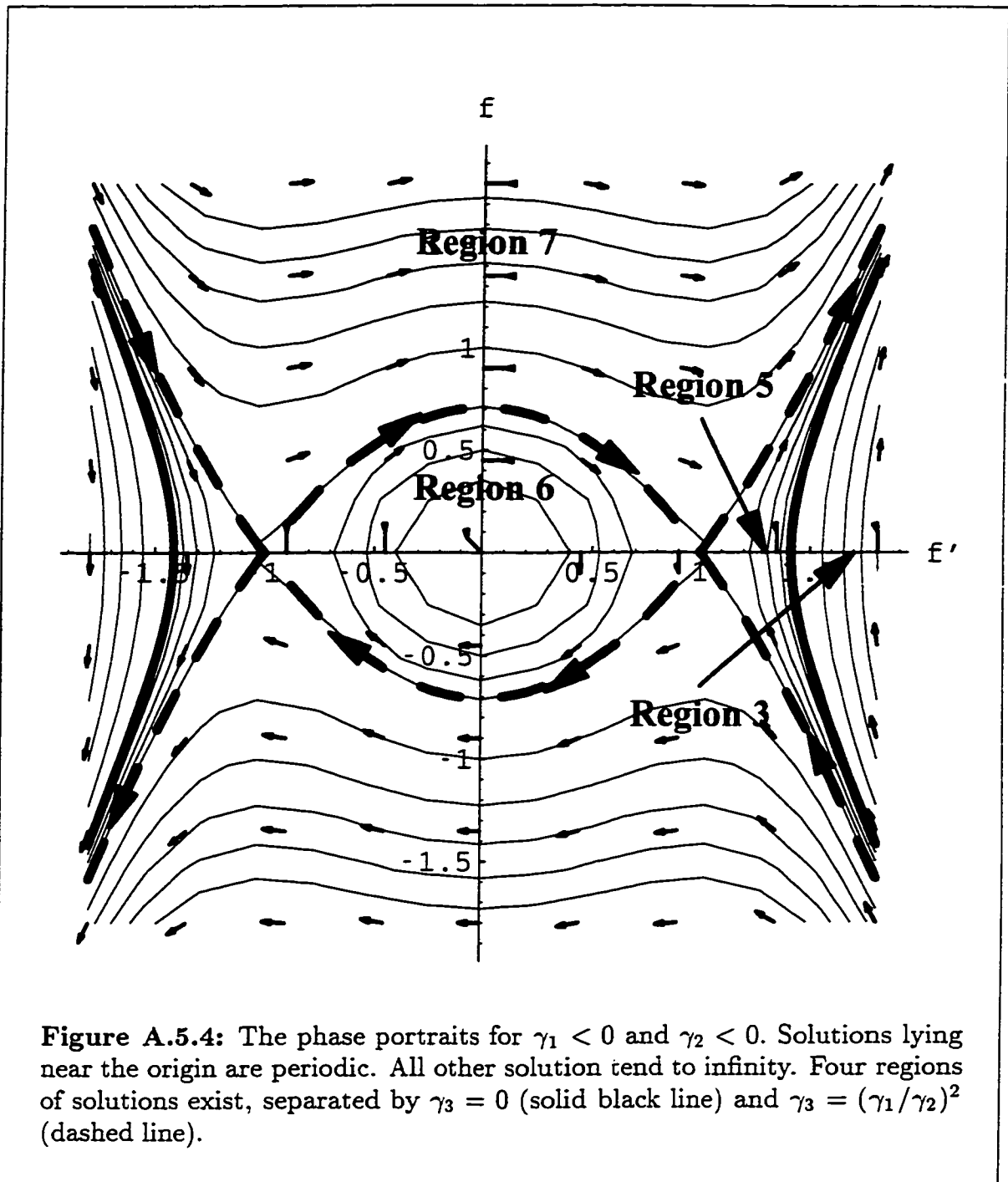
Figure A.5.4: The phase portraits for $\gamma_1 < 0$ and $\gamma_2 < 0$. Solutions lying near the origin are periodic. All other solution tend to infinity. Four regions of solutions exist, separated by $\gamma_3 = 0$ (solid black line) and $\gamma_3 = (\gamma_1/\gamma_2)^2$ (dashed line).

Appendices

Equation (A.5.1) can also be solved using Jacobi Elliptic functions. Multiplying (A.5.1) by f' and integrating gives

$$(f')^2 = -\frac{\gamma_2}{2}\left(f^4 - 2\frac{\gamma_1}{\gamma_2}f^2 + \gamma_3\right). \qquad (A.5.5)$$

where

$$\gamma_3 = -C^4 + 2\frac{\gamma_1}{\gamma_2}C^2 - \frac{2}{\gamma_2}D^2. \qquad (A.5.6)$$

The solutions depends on the roots of the quartic in f given by (A.5.5). Rearranging (A.5.5) gives

$$(f')^2 = -\frac{\gamma_2}{2}(f^2 - \Gamma_1)(f^2 - \Gamma_2). \qquad (A.5.7)$$

where

$$\Gamma_{1,2} = \frac{\gamma_1}{\gamma_2} \pm \sqrt{\frac{\gamma_1^2}{\gamma_2^2} - \gamma_3}, \qquad (A.5.8)$$

From (A.5.8), we can determine the roots of the quartic and hence the solution form. We examine the solution process for one region and simply list the solutions for the others. The solutions are given in terms of the Jacobian elliptic functions: the snoidal function, sn, the cnoidal function, cn, the dnoidal function, dn, and the functions

$$\text{ns} = \frac{1}{\text{sn}}, \quad \text{cd} = \frac{\text{cn}}{\text{dn}}, \quad \text{ds} = \frac{\text{dn}}{\text{sn}}, \quad \text{cs} = \frac{\text{cn}}{\text{sn}}.$$

The reader is referred to Milne-Thomson (1950) for the definitions and properties of the Jacobian elliptic functions. For simplicity we will only consider the solutions where $C, D \geq 0$. From the phase diagrams it is obvious that other solutions are similar in nature.

Consider Region 1 where $\gamma_2 > 0$ and $\gamma_3 < 0$. From (A.5.8) it follows that $\Gamma_1 > 0$ and $\Gamma_2 < 0$. Let

$$\Gamma_1 = a^2 \quad \text{and} \quad \Gamma_2 = -b^2, \qquad (A.5.9)$$

Appendices

so that (A.5.7) reduces to

$$(f')^2 = \frac{\gamma_2}{2}(a^2 - f^2)(f^2 + b^2),$$

or rearranging

$$\frac{df}{\sqrt{(a^2 - f^2)(f^2 + b^2)}} = \sqrt{\frac{\gamma_2}{2}}\, d\theta.$$

Integrating from $f(\theta_b) = b$ to $f(\theta)$ and using the integrals in Milne-Thomson (1950) gives

$$(a^2 + b^2)^{-\frac{1}{2}}\, cn^{-1}\left[\frac{f}{a}\,\middle|\,\frac{a^2}{a^2 + b^2}\right] = \sqrt{\frac{\gamma_2}{2}}(\theta_b - \theta),$$

or

$$f(\theta) = a\ cn\left[\left(\frac{\gamma_2(a^2 + b^2)}{2}\right)^{\frac{1}{2}}(\theta_b - \theta)\,\middle|\,\frac{a^2}{a^2 + b^2}\right], \qquad (A.5.10)$$

where from the initial conditions

$$\theta_b = \left(\frac{2}{\gamma_2(a^2 + b^2)}\right)^{\frac{1}{2}} cn^{-1}\left[\frac{C}{a}\,\middle|\,\frac{a^2}{a^2 + b^2}\right]. \qquad (A.5.11)$$

Similarly in Region 2 where $\gamma_2 > 0$ and $0 < \gamma_3 < \frac{\gamma_1^2}{\gamma_2}$, and letting $\Gamma_1 = a^2$, $\Gamma_2 = b^2$ gives the solution

$$f(\theta) = a\ dn\left[\left(\frac{\gamma_2 a^2}{2}\right)^{\frac{1}{2}}(\theta_a - \theta)\,\middle|\,\frac{a^2 - b^2}{a^2}\right]. \qquad (A.5.12)$$

where $f(\theta_a) = a$ and from the initial conditions

$$\theta_a = \left(\frac{2}{\gamma_2 a^2}\right)^{\frac{1}{2}} dn^{-1}\left[\frac{C}{a}\,\middle|\,\frac{a^2 - b^2}{a^2}\right]. \qquad (A.5.13)$$

In Region 3 where $\gamma_2 < 0$, and $\gamma_3 < 0$, and letting $\Gamma_1 = a^2, \Gamma_2 = -b^2$ gives the solution

$$f(\theta) = (a^2 + b^2)^{\frac{1}{2}}\ ds\left[\left(\frac{-\gamma_2(a^2 + b^2)}{2}\right)^{\frac{1}{2}}(\theta_\infty - \theta)\,\middle|\,\frac{b^2}{a^2 + b^2}\right], \qquad (A.5.14)$$

269

where $f(\theta_\infty) = \infty$ and from the initial conditions

$$\theta_\infty = \left(\frac{-2}{\gamma_2(a^2 + b^2)}\right)^{\frac{1}{2}} \mathrm{ds}^{-1}\left[\frac{C}{(a^2 + b^2)^{\frac{1}{2}}}\,\middle|\,\frac{b^2}{a^2 + b^2}\right]. \tag{A.5.15}$$

In Region 4 where $\gamma_1 > 0$, $\gamma_2 < 0$, and $0 < \gamma_3 < (\gamma_1/\gamma_2)^2$, and letting $\Gamma_1 = -a^2, \Gamma_2 = -b^2$ gives the solution

$$f(\theta) = b\,\mathrm{cs}\left[\left(\frac{-\gamma_2 b^2}{2}\right)^{\frac{1}{2}}(\theta_\infty - \theta)\,\middle|\,\frac{b^2 - a^2}{b^2}\right]. \tag{A.5.16}$$

where from the initial conditions

$$\theta_\infty = \left(\frac{-2}{\gamma_2 b^2}\right)^{\frac{1}{2}} \mathrm{cs}^{-1}\left[\frac{C}{b}\,\middle|\,\frac{b^2 - a^2}{b^2}\right]. \tag{A.5.17}$$

In Region 5 where $\gamma_1 < 0$, $\gamma_2 < 0$, $0 < \gamma_3 < (\gamma_1/\gamma_2)^2$, and $|C| > \gamma_1/\gamma_2$ and letting $\Gamma_1 = a^2, \Gamma_2 = b^2$ gives the solution

$$f(\theta) = a\,\mathrm{ns}\left[\left(\frac{-\gamma_2 a^2}{2}\right)^{\frac{1}{2}}(\theta_\infty - \theta)\,\middle|\,\frac{b}{a}\right]. \tag{A.5.18}$$

where from the initial conditions

$$\theta_\infty = \left(\frac{-2}{\gamma_2 a^2}\right)^{\frac{1}{2}} \mathrm{ns}^{-1}\left[\frac{C}{a}\,\middle|\,\frac{b}{a}\right]. \tag{A.5.19}$$

In Region 6 where $\gamma_1 < 0$, $\gamma_2 < 0$, $0 < \gamma_3 < \frac{\gamma_1^2}{\gamma_2^2}$, and $|C| < \frac{\gamma_1}{\gamma_2}$ and letting $\Gamma_1 = a^2, \Gamma_2 = b^2$ gives the solution

$$f(\theta) = a\,\mathrm{sn}\left[\left(\frac{-\gamma_2 a^2}{2}\right)^{\frac{1}{2}}(\theta - \theta_0)\,\middle|\,\frac{b}{a}\right], \tag{A.5.20}$$

where $f(\theta_0) = 0$ and from the initial conditions

$$\theta_0 = \left(\frac{-2}{\gamma_2 a^2}\right)^{\frac{1}{2}} \mathrm{sn}^{-1}\left[\frac{C}{a}\,\middle|\,\frac{b}{a}\right]. \tag{A.5.21}$$

Appendices

In Region 7 where $\gamma_3 > (\gamma_1/\gamma_2)^2$, the quartic has no roots and a slightly different approach must be taken. Following Milne-Thomson (1950) we set

$$g(\theta) = \frac{f - \gamma_3^{\frac{1}{4}}}{f + \gamma_3^{\frac{1}{4}}},$$

in (A.5.5) giving

$$(g')^2 = (b^2 - g^2)(g^2 + a^2), \qquad (A.5.22)$$

where

$$a^2 = \frac{\gamma_3^{\frac{1}{2}} - \gamma_1/\gamma_2}{\gamma_3^{\frac{1}{2}} + \gamma_1/\gamma_2},$$

$$b^2 = -\gamma_2\gamma_3^{\frac{1}{2}} \left(\gamma_3^{\frac{1}{2}} + \frac{\gamma_1}{\gamma_2}\right).$$

The solution to (A.5.22) is

$$g(\theta) = \operatorname{cn}\left[(-2\gamma_2\gamma_3)^{\frac{1}{2}} (\theta - \theta_b) \left| \frac{1}{1 + a^2}\right.\right], \qquad (A.5.23)$$

where we've used that $b^2(1 + a^2) = -2\gamma_2\gamma_3$. Using the identity

$$[\operatorname{ns}(\theta|m) \; \operatorname{cd}(\theta|m)]^2 = \frac{1 + \operatorname{cn}(2\theta|m)}{1 - \operatorname{cn}(2\theta|m)}.$$

gives the solution

$$f(\theta) = \gamma_3^{\frac{1}{4}} \operatorname{ns}\left[\left(\frac{-\gamma_2\gamma_3}{2}\right)^{\frac{1}{2}} (\theta - \theta_b) \left| \frac{1}{1 + a^2}\right.\right]$$

$$\times \; \operatorname{cd}\left[\left(\frac{-\gamma_2\gamma_3}{2}\right)^{\frac{1}{2}} (\theta - \theta_b) \left| \frac{1}{1 + a^2}\right.\right], \qquad (A.5.24)$$

where

$$\theta_\infty = \frac{1}{2\gamma_3^{\frac{1}{2}}} \operatorname{cn}^{-1}\left[\frac{C^2 - \gamma_3^{\frac{1}{2}}}{C^2 + \gamma_3^{\frac{1}{2}}} \left| \frac{1}{1 + a^2}\right.\right]. \qquad (A.5.25)$$
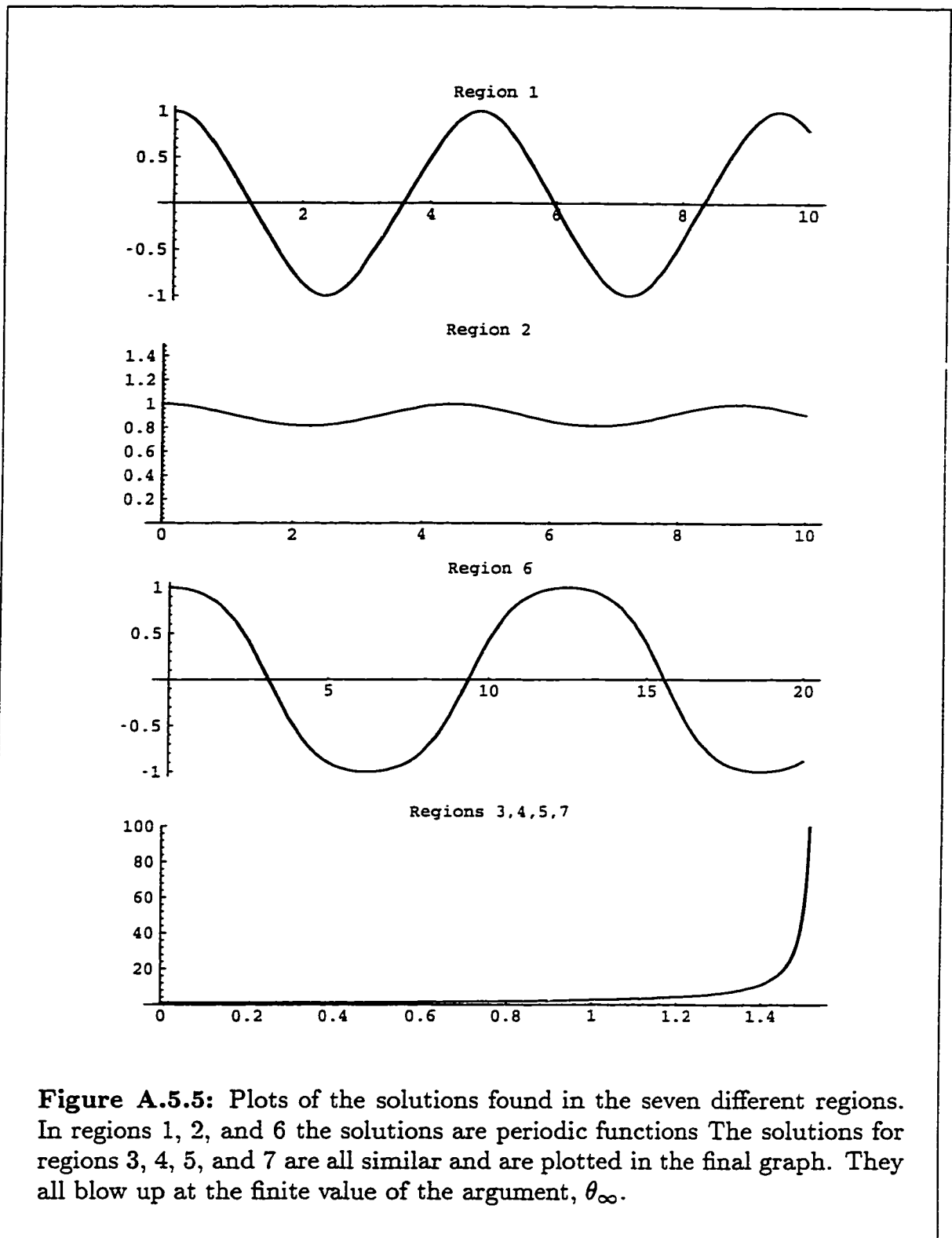
271

Figure A.5.5: Plots of the solutions found in the seven different regions. In regions 1, 2, and 6 the solutions are periodic functions The solutions for regions 3, 4, 5, and 7 are all similar and are plotted in the final graph. They all blow up at the finite value of the argument, θ_∞.

Appendices

Typical plots of the solutions for all regions are given in Figure A.5.5. In regions 1, 2, and 6 the solutions are bounded periodic functions. Note that in region 2 the solution does not oscillate through zero. The other region have solutions that become unbounded in a finite, and relatively small, time. (Note that the time scale change in the final diagram.) In regions 3, 4, 5, and 7, the parameter θ_∞ represents the finite time in which the solution becomes infinite.

The solution that exists on the special curves between these regions also offer simple insight into the nature of the solutions. The solutions are given in terms of functions that are more familiar making the nature of the solutions more evident. Between regions 1 and 3, and between 2 and 4, where $\gamma_2 = 0$ the solution is given by

$$ f = \frac{D}{\sqrt{\gamma_1}} \sinh[\sqrt{\gamma_1}\theta] + C \cosh[\sqrt{\gamma_1}\theta)]. \tag{A.5.26} $$

Between regions 1 and 2, where $\gamma_2 > 0$ and $\gamma_3 = 0$, the solution is the limit of (A.5.10) and (A.5.12) as $b \to 0$ and is given by

$$ f = a \, \text{sech} \left[\left(\frac{\gamma_2 a^2}{2} \right)^{\frac{1}{2}} (\theta_a - \theta) \right] . \tag{A.5.27} $$

where

$$ \theta_a = \left(\frac{2}{\gamma_2 a^2} \right)^{\frac{1}{2}} \text{sech}^{-1} \left[\frac{C}{a} \right] . $$

Between regions 3 and 4, where $\gamma_3 = 0$ the solution is the limit of (A.5.14) and (A.5.16) as $a \to 0$ and is given by

$$ f = b \, \text{csch} \left[\left(\frac{-\gamma_2 b^2}{2} \right)^{\frac{1}{2}} (\theta_\infty - \theta) \right] , \tag{A.5.28} $$

where

$$ \theta_\infty = \left(\frac{-2}{\gamma_2 b^2} \right)^{\frac{1}{2}} \text{csch}^{-1} \left[\frac{C}{b} \right] . $$

273

Appendices

Between regions 3 and 5, where $\gamma_3 = 0$ the solution is the limit of (A.5.14) and (A.5.18) as $b \to 0$ and is given by

$$f = a \csc \left[\left(\frac{-\gamma_2 a^2}{2} \right)^{\frac{1}{2}} (\theta_\infty - \theta) \right],$$

(A.5.29)

where from the initial conditions

$$\theta_\infty = \left(\frac{-2}{\gamma_2 a^2} \right)^{\frac{1}{2}} \csc^{-1} \left[\frac{C}{a} \right].$$

(A.5.30)

Between regions 4 and 7, where $\gamma_3 = (\gamma_1/\gamma_2)^2$ the solution is the limit of (A.5.18) as $b \to a$ and (A.5.24) as $a \to \infty$ and is given by

$$f = \gamma_3^{\frac{1}{4}} \csc \left[\left(\frac{-\gamma_2 \gamma_3}{2} \right)^{\frac{1}{2}} (\theta - \theta_b) \right],$$

(A.5.31)

where from the initial conditions

$$\theta_b = \left(\frac{2}{\gamma_2 a^2} \right)^{\frac{1}{2}} \csc^{-1} \left[\frac{C}{a} \right].$$

(A.5.32)

Between regions 5 and 7, where $\gamma_3 = (\gamma_1/\gamma_2)^2$ the solution is the limit of (A.5.18) as $b \to a$ and (A.5.24) as $a \to 0$ and is given by

$$f = \gamma_3^{\frac{1}{4}} \coth \left[\left(\frac{-\gamma_2 \gamma_3}{2} \right)^{\frac{1}{2}} (\theta - \theta_b) \right],$$

(A.5.33)

where from the initial conditions

$$\theta_b = \left(\frac{2}{-\gamma_2 \gamma_3} \right)^{\frac{1}{2}} \coth^{-1} \left[\frac{C}{a} \right].$$

(A.5.34)

Between regions 6 and 7, where $\gamma_3 = (\gamma_1/\gamma_2)^2$ the solution is the limit of (A.5.18) as $b \to a$ and (A.5.24) as $a \to 0$ and is given by

$$f = \gamma_3^{\frac{1}{4}} \tanh \left[\left(\frac{-\gamma_2 \gamma_3^{\frac{1}{2}}}{2} \right)^{\frac{1}{2}} (\theta - \theta_b) \right],$$
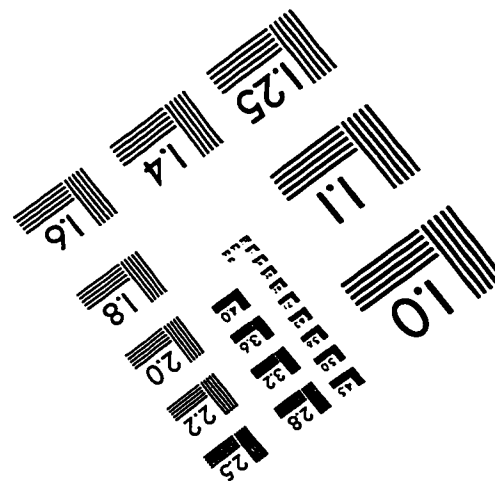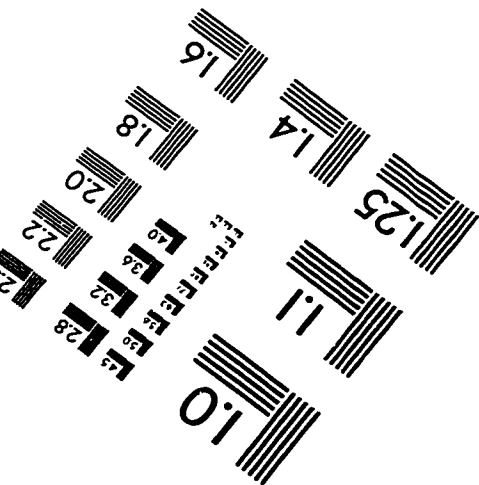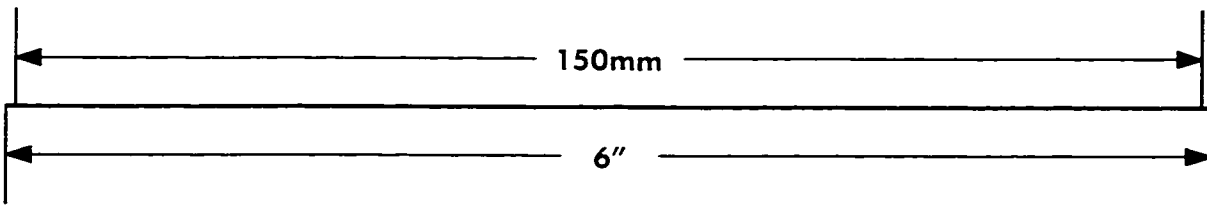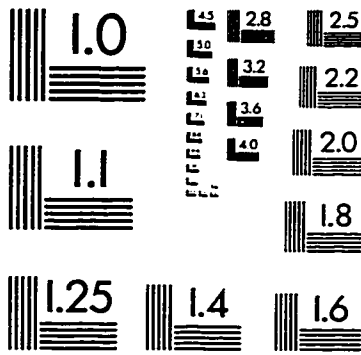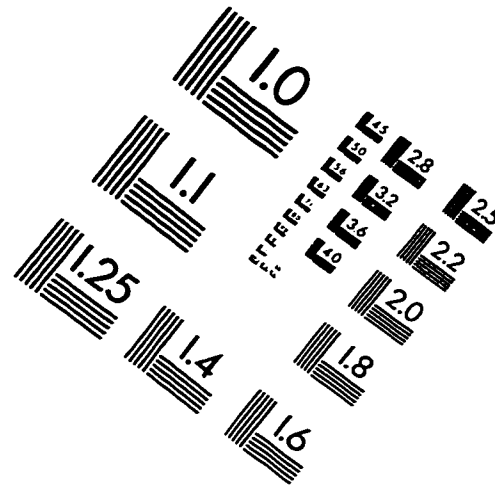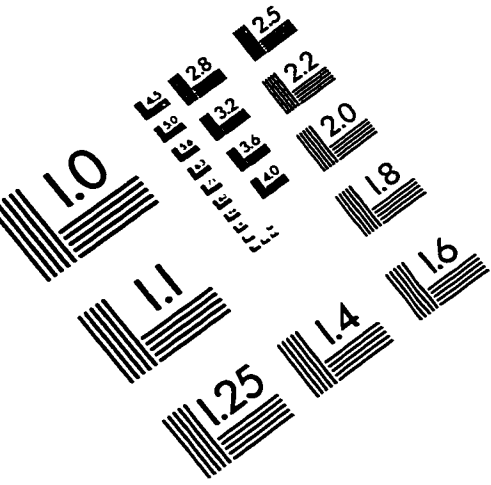
(A.5.35)

Appendices

where from the initial conditions

$$\theta_b = \left(\frac{2}{-\gamma_2 \gamma_3^{\frac{1}{2}}} \right)^{\frac{1}{2}} \tanh^{-1} \left[\frac{C}{\gamma_3^{\frac{1}{4}}} \right].$$
(A.5.36)

Soliton solutions are possible when θ represents a travelling-wave coordinate and f tends to zero (a constant) as $\theta \to \pm\infty$ for a bright (dark) soliton. From the phase diagrams and the solutions, it follows that solution (A.5.27) represents a bright soliton and solution (A.5.35) a dark soliton.

IMAGE EVALUATION
TEST TARGET (QA-3)

150mm

6"